BONE METASTASIS FOR SOLID TUMORS: FROM MECHANISMS TO CLINICAL TREATMENT

EDITED BY: Dianwen Song, Kotaro Nishida and Wangjun Yan
PUBLISHED IN: Frontiers in Oncology and Frontiers in Genetics

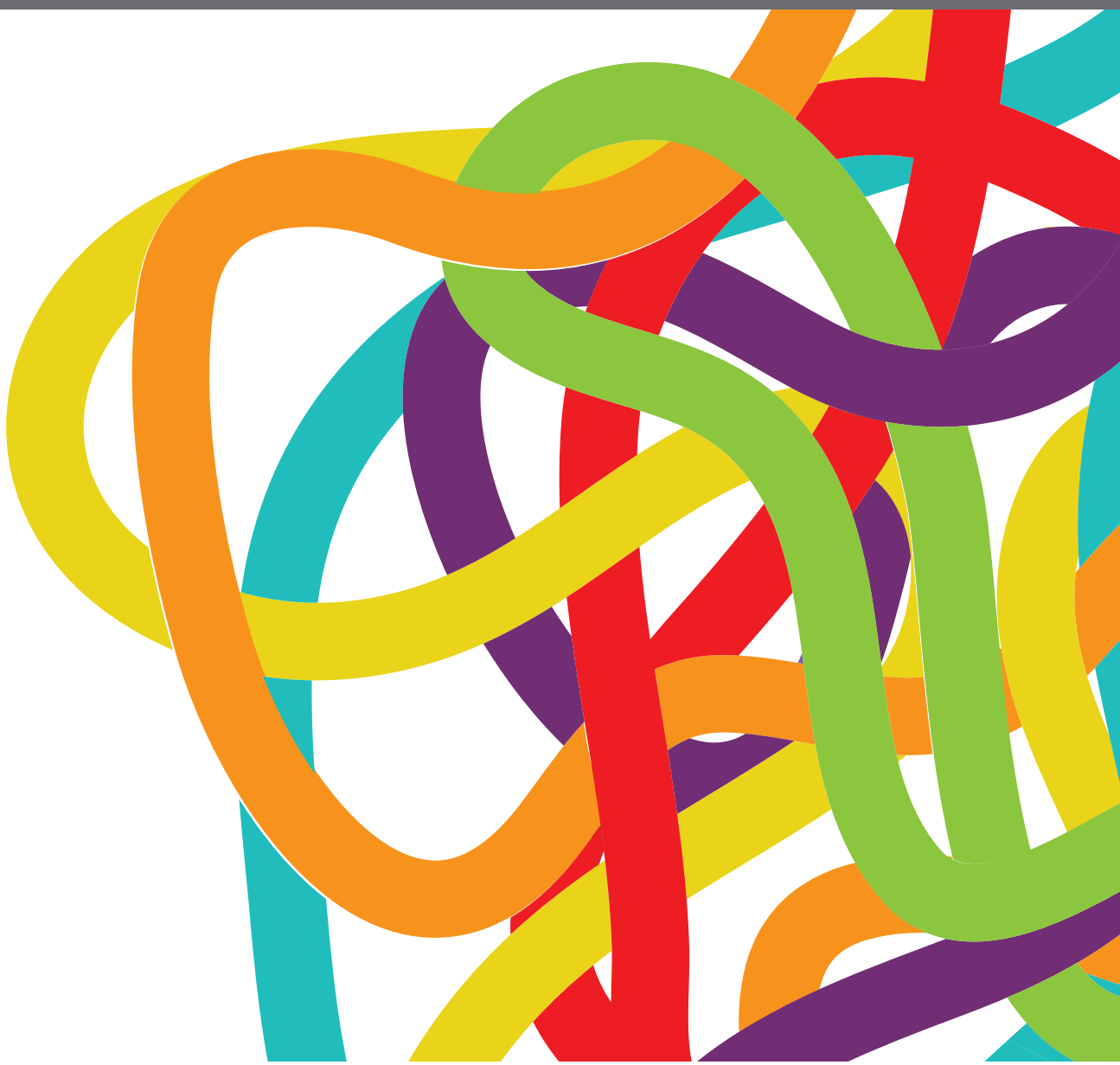

frontiers Research Topics

ISSN 1664-8714
ISBN 978-2-88974-183-0
DOI 10.3389/978-2-88974-183-0

About Frontiers

Frontiers is more than just an open-access publisher of scholarly articles: it is a pioneering approach to the world of academia, radically improving the way scholarly research is managed. The grand vision of Frontiers is a world where all people have an equal opportunity to seek, share and generate knowledge. Frontiers provides immediate and permanent online open access to all its publications, but this alone is not enough to realize our grand goals.

Frontiers Journal Series

The Frontiers Journal Series is a multi-tier and interdisciplinary set of open-access, online journals, promising a paradigm shift from the current review, selection and dissemination processes in academic publishing. All Frontiers journals are driven by researchers for researchers; therefore, they constitute a service to the scholarly community. At the same time, the Frontiers Journal Series operates on a revolutionary invention, the tiered publishing system, initially addressing specific communities of scholars, and gradually climbing up to broader public understanding, thus serving the interests of the lay society, too.

Dedication to Quality

Each Frontiers article is a landmark of the highest quality, thanks to genuinely collaborative interactions between authors and review editors, who include some of the world's best academicians. Research must be certified by peers before entering a stream of knowledge that may eventually reach the public - and shape society; therefore, Frontiers only applies the most rigorous and unbiased reviews.
Frontiers revolutionizes research publishing by freely delivering the most outstanding research, evaluated with no bias from both the academic and social point of view. By applying the most advanced information technologies, Frontiers is catapulting scholarly publishing into a new generation.

What are Frontiers Research Topics?

Frontiers Research Topics are very popular trademarks of the Frontiers Journals Series: they are collections of at least ten articles, all centered on a particular subject. With their unique mix of varied contributions from Original Research to Review Articles, Frontiers Research Topics unify the most influential researchers, the latest key findings and historical advances in a hot research area! Find out more on how to host your own Frontiers Research Topic or contribute to one as an author by contacting the Frontiers Editorial Office: frontiersin.org/about/contact

BONE METASTASIS FOR SOLID TUMORS: FROM MECHANISMS TO CLINICAL TREATMENT

Topic Editors:
Dianwen Song, Shanghai First People's Hospital, China
Kotaro Nishida, University of the Ryukyus, Japan
Wangjun Yan, Fudan University, China

Citation: Song, D., Nishida, K., Yan, W., eds. (2022). Bone Metastasis for Solid Tumors: From Mechanisms to Clinical Treatment. Lausanne: Frontiers Media SA. doi: 10.3389/978-2-88974-183-0

Table of Contents

frontiers in Oncology

ORIGINAL RESEARCH
published: 12 November 2020
doi: 10.3389/fonc.2020.588862

High Prevalence and Early Occurrence of Skeletal Complications in EGFR Mutated NSCLC Patients With Bone Metastases

*Marta Laganà[1], Cristina Gurizzan[1], Elisa Roca[1], Diego Cortinovis[2], Diego Signorelli[3], Filippo Pagani[3], Anna Bettini[4], Lucia Bonomi[4], Silvia Rinaldi[5], Rossana Berardi[5], Marco Filetti[6], Raffaele Giusti[6], Sara Pilotto[7], Michele Milella[7], Salvatore Intagliata[1], Alice Baggi[1], Alessio Cortellini[8], Hector Soto Parra[9], Matteo Brighenti[10], Fausto Petrelli[11], Chiara Bennati[12], Paolo Bidoli[2], Marina Chiara Garassino[3] and Alfredo Berruti[1]**

[1] Medical Oncology, Department of Medical and Surgical Specialties, Radiological Sciences and Public Health University of Brescia, ASST-Spedali Civili, Brescia, Italy, [2] Medical Oncology, Ospedale S. Gerardo di Monza, Monza, Italy, [3] Medical Oncology, Fondazione IRCCS Istituto Nazionale Tumori, Milano, Italy, [4] Medical Oncology, ASST Papa Giovanni XXIII di Bergamo, Bergamo, Italy, [5] Medical Oncology, Ospedali Riuniti di Ancona, Ancona, Italy, [6] Medical Oncology, Azienda Ospedaliero Universitaria S. Andrea di Roma, Roma, Italy, [7] Medical Oncology, Università degli studi di Verona, Azienda Ospedaliera Universitaria Integrata, Verona, Italy, [8] Medical Oncology, Ospedale San Salvatore di L'Aquila, L'Aquila, Italy, [9] Medical Oncology, Policlinico Vittorio Emanuele di Catania, Catania, Italy, [10] Medical Oncology, Ospedale di Cremona, Cremona, Italy, [11] Ospedale Treviglio, ASST Bergamo Ovest, Treviglio, Italy, [12] Ospedale Santa Maria delle Croci di Ravenna, Ravenna, Italy

OPEN ACCESS

Edited by:
Dianwen Song, Shanghai First People's Hospital, China

Reviewed by:
Abdul Malik Tyagi, Emory University, United States
Maria Francesca Baietti, VIB KU Leuven Center for Cancer Biology, Belgium

***Correspondence:**
Alfredo Berruti
alfredo.berruti@gmail.com

Specialty section:
This article was submitted to Molecular and Cellular Oncology, a section of the journal Frontiers in Oncology

Received: *20 August 2020*
Accepted: *19 October 2020*
Published: *12 November 2020*

Citation:
Laganà M, Gurizzan C, Roca E, Cortinovis D, Signorelli D, Pagani F, Bettini A, Bonomi L, Rinaldi S, Berardi R, Filetti M, Giusti R, Pilotto S, Milella M, Intagliata S, Baggi A, Cortellini A, Soto Parra H, Brighenti M, Petrelli F, Bennati C, Bidoli P, Garassino MC and Berruti A (2020) High Prevalence and Early Occurrence of Skeletal Complications in EGFR Mutated NSCLC Patients With Bone Metastases. Front. Oncol. 10:588862. doi: 10.3389/fonc.2020.588862

Objectives: The prevalence of Skeletal Related Adverse Events (SREs) in EGFR mutated non-small cell lung cancer (NSCLC) patients with bone metastases, treated with modern tyrosine kinase inhibitors (TKIs), has been scarcely investigated.

Materials and Methods: We retrospectively evaluated the data of EGFR mutated NSCLC patients with bone metastases treated with TKIs in 12 Italian centers from 2014 to 2019, with the primary aim to explore type and frequency of SREs.

Results: Seventy-seven out of 274 patients enrolled (28%) developed at least one major SRE: 55/274 (20%) bone fractures, 30/274 (11%) spinal cord compression, 5/274 (2%) hypercalcemia. Median time to the onset of SRE was 3.63 months. Nine patients (3%) underwent bone surgery and 150 (55%) radiation therapy on bone. SREs were more frequently observed within the 12 months from TKI start than afterwards (71 *vs* 29%, p 0.000). Patient Performance Status and liver metastases where independently associated with the risk of developing SREs. Median TKI exposure and overall survival were 11 and 28 months, respectively. Bone resorption inhibitors were associated with a lower risk of death (HR 0.722, 95% CI: 0.504–1.033, p = 0.075) although not statistically significant at multivariate analysis.

Conclusion: Bone metastatic NSCLC patients with EGFR mutated disease, treated with EGFR TKIs, have a relatively long survival expectancy and are at high risk to develop

SREs. The early SRE occurrence after the TKI start provides the rationale to administer bone resorption inhibitors.

Keywords: bone metastasis, non-small cell lung cancer, skeletal related events, tyrosine kinase inhibitors, epidermal growth factor receptor

INTRODUCTION

Lung cancer is the leading cause of cancer death worldwide (1).

Despite the introduction of modern efficacious therapies, the prognosis of patients with metastatic disease still remains poor although highly variable, being dependent on genomic abnormalities and programmed death-ligand 1 (PD-L1) expression (2).

Genetic analysis allows the identification of somatic sensitizing mutations in epidermal growth factor receptor (EGFR), typically exon 19 deletion (Ex19del) and L858R. These mutations are found in among 15% of lung adenocarcinoma in European patients (2).

First- or second-generation EGFR tyrosine kinase inhibitors (EGFR-TKIs) (e.g., erlotinib, gefitinib, and afatinib), administered to patients whose tumors harbor these genotype alterations, led to marked tumor response and improved progression-free survival and quality of life over chemotherapy (3–5). Thanks to these efficacious drugs the overall survival of patients with activating EGFR mutations has increased from a median of 7.9 months in 2002 to 27.3 months in 2015 (6).

The prognosis of these patients is destined to further improve with the recent introduction in clinics of the third generation EGFR-TKI osimertinib (7).

NSCLC often metastasizes to bone and the frequency of bone metastasis (BM) is 30–40% during the clinical course of the disease (8).

The diagnosis of BM negatively impacts on patient's quality of life (QoL) and is associated with poor survival (9). About 80% of bone metastatic lung cancer patients experience significant pain and more than 60% develop skeletal-related events (SREs), usually defined as bone surgery, bone radiation therapy, pathological fractures, spinal cord compression, and hypercalcemia (9).

SREs is therefore a composite endpoint, which encompasses both major complications, such as fractures, spinal cord compression, hypercalcemia, and local bone treatments, such as surgery and radiation therapy (10).

Published randomized clinical trials did not report whether the greater benefit obtained by modern TKIs over chemotherapy could translate or not into a fewer proportion of SREs (11).

The therapeutic strategies to manage BM and reduce the incidence of SREs include the administration of bisphosphonates (i.e. zoledronic acid) and Receptor Activator of Nuclear factor Kappa B Ligand (RANKL) inhibitors (denosumab). The results of a randomized prospective placebo controlled clinical trial have demonstrated that zoledronic acid is efficacious in preventing and delaying the SRE onset in lung cancer patients with bone metastases (10). In the same patient population, a subsequent prospective phase III randomized clinical trial demonstrated the superiority of denosumab over zoledronic acid in terms of prevention and delay of SREs (12). These randomized clinical trials were conducted before the introduction of TKIs in the management of lung cancer.

In this paper, we present the results of a retrospective multicenter study aiming to define the prevalence of SREs in EGFR mutated NSCLC patients, treated with first/second generation TKIs.

We also investigated the natural history of EGFR mutated NSCLC with BM, the prognostic factors, and the impact of bone resorption inhibitors on patient's outcome.

PATIENTS AND METHODS

Study Design

We conducted a retrospective, observational, multicenter study. Medical records of patients with bone metastases from EGFR-mutated NSCLC, treated with TKIs in 12 referral Italian centers from 2014 to 2019, were analyzed.

The primary aim of the study was to estimate the frequency of SREs. Secondary endpoints were to define in this study population overall survival, time to TKIs exposure and time to SRE. We also explored, both in univariate and multivariate analyses, prognostic factors, and factors predictive of SREs.

To be included in our study adult patients (≥18 years) with EGFR-mutated lung adenocarcinoma should have had bone metastatic involvement either at diagnosis or during the disease course (synchronous *versus* metachronous bone metastases) and identified through imaging assessment (e.g. standard x-rays, computed tomography scans, magnetic resonance imaging, or 18fluoro-deoxy-glucose positron-emission tomography of the skeleton). Patients with bone invasion by contiguity were excluded.

Clinical data were collected in an anonymized database, including demographic data such as age at cancer diagnosis, gender, Performance Status (PS) according to ECOG, major comorbidities, current or past smoking history, site and number of visceral metastases. We also recorded pathological data, including EGFR mutations, and blood chemistry data: i.e. alkaline phosphatase (ALP), lactate dehydrogenase (LDH), hemoglobin (HB).

For each patient, the type of TKI used was collected, specifying date of start and end of treatment. Dates of disease progression under TKI therapy (defined according Response Evaluation Criteria in Solid Tumors [RECIST] version 1.1), last follow-up, or death were also recorded.

Regarding bone involvement, the following data were collected: time of onset of BMs, if BMs were synchronous or metachronous with respect to first disease diagnosis; if they were osteolytic, osteoblastic, or mixed; and the number of bone sites involved. Furthermore, data about the occurrence of SREs, i.e. pathological

fractures, hypercalcemia, spinal cord compression, bone radiotherapy, and bone surgery, were collected as well as whether a specific bone anti-resorptive treatment (bisphosphonates or denosumab) was introduced or not.

The study was firstly approved by the Institutional Review Board of the Coordinating Center in Brescia (SURMOS Study no. NP1848) and subsequently by the ethic committees of each participating institution.

SURMOS study was conducted in accordance with the Declaration of Helsinki for clinical studies.

Statistical Analysis

The primary endpoint was to define the prevalence of major SREs (fractures, spinal cord compression, and hypercalcemia) in EGFR mutated NSCLC patients with bone metastases, treated with TKIs.

Among secondary endpoints, we evaluated: 1) the prevalence of SREs according to standard definition (including also bone surgery and bone radiation therapy), 2) overall survival, that was defined as the time interval between the date of diagnosis of bone metastases and the date of death or the last known alive date, 3) time between primary diagnosis and occurrence of bone metastases, 4) time to the occurrence of SRE from the diagnosis of bone metastases, i.e. the interval between date of diagnosis of bone metastases to the first occurrence of either bone fracture, spinal cord compression, or hypercalcemia, and 5) time of TKI exposure (from the start to the end of TKI treatment, even beyond disease progression).

Descriptive statistics were used for patients' demographics, tumor characteristics, and frequency of SREs. Categorized variables were expressed as percentages. Cut-off points were identified for continuous variables based on the median value or upper limit of normal ranges (for biochemical parameters).

Survival curves were calculated by the Kaplan-Meier method and differences compared by the log-rank test. The Cox's proportional hazards regression model was employed to assess the Hazard ratios (HRs) and 95% confidence intervals (95% CIs) both in univariate and multivariate analyses, with the lowest risk group as the reference group. Only parameters significantly associated with OS or time to SRE in the univariate analysis (at $p < 0.10$) were included in the multivariate analysis model.

All p values are two-sided and p values less than 0.05 were considered statistically significant. Due to the explorative nature of this study, a formal calculation of the sample size was not performed. It was considered, however, that a minimum of 200 patients would have been required to have an adequate power for statistical analyses. Statistical Package for Social Science, SPSS, software (version 23.00, Chicago, IL, USA) was used for statistical analysis.

RESULTS

Patient Characteristics and Treatment Administered

A total of 274 patients with bone metastatic, EGFR-mutated, NSCLC were collected to this study. Patient's characteristics are summarized in **Table 1**.

TABLE 1 | Patient's characteristics.

Patients number (274)	Characteristics	Number (%)
Gender	Female	171 (62)
	Male	103 (38)
Age at diagnosis	≥50 yrs	247 (90)
	<50 yrs	27 (10)
Smoking status	Yes	182 (66)
	No/Unknown	92 (34)
Performance status	0–1	222 (91)
	<1	21 (9)
	Missing	31
EGFR mutation	18/20	22 (9)
	19	144 (57)
	21	85 (34)
	Missing	23
EGFR mutation T790M	Yes	28 (55)
	No	23 (45)
	Missing	51
Number of metastatic sites	Only bone mets	12 (4)
	2 mets	36 (13)
	≥3	226 (83)
Synchronous mets	Yes	203 (74)
	No	71 (26)
Visceral mets	Yes	262 (96)
	No	12 (4)
Lung mets	Yes	162 (59)
	No	112 (41)
Liver mets	Yes	62 (23)
	No	212 (77)
Lymph nodes	Yes	205 (75)
	No	68 (25)
CNS mets	Yes	105 (38)
	No	169 (62)
Adrenal mets	Yes	41 (15)
	No	233 (85)
Comorbidities	Yes	133 (49)
	No	141 (51)
Bone mets	Osteolytic/Mixed	163 (66)
	Osteoblastic	84 (34)
	Missing	27
Number of bone mets sites	1–2	125 (47)
	3–4	83 (31)
	5–10	57 (22)
	Missing	9
Hemoglobin	≤12 g/dl (women); ≤14 (men)	85 (50)
	Normal value	84 (50)
	Missing	105
ALP	≥220 U/l	32 (26)
	Normal value	89 (74)
	Missing	153
LDH	≥300 U/l	70 (53)
	Normal value	63 (47)
	Missing	141
TKI	Gefitinib	184 (67)
	Erlotinib	43 (16)
	Afatinib	46 (17)
	Osimertinib	1 (0.4)

Clinical and pathological characteristics of patients with bone metastatic EGFR-mutated lung adenocarcinoma. (EGFR, epidermal growth factor receptor; CNS, central nervous system; ALP, alkaline phosphatase; LDH, lactate dehydrogenase; TKI, tyrosine kinase inhibitor).

The median age was 50 years, 171 (62%) were female and 103 (38%) were male. The PS, available in 243 (89%) cases, was 0–1 in 222 (91%) and higher than 1 in 21 (9%) patients, respectively. One hundred eighty-two patients (66%) had a history of smoking habit (present or past). The mutational status, available in 251

patients (92%), was as follows: exons 18 in 14 (6%), exon 19 in 144 (57%), exon 20 in 8 (3%), and exon 21 in 85 (34%) patients. Four patients presented compound EGFR mutations: 1 exon 18 and 21, 3 exon 18 and 20.

Twenty-eight out of 51 available patients (55%) presented T790M mutation.

One hundred eighty-four patients received gefitinib (67%), 46 afatinib (17%), 43 erlotinib (16%). One patient (0.4%) received osimertinib. The median time to TKI exposure was 11,1 months (95% Confidence Interval [CI]: 9,8–12,4).

In 203 patients (74%) BMs were synchronous with diagnosis of advanced NSCLC, while 71 patients (26%) developed bone metastasis during follow-up. In 12 patients (4%) bone was the only metastatic site, 13% had bone plus one metastatic site, and 83% had at least two different metastatic sites in addition to bone. Concomitant visceral metastatic sites were lung in 162 (59%), liver in 62 (23%), lymph nodes in 205 (75%), adrenal glands in 41 (15%), and Central Nervous System (CNS) in 105 (38%) patients respectively.

The burden of bone involvement was available in 265 patients (97%). It was limited (1–2 sites) in 125 (47%), intermediate (3–4 sites) in 83 (31%), and extensive (5–10 sites) in 57 cases (22%). Osteolytic and mixed bone lesions were documented in 163 (66%) cases, the remaining 84 (34%) patients had osteoblastic metastasis. In the minority of patients in which blood parameters were available, hemoglobin levels were often below the normal range and high levels of both ALP and LDH were frequently observed.

Skeletal-Related Events and Relevant Predictive Factors

A total of 173 adverse SREs were recorded in the 274 patients examined in the present study (63%). Seventy-seven (28%) developed at least one major SRE: 55/274 (20%) presented bone fractures, 5/274 (2%) hypercalcemia, 30/274 (11%) spinal cord compression. Fourteen patients (5%) developed both pathological fractures and spinal cord compression, three patients (1%) presented hypercalcemia and pathological fractures. Nine patients (3%) underwent bone surgery and 150/274 (55%) radiation therapy on bone (**Figure 1**).

The date of appearance of the first SRE was available in 135 out of the total of 173 SRE (78%). All the 77 major SREs were correctly placed during the treatment course. As shown on **Figure 2**, SREs occurred early after the diagnosis of BMs. In the patient subset who developed SREs, the median time to the onset of SRE from the diagnosis of BMs was 3.63 months (95% CI 0.79–6.47).

Forty-one (30%) patients developed the first event before TKI introduction, among the remaining 94 patients, 22/33 (67%) developed bone fractures within the first 12 months of TKI therapy and 11/33 (33%) afterwards; the corresponding distribution of spinal cord compression was 10/16 (63%) and 6/16 (37%), hypercalcemia: 2/4 (50%) and 2/4 (50%), bone surgery: 1/2 (50%) and 1/2 (50%), radiation therapy: 58/81 (72%) and 23/81 (28%), respectively (**Figure 3**).

One hundred and twenty-two patients (45%) received bone resorption inhibitors: 79 (29%) bisphosphonates, 46 (17%) denosumab, 3 patients (1%) received both drugs.

In the univariate analysis depicted in **Table 2**, PS and the presence of liver metastasis were significantly associated with the occurrence of SREs. Both variables maintained their predictive role in multivariate analysis: PS (HR 2.124, 95% CI: 1.046–4.313, p = 0.037), liver metastasis (HR 1.946, 95% CI: 1.169–3.239, p = 0.010).

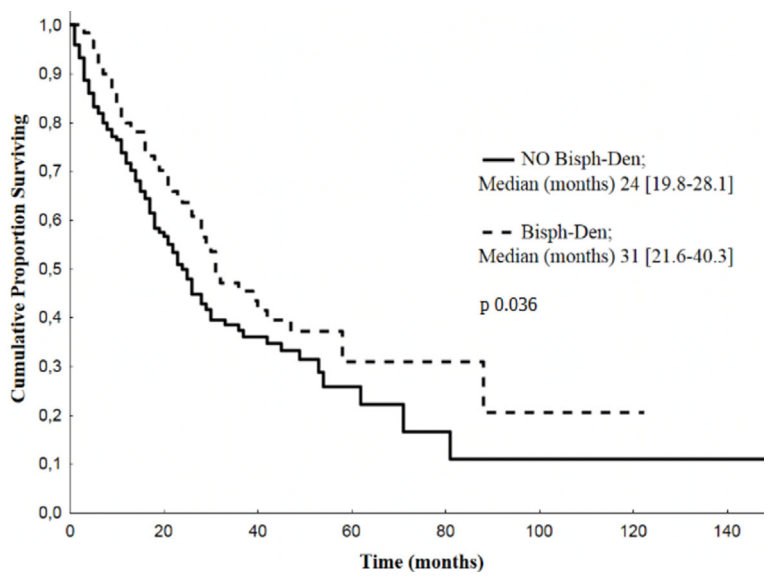

FIGURE 1 | Frequencies of SREs. Percentage and number of global SREs occurred after diagnosis of BM EGFR-mutated lung cancer (EGFR, epidermal growth factor receptor; SRE, skeletal related event; BM, bone metastases).

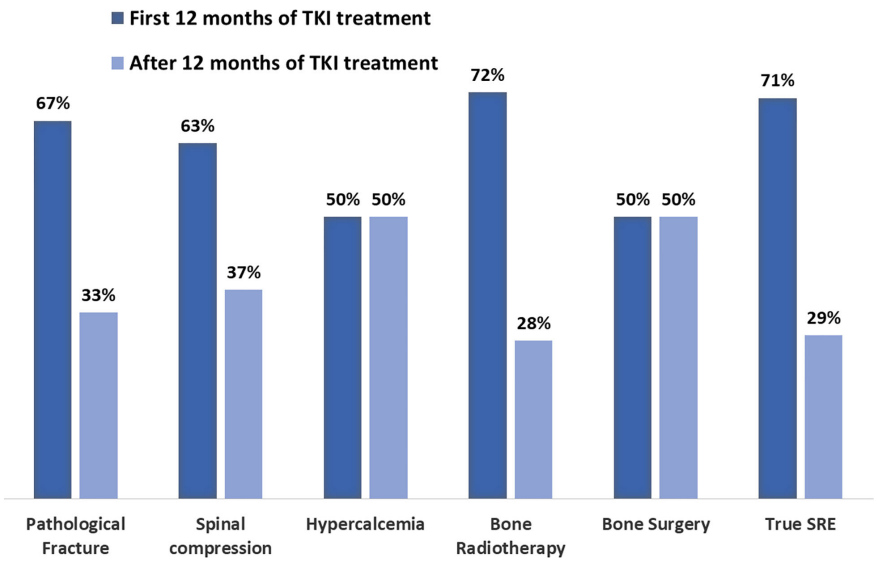

FIGURE 2 | Time to first SRE. Kaplan-Meier estimates of time from diagnosis of bone metastases to onset of first skeletal related event (SRE, skeletal related event).

Patient Prognosis and Survival Outcomes

Median follow-up of enrolled patients was 23 months (range 1–117). At the last follow-up examination, 152 patients (55%) were dead. Median overall survival (OS) from the diagnosis of bone metastases was 28 months (95% CI: 24.1–31.8) (**Figure 4**).

Median OS of patients who developed synchronous bone metastases was 29 months (95% CI: 22.8–35.2) as opposed to 24 months (range 15.4–32.6) of patients who presented metachronous bone metastases (p = 0.010).

Among the 33 potential prognostic factors analyzed in univariate analysis, the female gender (HR 0.684, 95% CI: 0.493–0.949, p = 0.023), EGFR Mutation of Exon 19 (HR 0.601, 95% CI: 0.416–0.867, p = 0.007) and the presence of synchronous bone metastasis (HR 0.631, 95% CI: 0.444–0.896, p= 0.010) were significantly associated with a lower risk of death.

On the contrary, smoking habit (HR 1.487, 95% CI: 1.061–2.084, p= 0.021), PS ≥ 2 (HR 1.877, 95% CI: 1.055–3.341, p = 0.032), ALP ≥220 U/I (HR 1.938, 95% CI: 1.147–3.276, p = 0.013), and LDH ≥300 U/I (HR 1.782, 95% CI: 1.126–2.821, p = 0.014) were significantly associated with a higher death risk (**Table 3**).

At multivariate analysis, smoking habit (HR 1.635, 95% CI: 1.134–2.356, p = 0.008), PS (HR 2.360, 95% CI: 1.296–4.297, p = 0.005), and the presence of synchronous bone metastasis (HR

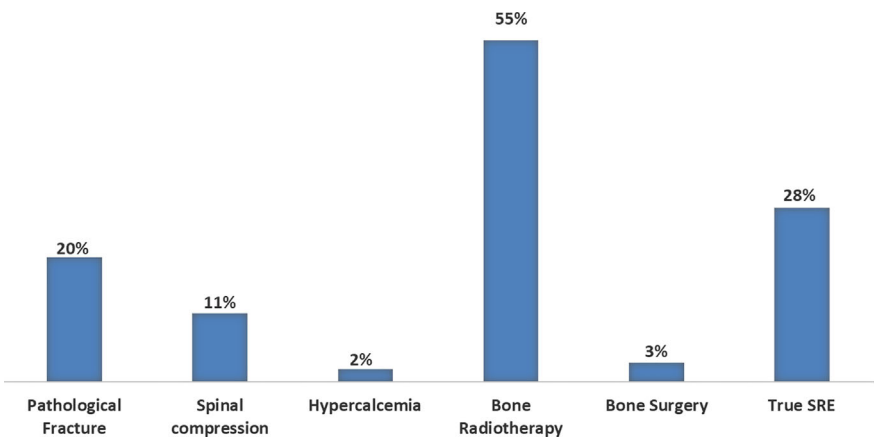

FIGURE 3 | Frequencies of SRE before and after the first 12 months of TKI treatment. Percentage and number of global SREs occurred after diagnosis of BM EGFR-mutated lung cancer before and after the first 12 months of TKI treatment, respectively (EGFR, epidermal growth factor receptor; SRE, skeletal related event; BM, bone metastases; TKI, tyrosine kinase inhibitor).

TABLE 2 | Predictive factors of SRE onset.

Time to SRE		Univariate analysis			Multivariate analysis		
		HR	95% CI	P	HR	95% CI	P
Gender	Female Male	0.713	0.451–1.125	0.146			
Age at diagnosis	≥50 <50	0.801	0.399–1.608	0.533			
Smoking status	Yes No/Unknown	1.425	0.893–2.273	0.137			
Performance status (ECOG)	≥2 0–1	2.103	1.037–4.263	**0.039**	2.124	1.046–4.313	**0.037**
EGFR mutation ex 19	Yes No	0.974	0.601–1.580	0.916			
Number of metastatic sites	Only BM	0.517	0.127–2.112	0.499			
	2	0.744	0.357–1.551	0.358			
	≥3			0.430			
Synchronous mets	Yes No	0.963	0.572–1.622	0.888			
Visceral mets	Yes No	1.233	0.718–2.118	0.448			
Lung mets	Yes No	0.931	0.737–1.177	0.550			
Liver mets	Yes No	1.741	1.070–2.833	**0.026**	1.946	1.169–3.239	**0.010**
Lymph nodes	Yes No	1.030	0.612–1.733	0.912			
SNC mets	Yes No	1.308	0.829–2.064	0.248			
Adrenal mets	Yes No	0.676	0.325–1.407	0.295			
Number of bone mets sites	1–2	0.671	0.382–1.178	0.337			
	3–4	0.691	0.374–1.275	0.165			
	5–10			0.237			
Hemoglobin	≤12 g/dl (women); ≤14 (men) Normal value	0.976	0.521–1.830	0.939			
ALP	≥220 U/l Normal value	1.725	0.798–3.729	0.166			
LDH	≥300 U/l Normal value	0.921	0.450–1.885	0.821			

Univariate and multivariate analyses of risk factors associated with SRE occurrence according to Cox's proportional hazards regression model (SRE, skeletal related event). Bold values denote statistical significance at the p < 0.005 level.

0.481, 95% CI: 0.328–0.707, p = 0.000) maintained a significant association with the death risk. Due to the low number of patients with available data, LDH and ALP were not included in the multivariate model.

The administration of bisphosphonates or denosumab was significantly associated with a lower risk of death at univariate analysis (HR 0.704, 95% CI: 0.507–0.978, p = 0.036) (**Figure 5**) with a tendency to maintain a prognostic significance at multivariate analysis (HR 0.722, 95% CI: 0.504–1.033, p = 0.075).

DISCUSSION

Bone metastases have a negative impact on quality of life and prognosis of lung cancer patients due to bone pain and the elevated risk of SREs (8). The frequency of SREs in EGFR mutated lung cancer with bone metastases have been scarcely documented in literature (**Table 4**) and the benefit of TKIs on bone pain and SREs prevention have not evaluated in randomized clinical trials (11). The natural history of the disease and frequency of SREs of lung cancer patients with bone metastases have been described in a large number of Italian patients (n = 661) (18). In this series, the median survival after bone metastases diagnosis was 9.5 months and the distribution of major SRE was 16% fractures, 6% spinal cord compression, and 2% hypercalcemia. In this paper, 30% of patients were treated of TKIs, but this subset was not analyzed separately.

In this multicenter retrospective series, involving bone metastatic patients with EGFR mutated NSCLC, the frequency of SREs, according to the standard definition that also includes bone surgery and radiation therapy was 58%. This proportion is similar to that reported in the above mentioned Italian series of bone metastatic lung cancer patients (18), 94.3% of them treated with chemotherapy. Also, the proportion of major SREs (28%), observed in the present study, is similar to that reported in the mentioned series as well as in other published bone metastatic

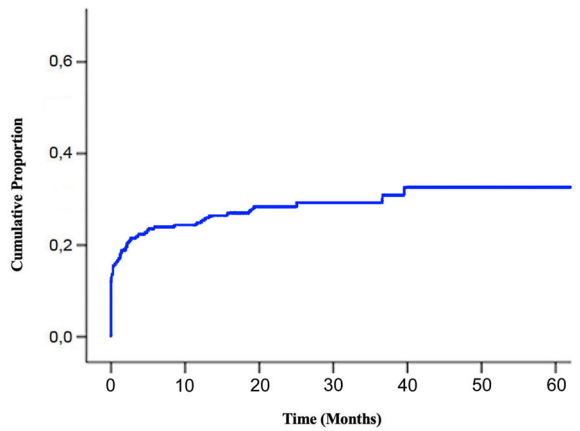

FIGURE 4 | Overall Survival of BM EGFR-mutated patients. Kaplan-Meier estimates of overall survival of EGFR-mutated lung cancer patients after diagnosis of bone metastases (BM, bone metastases; EGFR, epidermal growth factor receptor).

patient series with different primary histologies (19–21). The outcome of patients with EGFR mutated lung cancer with bone metastases have been evaluated in six published papers in which the SRE frequency was 0% in only one paper (22), while ranged between 20 and 51% in the remaining five papers (13–17) (**Table 4**). On the bases of these results, TKIs seem to be not effective in preventing SREs, despite their great efficacy in controlling the disease. This hypothesis is further strengthened by the short time from the diagnosis of BM to the appearance of SRE (3.63 months) observed in our series and the greater distribution of these events in the first 12 months, a period in which the tumor is generally responsive to TKIs.

Preclinical *in vivo* studies demonstrated that EGFR is essential for osteoblast proliferation (23) and down-regulated EGFR signaling was shown to favor the senescence of osteoprogenitors and the decline in bone formation on the endosteal surface of cortical bone (24). The administration of EGFR inhibitors, therefore, could impair the osteoblast mediated bone repair thus favoring the early occurrence of SREs despite the efficacy of these drugs. This hypothesis deserves to be further explored.

Wnt signaling is aberrantly activated in lung cancer (25). Abnormal activation of this pathway is implicated in driving the formation of lung cancer bone metastasis and has a relevant involvement in the cancer induced bone lesions (26). Moreover, Wnt signaling has also a significant negative impact on lung cancer prognosis and therapeutic resistance, specifically as regard as TKI therapy (25). On these bases there is a strong rationale for the testing drug targeting this pathway in association with currently available TKIs, with the aims of prevent bone progression, SREs and overcome/delay treatment resistance (25, 26).

The occurrence of SRE in prostate cancer patients is significantly associated with a poor prognosis (27). This was not the case in this series of TKI treated lung cancer patients. This observation may imply a long deterioration of quality of life in this patient subset in case of occurrence of an SRE.

The overall survival of 28 months, observed in this patient series does not differ from that observed in clinical trials and published case series (3–5), so the presence of bone metastases in TKI treated patients seem to be not related to poorer prognosis. The prognostic factors observed in univariate and multivariate analyses (i.e. ECOG Performance Status, smoking habit, and synchronous bone metastasis) in this study are in line to those observed in published series (3–5).

Several randomized prospective clinical trials have demonstrated that bone resorption inhibitors are efficacious in preventing SREs of bone metastatic lung cancer patients (10, 12). These trials were conducted before the introduction of TKIs in clinics, so we do not have a formal demonstration of their efficacy in this clinical setting. In the present series, these drugs failed to correlate with a lower SRE proportion, due to their delayed administration (i.e. after the onset of the first SRE) in many cases. The great proportion of SREs observed in the present study and their early onset provide a strong rationale for the introduction of bisphosphonates and denosumab in this setting. Interestingly, the administration of these drugs was associated with better prognosis, that just failed to attain the statistical significance in multivariate analysis. A positive effect of bisphosphonate administration on survival of EGFR mutated lung cancer patients submitted to TKIs was previously observed in 3 published series (13, 14, 22) (**Table 4**).

Despite the recommendation of using anti-bone reabsorption agents, only 45% of our population received these drugs and most of them start treatment after SREs onset. The reason could be related to the fact of TKI are expected to very efficacious in this setting. At last but not at least physicians are afraid of the possible occurrence of jawbone osteonecrosis, one of the most severe adverse reactions.

Bisphosphonates could enhance the antineoplastic effects of EGFR-TKIs in NSCLC with EGFR mutation both *in vitro* (28) and *in vivo* (14). Pertinently, the results of a randomized clinical trial of denosumab versus zoledronic acid in patients with various primary malignancies have shown a survival advantage favoring denosumab in the subset of patients with NSCLC (29). On the bases of this background, the synergism between bone resorption and EGFR inhibitors in lung cancer patients deserves to be explored.

The retrospective nature and the absence of a post progression analysis are the main limitations of this study.

CONCLUSIONS

In conclusion, bone metastatic NSCLC patients with EGFR mutated disease, treated with modern EGFR inhibitors, have a relatively long survival expectancy and are at high risk to develop skeletal related events. Since SREs occur early after the TKI start, there is a rationale to administer bone resorption inhibitors. Whether bisphosphonate or denosumab have the potential to improve survival when associated to TKIs is a matter of future research.

TABLE 3 | Prognostic factors of BM OS.

Overall Survival		Univariate analysis			Multivariate analysis		
		HR	95% CI	P	HR	95% CI	P
Gender	Female	0.684	0.493–0.949	**0.023**	0.740	0.514–1.064	0.104
	Male						
Age lung dg	≥50	1.167	0.645–2.111	0.610			
	<50						
Smoking status	Yes	1.487	1.061–2.084	**0.021**	1.635	1.134–2.356	**0.008**
	No/Unknown						
Performance status (ECOG)	≥ 2	1.877	1.055–3.341	**0.032**	2.360	1.296–4.297	**0.005**
	0–1						
EGFR mutation	18/20	0.601	0.416–0.867	0.014			
	19	1.010	0.557–1.831	**0.007**			
	21			0.974			
Number of metastatic sites	Only BM	0.812	0.356–1.848	0.829			
	2	0.908	0.566–1.458	0.619			
	≥3			0.690			
Synchronous mets	Yes	0.631	0.444–0.896	**0.010**	0.481	0.328–0.707	**0.000**
	No						
Visceral mets	Yes	0.865	0.603–1.239	0.429			
	No						
Lung mets	Yes	1.022	0.868–1.203	0.792			
	No						
Liver mets	Yes	0.872	0.724–1.050	0.149			
	No						
Lymph nodes	Yes	0.803	0.567–1.137	0.216			
	No						
SNC mets	Yes	1.335	0.967–1.844	0.079			
	No						
Adrenal mets	Yes	1.102	0.711–1.708	0.664			
	No						
Type of bone mets	Osteolytic	1.209	0.827–1.767	0.617			
	Mixed	1.155	0.697–1.913	0.328			
	Osteoblastic			0.577			
Number of bone mets sites	1–2	0.892	0.581–1.371	0.594			
	3–4	1.081	0.686–1.702	0.603			
	5–10			0.738			
Hemoglobin	≤12 g/dl (women); ≤14 (men)	1.229	0.817–1.851	0.323			
	Normal value						
ALP	≥220 U/l	1.938	1.147–3.276	**0.013**			
	Normal value						
LDH	≥300 U/l	1.782	1.126–2.821	**0.014**			
	Normal value						
Skeletal related events	Yes	0.976	0.679–1.403	0.894			
	No						
Pathological fracture	Yes	0.935	0.618–1.413	0.749			
	No						
Spinal compression	Yes	0.986	0.587–1.658	0.958			
	No						
Hypercalcemia	Yes	1.164	0.430–3.150	0.764			
	No						
Bone surgery	Yes	0.584	0.215–1.588	0.292			
	No						
Bone radiation therapy	Yes	1.105	0.794–1.537	0.554			
	No						
Denosumab/Bisphosphonate	Yes	0.704	0.507–0.978	**0.036**	0.722	0.504–1.033	0.075
	No						

Univariate and multivariate analyses of clinicopathological prognostic factors of OS in bone metastatic EGFR-mutated lung cancer patients according to Cox's proportional hazards regression model (BM, bone metastases; EGFR, epidermal growth factor receptor; OS, overall survival).
Bold values denote statistical significance at the p < 0.005 level.

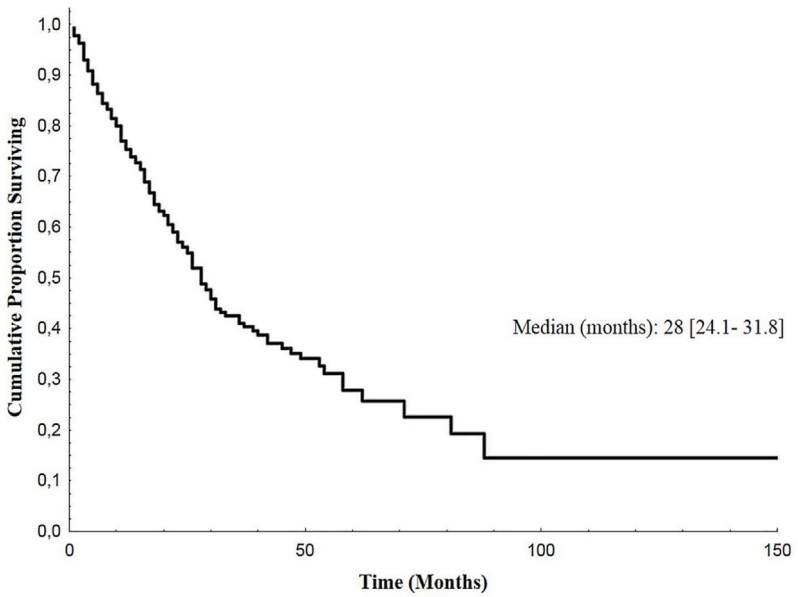

FIGURE 5 | Overall Survival according to administration of bone resorption inhibitors. Kaplan-Meier estimates of overall survival of EGFR-mutated lung cancer patients after diagnosis of bone metastases according to the administration of bisphosphonates/denosumab (EGFR, epidermal growth factor receptor).

TABLE 4 | Review of the literature.

Reference	N of BMpts EGFR+	SREsN (%)	Type ofSRE	Antiresorption treatment	Timeto SRE	OS (months)TKI alone	OS (months)TKI+BPH
Cui et al., *Oncol Lett* 2019 (13)	49	23 (47)	–	BPH (32 pts)	–	22	31
Huang et al., *Oncotarg* 2015	62	0 (0)	–	BPH (43 pts)	–	10.4	25.2
Zhang et al., *Sci Rep* 2017 (14)	356	70 (20)	–	BPH (111 pts)	–	19.5	20.5
Nagata et al., *Osaka City Med J* 2013 (15)	78	37 (47)	RT 15	–	14.2	–	–
Hendriks et al., *Lung Canc* 2014 (16)	37	19 (51)	–	–	12.9	–	–
Huang et al., *Oncotarg* 2017 (17)	201	75 (37)	RT 39 Surgery 3 Fracture 26 Spinal Comp 7	BPH (57 pts)	–	–	–

Analysis of six papers concerning outcome of patients with EGFR-mutated lung cancer with bone metastases (EGFR, epidermal growth factor receptor; SRE, skeletal related event; BPH, bisphosphonate; OS, overall survival; BM, bone metastases; TKI, tyrosine kinase inhibitor).

DATA AVAILABILITY STATEMENT

The raw data supporting the conclusions of this article will be made available by the authors, without undue reservation.

ETHICS STATEMENT

The study was firstly approved by the Institutional Review Board of the Coordinating Center in Brescia (SURMOS Study no. NP1848) and subsequently by the ethic committees of each participating institution.

AUTHOR CONTRIBUTIONS

All authors contributed to the study design and data collection for all the Italian institutions involved in the study. Material preparation and analysis were performed by ML and CG. The

first draft of the manuscript was written by ML, CG, and AlfB. All authors contributed to the article and approved the submitted version.

REFERENCES

1. Malvezzi M, Bertuccio P, Rosso T, Rota M, Levi F, La Vecchia C, et al. European cancer mortality predictions for the year 2015: does lung cancer have the highest death rate in EU women? *Ann Oncol* (2015) 26:779–86. doi: 10.1093/annonc/mdv001
2. Zappa C, Mousa SA. Non-small cell lung cancer: current treatment and future advances. *Transl Lung Cancer Res* (2016) 5:288–300. doi: 10.21037/tlcr.2016.06.07
3. Mok TS, Wu Y-L, Thongprasert S, Yang C-H, Chu D-T, Saijo N, et al. Gefitinib or Carboplatin–Paclitaxel in Pulmonary Adenocarcinoma. *N Engl J Med* (2009) 361:947–57. doi: 10.1056/NEJMoa0810699
4. Rosell R, Carcereny E, Gervais R, Vergnenegre A, Massuti B, Felip E, et al. Erlotinib versus standard chemotherapy as first-line treatment for European patients with advanced EGFR mutation-positive non-small-cell lung cancer (EURTAC): A multicentre, open-label, randomised phase 3 trial. *Lancet Oncol* (2012) 13:239–46. doi: 10.1016/S1470-2045(11)70393-X
5. Wu Y-L, Zhou C, Hu C-P, Feng J, Lu S, Huang Y, et al. Afatinib versus cisplatin plus gemcitabine for first-line treatment of Asian patients with advanced non-small-cell lung cancer harbouring EGFR mutations (LUX-Lung 6): an open-label, randomised phase 3 trial. *Lancet Oncol* (2014) 15:213–22. doi: 10.1016/S1470-2045(13)70604-1
6. Popat S. Osimertinib as First-Line Treatment in EGFR -Mutated Non–Small-Cell Lung Cancer. *N Engl J Med* (2018) 378:192–3. doi: 10.1056/NEJMe1714580
7. Ramalingam SS, Vansteenkiste J, Planchard D, Cho BC, Gray JE, Ohe Y, et al. Overall Survival with Osimertinib in Untreated, EGFR -Mutated Advanced NSCLC. *N Engl J Med* (2020) 382:41–50. doi: 10.1056/NEJMoa1913662
8. Kuchuk M, Kuchuk I, Sabri E, Hutton B, Clemons M, Wheatley-Price P. The incidence and clinical impact of bone metastases in non-small cell lung cancer. *Lung Cancer* (2015) 89:197–202. doi: 10.1016/j.lungcan.2015.04.007
9. Cho YJ, Cho YM, Kim SH, Shin KH, Jung ST, Kim HS. Clinical analysis of patients with skeletal metastasis of lung cancer. *BMC Cancer* (2019) 19:1–10. doi: 10.1186/s12885-019-5534-3
10. Rosen LS, Gordon D, Tchekmedyian NS, Yanagihara R, Hirsh V, Krzakowski M, et al. Long-term efficacy and safety of zoledronic acid in the treatment of skeletal metastases in patients with nonsmall cell lung carcinoma and other solid tumors. *Cancer* (2004) 100:2613–21. doi: 10.1002/cncr.20308
11. Vaidya A, Flores SK, Cheng Z-M, Nicolas M, Deng Y, Opotowsky AR, et al. EPAS1 Mutations and Paragangliomas in Cyanotic Congenital Heart Disease. *N Engl J Med* (2018) 378:1259–61. doi: 10.1056/NEJMc1716652
12. Henry DH, Costa L, Goldwasser F, Hirsh V, Hungria V, Prausova J, et al. Randomized, Double-Blind Study of Denosumab Versus Zoledronic Acid in the Treatment of Bone Metastases in Patients With Advanced Cancer (Excluding Breast and Prostate Cancer) or Multiple Myeloma. *J Clin Oncol* (2011) 29:1125–32. doi: 10.1200/JCO.2010.31.3304
13. Cui X, Li S, Gu J, Lin Z, Lai B, Huang L, et al. Retrospective study on the efficacy of bisphosphonates in tyrosine kinase inhibitor–treated patients with non–small cell lung cancer exhibiting bone metastasis. *Oncol Lett* (2019) 18 (5):5437–47. doi: 10.3892/ol.2019.10870
14. Zhang G, Cheng R, Zhang Z, Jiang T, Ren S, Ma Z, et al. Bisphosphonates enhance antitumor effect of EGFR-TKIs in patients with advanced EGFR mutant NSCLC and bone metastases. *Sci Rep* (2017) 7:42979. doi: 10.1038/srep42979
15. Nagata M, Kudoh S, Mitsuoka S, Suzumura T, Umekawa K, Tanaka H, et al. Skeletal-related events in advanced lung adenocarcinoma patients evaluated EGFR mutations. *Osaka City Med J* (2013) 59(1):45–52.
16. Hendriks LEL, Smit EF, Vosse BAH, Mellema WW, Heideman DAM, Bootsma GP, et al. EGFR mutated non-small cell lung cancer patients: More prone to development of bone and brain metastases? *Lung Cancer* (2014) 84:86–91. doi: 10.1016/j.lungcan.2014.01.006
17. Huang S-M, Yang J-J, Chen H-J, Wu S-P, Bai X-Y, Zhou Q, et al. Epidermal growth factor receptor is associated with the onset of skeletal related events in non-small cell lung cancer. *Oncotarget* (2017) 8:81369–76. doi: 10.18632/oncotarget.18759
18. Santini D, Barni S, Intagliata S, Falcone A, Ferraù F, Galetta D, et al. Natural History of Non-Small-Cell Lung Cancer with Bone Metastases. *Sci Rep* (2015) 5:18670. doi: 10.1038/srep18670
19. Berruti A, Libè R, Laganà M, Ettaieb H, Sukkari MA, Bertherat J, et al. Morbidity and mortality of bone metastases in advanced adrenocortical carcinoma: a multicenter retrospective study. *Eur J Endocrinol* (2019) 180:311–20. doi: 10.1530/EJE-19-0026
20. Grisanti S, Bianchi S, Locati LD, Triggiani L, Vecchio S, Bonetta A, et al. Bone metastases from head and neck malignancies: Prognostic factors and skeletal-related events. *PLoS One* (2019) 14:e0213934. doi: 10.1371/journal.pone.0213934
21. Iacovelli R, Santini D, Rizzo M, Felici A, Santoni M, Verzoni E, et al. Bone metastases affect prognosis but not effectiveness of third-line targeted therapies in patients with metastatic renal cell carcinoma. *Can Urol Assoc J* (2015) 9:263. doi: 10.5489/cuaj.2377
22. Huang C-Y, Wang L, Feng C-J, Yu P, Cai X-H, Yao W-X, et al. Bisphosphonates enhance EGFR-TKIs efficacy in advanced NSCLC patients with EGFR activating mutation: A retrospective study. *Oncotarget* (2016) 7:66480–90. doi: 10.18632/oncotarget.5515
23. Linder M, Hecking M, Glitzner E, Zwerina K, Holcmann M, Bakiri L, et al. EGFR controls bone development by negatively regulating mTOR-signaling during osteoblast differentiation. *Cell Death Differ* (2018) 25:1094–106. doi: 10.1038/s41418-017-0054-7
24. Liu G, Xie Y, Su J, Qin H, Wu H, Li K, et al. The role of EGFR signaling in age-related osteoporosis in mouse cortical bone. *FASEB J* (2019) 33:11137–47. doi: 10.1096/fj.201900436RR
25. Yang J, Chen J, He J, Li J, Shi J, Cho WC, et al. Wnt signaling as potential therapeutic target in lung cancer. *Expert Opin Ther Targets* (2016) 20:999–1015. doi: 10.1517/14728222.2016.1154945
26. Xi Y, Chen Y. Wnt signaling pathway: implications for therapy in lung cancer and bone metastasis. *Cancer Lett* (2014) 353:8–16. doi: 10.1016/j.canlet.2014.07.010
27. Oefelein MG, Ricchiuti V, Conrad W, Resnick MI. Skeletal Fractures Negatively Correlate With Overall Survival in Men With Prostate Cancer. *J Urol* (2002) 168:1005–7. doi: 10.1016/S0022-5347(05)64561-2
28. Chang JW-C, Hsieh J-J, Shen Y-C, Yeh K-Y, Wang C-H, Li Y-Y, et al. Bisphosphonate zoledronic acid enhances the inhibitory effects of gefitinib on EGFR-mutated non-small cell lung carcinoma cells. *Cancer Lett* (2009) 278:17–26. doi: 10.1016/j.canlet.2008.12.019
29. Scagliotti GV, Hirsh V, Siena S, Henry DH, Woll PJ, Manegold C, et al. Overall Survival Improvement in Patients with Lung Cancer and Bone Metastases Treated with Denosumab Versus Zoledronic Acid: Subgroup Analysis from a Randomized Phase 3 Study. *J Thorac Oncol* (2012) 7:1823–9. doi: 10.1097/JTO.0b013e31826aec2b

ACKNOWLEDGMENTS

We are grateful to our patients and their families.

Conflict of Interest: The authors declare that the research was conducted in the absence of any commercial or financial relationships that could be construed as a potential conflict of interest.

frontiers in Oncology

ORIGINAL RESEARCH
published: 17 November 2020
doi: 10.3389/fonc.2020.596330

Prognostic Significance of Cyclin E1 Expression in Patients With Chordoma: A Clinicopathological and Immunohistochemical Study

Ran Wei[1,2], Dylan C. Dean[2], Pichaya Thanindratarn[2,3], Francis J. Hornicek[2], Wei Guo[1] and Zhenfeng Duan[2]**

[1] Musculoskeletal Tumor Center, Beijing Key Laboratory of Musculoskeletal Tumor, Peking University People's Hospital, Beijing, China, [2] Sarcoma Biology Laboratory, Department of Orthopedic Surgery, David Geffen School of Medicine at UCLA, Los Angeles, CA, United States, [3] Department of Orthopedic Surgery, Chulabhorn Hospital, HRH Princess Chulabhorn College of Medical Science, Bangkok, Thailand

OPEN ACCESS

Edited by:
Dianwen Song, Shanghai First People's Hospital, China

Reviewed by:
Yi Ding, Geisinger Health System, United States
Francesca Benedetti, University of Maryland, United States

***Correspondence:**
Wei Guo
bonetumor@163.com
Zhenfeng Duan
zduan@mednet.ucla.edu

Specialty section:
This article was submitted to Molecular and Cellular Oncology, a section of the journal Frontiers in Oncology

Received: *19 August 2020*
Accepted: *19 October 2020*
Published: *17 November 2020*

Citation:
Wei R, Dean DC, Thanindratarn P, Hornicek FJ, Guo W and Duan Z (2020) Prognostic Significance of Cyclin E1 Expression in Patients With Chordoma: A Clinicopathological and Immunohistochemical Study. Front. Oncol. 10:596330. doi: 10.3389/fonc.2020.596330

Purpose: Chordomas are rare, slow-growing sarcomas without any accepted prognostic biomarkers. Owing to their proximity to critical neurovascular structures, discovering predictive biomarkers in chordoma has been a significant research effort because it may potentially reduce risky therapies in patients with less aggressive tumors. In response, because cyclin E1 overexpression correlates with patient prognosis in several malignancies, we investigated its expression in chordoma and whether it informs patient prognosis.

Methods: Seventy-five chordoma patient specimens were enrolled in a tissue microarray (TMA) to evaluate cyclin E1 expression *via* immunohistochemical staining. Western blot was used to assess cyclin E1 expression in chordoma cell lines and fresh tissues. We then correlated cyclin E1 staining intensity in the TMA to clinicopathological features and chordoma patient outcomes.

Results: Sixty-three percent of the chordoma patient specimens in the TMA, fifty-six percent of the fresh chordoma tissues, and all chordoma cell lines showed high cyclin E1 expression. In TMA analysis, cyclin E1 expression positively correlated to chordoma patient disease status. By survival analysis, high cyclin E1 expression was an independent prognostic risk factor for chordoma patients along with advanced disease status and positive surgical margin.

Conclusion: Cyclin E1 is a promising biomarker predicting chordoma patient prognosis.

Keywords: chordoma, cyclin E1, prognosis, biomarker, tissue microarray, immunohistochemical staining

INTRODUCTION

Chordomas are rare bone sarcomas that arise from the transformed remnants of notochord, with an incidence of 0.1/100,000 people per year (1). It principally affects elderly patients at the skull base (41.1%), mobile spine (27.4%) and sacrum (31.5%) (2). Surgery is the cornerstone therapeutic modality for chordoma, with adequate surgical margins representing the primary clinical goal for a favorable prognosis (3–5). And although the 5-year survival rate for chordoma patients is an optimistic 70-81%, local recurrence and subsequent metastasis occurs approximately half the time after surgery, with no systemic therapies having shown major benefit (1, 5, 6). And while their diagnosis is made according to clinicopathological features and brachyury expression which is a prominent transcription factor in notochord development, brachyury is a diagnostic biomarker and therapeutic target rather than a prognostic biomarker (7–10). In short, there are no well-recognized biomarkers predictive of chordoma patient prognosis. For the patient, the lack of accurate predictive biomarkers can result in overtreatment of less aggressive chordomas *via* surgery or adjuvant radiation therapy. In addition, even with aggressive surgery, recurrent rates remain high. There is, therefore, an urgent need for the identification of chordoma biomarkers to better ascertain patient prognosis and whether high-risk surgeries or adjuvant therapies are indicated.

Cyclin E1 was originally described in 1991 as the prototype cyclin E. It is a 47 kDa protein localized within both the nucleus and cytoplasm (11). By complexing with cyclin-dependent kinase 2 (CDK2), it phosphorylates numerous downstream proteins such as Rb and is strong promoter of G1-S transition, a well-known tumorigenic step (12). Cyclin E1 overexpression has been investigated in more common malignancies, and has shown to correlate with therapeutic response and prognosis (13–18). Despite these established findings in other cancers, the expression and clinical significance of cyclin E1 in chordoma is unknown.

In response, we sought to investigate the expression of cyclin E1 in chordoma and its correlation, if any, to clinicopathologic features or prognosis within chordoma patients. To our knowledge, this is the first and only work evaluating cyclin E1 expression in chordoma and its clinical significance.

MATERIALS AND METHODS

Ethics

The study protocol and the consent of the informed patients were approved by the Partners Human Research Committee (number: 2007-P-002464/5) of Partners HealthCare as previously described (19). All patients provided their written informed consent to participate in this study.

Chordoma Tissue Samples and Tissue Microarray

Seventy-five chordoma patient specimens in formalin fixed paraffin embedded (FFPE) blocks obtained during surgery were used to construct the tissue microarray (TMA) as previously described (19). The inclusion criteria included: 1) patients with chordoma confirmed by histological diagnosis; 2) patients underwent surgical treatment; 3) patients with complete clinical and follow-up data. The exclusion criteria included: 1) peri-operative death; 2) patients with incomplete clinical and follow-up data. The demographic and clinical information of 75 patients was reviewed and documented from a prospective database. In the course of the TMA construction, three sites of each FFPE block were selected to assemble the recipient master block. Representative triplicate 0.5 mm diameter core biopsies of each tissue block were obtained through pathology reports and pathologist read hematoxylin and eosin (HE)-stained slides. In addition, nine fresh chordoma tissue samples were obtained for study.

Immunohistochemistry Staining and Assessment

Immunohistochemistry (IHC) staining was performed to evaluate for cyclin E1 expression. In brief, the paraffin-embedded slide was baked for 1 h at 60°C before xylene deparaffinization. The slide was then rehydrated through graded ethanol (100% and 95%). We then used 3% hydrogen peroxide to quench endogenous peroxidase activity after heated epitope retrieval. After blocking for 1 h with normal goat serum, the slide was incubated with polyclonal rabbit antibody to human cyclin E1 (Cell Signaling Technology, MA, USA. Catalog# 20808S) overnight in a humidified chamber set at 4°C. Afterwards, the bound antibody was detected by SignalStain® Boost Detection Reagent (Cell Signaling Technology, MA, USA) and SignalStain® DAB (Cell Signaling Technology, MA, USA). Finally, all sections were counterstained with Hematoxylin QS (Vector Laboratories, CA, USA), and the slide was mounted with VectaMount AQ (Vector Laboratories, CA, USA) for long-term preservation.

Two independent pathologists blinded to patient clinical information and tumor characteristics assessed and scored the IHC-stained slide. Cyclin E1 expression was scored and categorized according to the staining intensity of chordoma tissues: 0, no staining; 1+, weak staining; 2+, moderate staining; 3+, strong staining. The low cyclin E1 expression subset included group 0 and 1+, while the high cyclin E1 expression subset included group 2+ and 3+ (**Figure 1**). A Nikon Eclipse Ti-U fluorescence microscope (Diagnostic Instruments Inc., MI, USA) with a SPOT RT™ digital camera (Diagnostic Instruments Inc., MI, USA) was used to obtain cyclin E1 staining images.

Human Chordoma Cell Lines and Cell Culture

The human chordoma cell line UCH2 was established and kindly provided by Dr. Silke Brüderlein (University Hospitals of Ulm, Ulm, Germany) (20). The cell line CH22 was established in our laboratory as previously reported (21). The UCH2 and CH22 cells were incubated at 37°C with 5% CO_2 in Dulbecco's Modified Eagle Medium (DMEM) (Life Technologies Corp.,

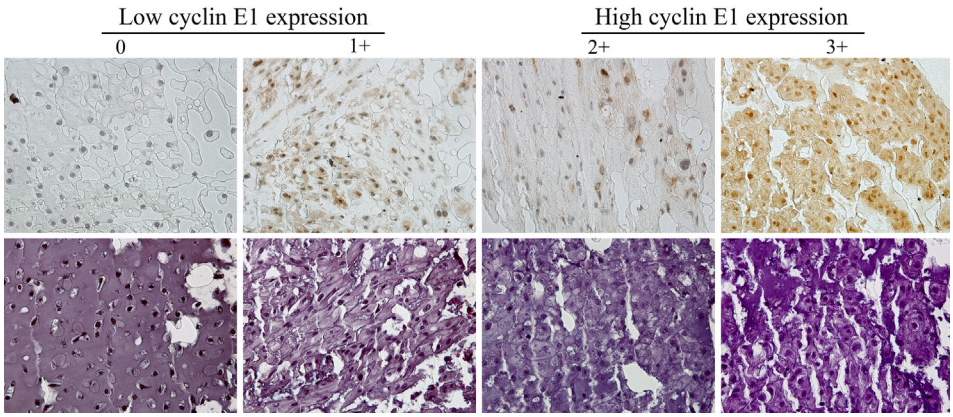

FIGURE 1 | Assessment of cyclin E1 expression in the chordoma tissue microarray by immunohistochemistry. Different immunohistochemistry staining intensities of cyclin E1 and HE in chordoma tissues are shown in representative images. Staining patterns were divided into 4 groups: 0, no staining; 1+, weak staining; 2+, moderate staining; 3+, strong staining (Original magnification, 400×). Low and high cyclin E1 expression groups included chordoma specimens with the staining score of 0 to 1+ and 2+ to 3+, respectively.

NY, USA) supplemented with 10% fetal bovine serum (Sigma-Aldrich, MO, USA) and 1% penicillin/streptomycin (Life Technologies, CA, USA).

Protein Preparation and Western Blot

We used 1× RIPA lysis buffer (Sigma-Aldrich, MO, USA) combined with protease inhibitor cocktail tablets (Roche Applied Science, IN, USA) to extract protein from cells and fresh tissues. The DC™ protein assay reagents (Bio-Rad, CA, USA) and a spectrophotometer SPECTRA max 340PC (Molecular Devices, LLC., CA, USA) were then used to determine the protein lysate concentrations. Briefly, our Western blot protocol began with an SDSPAGE gel to run the denatured proteins before transfer to nitrocellulose membranes. These membranes were incubated with monoclonal rabbit antibodies to human cyclin E1 (1:1,000 dilution, Cell Signaling Technology, MA, USA) and mouse monoclonal antibody for human β-actin (1:20,000 dilution, Sigma-Aldrich, MO, USA) at 4°C overnight after they were blocked in Odyssey Blocking Buffer (Li-COR Biosciences, NE, USA) for 1 h. Following incubation with the primary antibody, TBST was used as a membrane wash (4 times for 5 min each at room temperature). Next, goat anti-rabbit IRDye 800CW (926–32,211, 1:5,000 dilution) and goat anti-mouse IRDye 680LT secondary antibody (926–68,020, 1:15,000 dilution) (Li-COR Biosciences, NE, USA) were applied for 1 h at room temperature followed by another TBST membrane wash (four times for 5 min each at room temperature). Bands were detected using Odyssey Infrared Fluorescent Western Blot Imaging System from Li-COR Bioscience (NE, USA), and Odyssey software 3.0 was used to quantify the bands.

Statistical Analysis

GraphPad Prism 7 software (GraphPad Software, CA, USA) and SPSS 19.0 software (IBM Corp., Armonk, New York) were used for statistical analyses. Nonparametric testing (Mann-Whitney U test) was performed to compare the two groups and determine statistical significance. One-way analysis of variance and the least-significant difference test were performed for multiple comparisons. As for the survival analysis, overall survival (OS) was defined as the time from surgery (when the tissue was obtained) to death of the patient. Recurrence-free survival (RFS) was defined as the time from the surgery to the first local recurrence after this surgery. Metastasis-free survival (MFS) was defined as the time from surgery to the detection of new onset metastasis. The survival curves were produced by Kaplan-Meier methods. The relation between various key factors and OS, RFS, or MFS was evaluated by Cox regression both univariately and multivariately. Only those factors that were statistically significant ($P<0.05$) in the univariate analysis were involved in the multivariate analysis. A P-value < 0.05 was considered significant.

RESULTS

Clinicopathological Characteristics of 75 Chordoma Patients Enrolled in TMA

The demographic and clinicopathological characteristics of 75 patients are shown in **Table 1**. There were 53 (70.7%) males and 22 (29.3%) females, with an average age of 59.5 ± 13.7 years. Thirty-one patients (41.3%) were treated for primary localized lesions while 44 patients (58.7%) had advanced disease, including 39 patients treated for recurrent lesions and 5 patients with metastasis. The majority of the lesions were located at sacrum (44, 58.7%). Surgeries were performed through an anterior and posterior approach in most patients (47, 62.7%), and negative surgical margins were completed in 18 patients (24.0%). Neoadjuvant radiation was performed in 57 patients (76.0%)

TABLE 1 | Demographic and clinical information of 75 chordoma patients enrolled in a tissue microarray.

Variables		N (%) or mean ± SD
Age		59.5 ± 13.7 years
Sex	Male	53 (70.7)
	Female	22 (29.3)
Location of lesion	Sacrum	44 (58.7)
	Mobile spine	31 (41.3)
Disease status	Primary	31 (41.3)
	Advanced	44 (58.7)
	Recurrent	39 (52.0)
	Metastatic	5 (6.7)
Surgical approach	Posterior only	28 (37.3)
	Anterior and posterior	47 (62.7)
Margin	Negative	18 (24.0)
	Positive	57 (76.0)
Neoadjuvant radiation	Received	57 (76.0)
	Not received	18 (24.0)
Follow-up time		77.5 ± 54.2 months

without detailed information regarding the type and dose of the radiation.

Cyclin E1 Is Highly Expressed in Chordoma

Cyclin E1 expression was first evaluated in TMA by IHC staining. Among 75 specimens, no staining was found in 10 specimens (13.3%) with the remaining 65 specimens having various staining intensities, including 1+ staining in 18 specimens (24.0%), 2+ staining in 23 specimens (30.7%), and 3 + staining in 24 specimens (32.0%) (**Figure 2A**). According to the aforementioned categorization criteria, high and low cyclin E1 expression was found in 47 (62.7%) and 28 (37.3%) specimens, respectively (**Figure 2B**).

We further evaluated cyclin E1 expression in nine fresh chordoma tissues and two chordoma cell lines. All chordoma tissue samples showed cyclin E1 expression, including five with

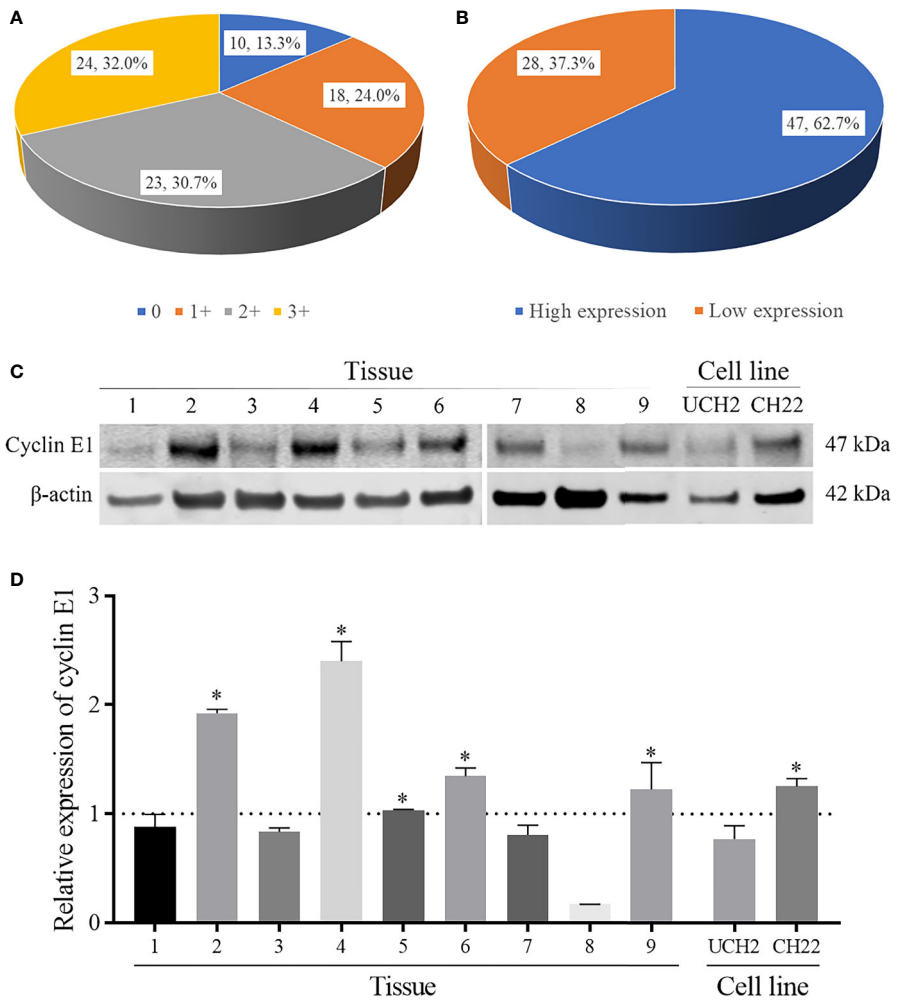

FIGURE 2 | The expression levels of cyclin E1 in chordoma. **(A, B)** Pie chart showing frequency and percentage of different cyclin E1 expression levels and high/low cyclin E1 expression groups in chordoma tissue microarrays. **(C)** Western blots showing cyclin E1 expression in nine chordoma fresh tissues and cell lines (UCH2 and CH22). **(D)** Densitometry quantification of the Western blots of cyclin E1 from **Figure 2C**, presented as relative to β-actin expression. The data are presented in as mean ± SD of the experiment carried out in triplicate. * means the expression of cyclin E1 is stronger than the β-actin, indicating high cyclin E1 expression.

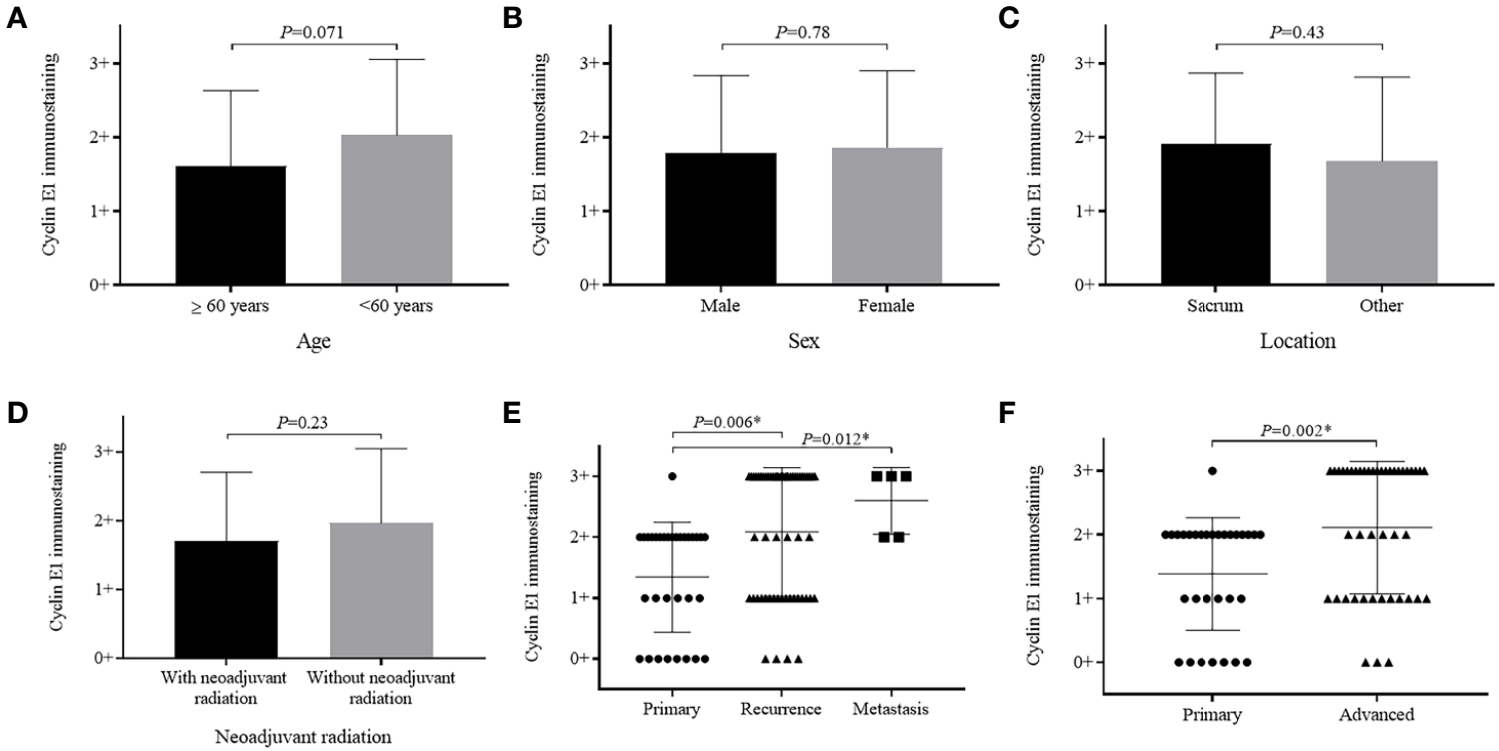

FIGURE 3 | Relationship between cyclin E1 expression and clinicopathological characteristics of chordoma patients. Graphics illustrate no significant differences in cyclin E1 expression level among patients based on **(A)** age group, **(B)** sex, **(C)** tumor location or **(D)** with and without neoadjuvant radiation. Significant differences were observed in cyclin E1 expression based on patient disease status **(E, F)**. *Statistical significance.

high expression (55.6%) and 4 with low expression (44.4%). In chordoma cell lines, Western blots showed cyclin E1 was expressed in both UCH2 and CH22, with CH22 having notably high expression. (**Figures 2C, D**)

Cyclin E1 Expression Correlated With Disease Status of Chordoma Patients

Cyclin E1 expression did not significantly vary based on patient age, sex, or lesion location (**Figures 3A–C**). When patients with and without neoadjuvant radiation were compared, cyclin E1 expression was weaker in radiation-treated patients versus those without radiation, but did not meet statistical significance (1.7 ± 1.0 versus 2.0 ± 1.1, *P*=0.23) (**Figure 3D**).

Importantly, patients who had recurrent and metastatic chordomas prior to surgery showed significantly higher cyclin E1 expression compared to those patients with primary lesions (recurrence versus primary, 2.1 ± 1.1 versus 1.4 ± 0.9, *P*=0.006; metastasis versus primary, 2.6 ± 0.5 versus 1.4 ± 0.9, *P*=0.012) (**Figure 3E**). Essentially, a more advanced chordoma staging correlated to higher cyclin E1 expression (advanced versus primary, 2.1 ± 1.0 versus 1.4 ± 0.9, *P*=0.002) (**Figure 3F**).

Cyclin E1 Overexpression Is an Independent Prognostic Factor in Chordoma

To identify whether cyclin E1 expression correlates to the prognosis of chordoma patients, survival analysis was

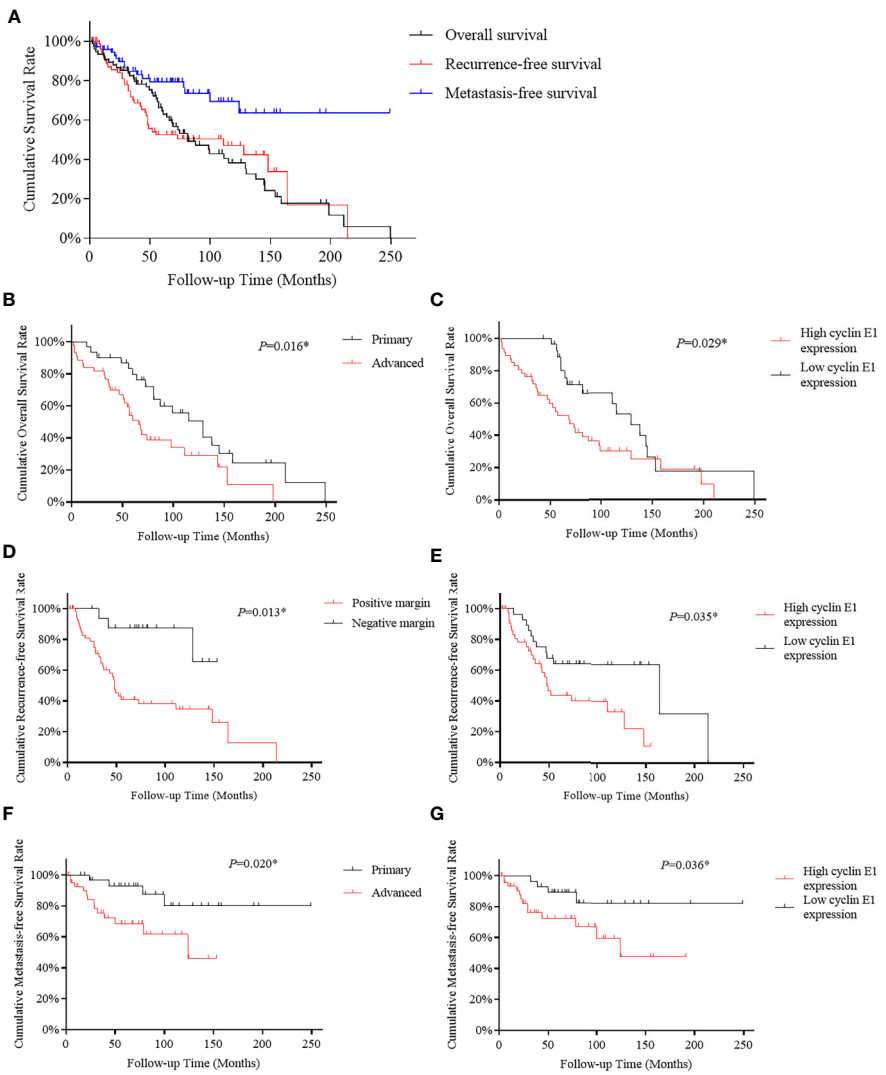

FIGURE 4 | Kaplan-Meier survival curve derived results of survival analysis. **(A)** Overall, recurrence-free and metastasis-free survival curves of 75 chordoma patients. **(B, C)** Advanced disease status and high cyclin E1 expression were independent risk factors for overall survival in 75 chordoma patients. **(D, E)** Positive surgical margins and high cyclin E1 expression were independent risk factors for recurrence-free survival in 75 chordoma patients. **(F, G)** Advanced disease status and high cyclin E1 expression were independent risk factors for metastasis-free survival in 75 chordoma patients. *Statistical significance.

performed on OS, RFS, and MFS of the 75 chordoma patients. In summary, after the tissue samples were obtained post-surgery, death occurred in 49 patients (65.3%), local recurrence was found in 37 patients (49.3%) and new onset metastasis was found in 17 patients (22.7%). Of the 75 chordoma patients, the mean OS in months was 102.3 (95% CI 83.7 to 121.0), RFS was 102.4 (95% CI 79.5 to 125.3) and MFS was 180.2 (95% CI 151.5 to 208.9). Five-year rates included OS of 63.1% (95% CI 51.7% to 74.5%), RFS was 52.4% (95% CI 40.2% to 64.6%), and MFS rate was 79.3% (95% CI 69.1% to 89.5%). Finally, the ten-year rates included OS of 38.2% (95% CI 25.3% to 51.1%), RFS of 47.0% (95% CI 33.9% to 60.1%), and MFS of 69.5% (95% CI 55.6% to 83.4%) (**Figure 4A**).

For OS, both univariate and multivariate analysis suggested advanced disease status and high cyclin E1 expression were independent risk factors (**Table 2**) (**Figures 4B, C**). For RFS, positive surgical margins and high cyclin E1 expression were identified by univariate and multivariate analysis to be independent risk factors (**Table 3**) (**Figures 4D, E**). And for MFS, advanced disease status and high cyclin E1 expression were independent risk factors (**Table 4**) (**Figures 4F, G**). Overall, cyclin E1 overexpression was an independent prognostic risk factor for poor chordoma patient outcomes.

DISCUSSION

Overexpression of cyclin E1 has been recognized in various malignancies including lung cancer (51%–62%), breast cancer (53%–61%), liver cancer (36%–68%) and some sarcomas (29%–61%) (15, 17, 22–28). This elevated cyclin E1 expression has been attributed to gene amplification, transcription upregulation, and disrupted degradation. In terms of frequency, the cyclin E1 gene is one of the most commonly amplified genes in ovarian cancer (19%), anaplastic thyroid cancer (29%) and osteosarcoma (27-33%) (14, 17, 18, 29). Overexpression of transcription factors such as c-MYC and MEIS2 directly up-regulate cyclin E1 expression (30, 31). In addition, inactivation of core units central to the ubiquitin protein ligase complex lead to cyclin E1 overexpression, as this is its principal degradative mechanism (32). In our study, overexpression of cyclin E1 occurred in 62.7% of chordoma patients, and is consistent with findings in more common cancers. In total, our work supports cyclin E1 as a diagnostic biomarker in chordoma.

Our TMA analysis showed cyclin E1 expression positively correlates with chordoma patient disease status. Of note, these results echo works in other malignancies where high cyclin E1 expression is associated with high-staging as well as tumor aggression and therapeutic-resistance (28, 33, 34). Functionally, it is proposed that these carcinogenic features are in part due to the cyclin E1 role in shortening mitosis and facilitating chromosome instability, both of which are known to incite tumorigenesis (35, 36). It therefore follows and is clear that cyclin E1 overexpression advances chordoma.

Cyclin E1 predicts poor prognosis in several malignancies (15, 28, 37). In our study, cyclin E1 showed prognostic significance with respect to OS, RFS and MFS in chordoma patients. Because recurrence and subsequent metastasis are of particular significance in determining chordoma outcomes, the ability of cyclin E1 overexpression to function as a prognostic biomarker is especially noteworthy for correlating with RFS and MFS in our study (4). As a specific prognostic biomarker rather than pure diagnostic biomarker, cyclin E1 has the potential to inform clinical decision-making and therapy selection based on predicted

TABLE 2 | Univariate and multivariate analysis of overall survival for 75 chordoma patients.

Variables	Univariate			Multivariate		
	HR	95% CI	*P*	HR	95% CI	*P*
Age	0.73	0.40 to 1.31	0.28			
≥60 yrs						
<60 yrs						
Sex	1.41	0.76 to 2.62	0.28			
Male						
Female						
Location	1.01	0.56 to 1.81	0.99			
Sacrum						
Other						
Disease status	2.04	1.12 to 3.74	0.020*	2.11	1.15 to 3.86	0.016*
Primary						
Advanced						
Surgical margin	0.69	0.34 to 1.39	0.30			
Positive						
Negative						
Neoadjuvant radiation	0.63	0.36 to 1.12	0.12			
With						
Without						
Cyclin E1 expression	0.52	0.28 to 0.96	0.037*	0.50	0.27 to 0.93	0.029*
High						
Low						

**Statistical significance; HR, hazard ratio; 95% CI, 95% confidence interval; yrs, years.*

TABLE 3 | Univariate and multivariate analysis for recurrence-free survival of 75 chordoma patients.

Variables	Univariate			Multivariate		
	HR	95% CI	*P*	HR	95% CI	*P*
Age	1.54	0.79 to 2.98	0.20			
≥60 yrs						
<60 yrs						
Sex	1.90	0.94 to 3.81	0.072			
Male						
Female						
Location	1.64	0.85 to 3.16	0.14			
Sacrum						
Other						
Disease status	1.67	0.84 to 3.33	0.14			
Primary						
Advanced						
Surgical margin	0.20	0.062 to 0.67	0.009*	0.22	0.067 to 0.73	0.013*
Positive						
Negative						
Neoadjuvant radiation	0.94	0.48 to 1.85	0.87			
With						
Without						
Cyclin E1 expression	0.41	0.20 to 0.86	0.018*	0.45	0.22 to 0.95	0.035*
High						
Low						

**Statistical significance; HR, hazard ratio; 95% CI, 95% confidence interval; yrs, years.*

TABLE 4 | Univariate and multivariate analysis for metastasis-free survival of 75 chordoma patients.

Variables	Univariate			Multivariate		
	HR	95% CI	*P*	HR	95% CI	*P*
Age	1.73	0.66 to 4.54	0.27			
≥60 yrs						
<60 yrs						
Sex	1.51	0.56 to 4.10	0.42			
Male						
Female						
Location	0.81	0.30 to 2.19	0.68			
Sacrum						
Other						
Disease status	3.66	1.18 to 11.34	0.025*	3.84	1.24 to 11.92	0.020*
Primary						
Advanced						
Surgical margin	0.33	0.075 to 1.43	0.14			
Positive						
Negative						
Neoadjuvant radiation	1.28	0.47 to 3.45	0.63			
With						
Without						
Cyclin E1 expression	0.32	0.10 to 0.97	0.045*	0.30	0.097 to 0.93	0.036*
High						
Low						

**Statistical significance; HR, hazard ratio; 95% CI, 95% confidence interval; yrs, years.*

progression and recurrence. This is especially important clinical information, as chordoma surgery and radiation therapy carry significant risks to the patient owing to its anatomic proximity to vital neurovascular structures. Taken together, cyclin E1 expression is a promising prognostic biomarker for chordoma patients that may help guide clinical decision making.

Finally, we assessed the predictive potential of other clinicopathological features for chordoma patients. As expected, an advanced disease status of chordomas engenders more aggressive future tumor behavior. It is an independent risk factor for OS and MFS in chordoma, which is similar to the results of previous studies (2, 5, 38). Moreover, we found a

contaminated surgical margin to be an independent risk factor for RFS in chordoma patients. This is consistent to previous studies, and further suggests that an adequate surgical margin is imperative to optimize chordoma treatment and to avoid local progression and recurrence (1, 5). Furthermore, we found no correlation between neoadjuvant radiation with prognosis/cyclin E1 expression level. While the therapeutic efficacy of radiation for chordoma remains controversial, our results, among others, do not clearly support neoadjuvant radiation in chordoma (4, 39).

To our knowledge, ours is the first study evaluating the expression and prognostic role of cyclin E1 specifically in chordoma. While we have identified a significant correlation between cyclin E1 expression and chordoma patient prognosis, future works should focus on the mechanism of the overexpression of cyclin E1 in chordoma and how cyclin E1 overexpression causes chordoma cell proliferation and poor outcomes. This would inform future targeted therapies and clinical trials making use of our initial findings. Moreover, while molecular targeting therapies have been investigated in chordoma but have largely been underwhelming, the cyclin E1 should be investigated as a novel therapeutic strategy for chordoma patients (40–43).

There are some limitations in our study. First, 75 chordoma cases is comparatively large sample size for this rare disease as compared to other previous studies on investigating prognostic biomarkers in chordoma (7, 41, 42). However, future studies to increase the number of specimens are needed to validate cyclin E1 as a biomarker for chordoma prognosis. Second, no chordoma samples in our study were from skull base. It might be attributed to that all chordoma samples included in this study were surgically treated *via* orthopedic surgeons, who usually treated chordoma on mobile spine or sacrum. Third, the mechanisms of cyclin E1 overexpression in chordoma remains unknown and need be further investigated. Future investigations to validate and build on the prognostic value of Cyclin E1 in chordoma will be carried out on a larger sample size collaborating with neurosurgeons to include skull base chordoma, and will focus on the detail mechanism and regulation of cyclin E1 expression in chordoma.

CONCLUSION

In summary, we show cyclin E1 is overexpressed in most chordomas, and its expression positively correlates to disease status and inversely correlates with OS, RFS, and MFS of chordoma patients. Our work suggests cyclin E1 as a prognostic biomarker for chordoma patients and supports future works investigating its mechanism and pathway as a potential drug target.

DATA AVAILABILITY STATEMENT

The raw data supporting the conclusions of this article will be made available by the authors, without undue reservation.

ETHICS STATEMENT

The study protocol and the consent of the informed patients were approved by the Partners Human Research Committee (number: 2007-P-002464/5) of Partners HealthCare as previously described. All patients provided their written informed consent to participate in this study.

AUTHOR CONTRIBUTIONS

Research design and data preparation: RW, PT, FH, WG, and ZD. Drafting and revising the paper: RW, DD, and ZD. Approval of the submitted and final versions: WG and ZD. All authors contributed to the article and approved the submitted version.

FUNDING

This work was supported, in part, by the Musculoskeletal Tumor Center and Beijing Key Laboratory of Musculoskeletal Tumor at Peking University People's Hospital, Beijing, China, and Department of Orthopaedic Surgery at UCLA, Los Angeles, California, USA. WG is supported, in part, through a grant from Sanming Project of Medicine in Shenzhen, China. ZD is supported, in part, through a grant from Sarcoma Foundation of America (SFA), 222433, a Grant from National Cancer Institute (NCI)/National Institutes of Health (NIH), U01, CA151452-01.

REFERENCES

1. Stacchiotti S, Sommer J. Chordoma Global Consensus G. Building a global consensus approach to chordoma: a position paper from the medical and patient community. *Lancet Oncol* (2015) 16(2):e71–83. doi: 10.1016/S1470-2045(14)71190-8
2. Zuckerman SL, Bilsky MH, Laufer I. Chordomas of the Skull Base, Mobile Spine, and Sacrum: An Epidemiologic Investigation of Presentation, Treatment, and Survival. *World Neurosurg* (2018) 113:e618–e27. doi: 10.1016/j.wneu.2018.02.109
3. Wei R, Guo W, Ji T, Zhang Y, Liang H, et al. One-step reconstruction with a 3D-printed, custom-made prosthesis after total en bloc sacrectomy: a technical note. *Eur Spine J* (2017) 26(7):1902–9. doi: 10.1007/s00586-016-4871-z
4. van Wulfften Palthe ODR, Tromp I, Ferreira A, Fiore A, Bramer JAM, van Dijk NC, et al. Sacral chordoma: a clinical review of 101 cases with 30-year experience in a single institution. *Spine J* (2019) 19(5):869–79. doi: 10.1016/j.spinee.2018.11.002
5. Ji T, Guo W, Yang R, Tang X, Wang Y, Huang L. What Are the Conditional Survival and Functional Outcomes After Surgical Treatment of 115 Patients With Sacral Chordoma? *Clin Orthop Relat Res* (2017) 475(3):620–30. doi: 10.1007/s11999-016-4773-8
6. Smoll NR, Gautschi OP, Radovanovic I, Schaller K, Weber DC. Incidence and relative survival of chordomas: the standardized mortality ratio and the impact of chordomas on a population. *Cancer* (2013) 119(11):2029–37. doi: 10.1002/cncr.28032
7. Vujovic S, Henderson S, Presneau N, Odell E, Jacques TS, Tirabosco R, et al. Brachyury, a crucial regulator of notochordal development, is a novel biomarker for chordomas. *J Pathol* (2006) 209(2):157–65. doi: 10.1002/path.1969

8. Whelan JS, Davis LE. Osteosarcoma, Chondrosarcoma, and Chordoma. *J Clin Oncol* (2018) 36(2):188–93. doi: 10.1200/JCO.2017.75.1743
9. Heery CR, Singh BH, Rauckhorst M, Marté JL, Donahue RN, Grenga I, et al. Phase I Trial of a Yeast-Based Therapeutic Cancer Vaccine (GI-6301) Targeting the Transcription Factor Brachyury. *Cancer Immunol Res* (2015) 3(11):1248–56. doi: 10.1158/2326-6066.CIR-15-0119
10. Sharifnia T, Wawer MJ, Chen T, Huang QY, Weir BA, Sizemore A, et al. Small-molecule targeting of brachyury transcription factor addiction in chordoma. *Nat Med* (2019) 25(2):292–300. doi: 10.1038/s41591-018-0312-3
11. Koff A, Cross F, Fisher A, Human cyclin E. a new cyclin that interacts with two members of the CDC2 gene family. *Cell* (1991) 66(6):1217–28. doi: 10.1016/0092-8674(91)90044-Y
12. Sauer K, Lehner CF. The role of cyclin E in the regulation of entry into S phase. *Prog Cell Cycle Res* (1995) 1:125–39. doi: 10.1007/978-1-4615-1809-9_10
13. Ayhan A, Kuhn E, Wu RC, Ogawa H, Bahadirli-Talbott A, Mao TL, et al. CCNE1 copy-number gain and overexpression identify ovarian clear cell carcinoma with a poor prognosis. *Mod Pathol* (2017) 30(2):297–303. doi: 10.1038/modpathol.2016.160
14. Patch AM, Christie EL, Etemadmoghadam D, Garsed DW, George J, Fereday S, et al. Whole-genome characterization of chemoresistant ovarian cancer. *Nature* (2015) 521(7553):489–94. doi: 10.1038/nature14410
15. Keyomarsi K, Tucker SL, Buchholz TA, Cyclin E. and survival in patients with breast cancer. *N Engl J Med* (2002) 347(20):1566–75. doi: 10.1056/NEJMoa021153
16. Scaltriti M, Eichhorn PJ, Cortes J, Prudkin L, Aura C, Jiménez J, et al. Cyclin E amplification/overexpression is a mechanism of trastuzumab resistance in HER2+ breast cancer patients. *Proc Natl Acad Sci U S A* (2011) 108(9):3761–6. doi: 10.1073/pnas.1014835108
17. Lockwood WW, Stack D, Morris T, Grehan D, O'Keane C, Stewart GL, et al. Cyclin E1 is amplified and overexpressed in osteosarcoma. *J Mol Diagn* (2011) 13(3):289–96. doi: 10.1016/j.jmoldx.2010.11.020
18. Sayles LC, Breese MR, Koehne AL, Leung SG, Lee AG, Liu HY, et al. Genome-Informed Targeted Therapy for Osteosarcoma. *Cancer Discov* (2019) 9(1):46–63. doi: 10.1158/2159-8290.CD-17-1152
19. Chen H, Garbutt CC, Spentzos D, Choy E, Hornicek FJ, Duan Z, et al. Expression and Therapeutic Potential of SOX9 in Chordoma. *Clin Cancer Res* (2017) 23(17):5176–86. doi: 10.1158/1078-0432.CCR-17-0177
20. Bruderlein S, Sommer JB, Meltzer PS, Li S, Osada T, Ng D, et al. Molecular characterization of putative chordoma cell lines. *Sarcoma* (2010) 2010:630129. doi: 10.1155/2010/630129
21. Liu X, Nielsen GP, Rosenberg AE, Waterman PR, Yang W, Choy E, et al. Establishment and characterization of a novel chordoma cell line: CH22. *J Orthop Res* (2012) 30(10):1666–73. doi: 10.1002/jor.22113
22. Hunt KK, Karakas C, Ha MJ, Biernacka A, Yi M, Sahin AA, et al. Cytoplasmic Cyclin E Predicts Recurrence in Patients with Breast Cancer. *Clin Cancer Res* (2017) 23(12):2991–3002. doi: 10.1158/1078-0432.CCR-16-2217
23. Salon C, Merdzhanova G, Brambilla C, Brambilla E, Gazzeri S, Eymin B, et al. E2F-1, Skp2 and cyclin E oncoproteins are upregulated and directly correlated in high-grade neuroendocrine lung tumors. *Oncogene* (2007) 26(48):6927–36. doi: 10.1038/sj.onc.1210499
24. Ito Y, Matsuura N, Sakon M, Miyoshi E, Noda K, Takeda T, et al. Expression and prognostic roles of the G1-S modulators in hepatocellular carcinoma: p27 independently predicts the recurrence. *Hepatology* (1999) 30(1):90–9. doi: 10.1002/hep.510300114
25. Jung YJ, Lee KH, Choi DW, Han CJ, Jeong SH, Kim KC, et al. Reciprocal expressions of cyclin E and cyclin D1 in hepatocellular carcinoma. *Cancer Lett* (2001) 168(1):57–63. doi: 10.1016/S0304-3835(01)00403-7
26. Molendini L, Benassi MS, Magagnoli G, Merli M, Sollazzo MR, Ragazzini P, et al. Prognostic significance of cyclin expression in human osteosarcoma. *Int J Oncol* (1998) 12(5):1007–11. doi: 10.3892/ijo.12.5.1007
27. Goto Y, Kawauchi S, Ihara K, Ikemoto K, Ohi R, Kawai S, et al. The prognosis in spindle-cell sarcoma depends on the expression of cyclin-dependent kinase inhibitor p27(Kip1) and cyclin E. *Cancer Sci* (2003) 94(5):412–7. doi: 10.1111/j.1349-7006.2003.tb01456.x
28. Wei R, Thanindratarn P, Dean DC, Hornicek FJ, Guo W, Duan Z, et al. Cyclin E1 is a prognostic biomarker and potential therapeutic target in osteosarcoma. *J Orthop Res* (2020) 38(9):1952–64. doi: 10.1002/jor.24659
29. Ravi N, Yang M, Gretarsson S, Jansson C, Mylona N, Sydow SR, et al. Identification of Targetable Lesions in Anaplastic Thyroid Cancer by Genome Profiling. *Cancers (Basel)* (2019) 11(3):402. doi: 10.3390/cancers11030402
30. Abruzzese MP, Bilotta MT, Fionda C, Zingoni A, Soriani A, Petrucci MT, et al. The homeobox transcription factor MEIS2 is a regulator of cancer cell survival and IMiDs activity in Multiple Myeloma: modulation by Bromodomain and Extra-Terminal (BET) protein inhibitors. *Cell Death Dis* (2019) 10(4):324. doi: 10.1038/s41419-019-1562-9
31. Deb-Basu D, Karlsson A, Li Q, Dang CV, Felsher DW. MYC can enforce cell cycle transit from G1 to S and G2 to S, but not mitotic cellular division, independent of p27-mediated inihibition of cyclin E/CDK2. *Cell Cycle* (2006) 5(12):1348–55. doi: 10.4161/cc.5.12.2860
32. Gong Y, Zack TI, Morris LG, Lin K, Hukkelhoven E, Raheja R, et al. Pan-cancer genetic analysis identifies PARK2 as a master regulator of G1/S cyclins. *Nat Genet* (2014) 46(6):588–94. doi: 10.1038/ng.2981
33. Karakas C, Biernacka A, Bui T, Sahin AA, Yi M, Akli S, et al. Cytoplasmic Cyclin Eand Phospho-Cyclin-Dependent Kinase 2 Are Biomarkers of Aggressive Breast Cancer. *Am J Pathol* (2016) 186(7):1900–12. doi: 10.1016/j.ajpath.2016.02.024
34. Etemadmoghadam D, deFazio A, Beroukhim R, Mermel C, George J, Getz G, et al. Integrated genome-wide DNA copy number and expression analysis identifies distinct mechanisms of primary chemoresistance in ovarian carcinomas. *Clin Cancer Res* (2009) 15(4):1417–27. doi: 10.1158/1078-0432.CCR-08-1564
35. Spruck CH, Won KA, Reed SI. Deregulated cyclin E induces chromosome instability. *Nature* (1999) 401(6750):297–300. doi: 10.1038/45836
36. Aziz K, Limzerwala JF, Sturmlechner I, Hurley E, Zhang C, Jeganathan KB, et al. Ccne1 Overexpression Causes Chromosome Instability in Liver Cells and Liver Tumor Development in Mice. *Gastroenterology* (2019) 157(1):210–26 e12. doi: 10.1053/j.gastro.2019.03.016
37. Rosen DG, Yang G, Deavers MT, Malpica A, Kavanagh JJ, Mills GB, et al. Cyclin E expression is correlated with tumor progression and predicts a poor prognosis in patients with ovarian carcinoma. *Cancer* (2006) 106(9):1925–32. doi: 10.1002/cncr.21767
38. Zheng W, Huang Y, Guan T, Lu S, Yao L, Wu S, et al. Application of nomograms to predict overall and cancer-specific survival in patients with chordoma. *J Bone Oncol* (2019) 18:100247. doi: 10.1016/j.jbo.2019.100247
39. Houdek MT, Rose PS, Hevesi M, Schwab JH, Griffin AM, Healey JH, et al. Low dose radiotherapy is associated with local complications but not disease control in sacral chordoma. *J Surg Oncol* (2019) 119(7):856–63. doi: 10.1002/jso.25399
40. Stacchiotti S, Morosi C, Lo Vullo S, Casale A, Palassini E, Frezza AM, et al. Imatinib and everolimus in patients with progressing advanced chordoma: A phase 2 clinical study. *Cancer* (2018) 124(20):4056–63. doi: 10.1002/cncr.31685
41. Yamaguchi T, Imada H, Iida S, Szuhai K. Notochordal Tumors: An Update on Molecular Pathology with Therapeutic Implications. *Surg Pathol Clin* (2017) 10(3):637–56. doi: 10.1016/j.path.2017.04.008
42. Lebellec L, Chauffert B, Blay JY, Le Cesne A, Chevreau C, Bompas E, et al. Advanced chordoma treated by first-line molecular targeted therapies: Outcomes and prognostic factors. A retrospective study of the French Sarcoma Group (GSF/GETO) and the Association des Neuro-Oncologues d'Expression Francaise (ANOCEF). *Eur J Cancer* (2017) 79:119–28. doi: 10.1016/j.ejca.2017.03.037
43. Colia V, Stacchiotti S. Medical treatment of advanced chordomas. *Eur J Cancer* (2017) 83:220–8. doi: 10.1016/j.ejca.2017.06.038

Conflict of Interest: The authors declare that the research was conducted in the absence of any commercial or financial relationships that could be construed as a potential conflict of interest.

frontiers in Oncology

ORIGINAL RESEARCH
published: 27 January 2021
doi: 10.3389/fonc.2020.613333

Construction of Bone Metastasis-Specific Regulation Network Based on Prognostic Stemness-Related Signatures in Breast Invasive Carcinoma

Runzhi Huang[1,2,3†], Zhenyu Li[3†], Jiayao Zhang[4†], Zhiwei Zeng[1], Jiaqi Zhang[1], Mingxiao Li[1], Siqao Wang[3], Shuyuan Xian[3], Yuna Xue[1], Xi Chen[1], Jie Li[1], Wenjun Cheng[1], Bin Wang[5], Penghui Yan[1*], Daoke Yang[6*] and Zongqiang Huang[1*]*

[1] Department of Orthopedics, The First Affiliated Hospital of Zhengzhou University, Zhengzhou, China, [2] Division of Spine, Department of Orthopedics, Tongji Hospital Affiliated to Tongji University School of Medicine, Shanghai, China, [3] Tongji University School of Medicine, Tongji University, Shanghai, China, [4] Tongji University School of Mathematical Sciences, Tongji University, Shanghai, China, [5] Department of General Surgery, Changzheng Hospital, Second Military Medical University, Shanghai, China, [6] Department of Radiotherpy, The First Affiliated Hospital of Zhengzhou University, Zhengzhou, China

Background: Bone is the most common metastatic site of Breast invasive carcinoma (BRCA). In this study, the bone metastasis-specific regulation network of BRCA was constructed based on prognostic stemness-related signatures (PSRSs), their upstream transcription factors (TFs) and downstream pathways.

Methods: Clinical information and RNA-seq data of 1,080 primary BRCA samples (1,048 samples without bone metastasis and 32 samples with bone metastasis) were downloaded from The Cancer Genome Atlas (TCGA). The edgeR method was performed to identify differential expressed genes (DEGs). Next, mRNA stemness index (mRNAsi) was calculated by one-class logistic regression (OCLR). To analyze DEGs by classification, similar genes were integrated into the same module by weighted gene co-expression network analysis (WGCNA). Then, univariate and multivariate Cox proportional hazard regression were applied to find the PSRSs. Furthermore, PSRSs, 318 TFs obtained from Cistrome database and 50 hallmark pathways quantified by GSVA were integrated into co-expression analysis. Significant co-expression patterns were used to construct the bone metastasis-specific regulation network. Finally, spatial single-cell RNA-seq and chromatin immunoprecipitation sequence (ChIP-seq) data and multi-omics databases were applied to validate the key scientific hypothesis in the regulation network. Additionally, Connectivity Map (CMap) was utilized to select the potential inhibitors of bone metastasis-specific regulation network in BRCA.

Results: Based on edgeR and WGCNA method, 43 PSRSs were identified. In the bone metastasis-specific regulation network, MAF positively regulated CD248 ($R = 0.435$, $P < 0.001$), and hallmark apical junction was the potential pathway of CD248 ($R = 0.353$, $P < 0.001$). This regulatory pattern was supported by spatial single-cell RNA sequence, ChIP-

OPEN ACCESS

Edited by:
Dianwen Song, Shanghai First People's Hospital, China

Reviewed by:
Zhang Hui, Fujian Medical University, China
Peng-Chan Lin, National Cheng Kung University, Taiwan
Haoran Lv, Second Affiliated Hospital of Guangzhou Medical University, China

***Correspondence:**
Zongqiang Huang
gzhuangzq@163.com
Bin Wang
wangbin12048@163.com
Penghui Yan
877492185@qq.com
Daoke Yang
15903650068@163.com

†These authors have contributed equally to this work and share first authorship

Specialty section:
This article was submitted to Molecular and Cellular Oncology, a section of the journal Frontiers in Oncology

Received: *02 October 2020*
Accepted: *26 November 2020*
Published: *27 January 2021*

Citation:
Huang R, Li Z, Zhang J, Zeng Z, Zhang J, Li M, Wang S, Xian S, Xue Y, Chen X, Li J, Cheng W, Wang B, Yan P, Yang D and Huang Z (2021) Construction of Bone Metastasis-Specific Regulation Network Based on Prognostic Stemness-Related Signatures in Breast Invasive Carcinoma. Front. Oncol. 10:613333. doi: 10.3389/fonc.2020.613333

seq data and multi-omics online databases. Additionally, alexidine was identified as the possible inhibitor for bone metastasis of BRCA by CMap analysis.

Conclusion: PSRSs played important roles in bone metastasis of BRCA, and the prognostic model based on PSRSs showed good performance. Especially, we proposed that CD248 was the most significant PSRS, which was positively regulated by MAF, influenced bone metastasis *via* apical junction pathway. And this axis might be inhibited by alexidine, which providing a potential treatment strategy for bone metastasis of BRCA.

Keywords: breast invasive carcinoma, bone metastasis, apical junction, MAF, CD248, mRNA stemness index (mRNAsi), weighted gene co-expression network analysis (WGCNA), spatial transcriptome

INTRODUCTION

Breast Invasive Carcinoma (BRCA) was the most common tumor in female, which originated from ducts and acinar epithelium at all levels of the breast, and most patients suffered from malignant epithelial tumor. And the BRCA can be classified into several types according to the state of progesterone receptor (PR), estrogen receptor (ER), and ERBB2 receptor (HER2) in histological stratification, which was applied in clinical practice (1). Estimated by American Cancer Society (ACS), there were 279,100 new cases, and 42,690 new death BRCA patients in 2020 (2). Besides, the five-year survival rate for BRCA in stage I, II, III, and IV were 98, 92, 75, and 27% according to the statistic from 2009 to 2015, respectively (3). Although the five-year survival rate of primary BRCA was high, the five-year survival rate of bone metastasis was only 20%, and patients were trapped in a vicious cycle between osteolytic degeneration and proliferation of cancer cells (4). Besides, the osteolytic lesions like pain in bone, fractures, spinal compression and hypercalcemia leaded to poor survival quality and death (4).

Machine learning based on high-throughput data played an important role in prognosis of cancer, and new characters defined by algorithm like mRNA stemness index (mRNAsi) and stemness-related gene provided a new way for analysis (5). Recently, analysis on triple-negative breast cancer were launched to explore the key gene related to the stemness and find the target for further therapy (6). Therefore, molecules participated in the bone metastasis required to be explored, and corresponded biomarkers and possible mechanism needed to be drug for clinical strategy and therapy.

In this study, data of RNA-seq in BRCA were identified by edgeR, and differential expressed genes (DEGs) were performed by machine-learning algorithm to define the mRNAsi. Then, the profiling of DEGs were integrated into weighted gene co-expression network analysis (WGCNA) to classify similar genes into multiply modules and outline the phenotypic characteristics of modules. Besides, the mRNAsi and Hallmark gene sets were qualified to annotate modules. Then, the key module and genes most associated with mRNAsi were selected. Univariate and multivariate Cox regression analysis were applied to access the prognostic value of genes. What is more, based on the Pearson analysis for TF, genes, and Hallmark gene sets, a bone metastasis-specific network was constructed. The scientific hypothesis was determined by the correlation coefficient. Moreover, the CMap analysis was applied to find potential inhibitors for signal axis. Finally, spatial single-cell RNA sequence and chromatin immunoprecipitation sequence (ChIP-seq) data and multi-omics online databases were applied to validate the key scientific hypothesis in the regulation network. The bone metastasis-specific regulation network and inhibitors provided potential treatment strategy for bone metastasis of BRCA.

METHODS

Data Acquisition

Based on the Cancer Genome Atlas (TCGA) database (https://portal.gdc.cancer.gov/), RNA-seq data of 1,080 primary BRCA samples were downloaded, including 1,048 samples without bone metastasis and 32 samples with bone metastasis. And the bone metastasis was diagnosed by imaging examinations like CT or PET-CT. Besides, demographics like age and gender, tumor information like TNM stage and grade, and follow-up data of all patients were also obtained from the TCGA database. Besides, samples without follow-up information were excluded.

Differentially Expressed Genes Identification

The edgeR package was used to screen the RNA-seq data to define DEGs between primary BRCA patients with and without

Abbreviations: BRCA, Breast invasive carcinoma; ACS, American Cancer Society; TF, Transcription Factor; TCGA, The Cancer Genome Atlas; mRNAsi, mRNA stemness index; PSRS, prognostic stemness-related signature; KEGG, Kyoto Encyclopedia of Genes and Genomes; GSEA, Gene-Set Enrichment Analysis; GSVA, Gene Set Variation Analysis; CCLE, Cancer Cell Line Encyclopedia; GEPIA, Gene Expression Profiling Interactive Analysis; GTEx, Genotype-Tissue Expression; ROC, The Receiver Operator Characteristic; AUC, Area Under the Curve; FDR, False Discovery Rate; GO, Gene Oncology; KEGG, Kyoto Encyclopedia of Genes and Genomes; DEG, Differential Expressed Gene; FC, Fold charge; mRNAsi, mRNA Expression-Based Stemness Index; GS, gene significance; MS, module significance; ME, module eigengenes; MM, module membership; PCA, principal component analysis; PC, principal component; t-SNE, t-distributed Stochastic Neighbor Embedding; UMAP, Uniform Manifold Approximation and Projection; HE, Haematoxylin and Eosin; MMP9, matrix metalloproteinase 9; EMT, epithelial–mesenchymal transition.

bone metastasis, and the criteria must fit following two points at the same time: the absolute value of log Fold Change (log FC) must more than 1, and the False Discovery Rate (FDR) must less than 0.05. Then, Gene Oncology (GO) and Kyoto Encyclopedia of Genes and Genomes (KEGG) enrichment analysis were utilized to annotate DEGs.

mRNAsi

The mRNAsi was calculated by the one-class logistic regression (OCLR) machine-learning algorithm (7) based on the RNA-seq data of 1,080 primary BRCA samples.

Weighted Gene Co-Expression Network Analysis

With the aim to holistically analyze DEGs, modules were classified by WGCNA (8) R package (http://www.r-project.org/), every single module gathered highly similar DEGs. Then based on RNA-seq profiling, the Pearson correlation analysis was utilized to construct the gene co-expression network. Additionally, the power function was applied to build a weighted adjacency matrix:

$$a_{ij} = \left|s_{ij}\right|^{\beta}$$

S_{ij} represented the Pearson correlation between gene i and j, a_{ij} represented the weighted network adjacency between gene i and j. And β equaled to 4 was the soft-threshold parameter set by pickSoft Threshold from WGCNA R package. What's more, the application of soft-threshold parameter of weighted network make it possible to show the continuous variety of co-expression information in [0,1], and it might promote the idea of scale-free co-expression network come true. In addition, the correlation coefficients were utilized to construct hierarchical clustering, and a topological overlap method was performed to classify DEGs with the similar expression patterns into same module. Besides, the capacity of module must more than 20 genes, and when a certain module with less than 20 genes, similar modules will be merged.

Based on the H Collection of Molecular Signatures Database (MSigDB) v7.0 (https://www.gsea-msigdb.org/gsea/msigdb/genesets.jsp?collection=H) (9), 50 Hallmark gene sets were qualitied by the computational approach named Gene Set Variation Analysis (GSVA). And these Hallmark gene sets were related to biological process and states. Then, with the aim to annotate the specific phenotypic traits for module, 50 Hallmark gene sets and mRNAsi were defined as phenotypes for a co-analysis with modules. Besides, gene significance (GS) coefficients and *p* values were illustrated the correlation between DEGs and phenotypes. Similarly, module significance (MS) coefficients and *p* values showed the correlation between modules and phenotypes, and the MS was calculated from the average absolute GS for all genes in every single module. Moreover, the first principle component of module genes showed the gene expression level in the certain module, and module eigengenes (MEs) represented the first principle component. And module membership (MM) represented the correlation between gene to MEs. Next, mRNAsi was the key phenotype to choose the stemness-related module, and the largest MS with *p* value less than 0.05 were applied to determine the key module for next exploration. What's more, the Hallmark gene set significantly related to the key module and *p* value less than 0.05 was selected as the key Hallmark gene set, and the key Hallmark gene set was defined as the key pathway for stemness-related signatures (SRSs). Besides, SRSs with MM >0.300 and GS >0.300 were obtained from the key module for further analysis.

Multivariate Prognosis Model Construction

The univariate and multivariate Cox proportional hazard regression were applied to find prognostic stemness-related signatures (PSRSs). SRSs with *p* value <0.001 in univariate Cox proportional hazard regression were defined as PSRSs. Then, the LASSO regression analysis was applied to avoid the over-fitness. Then, residual PSRSs were integrated into the multivariate Cox regression model, and risk score for each BRCA patient was calculated by the formula:

$$Risk\ \ score_m = \beta_1 \times gene_1 + \beta_2 \times gene_2 + \ \beta_3 \times gene_3 \ldots \ldots + \beta_n \times gene_n$$

In the formula, "m" represented the number of each patient, "n" represented prognostic PSRS, and "β" represented the coefficient of each prognostic PSRS. Then, patients with BRCA were divided into low- and high-risk groups according to risk score. And the efficiency of risk score of the model was detected by Kaplan-Meier survival analysis. What's more, and accuracy was detected by the Receiver Operating Characteristic Curve (ROC) curve and C-index. Finally, the demographic information, TNM stage and risk score were applied for correction, and univariate and multivariate Cox regression were performed to validate the independent prognostic value.

Potential Signal Axis Identification

Based on the Cistrome database (http://cistrome.org/) (10), the list of 318 Translate factors (TFs) were downloaded. And edgeR was utilized to find differential expressed TFs. Then co-expression analysis for TFs and PSRSs by Pearson correlation analysis, and the significant paired TF-PSRSs were selected.

Aim to identify the significantly co-expressed pathway, the absolute quantification of 50 Hallmark gene sets between non-metastasis and metastasis patients was screened by GSVA. And to explore the up- and down-regulated pathways between non-metastasis and metastasis patients, Gene Set Enrichment Analysis (GSEA) was conducted based on the 50 gene sets of Hallmark (11). In addition, the intersection of GSVA, GSEA, and module phenotypic traits was defined as the key pathway. Then, the Pearson correlation analysis was utilized to analysis the interaction between Hallmark gene sets and PSRSs.

Eventually, the network based on TFs, PSRSs and Hallmark gene sets was constructed. And String database (12) was applied to plot a protein-protein interaction (PPI) network. Besides, the criteria for TF-PSRS paired was the absolute value of the correlation coefficient more than 0.400 and *p* value less than 0.05, for PSRS-Hallmark gene set was the absolute value of correlation coefficient more than 0.300 and *p* value less than 0.05.

Connectivity Map Analysis

To expend the application of potential signal axis, inhibitors of the signal pathway were selected by the Connectivity Map (build 02) (CMap) (https://portals.broadinstitute.org/cmap/) (13). Then, inhibitors for BCRA were identified. Besides, the information like chemical structural formula and biologic function of inhibitor compounds were available from the mechanism of actions (MoA) (http://clue.io/) (14). Ultimately, the key inhibitor was found according to the TF, PSRS, and Hallmark gene set.

Assay for Targeting Accessible-Chromatin With High-Throughout Sequencing-Seq and Chromatin Immunoprecipitation Sequence Validation

Assay for Targeting Accessible-Chromatin with high-throughout sequencing (ATAC-seq) and ChIP-seq data were used to validated the regulation mechanism of the network. ATAC-seq and ChIP-seq data were obtained from TCGA GDC (https://gdc.cancer.gov/about-data/publications/ATACseq-AWG) and Cistrome database (http://cistrome.org/), respectively (10, 15). WashU Epigenome Browser and Gviz package were used to visualize the binding peaks (16, 17).

Spatial Transcriptome Validation

The regulatory relationship between TF and PSRS, PSRS and Hallmark gene set required to be validated the direct mechanism in the molecular experiment. When linked with single-cell RNA sequence data, spatial transcriptome data can validate the cell subtype localization of the key genes (https://support.10xgenomics.com/spatial-gene-expression/datasets/1.1.0/V1_Breast_Cancer_Block_A_Section_1). For quality control, only fit the following standards at the same time can be selected: genes must express in more than 3 single cells, gene counts more than 1, cell transcripts range from 1,500 to 100,000.

To integrate data analysis, the Seurat method was performed (18). Then, the "sctransform" algorithm was utilized for normalization. In addition, to identify variable genes and spatial-specific genes, "vst" and "markvariogram" method were utilized, respectively. Next, the principal component analysis (PCA) was performed based on variable genes (18). In addition, the jackstraw analysis was utilized to select the principal components (PCs), and p value must less than 0.05. Then, the further t-distributed Stochastic Neighbor Embedding (t-SNE), Haematoxylin and Eosin (HE) and UMAP (Uniform Manifold Approximation and Projection) were applied to identify the cell sub-cluster based on the PCs (resolution = 0.50) (19). And in sub-cluster, DEGs were filtered when the absolute value of log FC less than 0.5 and FDR more than 0.05. Moreover, the location and expression of DEGs were demonstrated in feature plots and violin plots, respectively. Besides, every cluster was annotated by scMatch (20), singleR (21), and CellMarker (22) databases. Aim to annotate single cells, 50 hallmark gene sets were performed to absolutely quantify the signaling pathway activity in each single cell.

Multidimension Validation

To decrease the inherent defects of analysis in silicon, multiply online databases were utilized to validate the scientific hypothesis in several aspects. And top five genes in the key pathway selected by GeneCard (https://www.genecards.org/) were also validated with TFs and PSRSs.

Gene Expression Profilling Interactive Analysis (GEPIA) (23), Oncomine (24), PROGgeneV2 (25), UALCAN (26), Linkedomics (27), SurvExpress (28), cBioportal (29), Genotype-Tissue Expression (GTEx) (30) and UCSC xena (31) validated in gene level based, Cancer Cell Line Encyclopedia (CCLE) (32) validated in cancer cell line level, The human protein altas (33) validated in tissue level in BRCA patient. Finally, String database (12) was utilized to construct the Protein-Protein Interaction network.

Statistics Analysis

The R software (www.r-project.org; version 3.6.1; Institute for Statistics and Mathematics, Vienna, Austria) was applied in all statistics analysis in our study, and two-sided p value <0.05 was determined as statistically significant.

RESULTS

Differentially Expressed Genes Identification

The expression profiling of 1,048 primary BRCA samples without bone metastasis and 32 primary BRCA samples with bone metastasis were obtained from TCGA database, and all patients' demographics information was summarized in **Table 1**. And all analysis processes were illustrated in **Figure 1**.

TABLE 1 | Baseline information of 813 patients diagnosed with breast invasive carcinoma.

Variables	Total Patients (N = 813)
Age, years	
Mean ± SD	57.54 ± 12.66
Median (Range)	58 (26–90)
T stage	
T0	0
T1	222 (27.31%)
T2	477 (58.67%)
T3	88 (10.82%)
T4	26 (3.20%)
N stage	
N0	670 (82.41%)
N1	0
N2	92 (11.32%)
N3	51 (6.27%)
M stage	
M0	798 (98.15%)
M1	15 (1.85%)
Stage	
Stage I	152 (18.70%)
Stage II	468 (57.56%)
Stage III	178 (21.89%)
Stage IV	15 (1.85%)
Metastasis	
Bone metastasis	5 (0.62%)
Other metastasis	10 (1.23%)
No metastasis	798 (98.15%)

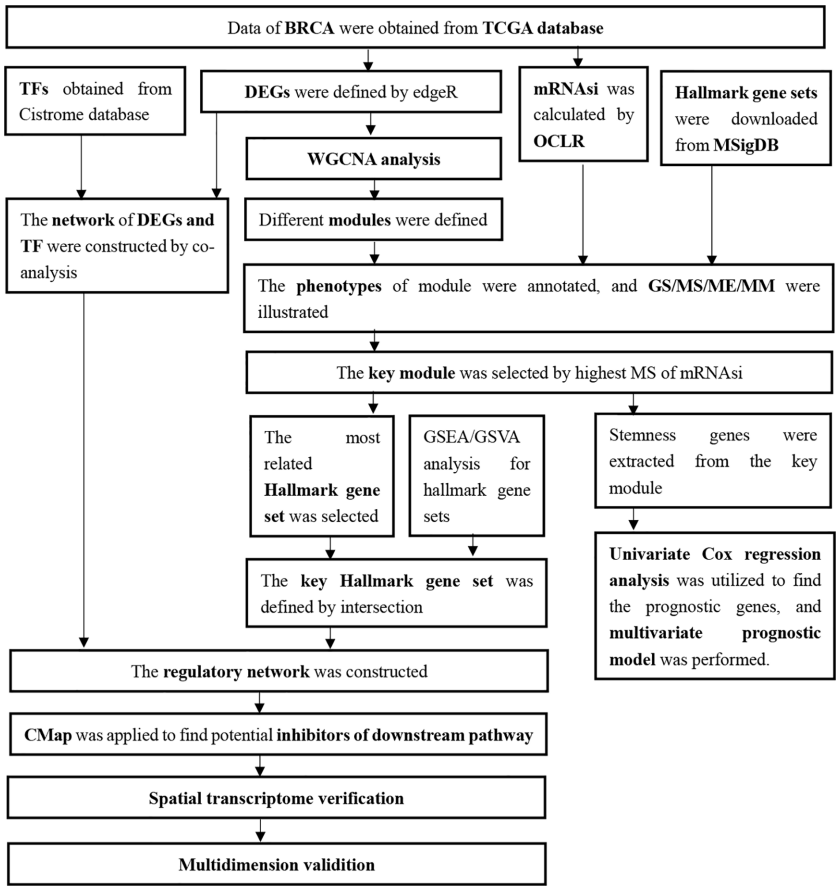

FIGURE 1 | Flow chart of analysis.

RNA-seq data from TCGA database was screened by edgeR to filter DEGs, and the information of BRCA (**Figure 2A**), the heatmap of RNA expression level in BRCA samples (**Figure 2B**) and volcano plots of DEGs and non-DEGs (**Figure 2C**) were launched. And 31 DEGs were founded. Besides, GO (**Figure 2D**) enrichment analysis for DEGs was performed, and cell-cell adhesion *via* plasma-membrane adhesion molecules (BP, GeneRatio = 0.048, p = 0.001, count = 21), contractile fiber (CC, GeneRatio = 0.045, $p < 0.001$, count = 20), receptor ligand activity (MF, GeneRatio = 0.066, p = 0.007, count = 27) were the most significant GO items. And KEGG (**Figure 2E**) enrichment analysis for DEGs showed Neuroactive ligand-receptor interaction (GeneRatio = 0.125, p = 0.001, count = 23) was the most significant KEGG item.

WGCNA

Based on WGGCNA package, seven modules were defined (**Figures 3A, B**). Aim to annotate the phenotype of modules, 50 Hallmark gene sets and mRNAsi were co-analysis with modules in the heatmap plot (**Figure 3C**). Module turquoise (MS = 0.550; $p < 0.001$) was the module most relevant to mRNAsi (MS = 0.670; $p < 0.001$) and 125 SRSs in turquoise were integrated into the further analysis. In addition, three Hallmark gene sets were highly correlated with module turquoise: hallmark apical junction (MS = 0.670; $p < 0.001$), hallmark myogenesis (MS = 0.66; $p < 0.001$), and hallmark IL6-JAK-STAT3 signaling (MS = 0.660; $p < 0.001$) (**Figure 3D**).

Multivariate Prognostic Model Construction

The heatmap (**Figure 4A**) and volcano plot (**Figure 4B**) demonstrated the results of DEG analysis of 125 SRSs. And univariate Cox regression analysis was utilized to find the prognostic genes, and 43 PSRSs were identified. In addition, forest plot (**Figure 4C**) showed CD248 (HR = 1.00004, 95%CI (1.00001-1.00006), p = 0.007) was significantly associated with prognosis of BRCA. Then, the PSRSs were integrated into

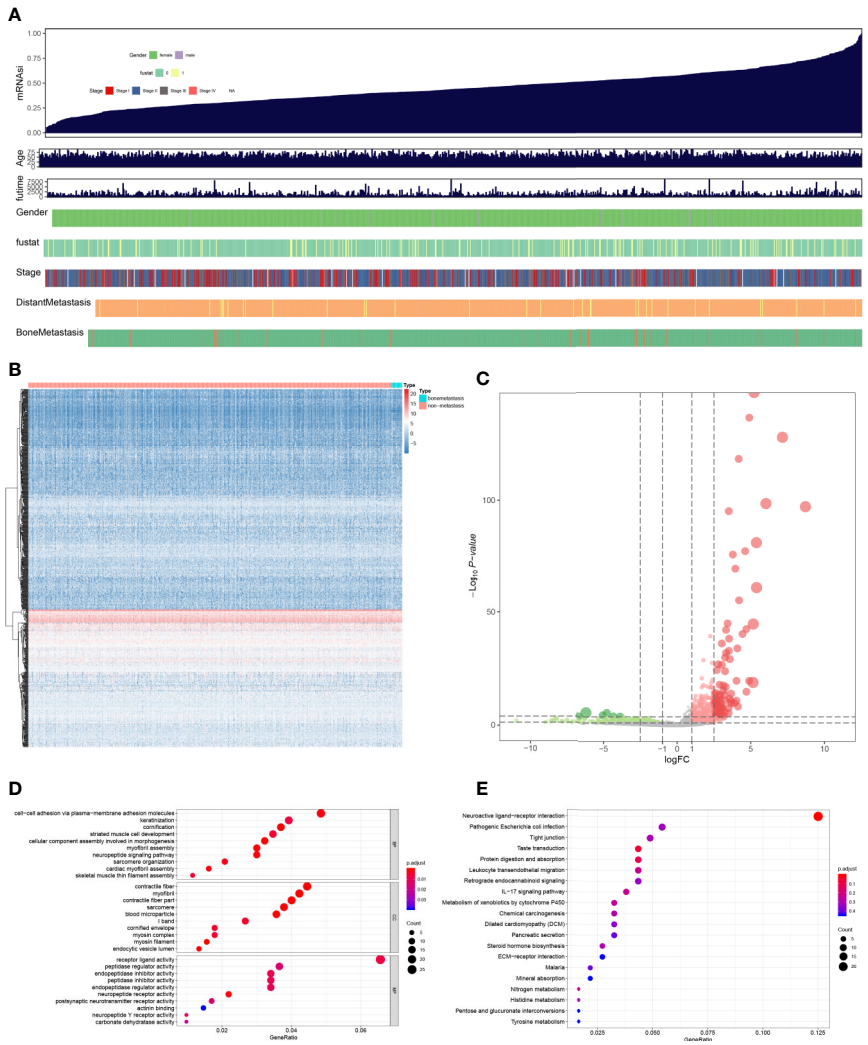

FIGURE 2 | The summary of mRNAsi **(A)**, heatmap plot **(B)**, volcano plot **(C)**, GO **(D)**, and KEGG **(E)** enrichment analysis of differential expressed genes. Cell-cell adhesion *via* plasma-membrane adhesion molecules, contractile fiber, receptor ligand activity were the most significant GO items, and Neuroactive ligand-receptor interaction was the most significant KEGG item.

multivariate Cox regression analysis, and a prognostic model was constructed. The scatter plot (**Figure 5A**) and risk line plot (**Figure 5B**) were drawn to illustrated the risk distribution of each patient. In addition, in term of model diagnosis, area under curve (AUC) of ROC curve was 0.711 (**Figure 5C**). Based on the median risk score calculated by multivariate model, low- and high-risk groups were accessed by Kaplan-Meier survival analysis (**Figure 5D**), and the result displayed a significant difference ($p < 0.001$). Finally, the risk score was co-analysis with age, T stage, N stage, M stage, stage, the univariate (**Figure 5E**) (HR = 167.019, 95%CI (39.677–703.066), $p < 0.001$) and multivariate (**Figure 5F**) (HR = 1.050, 95%CI (1.033–1.067), $p < 0.001$) Cox regression, suggesting that the risk score was an independent prognostic factor.

Potential Signal Axis Identification

The expression levels of Hallmark gene sets were shown in heatmap plot (**Figure 6A**), and differential expressed gene sets showed in volcano plots (**Figure 6B**). A total of 47 significant expressed Hallmark gene sets were identified by GSVA (**Figure 6C**), and five up-regulated and 15 down-regulated Hallmark gene sets were identified by GSEA (**Figure 6D**). What's more, Hallmark gene sets were co-analyzed with PSRSs by the Pearson correlation analysis.

Based on data of 318 TFs from the Cistrome database, a series of analysis on expression launched, and heatmap plot (**Figure 7A**) and volcano plot (**Figure 7B**) were applied. Moreover, 96 TFs were significantly differential expressed. Then, the Pearson correlation analysis was utilized to find the relation between TFs and PSRSs.

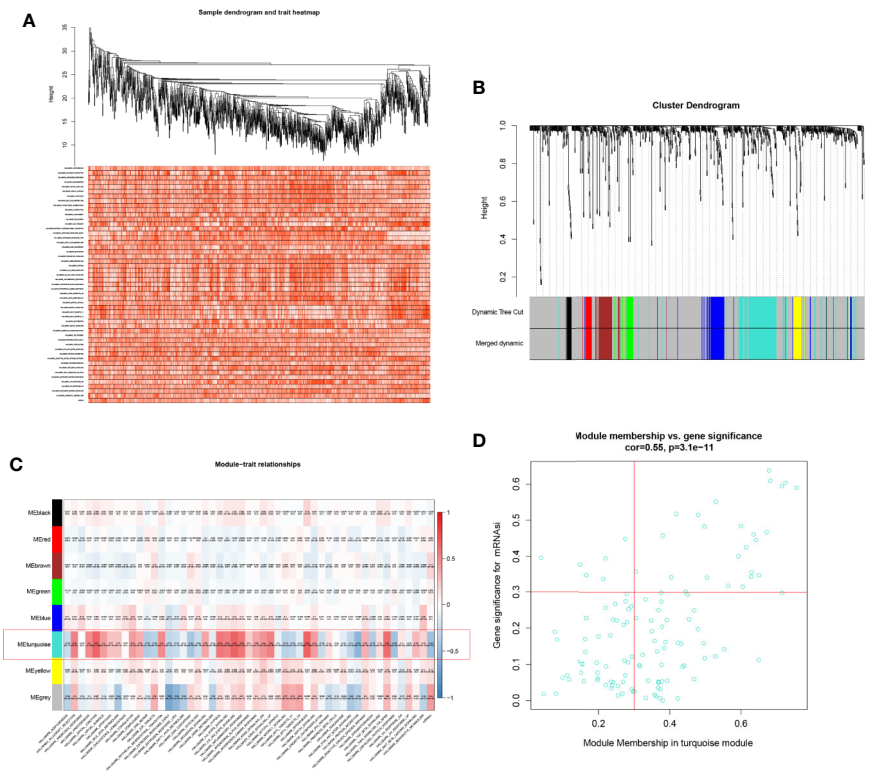

FIGURE 3 | Heatmap of sample **(A)**, Cluster dendrogram of WGCNA **(B)**, co-expression heatmap of modules and phenotypes **(C)**, and the correlation between the mRNAsi and the module **(D)**. Module turquoise and hallmark apical junction was the key module and phenotype.

In addition, the intersection between co-analysis Hallmark gene sets in GSVA and significant Hallmark gene sets in GSVA was illustrated in Venn plots (**Figure 7C**), 22 Hallmark gene sets were found.

Next, the network (**Figure 7D**) of TFs, PSRSs and Hallmark gene sets were constructed based on the coefficient correlation of the Pearson correlation analysis. Therefore, key TF-PSRS paired was MAF-CD248 (Correlation coefficient = 0.435, $p < 0.001$, positive), and PSRS-Hallmark gene set paired was CD248-apical junction (Correlation coefficient = 0.353, $p < 0.001$) (**Figure 7E**).

In sum, the scientific hypothesis was defined: MAF positively regulated CD248, promoting apical junction pathway in BRCA, which might play a role in bone metastasis.

Cmap Analysis

To find the latent inhibitor of the bone metastasis-specific regulation network and proposed signal axis, the CMap analysis was utilized, and alexidine (enrichment = 0.6393, $p = 0.046$), clomipramine (enrichment = 0.654, $p = 0.034$), trifluoperazine (enrichment = 0.434, $p = 0.003$), thioridazine (enrichment = 0.337, $p = 0.016$) and valinomycin (enrichment =-0.639, $p = 0.041$) were significant compounds in BRCA (**Figure 8A**). Based on the clue database, the detail information of trifluoperazine (**Figure 8B**), clomipramine (**Figure 8C**) and thioridazine (**Figure 8D**) were found, and trifluoperazine was most related to metastasis BRCA according to literature review results.

Spatial Transcriptome and Chromatin Immunoprecipitation Sequence Validation

With the aim to further explore the location of key genes in subtype cell clusters, the profiling of scRNA-seq and spatial transcriptome were co-analyzed. Fourteen clusters were identified in UMAP and t-SNE, and pare-carcinoma, invasive ductal carcinoma and intraductal carcinoma *in situ* were illustrated in HE-stained section (**Figure 9A**). For validation, the feature and spatial feature plots of MAF, CD248, GJA1, LAMA3, TJP1, LAMC2, and COL17A1 demonstrated to show the location in BRCA samples, and they were highly-expressed in the invasive ductal carcinoma tissue (cluster 2, 4, 7, 9, 12) (**Figures 9B, C**). Besides, a series of analysis based on cell cycle indicated that genes in cluster 4 and 7 of invasive ductal carcinoma and 10 of intraductal carcinoma highly related to phase G2M and S (**Figure 9D**). In addition, tumor inhibited pathways like apoptosis, p53 pathway and TNFα signaling *via*

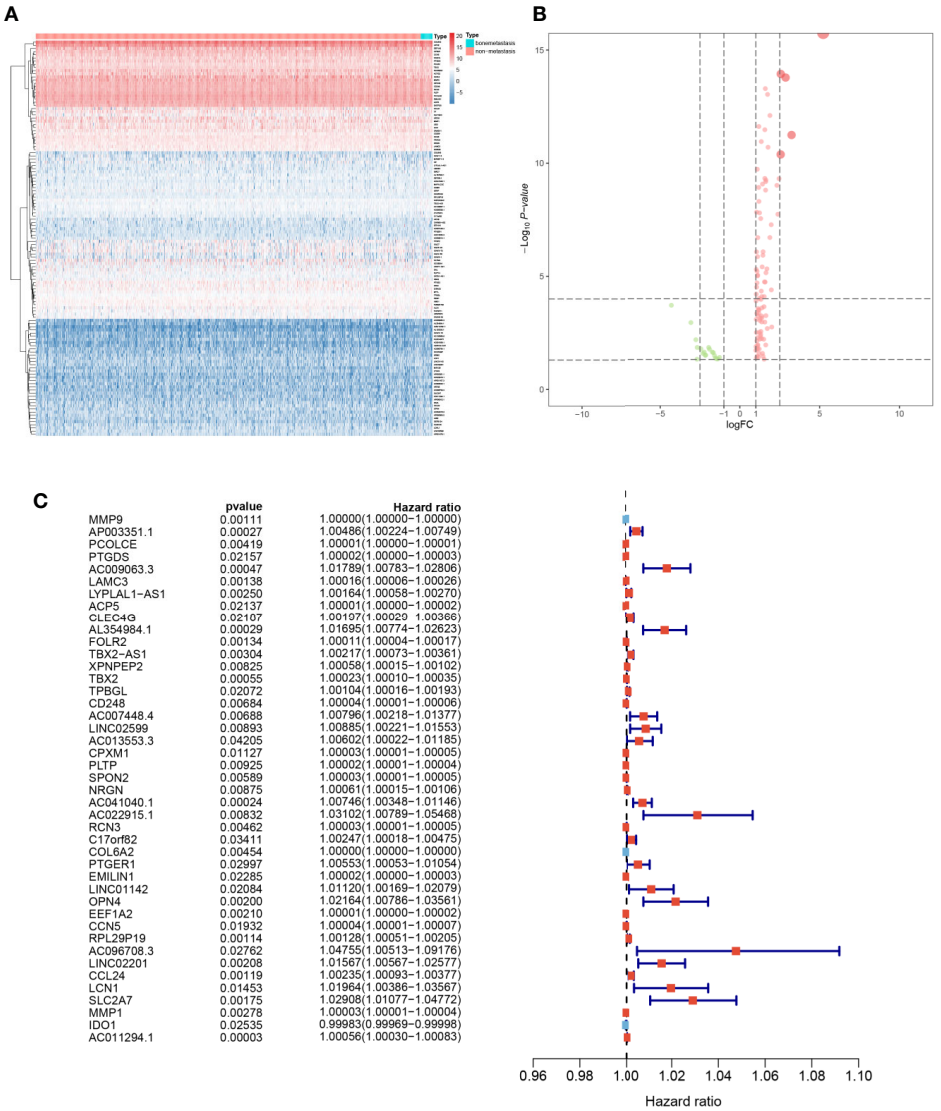

FIGURE 4 | The heatmap **(A)**, volcano plot **(B)**, and forest plots **(C)** of key genes from key module.

NF-kB were down-regulated while tumor genesis related pathways G2M checkpoint and E2F targets were up-regulated (**Figure 9E**). In ChIP-seq analysis, binding peaks were illustrated in CD248 sequence (**Figure 10**). Moreover, genes in our hypothesis were validated in ATAC-seq (**Figure 11**), and they were all regulated in BRCA samples. Therefore, patterns of direct transcriptional regulatory between TF-PSRS interaction pairs were identified.

Multidimensional Validation

The correlation of key genes in signal axis based on cBioportal database was summarized in **Table S1**. And top five genes in apical junction were GJA1, LAMA3, TJP1, LAMC2, and COL17A1. Several databases were applied to validate the expression level (**Table S2**) and prognosis value (**Table S3**) of key genes in hypothesis signal axis. Besides, details were demonstrated in **Figure S1**-**12**. MAF showed down-regulated in BRCA, and CD248, GJA1, LAMA3, TJP1, LAMC2, and COL17A1 showed up-regulated in primary BRCA. Besides, MAF was highly-expressed in the metastasis sample. What' more, MAF (**Figure S3C**, $p = 0.013$), CD248 (**Figure S3B**, $p = 0.036$), GJA1 (**Figure S3A**, $p = 0.005$; **Figure S6B**, $p = 0.003$), LAMA3 (**Figure S3A**, $p = 0.008$; **Figure S6B**, $p = 0.006$), TPJ1 (**Figure S6B**, $p = 0.019$) and LAMC2 (**Figure S3B**, $p = 0.018$) showed significantly related metastasis; MAF (**Figure S3C**, $p = 0.002$; S6C, $p = 0.048$), CD248 (**Figure S3D**, $p = 0.021$; S6C, $p = 0.015$), GJA1 (**Figure S3E**, $p = 0.001$; S6A, $p < 0.001$), LAMA3

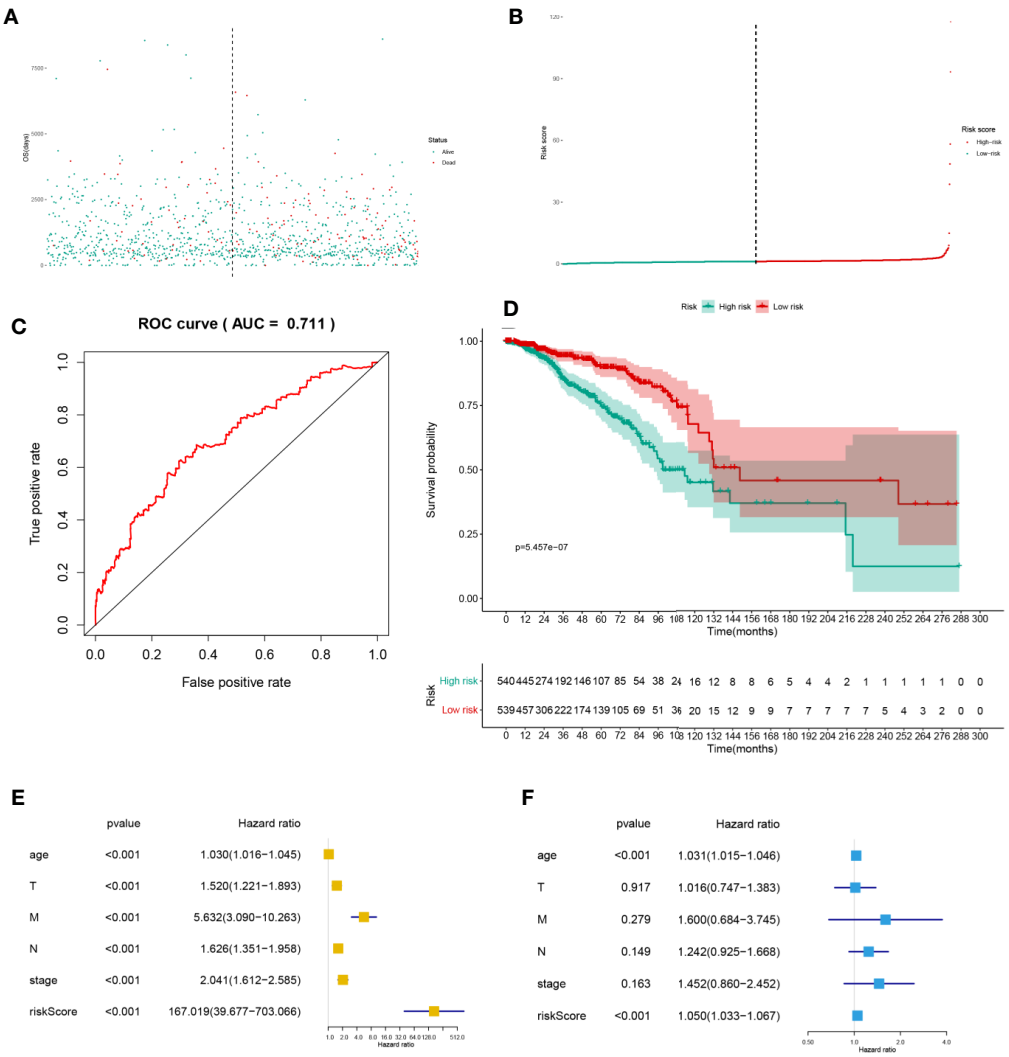

FIGURE 5 | The scatter plot **(A)**, risk line plot **(B)**, ROC curve (AUC = 0.711) **(C)**, and Kaplan-Meier plot ($p < 0.001$) **(D)** for multivariate prognosis model. And univariate **(E)** and multivariate **(F)** Cox regression analysis for risk score. And the risk score was the independent predict factor.

(S6A, $p = 0.047$),TJP1 (**Figure S3D**, $p = 0.031$; **Figure S6A**, $p = 0.044$; **Figure S7A**, $p = 0.027$), LAMC2 (**Figure S5F**, $p = 0.038$) and COL17A1 (**Figure S1R**, $p = 0.014$; **Figure S3D**, $p = 0.007$; **Figure S5G**, $p = 0.001$; **Figure S6A**, $p = 0.048$) showed significantly related prognosis; LAMC2 (**Figure S7C**, $p = 0.047$) and COL17A1 (**Figure S7C**, $p = 0.001$) were significantly related to progression free.

DISCUSSION

BRCA was a common tumor in female, and patients with bone metastasis suffered from the pain and the risk of fracture and even death (4). What's worse, tumor genesis and osteolytic damage could be mutually reinforcing (4). As consequence, the mechanism of bone metastasis must be expounded for early diagnosis and precise therapy.

In the recent study, a total of 813 primary BRCA samples were analyzed. Based on WGCNA method and univariate Cox regression analysis, several modules were annotated by mRNAsi and Hallmark gene sets to find the key module and correspond PSRSs. And the multivariate Cox model was constructed. In addition, multivariate Cox model and risk score were accessed by ROC curve and Kaplan-Meier survival analysis. And the risk score was an independent predict factor. Then, a metastasis-specific regulation network was constructed by the Pearson analysis, and MAF, CD248 and apical junction were significant. Moreover, the regulatory pattern was supported by

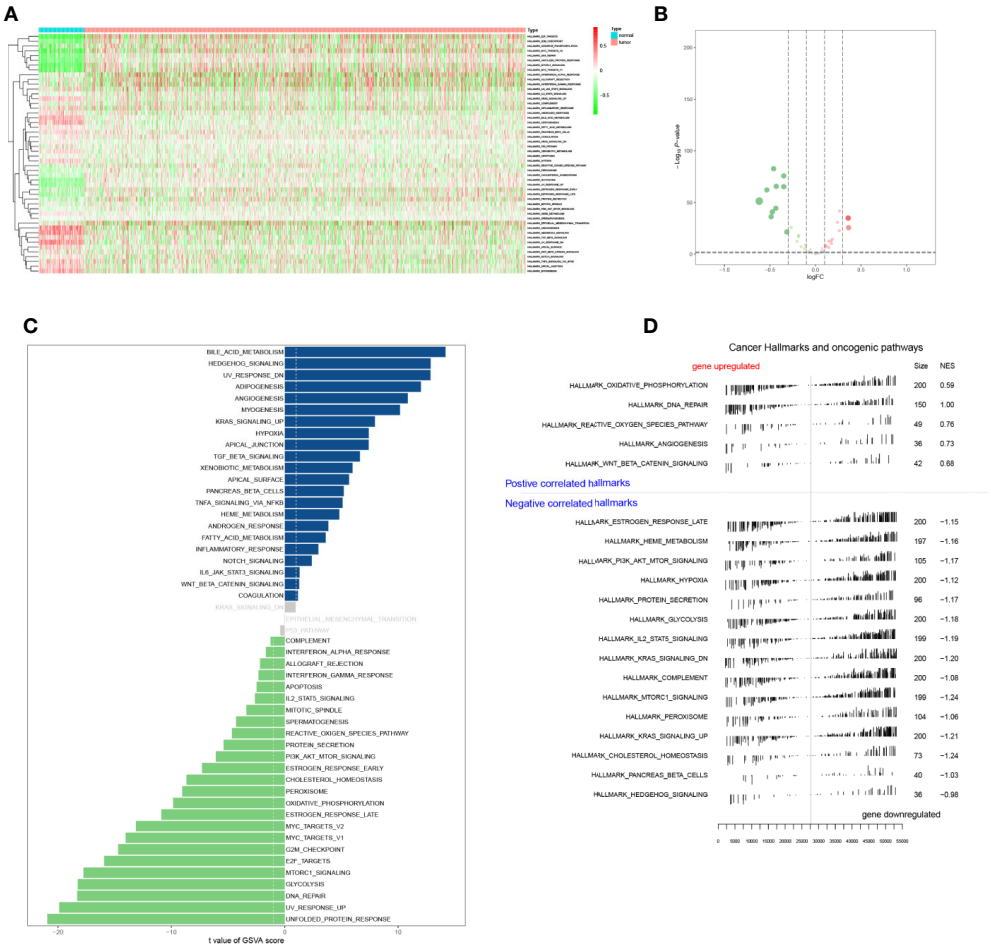

FIGURE 6 | The heatmap **(A)**, volcano plot **(B)**, GSVA **(C)**, and GSEA **(D)** analysis of hallmark gene sets.

spatial single-cell RNA sequence and ChIP-seq data and multi-omics online databases. Based on CMap analysis, trifluoperazine was identified as the possible inhibitor for bone metastasis of BRCA.

MAF was MAF basic leucine zipper transcription factor, which belonged to AP-1 super family, and it regulated the terminal differentiation (34). Besides, MAF was crucial in promoting osteoblast differentiation of bone marrow stromal cell (35). What' more, MAF directly regulated osteoblast-specifical promoter Bglap1, and co-regulated the osteoblast differentiation with RUNX2 (35). In addition, Milica Pavlovic et al. found that high-expressed MAF was significant related to bone metastasis instead of visceral metastasis based on Genomic copy number distortion analysis and immunohistochemistry, and MAF was also correlated to overall survival (36). Moreover, MAF played a role in promoting bone metastasis rather than cancer cell proliferation *in vivo* (36), which was consistent with our scientific hypothesis. Additionally, MAF also potentially controlled biological processes like migration, adhesion, and osteoclast differentiation in bone metastasis (36).

CD248 highly-expressed in tumor tissue, especially in BRCA, and it was related to the prognosis of patients (37). And the transcription product of CD248 was endosialin, which expressed on the cell surface of fibroblasts and pericytes in tumor instead of tumor endothelium (38). Further, Carmen Viski et al. found CD248 played a pivotal role by promoting the step of infiltration from primary to circulatory system *via* pericytes in metastasis, which affected on tumor microenvironment (39). Besides, CD248 enhanced the adhesion to the extracellular matrix, and activated the matrix metalloproteinase 9 (MMP9) in tumor metastasis (40). Moreover, CD248 expressed in osteoblast instead of osteoclast, and it has negative effects on osteoblast maturation and ossification (41).

Although none of the study reported the correlation of MAF and CD248, we proposed that MAF positively regulated the transcription of CD248: promoted the function of the transcript in cell adhesion, invasion and migration, and regulated osteoblast function (36, 40, 41).

Apical junction was a structure of apical domain of epithelial cells, and it linked adjacent epithelial cells by tight and adherent

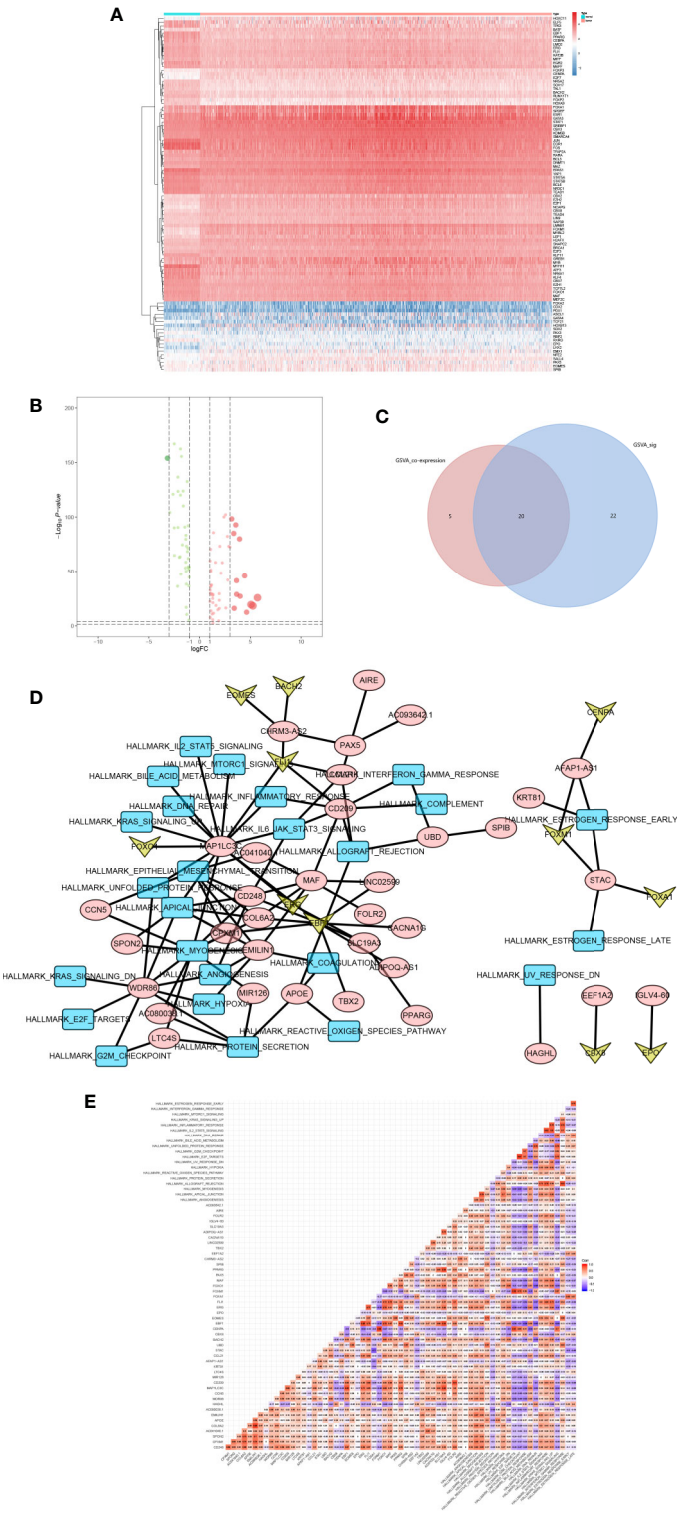

FIGURE 7 | The heatmap **(A)** and volcano plot **(B)** of TFs. And the venn plot of hallmark gene sets **(C)**. The network plot of TFs, DEGs and hallmark gene sets **(D)**. And the co-analysis result for TFs, DEGs and hallmark gene sets **(E)**.

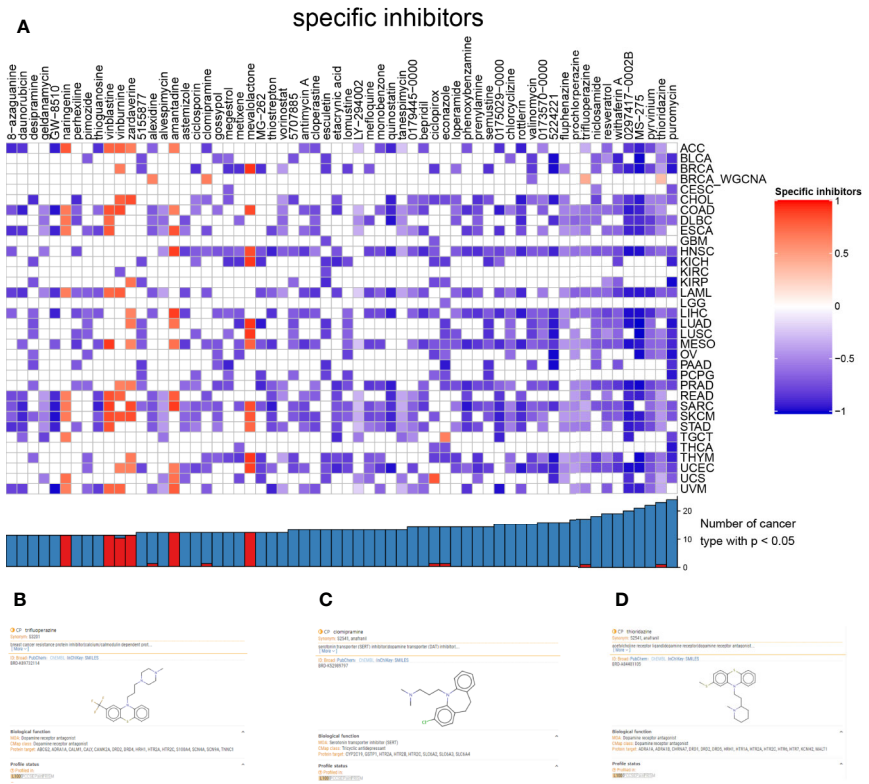

FIGURE 8 | The heatmap of inhibitor and different cancers **(A)**. The information of trifluoperazine **(B)**, clomipramine **(C)**, thioridazine **(D)** from clue database.

junction, which was essential for maintaining the epithelial barrier (42). And in type III epithelial–mesenchymal transition (EMT), the apical junction was disrupted, the apical–basal polarity lost, and the mesenchymal characteristics emerged, finally cells migrated to vessels and traveled to multiply organs and tissues (43). However, some epithelial characteristics were retained, especially the E-cadherin, and the collective migration was observed in metastasis BRCA (44, 45). What's more, when in the stage of transplanting to the bone, E-cadherin and E-cadherin adherent junction formed between cancer cells, then the E-cadherin and N-cadherin adherent junction formed between cancer cells and osteoblasts, and cell-cell contact promoted the tumor proliferation *via* activated mTOR pathway in tumor microenvironment (46).

Up to date, few of study focused on the relationship between CD248 and apical junction. We speculated that CD248 regulated the apical junction by promoting the bone colonization in bone metastasis (41, 46).

Trifluoperazine was a type of calmodulin blocker and dopamine D2 like receptor antagonist, which could inhibit the cancer cell metastasis *in vitro*, but the collective migration can be promoted by knocking out MRP (47). However, trifluoperazine might disturb the electrostatic surface potential (47). Besides, it inhibited the differentiation of osteoclasts, tumor genesis, metastasis and bone loss and promoted bone formation in breast cancer (48). Therefore, we proposed trifluoperazine might target on the MAF-CD248-apical junction axis, and play a role in inhibiting metastasis.

Last but not least, there were some limitations in our study. Firstly, our analysis was only based on high-throughput bioinformatic analysis rather than mechanism exploration. Then, data and platform were also limited, and more validations based on different data sets were needed (e.g. most ChIP-seq samples were not BRCA). And verifications based on clinical samples (with and without metastasis) were required. Next, more function experiments and directly mechanism needed to be verified. Therefore, gain/loss experiments based on MAF-CD248, CD248-apical junction and MAF-apical junction, rescue experiments on MAF-CD248-apical junction axis *in vivo* and vitro and Co-Immunoprecipitation will be lunched. Importantly, the MAF-CD248-apical junction axis in bone metastasis BRCA was firstly reported, and our study provided the idea of application on clinical prognosis and precise therapy.

CONCLUSION

In summary, we proposed that MAF positively regulated CD248, then promoted apical junction pathway in BRCA, which played a

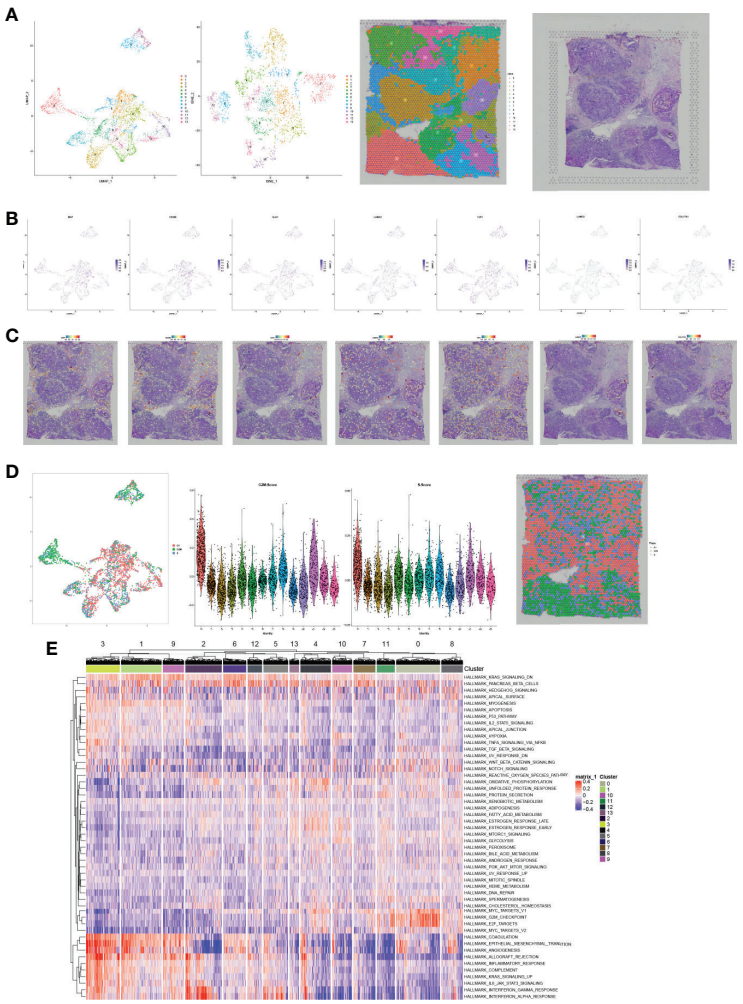

FIGURE 9 | The UMAP, t-SNE plots, and pare-carcinoma, invasive ductal carcinoma and intraductal carcinoma *in situ* were illustrated in HE-stained section **(A)**. The feature and spatial plots of MAF, CD248, GJA1, LAMA3, TJP1, LAMC2, and COL17A1, showing that these key genes were highly expressed in the invasive ductal carcinoma tissue **(B, C)**. UMAP plot related to cell cycle, violin plots of phase G2M and S, and phase annotated section **(D)**, and cluster 4 and 7 of invasive ductal carcinoma and 10 of intraductal carcinoma highly related to phase G2M and S. The heatmap of Hallmark gene sets in cell clusters **(E)**.

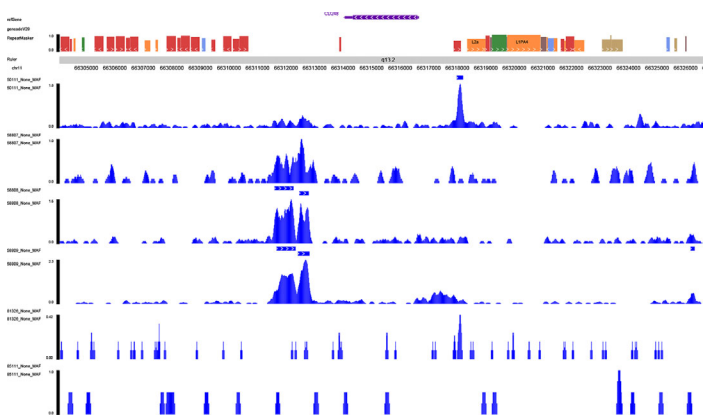

FIGURE 10 | Validation of the transcriptional regulation mechanisms of MAF-CD248 in ChIP-seq data available from Cistrome database.

FIGURE 11 | Validation of seven key genes [MAF **(A)**, CD248 **(B)**, GJA1 **(C)**, LAMA3 **(D)**, TJP1 **(E)**, LAMC2 **(F)**, and COL17A1 **(G)**] in ATAC-seq data available from TCGA.

role in bone metastasis. And it could be inhibited by trifluoperazine. Besides, the MAF-CD248-apical junction signal axis was verified by spatial single-cell RNA sequence and ChIP-seq data and multi-omics online databases.

DATA AVAILABILITY STATEMENT

Publicly available datasets were analyzed in this study. This data can be found here: TCGA program (https://portal.gdc.cancer.gov) and 10x genomics support center (https://support.10xgenomics.com/spatial-gene-expression/datasets).

ETHICS STATEMENT

The study was approved by the Ethics Committee of the First Affiliated Hospital of Zhengzhou University. The patients/participants provided their written informed consent to participate in this study.

AUTHOR CONTRIBUTIONS

RH, ZL, JiayZ, ZZ, JiaqZ, ML, SW, SX, YX, XC, JL, WC, BW, PY, DY, and ZH conceived and designed the study. RH, ZL, JiayZ, ZZ, JiaqZ, ML, SW, SX, YX, XC, JL, WC, BW, PY, DY, and ZH collected and/or assembled the data. RH, ZL, JiayZ, ZZ, JiaqZ, ML, SW, SX, YX, XC, JL, WC, BW, PY, DY, and ZH analyzed and interpreted the data. RH, ZL, JiayZ, ZZ, JiaqZ, ML, SW, SX, YX, XC, JL, WC, BW, PY, DY, and ZH wrote the manuscript. RH, ZL, JiayZ, ZZ, Jiaq, ML, SW, SX, YX, XC, JL, WC, BW, PY, DY, and ZH gave the final approval of the manuscript. All authors contributed to the article and approved the submitted version.

FUNDING

The study was supported by the National Natural Science Foundation of China, joint fund cultivation project (Grant No. U1504822); Henan Medical Science and Technology Research Project (No. 201602031); Henan Medical Science and technology Research Plan, Joint Project of the Ministry and the Province, (No. SB201901037); Henan Provincial Department of Science and Technology, Social Development Project (No. 142102310055). The funders had no role in study design, data collection and analysis, decision to publish, or preparation of the manuscript.

ACKNOWLEDGMENTS

We thank the The Cancer Genome Atlas (TCGA) team for using their data.

SUPPLEMENTARY MATERIAL

The Supplementary Material for this article can be found online at: https://www.frontiersin.org/articles/10.3389/fonc.2020.613333/full#supplementary-material

Supplementary Figure 1 | The expression level of MAF **(A)**, CD248 **(B)**, GJA1 **(C)**, LAMA3 **(D)**, TJP1 **(E)**, LAMC2 **(F)**, and COL17A1 **(G)** between tumor and normal. The stage plot of MAF **(H)**, CD248 **(I)**, GJA1 **(J)**, LAMA3 **(K)**, TJP1 **(L)**, LAMC2 **(M)**, and COL17A1 **(N)** in BRCA. The Kaplan-Meier survival analysis for overall survival in MAF **(O)**, CD248 **(P)**, LAMA3 **(Q)**, and COL17A1 **(R)**, for Disease free survival in MAF **(S)**, CD248 **(T)**, LAMA3 **(U)**, and COL17A1 **(V)**.

Supplementary Figure 2 | The expression level of MAF **(A)**, CD248 **(B)**, GJA1 **(C)**, LAMA3 **(D)**, TJP1 **(E)**, LAMC2 **(F)**, and COL17A1 **(G)** between tumor and normal.

Supplementary Figure 3 | The Kaplan-Meier survival analysis for MAF, GJA1, LAMA3, TJP1, LAMC2, COL17A1, and integrated genes in BRCA metastasis in NKI **(A)**; MAF, CD248, GJA1, LAMA3, TJP1, LAMC2, COL17A1, and integrated genes in BRCA metastasis in GSE2990 **(B)**; MAF, CD248, GJA1, LAMA3, TJP1, LAMC2, COL17A1, and integrated genes in BRCA metastasis in GSE11121 **(C)**. The Kaplan-Meier survival analysis for MAF, CD248, GJA1, LAMA3, TJP1, LAMC2, COL17A1, and integrated genes in BRCA overall survival in GSE19783 **(D)**; MAF, CD248, GJA1, LAMA3, TJP1, LAMC2, COL17A1, and integrated genes in BRCA overall survival in GSE3494 **(E)**.

Supplementary Figure 4 | The expression level of MAF **(A)**, CD248 **(B)**, GJA1 **(C)**, LAMA3 **(D)**, TJP1 **(E)**, LAMC2 **(F)**, and COL17A1 **(G)** between tumor and normal.

Supplementary Figure 5 | The Kaplan-Meier survival analysis of MAF **(A)**, CD248 **(B)**, GJA1 **(C)**, LAMA3 **(D)**, TJP1 **(E)**, LAMC2 **(F)**, and COL17A1 **(G)** between high- and low-expression groups. The positively **(H)** and negatively **(I)** related genes of BRCA.

Supplementary Figure 6 | The Kaplan-Meier survival analysis for MAF, CD248, GJA1, LAMA3, TJP1, LAMC2, COL17A1, and integrated genes in BRCA overall survival in Van **(A)**; MAF, CD248, GJA1, LAMA3, TJP1, LAMC2, COL17A1, and integrated genes in BRCA metastasis in Van **(B)**; MAF, CD248, GJA1, LAMA3, TJP1, LAMC2, COL17A1, and integrated genes in BRCA overall survival in TCGA **(C)**.

Supplementary Figure 7 | The Kaplan-Meier survival analysis for MAF, CD248, GJA1, LAMA3, TJP1, LAMC2, COL17A1, and integrated genes in BRCA overall survival **(A)**; MAF, CD248, GJA1, LAMA3, TJP1, LAMC2, COL17A1, and integrated genes in BRCA disease free **(B)**; MAF, CD248, GJA1, LAMA3, TJP1, LAMC2, COL17A1, and integrated genes in BRCA progression free **(C)**.

Supplementary Figure 8 | The expression level of MAF, CD248, GJA1, LAMA3, TJP1, LAMC2, and COL17A1 in normal people tissue.

Supplementary Figure 9 | The expression level of MAF, CD248, GJA1, LAMA3, TJP1, LAMC2, and COL17A1 in BRCA **(A)**. The PCA plot of MAF, CD248, GJA1, LAMA3, TJP1, LAMC2, and COL17A1 **(B)**. The heatmap of MAF, CD248, GJA1, LAMA3, TJP1, LAMC2, and COL17A1 **(C)**.

Supplementary Figure 10 | The expression level of MAF **(A)**, CD248 **(B)**, GJA1 **(C)**, LAMA3 **(D)**, TJP1 **(E)**, LAMC2 **(F)**, and COL17A1 **(G)** in cancer cell lines.

Supplementary Figure 11 | The expression level of MAF **(A)**, CD248 **(B)**, GJA1 **(C)**, LAMA3 **(D)**, TJP1 **(E)**, LAMC2 **(F)**, and COL17A1 **(G)** in normal and BRCA tissue.

Supplementary Figure 12 | The protein-protein interaction network of MAF, CD248, GJA1, LAMA3, TJP1, LAMC2, and COL17A1.

REFERENCES

1. Yeo SK, Guan JL. Breast Cancer: Multiple Subtypes within a Tumor? *Trends Cancer* (2017) 3(11):753–60. doi: 10.1016/j.trecan.2017.09.001
2. Siegel RL, Miller KD, Jemal A. Cancer statistics, 2020. *CA Cancer J Clin* (2020) 70(1):7–30. doi: 10.3322/caac.21590
3. DeSantis CE, Ma J, Gaudet MM, Newman LA, Miller KD, Goding Sauer A, et al. Breast cancer statistics, 2019. *CA Cancer J Clin* (2019) 69(6):438–51. doi: 10.3322/caac.21583
4. Shemanko CS, Cong Y, Forsyth A. What Is Breast in the Bone? *Int J Mol Sci* (2016) 17(10):1764. doi: 10.3390/ijms17101764
5. Bai KH, He SY, Shu LL, Wang WD, Lin SY, Zhang QY, et al. Identification of cancer stem cell characteristics in liver hepatocellular carcinoma by WGCNA analysis of transcriptome stemness index. *Cancer Med* (2020) 9(12):4290–8. doi: 10.1002/cam4.3047
6. Suo HD, Tao Z, Zhang L, Jin ZN, Li XY, Ma W, et al. Coexpression Network Analysis of Genes Related to the Characteristics of Tumor Stemness in Triple-Negative Breast Cancer. *BioMed Res Int* (2020) 2020:7575862. doi: 10.1155/2020/7575862
7. Malta TM, Sokolov A, Gentles AJ, Burzykowski T, Poisson L, Weinstein JN, et al. Machine Learning Identifies Stemness Features Associated with Oncogenic Dedifferentiation. *Cell* (2018) 173(2):338–54 e15. doi: 10.1016/j.cell.2018.03.034
8. Langfelder P, Horvath S. WGCNA: an R package for weighted correlation network analysis. *BMC Bioinform* (2008) 9:559. doi: 10.1186/1471-2105-9-559
9. Liberzon A, Birger C, Thorvaldsdóttir H, Ghandi M, Mesirov JP, Tamayo P. The Molecular Signatures Database (MSigDB) hallmark gene set collection. *Cell Syst* (2015) 1(6):417–25. doi: 10.1016/j.cels.2015.12.004
10. Zheng R, Wan C, Mei S, Qin Q, Wu Q, Sun H, et al. Cistrome Data Browser: expanded datasets and new tools for gene regulatory analysis. *Nucleic Acids Res* (2019) 47(D1):D729–D35. doi: 10.1093/nar/gky1094
11. Subramanian A, Tamayo P, Mootha VK, Mukherjee S, Ebert BL, Gillette MA, et al. Gene set enrichment analysis: a knowledge-based approach for interpreting genome-wide expression profiles. *Proc Natl Acad Sci U S A* (2005) 102(43):15545–50. doi: 10.1073/pnas.0506580102
12. Snel B, Lehmann G, Bork P, Huynen MA. STRING: a web-server to retrieve and display the repeatedly occurring neighbourhood of a gene. *Nucleic Acids Res* (2000) 28(18):3442–4. doi: 10.1093/nar/28.18.3442
13. Szklarczyk D, Morris JH, Cook H, Kuhn M, Wyder S, Simonovic M, et al. The STRING database in 2017: quality-controlled protein-protein association networks, made broadly accessible. *Nucleic Acids Res* (2017) 45(D1):D362–d8. doi: 10.1093/nar/gkw937
14. Huang RZ, Liu ZQ, Tian TL, Song DW, Yan PH, Yin HB, et al. The construction and analysis of tumor-infiltrating immune cells and ceRNA networks in metastatic adrenal cortical carcinoma. *Biosci Rep* (2020) 40:16. doi: 10.1042/bsr20200049
15. Corces MR, Granja JM, Shams S, Louie BH, Seoane JA, Zhou W, et al. The chromatin accessibility landscape of primary human cancers. *Science (New York NY)* (2018) 362(6413):eaav1898. doi: 10.1126/science.aav1898
16. Li D, Hsu S, Purushotham D, Sears RL, Wang T. WashU Epigenome Browser update 2019. *Nucleic Acids Res* (2019) 47(W1):W158–w65. doi: 10.1093/nar/gkz348
17. Hahne F, Ivanek R. Visualizing Genomic Data Using Gviz and Bioconductor. *Methods Mol Biol (Clifton NJ)* (2016) 1418:335–51. doi: 10.1007/978-1-4939-3578-9_16
18. Butler A, Hoffman P, Smibert P, Papalexi E, Satija R. Integrating single-cell transcriptomic data across different conditions, technologies, and species. *Nat Biotechnol* (2018) 36(5):411–20. doi: 10.1038/nbt.4096
19. Chung NC, Storey JD. Statistical significance of variables driving systematic variation in high-dimensional data. *Bioinformatics (Oxford England)* (2015) 31(4):545–54. doi: 10.1093/bioinformatics/btu674
20. Hou R, Denisenko E, Forrest ARR. scMatch: a single-cell gene expression profile annotation tool using reference datasets. *Bioinformatics (Oxford England)* (2019) 35(22):4688–95. doi: 10.1093/bioinformatics/btz292
21. Aran D, Looney AP, Liu L, Wu E, Fong V, Hsu A, et al. Reference-based analysis of lung single-cell sequencing reveals a transitional profibrotic macrophage. *Nat Immunol* (2019) 20(2):163–72. doi: 10.1038/s41590-018-0276-y
22. Zhang X, Lan Y, Xu J, Quan F, Zhao E, Deng C, et al. CellMarker: a manually curated resource of cell markers in human and mouse. *Nucleic Acids Res* (2019) 47(D1):D721–d8. doi: 10.1093/nar/gky900
23. Qiu X, Mao Q, Tang Y, Wang L, Chawla R, Pliner HA, et al. Reversed graph embedding resolves complex single-cell trajectories. *Nat Methods* (2017) 14(10):979–82. doi: 10.1038/nmeth.4402
24. Rhodes DR, Yu J, Shanker K, Deshpande N, Varambally R, Ghosh D, et al. ONCOMINE: a cancer microarray database and integrated data-mining platform. *Neoplasia* (2004) 6(1):1–6. doi: 10.1016/s1476-5586(04)80047-2
25. Goswami CP, Nakshatri H. PROGgeneV2: enhancements on the existing database. *BMC Cancer* (2014) 14:970. doi: 10.1186/1471-2407-14-970
26. Chandrashekar DS, Bashel B, Balasubramanya SAH, Creighton CJ, Ponce-Rodriguez I, Chakravarthi B, et al. UALCAN: A Portal for Facilitating Tumor Subgroup Gene Expression and Survival Analyses. *Neoplasia* (2017) 19(8):649–58. doi: 10.1016/j.neo.2017.05.002
27. Vasaikar SV, Straub P, Wang J, Zhang B. LinkedOmics: analyzing multi-omics data within and across 32 cancer types. *Nucleic Acids Res* (2018) 46(D1):D956–D63. doi: 10.1093/nar/gkx1090
28. Aguirre-Gamboa R, Gomez-Rueda H, Martinez-Ledesma E, Martinez-Torteya A, Chacolla-Huaringa R, Rodriguez-Barrientos A, et al. SurvExpress: an online biomarker validation tool and database for cancer gene expression data using survival analysis. *PloS One* (2013) 8(9):e74250. doi: 10.1371/journal.pone.0074250
29. Cerami E, Gao J, Dogrusoz U, Gross BE, Sumer SO, Aksoy BA, et al. The cBio Cancer Genomics Portal: An Open Platform for Exploring Multidimensional Cancer Genomics Data. *Cancer Discov* (2012) 2(5):401–4. doi: 10.1158/2159-8290.cd-12-0095
30. Consortium G. Human genomics. The Genotype-Tissue Expression (GTEx) pilot analysis: multitissue gene regulation in humans. *Science (New York NY)* (2015) 348(6235):648–60. doi: 10.1126/science.1262110
31. Goldman M, Craft B, Swatloski T, Cline M, Morozova O, Diekhans M, et al. The UCSC Cancer Genomics Browser: update 2015. *Nucleic Acids Res* (2015) 43(Database issue):D812–7. doi: 10.1093/nar/gku1073
32. Ghandi M, Huang FW, Jane-Valbuena J, Kryukov GV, Lo CC, McDonald ER3rd, et al. Next-generation characterization of the Cancer Cell Line Encyclopedia. *Nature* (2019) 569(7757):503–8. doi: 10.1038/s41586-019-1186-3
33. Uhlen M, Fagerberg L, Hallstrom BM, Lindskog C, Oksvold P, Mardinoglu A, et al. Proteomics. Tissue-based map of the human proteome. *Science (New York NY)* (2015) 347(6220):1260419. doi: 10.1126/science.1260419
34. Labott AT, Lopez-Pajares V. Epidermal differentiation gene regulatory networks controlled by MAF and MAFB. *Cell Cycle* (2016) 15(11):1405–9. doi: 10.1080/15384101.2016.1172148
35. Nishikawa K, Nakashima T, Takeda S, Isogai M, Hamada M, Kimura A, et al. Maf promotes osteoblast differentiation in mice by mediating the age-related switch in mesenchymal cell differentiation. *J Clin Invest* (2010) 120(10):3455–65. doi: 10.1172/JCI42528
36. Pavlovic M, Arnal-Estape A, Rojo F, Bellmunt A, Tarragona M, Guiu M, et al. Enhanced MAF Oncogene Expression and Breast Cancer Bone Metastasis. *J Natl Cancer Inst* (2015) 107(12):djv256. doi: 10.1093/jnci/djv256
37. Davies G, Cunnick GH, Mansel RE, Mason MD, Jiang WG. Levels of expression of endothelial markers specific to tumour-associated endothelial cells and their correlation with prognosis in patients with breast cancer. *Clin Exp Metastasis* (2004) 21(1):31–7. doi: 10.1023/b:clin.0000017168.83616.d0
38. MacFadyen JR, Haworth O, Roberston D, Hardie D, Webster MT, Morris HR, et al. Endosialin (TEM1, CD248) is a marker of stromal fibroblasts and is not selectively expressed on tumour endothelium. *FEBS Lett* (2005) 579(12):2569–75. doi: 10.1016/j.febslet.2005.03.071
39. Viski C, Konig C, Kijewska M, Mogler C, Isacke CM, Augustin HG. Endosialin-Expressing Pericytes Promote Metastatic Dissemination. *Cancer Res* (2016) 76(18):5313–25. doi: 10.1158/0008-5472.CAN-16-0932
40. Tomkowicz B, Rybinski K, Foley B, Ebel W, Kline B, Routhier E, et al. Interaction of endosialin/TEM1 with extracellular matrix proteins mediates cell adhesion and migration. *Proc Natl Acad Sci U S A* (2007) 104(46):17965–70. doi: 10.1073/pnas.0705647104
41. Naylor AJ, Azzam E, Smith S, Croft A, Poyser C, Duffield JS, et al. The mesenchymal stem cell marker CD248 (endosialin) is a negative regulator of bone formation in mice. *Arthritis Rheum* (2012) 64(10):3334–43. doi: 10.1002/art.34556
42. Zhu MJ, Sun X, Du M. AMPK in regulation of apical junctions and barrier function of intestinal epithelium. *Tissue Barriers* (2018) 6(2):1–13. doi: 10.1080/21688370.2018.1487249
43. Silvestrini VC, Lanfredi GP, Masson AP, Poersch A, Ferreira GA, Thome CH, et al. A proteomics outlook towards the elucidation of epithelial-mesenchymal

transition molecular events. *Mol Omics* (2019) 15(5):316–30. doi: 10.1039/c9mo00095j
44. Hollestelle A, Peeters JK, Smid M, Timmermans M, Verhoog LC, Westenend PJ, et al. Loss of E-cadherin is not a necessity for epithelial to mesenchymal transition in human breast cancer. *Breast Cancer Res Treat* (2013) 138(1):47–57. doi: 10.1007/s10549-013-2415-3
45. Gonzalez-Mariscal L, Miranda J, Gallego-Gutierrez H, Cano-Cortina M, Amaya E. Relationship between apical junction proteins, gene expression and cancer. *Biochim Biophys Acta Biomembr* (2020) 1862(9):183278. doi: 10.1016/j.bbamem.2020.183278
46. Wang H, Yu C, Gao X, Welte T, Muscarella AM, Tian L, et al. The osteogenic niche promotes early-stage bone colonization of disseminated breast cancer cells. *Cancer Cell* (2015) 27(2):193–210. doi: 10.1016/j.ccell.2014.11.017
47. Finlayson AE, Freeman KW. A cell motility screen reveals role for MARCKS-related protein in adherens junction formation and tumorigenesis. *PloS One* (2009) 4(11):e7833. doi: 10.1371/journal.pone.0007833
48. Liu S, Fan Y, Chen A, Jalali A, Minami K, Ogawa K, et al. Osteocyte-Driven Downregulation of Snail Restrains Effects of Drd2 Inhibitors on Mammary Tumor Cells. *Cancer Res* (2018) 78(14):3865–76. doi: 10.1158/0008-5472.CAN-18-0056

Conflict of Interest: The authors declare that the research was conducted in the absence of any commercial or financial relationships that could be construed as a potential conflict of interest.

frontiers in Oncology

HYPOTHESIS AND THEORY
published: 05 February 2021
doi: 10.3389/fonc.2020.611054

The Potential Roles of Exosomal miR-214 in Bone Metastasis of Lung Adenocarcinoma

Jian Zhang[1*†] *and Jiangmei Wu*[2†]

[1] Institute of Laboratory Animal Science, Guizhou University of Traditional Chinese Medicine, Guiyang, China, [2] School of Pharmacy, Guizhou University of Traditional Chinese Medicine, Guiyang, China

Bone metastasis is closely related to the alterations of bone microenvironment. In this article, we hypothesize that exosomes may be involved in the "vicious circle" by transferring miR-214. miR-214 is highly expressed in lung adenocarcinoma, and is closely related to the degree of lung cancer progression. As a key regulator of bone homeostasis, miR-214 promotes osteoclast differentiation and mediates intercellular communication between osteoclasts and osteoblasts *via* the way of exosomal miRNA. Therefore, it is highly probable that exosomal miR-214 derived from lung adenocarcinoma may disrupt bone homeostasis by enhancing bone resorption. Exosomal miR-214 can be released by lung adenocarcinoma cells, enters peripheral circulation, and is taken up by osteoclasts, consequently stimulating osteoclast differentiation. The enhanced bone resorption alters the bone microenvironment by releasing multiple cytokines and growth factors favoring cancer cells. The circulating cancer cells migrate to bone, proliferate, and colonize, resulting in the formation of metastasis. Furthermore, osteoclasts derived exosomal miR-214 may in turn contribute to cancer progression. In this way, the exosomal miR-214 from osteoclasts and lung adenocarcinoma cells mediates the positive interaction between bone resorption and bone metastasis. The levels of exosomal miR-214 in the peripheral circulation may help predict the risk of bone metastasis. The exosomal miR-214 may be a potential therapeutic target for both prevention and treatment of bone metastasis in patients with lung adenocarcinoma.

Keywords: exosome, miR-214, bone metastasis, osteoclast, lung adenocarcinoma

OPEN ACCESS

Edited by:
Dianwen Song, Shanghai First People's Hospital, China

Reviewed by:
Lavinia Raimondi, Rizzoli Orthopedic Institute (IRCCS), Italy
Penelope Dawn Ottewell, The University of Sheffield, United Kingdom

****Correspondence:***
Jian Zhang
zhangjian075@gzy.edu.cn

[†]These authors have contributed equally to this work

Specialty section:
This article was submitted to Molecular and Cellular Oncology, a section of the journal Frontiers in Oncology

Received: *28 September 2020*
Accepted: *18 December 2020*
Published: *05 February 2021*

Citation:
Zhang J and Wu J (2021) The Potential Roles of Exosomal miR-214 in Bone Metastasis of Lung Adenocarcinoma. Front. Oncol. 10:611054. doi: 10.3389/fonc.2020.611054

INTRODUCTION

Lung cancer is the most common cancer worldwide, and is also the leading cause of cancer incidence and mortality (1). Bone is one of the most common sites for metastasis. About 30%-40% of patients with lung cancer are found to have bone metastasis (2). The majority of lung cancer metastases are osteolytic, characterized by high activities of osteoclasts. Therefore, bone metastases usually develop skeleton-related events (SREs), such as bone pain, pathologic fractures, spinal cord compression, and hypercalcemia (3). These sequelae negatively influence the quality of patients' life, and are a major cause for mortality. The goals of treating bone metastasis in lung cancer is to improve the quality of life, prolong life expectancy, relieve symptoms, and prevent pathological

fractures and other SREs. The main therapeutic methods include systemic therapy (chemotherapy, targeted therapy, hormone therapy, and immunotherapy), local therapy (radiotherapy, ablation, and surgery), and antiresorptive agents (bisphosphonates and denosumab) (3). Both systemic and local therapies are used to directly kill the cancer cells in primary and metastatic tumors. The antiresorptive agents can efficiently prevent and delay the occurrence of SREs, and are the standard treatments for tumor-induced hypercalcemia. The antiresorptive agents also exert their antitumor effects by interrupting the vicious cycle of increased osteolysis coupled with increased tumor growth (4). To date, the currently available treatments are not effective for curing bone metastasis, but they can relieve pain, help prevent complications, and improve the quality of life. Investigating the underlying mechanism involved in bone metastasis is critical for the development of molecular targeted therapy and precise biomarkers for liquid biopsy.

Exosomes are small membrane-bound extracellular vesicles (30–100 nm in diameter) released from most eukaryotic cells, and are recognized as carriers of multiple biomolecules to mediate intercellular communication. Under pathophysiological conditions, more exosomes are released in cancer cells than normal cells, and mediate the communication between primary tumor cells and the distant organs. Accumulating studies have indicated that exosomes play pivotal roles in tumor growth, invasion, metastasis, angiogenesis and drug resistance. Exosomes and their cargos may be potentially used as biomarkers, therapeutic targets and carriers of anticancer drugs (5). Recently, numerous studies demonstrate various functions of exosomal microRNAs (miRNAs) in the interactions between cancer cells and its microenvironment (6). Identifying the key exosomal miRNAs mediating the interactions between cancer cells and bone microenvironment could be beneficial for understanding the pathogenesis of bone metastasis. Exosomal miRNAs may serve as a potential therapeutic target and prognostic marker for bone metastasis.

miR-214 is involved in the progression of lung adenocarcinoma and plays important roles in the balance of bone metabolism (7, 8). Since cancer cells derived exosomes can mediate the interaction between cancer cells and bone microenvironment (9, 10), we raise a hypothesis that exosomal miR-214 derived from lung adenocarcinoma and osteoclasts may mediate bone metastasis. The present article critically evaluated the potential roles of exosomal miR-214 in bone metastasis of lung adenocarcinoma. Exosomal miR-214 from lung adenocarcinoma can be taken up by osteoclasts and then enhances bone resorption, consequently affecting the bone microenvironment (11). On the other hand, osteoclasts-derived exosomal miR-214 may in turn contribute to cancer progression.

EXOSOMES AND EXOSOMAL MICRORNAS

Exosomes are cell-secreted nanoparticles with the size of 30–100 nm, and can be found in various body fluids such as blood, lymph, urine, saliva, breast milk, and semen (12). Exosomes are lipid bilayer-enclosed biological nanoparticles, and their formation is associated with the endocytic pathway. When the late endosomes are fused with plasma membrane, the exosomes are released into the extracellular environment (13). The exosomes carry various biomolecules, including lipids, proteins, and nucleic acids, which can be transferred to neighboring cells or distant organs through circulation (14, 15). The uptake of exosomes in recipient cells is mediated by the endocytosis process. Both normal and cancerous cells can secret exosomes. However, cancer cells produce and release more abundant exosomes than normal cells. Tumor-derived exosomes have multifunctions, such as tumor progression, immune suppression, angiogenesis, metastasis, and chemoresistance. Furthermore, exosomes are valuable source for liquid biopsy. As the exosomes enclose a variety of molecules from the parent cells, they can predict their origin and the state of tumor cells. The tumor-derived exosomes have great potential application for cancer diagnosis, prognosis and treatment response assessment (16).

MicroRNAs (miRNAs) are a class of non-coding RNAs (about 22 nucleotides) involved in post-transcriptional regulation of gene expression by RNA silencing. As the most extensively studied class of short non-coding RNAs, miRNAs are closely associated with a variety of cellular processes. The dysregulation of miRNA expression leads to the pathogenesis of many diseases, including cancer. miRNAs are critical constituents in the cargo of exosomes. There are two potential ways for miRNA packaging into exosomes. The neural sphingomyelinase 2 (nSMase2)-dependent pathway is the first mechanism found to guide miRNAs sorting into exosomes. nSMase2 overexpression increases the levels of exosomal miRNAs, while nSMase2 downregulation has an inhibitory effects (17). The heterogeneous nuclear ribonucleoprotein (hnRNP) proteins can bind miRNAs through the recognition of specific motifs, and help the sorting of miRNAs into exosomes (18). The exosomal miRNAs also play a pivotal role in the onset and progression of cancer, including proliferation, metastasis, chemoresistance, and immune escape. For metastasis, the exosomal microRNAs can be transferred to distant organs and regulate the signaling pathways and gene expression of the targeted cells, favoring the distant metastasis to specific target organs (19). A number of exosomal miRNAs from tumors has been identified to participate in cancer metastasis, including EMT, angiogenesis and invasion (20). Intercellular communication mediated by exosomal miRNAs plays an important role in carcinogenesis and cancer progression.

EXOSOMAL MIRNAS DERIVED FROM LUNG ADENOCARCINOMA ARE INVOLVED IN BONE METASTASIS

Bone is one of the most frequent sites for lung cancer metastasis. The bone microenvironment is a favorable soil for lung cancer cells due to the cytokines released by the bone matrix. Tumor-derived exosomes not only play a crucial role in cancer survival, invasion,

angiogenesis, and chemoresistance, but also are involved in bone metastasis by affecting bone microenvironment (21).

Recent studies have shown that lung adenocarcinoma exosomes play an important role in bone metastasis (10). During bone metastasis, the lung adenocarcinoma exosomes can regulate osteoclasts and their precursors, and facilitate the formation of metastatic bone microenvironment by releasing a variety of growth factors during bone resorption (22). Exosomal amphiregulin (AREG) from adenocarcinoma cells can promote osteoclast differentiation by activating epidermal growth factor receptor (EGFR) pathway (23). Besides, microRNAs facilitating osteoclast differentiation have been found in lung adenocarcinoma cell-derived exosomes. Exosomal miR-21 from A549 cells enhances osteoclastogenesis *via* targeting programmed cell death 4 (Pdcd4), and is associated with poor survival in lung adenocarcinoma patients (24). Forced expression of miR-192 can reduced bone metastasis by the way of exosomes. miR-192-enriched exosomes from A549 cells specifically transfer to target vein endothelial cells and impair tumor-induced angiogenesis, thereby reducing the metastatic burden (25). Studies on the functions of exosomal miRNAs in communications between cancer and bone cells are an emerging area of bone metastasis. These studies suggest that the exosomal microRNAs regulating bone homeostasis may be associated with bone metastasis.

THE ROLES OF BONE-DERIVED EXOSOMES WITHIN BONE MICROENVIRONMENT

Bone metastasis requires the tumor-derived factors that affects the bone microenvironment. In this section, we summarize the bone-derived exosomes within bone microenvironment, and discuss their roles in bone homeostasis.

Bone is a dynamic tissue that undergoes a constant remodeling to maintain skeleton integrity. The removal of old bone by osteoclasts and synthesis of new bone by osteoblasts are tightly and finely coupled to ensure the balance of bone remodeling. The imbalanced process causes many metabolic bone diseases, such as osteoporosis. In addition to osteoblasts and osteoclasts, bone mesenchymal stem cells (BMSCs) and osteocytes are included within bone microenvironment. The intercellular communications among these bone cells are critical to maintain bone homeostasis. At present, most of the research on intercellular communication focuses on direct cell-cell contact, cytokines, and extracellular matrix interaction (26). However, recent studies have demonstrated all these bone cells can secret exosomes, which have an essential role in intercellular communication within bone microenvironment and regulation of bone homeostasis (27). Exosomes-mediated intercellular communication between bone cells represent a novel mechanism of bone modeling and remodeling.

BMSCs-Derived Exosomes

BMSCs are multipotent stem cells in bone marrow that can different into multiple types of cells, including osteoblasts, chondrocytes, and adipocytes. The BMSCs-derived exosomes play an important role in maintain bone homeostasis. Exosomes derived from BMSCs promote osteogenic differentiation of osteoblasts. BMSCs-derived exosomes stimulate proliferation of osteoblastic hFOB 1.19 cells *via* mitogen-activated protein kinase (MAPK) signaling (28). Exosomal lncRNA-MALAT1 are also involved in the stimulation of proliferation, alkaline phosphatase activity, and mineralization in hFOB1.19 cells. When exosomal lncRNA-MALAT1 is taken up, lnc-MALAT1 promotes special AT-rich sequence-binding protein 2 (SATB2) expression by sponging miR-34c, and enhances osteoblast differentiation (29). Interestingly, BMSCs-derived exosomes extracted from osteoporosis patients inhibit osteogenesis *via* microRNA-21/SMAD7 (30). BMSCs also regulate their osteogenic differentiation through exosomes. BMSCs transfer Fas proteins to the neighboring BMSCs through exosomes, and downregulate miR-29b and Notch, consequently improving the osteogenic differentiation (31). Exosomes derived from Wharton's jelly of human umbilical cord MSCs have protective effects on osteocyte. Exosomal miR-214 can inhibit osteocyte apoptosis (in MLO-Y4 cells) and prevent glucocorticoid-induced osteonecrosis of the femoral head (32).

Some studies demonstrated the therapeutic effects of BMSCs-derived exosomes on bone loss, regeneration, and defect repair. Exosomes derived from human-induced pluripotent stem cell-derived MSCs (hiPS-MSC-Exos) effectively promote the proliferation and osteogenic differentiation of BMSCs isolated from ovariectomized (OVX) rats, and accelerate bone regeneration in critical-sized calvarial defects by enhancing angiogenesis and osteogenesis (33). The hiPS-MSC-Exos also enhance the osteoinductivity of β-TCP through activating the PI3K/Akt signaling pathway of BMSCs (34). Transplantation of iPS-MSC-Exos also exerts a preventative effect on osteonecrosis of the femoral head (ONFH) by promoting local angiogenesis and preventing bone loss (35). Exosomal miR-1263 derived from human umbilical cord MSCs reduces BMSCs apoptosis and ameliorates hindlimb unloading induced osteoporosis (36). Exosomes derived from BMSCs upregulate expression of osteogenic genes and osteogenic differentiation in osteoblasts, and stimulate bone formation in the critical-size calvarial bone defects (37).

BMSCs-derived exosomes also contribute to fracture healing. The fracture-healing process of $CD9^{-/-}$ mice, a strain produces reduced levels of exosomes, is decreased with lower rate of bone union than wild-type. The retardation of fracture healing in $CD9^{-/-}$ mice can be partially rescued by the injection of exosomes isolated from BMSCs-conditioned medium (CM) (38). Transplantation of BMSCs-Exos significantly enhances bone healing processes in a rat model of femoral nonunion *via* stimulating osteogenesis and angiogenesis. The BMSCs-Exos can be taken up by MC3T3-E1 *in vitro*, and improves their proliferation and migration (39). The exosomes from hypoxic BMSCs have a high expression of miR-126, and enhances bone fracture healing by the transfer of miR-126 (40).

Osteoblasts-Derived Exosomes

Osteoblasts are differentiated from BMSCs, and are responsible for the synthesis and mineralization of bone matrix. Osteoblasts-derived exosomes can be taken up by surrounding osteoblasts,

BMSCs, and osteoclasts, and regulate their differentiation. The exosomes from osteoblastic MC3T3-E1 cells contain the potential osteogenesis-related proteins (41). 172 proteins are identified by mass spectrometry to be involved in bone metabolism (42). Exosomes derived from mineralizing pre-osteoblast MC3T3-E1 cells can promote bone marrow stromal cells (ST2) differentiation to osteoblasts by transferring miRNAs (43). Receptor activator of NFκB ligand (RANKL), a TNF-family cytokine required for osteoclast formation, is enriched in osteoblast derived microvesicles, and supports osteoclast survival. RANKL knockout mice lacks the osteoclasts, which can be reversed by the wild-type osteoblast micorvesicles (44). The osteoprotective effects of imipramine are associated with the inhibited secretion of exosomes from osteoblasts. Imipramine treatment blocks the release of osteoblasts derived micorvesicles and consequently reduces micorvesicles-induced osteoclast formation (45).

Osteocytes-Derived Exosomes

Osteocytes are terminally differentiated osteoblasts within bone matrix. Osteocytes account for 90%–95% of the total bone cells, and are the most abundant cell type in bone. Osteocytes are demonstrated to the orchestrator of bone remodeling by directly regulating osteoblasts and osteoclasts (46). A variety of cytokines, found to have regulated roles in bone remodeling, is secreted by osteocytes, including sclerostin, cathepsin K, prostaglandin E2, nitric oxide, insulin-like growth factor 1, and RANKL (46). Osteocytes also secret exosomes to regulate bone cells. Exosomes produced by osteocytic Ocy454 cells can be taken by osteoblastic MC3T3-E1 cells and inhibit osteoblast differentiation by exosomal miR-218 (47). So far, we have little information about the osteocytes-derived exosomes and their roles within bone microenvironment.

Osteoclasts-Derived Exosomes

Unlike osteoblast-lineage cells, osteoclasts are differentiated from hematopoietic stem cells, and responsible for bone resorption. Huynh et al. firstly identify osteoclasts-derived exosomes, and find that the exosomes can regulate osteoclast differentiation in a paracrine manner. Interestingly, the exosomes from osteoclast precursors promote osteoclastogenesis, while the exosomes from mature osteoclasts have a negative effect (48). In addition, the exosomes can be taken up by osteoblasts and regulate osteogenic differentiation. Osteoclast-derived exosomes can selectively inhibit osteoblast activity by transferring miR-214 (11, 49). The exosomal miR-214 is significantly elevated in elderly women with fractures and in ovariectomized (OVX) mice, and can be used as a biomarker for osteoporosis with enhanced osteoclast activity (11). Exosomal miR-23a-5p is also highly expressed in differentiating osteoclasts. An increased level of miR-23a-5p in exosomes can be induced in RANKL-induced RAW264.7 cells. Exosomal miR-23a-5p inhibits osteoblast activity by targeting Runx2 (50). However, the exosomes from osteoclast precursors (i.e., monocytes) have inhibitory effects on osteogenic differentiation. The monocytes-derived exosomes can stimulate the osteogenic gene expression of BMSCs (51).

THE VICIOUS CYCLE OF BONE METASTASIS

The development of bone metastasis can be divided into 4 steps: (1) colonization: circulating cancer cells migrate to the bone; (2) dormancy: cancer cells adapt to the bone microenvironment; (3) reactivation and development: the cancer cells are reactivated and transit into a proliferation state; (4) reconstruction: cytokines released from cancer cells modulate bone homeostasis. For osteolytic metastasis, the metastatic lung cancer cells produce amounts of cytokines favoring osteoclasts, and stimulate bone resorption. The cancer cells, osteoclasts, and bone microenvironment have been reported to involved in the process of bone metastasis, and form a "vicious cycle" (52).

The bone microenvironment has emerged to be a key modulator for bone metastasis by providing stimulatory growth factors. The bone matrix is actually a storehouse for diverse growth factors. A series of cytokines are released during the degradation of bone matrix, including insulin-like growth factor (IGF), transforming growth factor β (TGFβ), fibroblast growth factor (FGF), etc. These factors facilitate the cancer cells migrate to bone, proliferate, and colonize, resulting in the formation of metastasis. For osteolytic metastasis, the cancer cells release some cytokines that promotes the activation and maturation of osteoclasts, such as tumor necrosis factor α (TNF-α), macrophage colony-stimulating factor (M-CSF), interleukin 8 (IL8), IL11, etc. (52). These factors interact with bone cells in the bone microenvironment and disrupt the balance of bone metabolism, resulting in enhanced bone resorption and causing osteolytic damage. The positive feedback between tumor growth and bone resorption forms a "vicious circle" (53). The "vicious circle" theory suggests that exacerbated osteoclast activity is of great importance for osteolytic metastasis, and the osteoclasts may be considered to be an effective therapeutic target. From the perspective of bone resorption, the application of antiresorptive drugs is highly recommended, since it significantly reduces the risks of SRE (54).

MIR-214 IS INVOLVED IN THE PROGRESSION OF LUNG ADENOCARCINOMA AND REGULATION OF BONE HOMEOSTASIS

According to the theory of "vicious cycle", the tumor derived factors can modulate bone microenvironment by affecting the activities of bone cells. The factors within the altered microenvironment in turn favors tumor localization. Usually, the factors from tumor are different from the factors within bone microenvironment. Interestingly, miR-214 is found to be involved in both lung cancer progression and bone resorption. In both osteoclasts and lung adenocarcinoma cells, miR-214 can be selectively incorporated into the exosomes, and is released into the extracellular space. Exosomal miR-214 may be a potential mediator in the "vicious cycle" of bone metastasis.

miR-214 in Lung Adenocarcinoma

miR-214 is closely associated with various physiological and pathological processes including carcinogenesis (55). It has been demonstrated that miR-214 is dysregulated in a variety of human cancers (7). The reported studies about the role of miR-214 in lung cancer mainly focuses on lung adenocarcinoma, and its role in lung squamous cell carcinoma has not been elucidated. Lung adenocarcinoma cell lines (A549, 95D, H1299, SPC-A-1, H522, H460, and H358) have a higher expression of miR-214 than human bronchial epithelial cells (16-HBE) (56–58). Increased miR-214 can be also detected in lung adenocarcinoma tissue and plasma samples from the patients (57). Down-regulation of miR-214 inhibits cell proliferation, glucose consumption and lactate production by targeting phosphatase and tensin homolog (PTEN) and regulating PTEN/Akt/mTOR pathway (56) Besides, the tumor growth *in vivo* is associated with cancer immune evasion induced by miR-214. The tumor derived miR-214 can be transferred into the recipient $CD4^+$T cells through microvesicles induces Treg expansion, thereby inducing immune suppression and enhanced tumor growth (57). miR-214 also contributes to stemness of cancer stem-like cells by targeting catenin beta interacting protein 1 (CTNNBIP1) in lung adenocarcinoma (59). miR-214 overexpression results in a significant increase in spheroid formation in A549 and NCI-H1650 cells. Conversely, miR-214 downregulation would cause a decreased expression of stem-cell markers Nanog, Oct-4, and Sox-2. CTNNBIP1 is revealed to be a target gene of miR-214, and is negatively correlated with longer overall survival in lung adenocarcinoma patients (59). miR-214 in plasma is mainly stored in the exosomes (57–60). miR-214 of lung adenocarcinoma can be delivered into recipient cells through the way of exosomes. Exosomal miR-214 in gefitinib-resistant PC-9GR cells could be transferred to recipient sensitive PC-9 cells, enabling the normal PC-9 cells acquire resistance (61).

Taken together, miR-214 is highly expressed in lung adenocarcinoma, and is positively associated with proliferation, drug resistance, and stemness. Exosomal miR-214 derived from lung adenocarcinoma can be transferred to the recipient cells, which may accelerate cancer progression.

miR-214 in Bone Homeostasis

miR-214 plays a key regulatory role in the balance of bone metabolism. Both miR-214 and exosomal miR-214 directly regulate the activities of osteoblasts and osteoclasts. Wang et al. firstly demonstrated that miR-214 levels are negatively correlated with the degree of bone formation in bone specimens from aged patients with fractures. MiR-214 is also highly expressed in osteoblasts isolated from ovariectomized and hindlimb-unloading mice (62). The inhibited bone formation in these animal models can be partially reversed by antagomir-214 treatment (62). During osteogenic differentiation of BMSCs, miR-214 is gradually down-regulated. MiR-214 overexpression exerts an inhibitory effect (63). Several target genes of miR-214 are identified to be involved in the regulatory role in osteogenesis, including activating transcription factor 4 (ATF4) (62), fibroblast growth factor receptor 1 (FGFR1) (63), Wnt-induced secreted protein 1 (WISP-1) (64), E3 ubiquitin ligase Cbl (Cbl) (65), osterix (66), and baculoviral IAP repeat-containing 7 (BIRC7) (67).

In contrast to osteoblasts, high expression of miR-214 can promote osteoclast differentiation and maturation, thereby enhancing bone resorption (8). The expression of miR-214 is increased during osteoclast differentiation. Overexpression of miR-214 can promote osteoclast formation by targeting PTEN and TNF receptor associated factor 3 (Traf3) (68, 69). Animal studies also demonstrate that osteoclast-specific high expression of miR-214 induces a significant decrease in both bone density and bone mass, accompanied by a marked increase of osteoclast activity (68, 69). Remarkably, exosomal miR-214 mediates the intercellular communication between osteoclasts and osteoblasts. Increased expression of osteoclastic miR-214 is associated with both elevated serum exosomal miR-214 and reduced bone formation in elderly women with fractures and in ovariectomized (OVX) mice (11). Osteoclast-specific miR-214 knock-in mice have elevated serum exosomal miR-214 and reduced bone formation, which can be reversed by osteoclast-targeted antagomir-214-3p treatment (11). Osteoclast-derived exosomal miR-214 can selectively recognize osteoblasts *via* the interaction between ephrinA2 and EphA2 (70). After that, the exosomal miR-214 inhibits osteoblast differentiation (11, 49). Rb27a is involved in the exosome secretion pathway. Rab27b silencing would inhibit exosome secretion (71). When exosome secretion from osteoclasts is inhibited through Rab27a RNA interference, the effects of osteoclasts on osteoblasts would be attenuated. Systemic administration of Rab27a siRNA in ovariectomized mice decreases the level of circulating exosomes, and upregulates osteoblast activity (49).

Taken together, high expression of miR-214 in osteoclasts breaks the balance of bone metabolism by stimulating bone resorption and inhibiting bone formation *via* exosomes from osteoclast, eventually reducing the bone mass.

As mentioned above, exosomes derived from lung adenocarcinoma cells can enhance osteoclastogenesis (23, 24). Since miR-214 is involved in both carcinogenesis and osteoclastogenesis, we raised the hypothesis that exosomal miR-214 from lung adenocarcinoma facilitated osteoclast differentiation and bone metastasis.

THE POTENTIAL ROLE OF EXOSOMAL MIR-214 DURING BONE METASTASIS

miR-214 plays dual roles in both cancer progression and bone homeostasis. miR-214 is highly expressed in lung adenocarcinoma, and is positively related to the progression of lung cancer (56, 57). miR-214 also enhances bone resorption by stimulating osteoclast differentiation (68, 69). Exosomal miR-214 from osteoclast directly inhibit osteoblast differentiation (11, 49). Since exosomes can transfer vital microRNAs into recipient cells, it is highly possible that exosomal miR-214 is involved in the process of bone metastasis.

Colonization

Lung adenocarcinoma cells may secrete the exosomes containing miR-214, and are taken up by osteoclasts. miR-214 promotes osteoclasts mediated bone resorption by targeting PTEN (68). The enhanced degradation of bone matrix releases multiple cytokines, such as IGF, TGFβ, and FGF, thereby favoring the directional migration and invasion of cancer cells (6). In this way, the lung adenocarcinoma cells can accurately metastasize to the bones.

Adaptation and Reactivation

Considering the essential role of miR-214 during the progression of lung adenocarcinoma, osteoclast-derived exosomal miR-214 might be transferred into metastatic cancer cells, and enhances the progression of metastatic colonization by targeting PTEN. Furthermore, the released multiple factors during bone degradation help the dormant cancer cells adapt to the bone environment and be reactivated to proliferation state.

Reconstruction

Exosomal miR-214 derived from metastatic cancer cells may be taken up by osteoclasts, and promotes bone resorption by targeting PTEN and Traf3. When the exosomal miR-214 is transferred into osteoblasts, bone formation is inhibited *via* targeting ATF4. Through stimulating bone resorption and inhibit bone formation, the bone homeostasis balance is disrupted, causing serious bone loss.

Through the way of exosomal miR-214, bone metastasis and bone resorption may be positively interacted, forming a "vicious circle" (**Figure 1**). This hypothesis suggests that Exosomal miR-214 seems to be a potential therapeutic target of metastatic lung cancer. Eliminating exosomal miR-214 can potentially inhibit the progression of bone metastasis. The levels of exosomal miR-214 in the peripheral circulation may help predict the risk of bone metastasis for patients with lung adenocarcinoma.

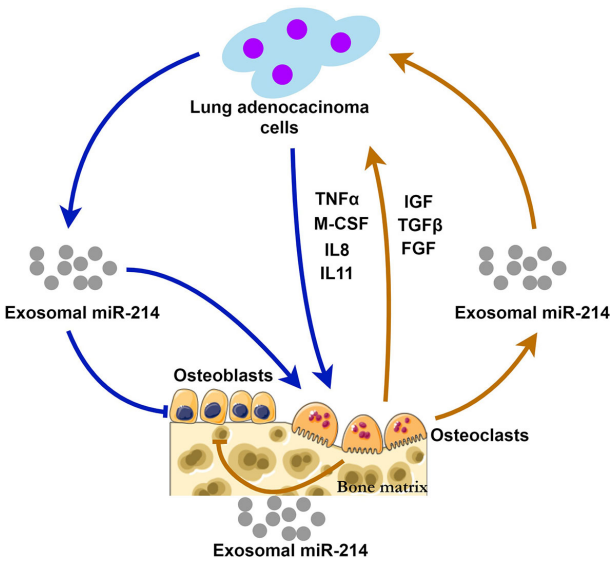

FIGURE 1 | The possible mechanisms of exosomal miR-214 derived from lung adenocarcinoma and osteoclasts during bone metastasis. Lung adenocarcinoma cells release exosomal miR-214 and multiple cytokines (TNFα, M-CSF, IL-8 and IL11) stimulating osteoclastogenesis and bone resorption. At the same time, osteoclast-derived exosomal miR-214 and the factors (IGF, TGFβ, and FGF) released from the bone matrix promote tumor growth. Exosomal miR-214 has inhibitory effects on bone formation mediated by osteoblasts. Exosomal miR-214 plays a central role in the positive feedback loop, i.e., the vicious circle.

THE POTENTIAL APPLICATION OF EXOSOMAL MIRNAS IN LIQUID BIOPSY AND THERAPEUTIC TARGETS

Tissue biopsy is the current gold standard for tumor pathological confirmation. This invasive procedure can be painful, and is not suitable for clinical longitudinal monitoring. In some cases, the amount of tissue obtained from a needle biopsy may not be sufficient and the biopsy may have to be repeated. In addition, tissue biopsy cannot fully obtain the intratumoral and intertumoral heterogeneity (72). Development of noninvasive techniques for longitudinal monitoring and accurate detection is required. Liquid biopsy refers to the detection of cancer biomarkers in the liquid biological sources, typically blood, for cancer screening, diagnosis, and prognosis. These biomarkers can be cell-free DNA (cfDNA) and RNA (cfRNA), proteins, cells, and exosomes, helping detect genomic alteration and monitor disease progression. Liquid biopsy has multiple advantages over conventional tissue biopsy, such as minimal invasiveness, no pain, no risk of complications, representation of tumor heterogeneity, and compatibility with longitudinal monitoring (73–75). In 2016, the US Food and Drug Administration (FDA) firstly approved a liquid biopsy test, called the cobas EGFR Mutation Test v2, a blood-based companion diagnostic for the cancer drug Tarceva (erlotinib). The tests are used to identify the non-small cell lung cancer patients with epidermal growth factor receptor (EGFR) gene mutations (72).

Among the cargos in exosome, miRNAs are relatively stable. miRNAs in plasma and serum have been extensively studied as cancer biomarker. However, different methods of sample processing and different sources of the samples may lead to conflicting results (76). Compared with non-vesicle enclosed miRNAs, exosomal miRNAs are highly stable and resistant to degradation. In addition to their lipid bilayers, exosomes can be protected from complement-mediated lysis by expression of CD55 and CD59 (77). Therefore, exosomal miRNAs have greater sensitivity and specificity, and may serve as useful biomarkers. So far, some exosomal miRNAs have been demonstrated to be the potential markers (78, 79). Exosomal miR-21 and miR-4257 in the plasma of lung adenocarcinoma patients was significantly increased and is positively correlated with the recurrence (80). Advanced lung adenocarcinoma patients have low levels of serum exosomal miR-146a-5p. The upregulated exosomal miR-146a-5p could predict the therapeutic effects of cisplatin (81). Plasma exosomal miR-23b-3p, miR-10b-5p, and miR-21-5p are independently associated

with poor overall survival, and are promising prognostic biomarkers (82). Clinical studies also reveal that there is a correlation of exosomal microRNA clusters with bone metastasis in lung adenocarcinoma cancer (83). It should be noted that there have been limited research regarding the potential markers of exosomal miRNAs in bone metastasis. We speculate that exosomal miR-214 is a potential biomarker of prognosis in lung cancer. Biological functions of exosomal miR-214 and clinical correlation are needed to be further evaluated.

Due to the significance of exosomes in cancer progression, exosomes provide a novel therapeutic target. The drugs, affecting the biogenesis and release of exosomes, have been investigated (76). For example, gefitinib can enhance the uptake of drug-loaded exosomes in lung adenocarcinoma cells, thereby improving the anticancer effects of the drugs (84). GW4869 can inhibit the biogenesis and release of exosomes in Lewis lung cancer cells by targeting nSMase2 (85). In spite of that, there is still limited information whether these drugs influence the exosomes in normal cells. Further understanding about the difference between cancer cells and normal cells is needed.

CONCLUSIONS

Metastatic lung cancer is one of the main causes of death in lung cancer patients. There have been no effective treatments. The mechanisms of bone metastasis are very complex, and have not been fully understood yet. The interactions between cancer cells and bone microenvironment are particularly critical for bone metastasis. Here, we speculated that the exosomal miR-214 is involved in the "vicious cycle". Exosomal miR-214 can be released from both cancer cells and osteoclasts. Through the way of exosomal miR-214, the metastatic lung cancer cells and osteoclasts were mutually and positively influenced, leading to the occurrence of osteolytic metastasis. Targeted miR-214 could be used as one of the potential therapies to treat bone metastasis. Further studies are needed to verify our hypothesis.

DATA AVAILABILITY STATEMENT

The original contributions presented in the study are included in the article/supplementary materials. Further inquiries can be directed to the corresponding author.

AUTHOR CONTRIBUTIONS

All the authors contributed to the study conception and design. JW conducted literature search. JZ wrote the manuscript. All authors contributed to the article and approved the submitted version.

FUNDING

This work was supported by the National Natural Science Foundation of China (82060168), the Young Scientific Talents Growth Project of Department of Education of Guizhou Province (QJHKYZ [2021]199), the Science and Technology Fund of Guizhou Health Commission (gzwjkj2019-1-226), and the Doctoral Funds of Guizhou University of Traditional Chinese Medicine [(2019)44].

REFERENCES

1. Hirsch FR, Scagliotti GV, Mulshine JL, Kwon R, Curran WJ Jr, Wu YL, et al. Lung cancer: current therapies and new targeted treatments. *Lancet* (2017) 389:299–311. doi: 10.1016/S0140-6736(16)30958-8
2. Cho YJ, Cho YM, Kim SH, Shin KH, Jung ST, Kim HS. Clinical analysis of patients with skeletal metastasis of lung cancer. *BMC Cancer* (2019) 19:303. doi: 10.1186/s12885-019-5534-3
3. Macedo F, Ladeira K, Pinho F, Saraiva N, Bonito N, Pinto L, et al. Bone metastases: An overview. *Oncol Rev* (2017) 11:321. doi: 10.4081/oncol.2017.321
4. Kimura T. Multidisciplinary approach for bone metastasis: A review. *Cancers* (2018) 10:156. doi: 10.3390/cancers10060156
5. Dai J, Su Y, Zhong S, Cong L, Liu B, Yang J, et al. Exosomes: key players in cancer and potential therapeutic strategy. *Signal Transduct Target Ther* (2020) 5:145. doi: 10.1038/s41392-020-00261-0
6. Liu Q, Peng F, Chen J. The Role of Exosomal MicroRNAs in the Tumor Microenvironment of Breast Cancer. *Int J Mol Sci* (2019) 20:3884. doi: 10.3390/ijms20163884
7. Penna E, Orso F, Taverna D. miR-214 as a key hub that controls cancer networks: small player, multiple functions. *J Invest Dermatol* (2015) 135:960–9. doi: 10.1038/jid.2014.479
8. Sun Y, Kuek V, Liu Y, Tickner J, Yuan Y, Chen L, et al. MiR-214 is an important regulator of the musculoskeletal metabolism and disease. *J Cell Physiol* (2018) 234:231–45. doi: 10.1002/jcp.26856
9. Rossi M, Battafarano G, D'Agostini M, Del Fattore A. The role of extracellular vesicles in bone metastasis. *Int J Mol Sci* (2018) 19:1136. doi: 10.3390/ijms19041136
10. Li FX, Liu JJ, Xu F, Lin X, Zhong JY, Wu F, et al. Role of tumor-derived exosomes in bone metastasis. *Oncol Lett* (2019) 18:3935–45. doi: 10.3892/ol.2019.10776
11. Li D, Liu J, Guo B, Liang C, Dang L, Lu C, et al. Osteoclast-derived exosomal miR-214-3p inhibits osteoblastic bone formation. *Nat Commun* (2016) 7:10872. doi: 10.1038/ncomms10872
12. Kanninen KM, Bister N, Koistinaho J, Malm T. Exosomes as new diagnostic tools in CNS diseases. *Biochim Biophys Acta* (2016) 1862:403–10. doi: 10.1016/j.bbadis.2015.09.020
13. Dilsiz N. Role of exosomes and exosomal microRNAs in cancer. *Future Sci OA* (2020) 6:FSO465. doi: 10.2144/fsoa-2019-0116
14. Zhang Y, Liu Y, Liu H, Tang WH. Exosomes: biogenesis, biologic function and clinical potential. *Cell Biosci* (2019) 9:19. doi: 10.1186/s13578-019-0282-2
15. Maia J, Caja S, Strano Moraes MC, Couto N, Costa-Silva B. Exosome-based cell-cell communication in the tumor microenvironment. *Front Cell Dev Biol* (2018) 6:18. doi: 10.3389/fcell.2018.00018
16. Zhou B, Xu K, Zheng X, Chen T, Wang J, Song Y, et al. Application of exosomes as liquid biopsy in clinical diagnosis. *Signal Transduct Target Ther* (2020) 5:144. doi: 10.1038/s41392-020-00258-9
17. Kosaka N, Iguchi H, Hagiwara K, Yoshioka Y, Takeshita F, Ochiya T. Neutral sphingomyelinase 2 (nSMase2)-dependent exosomal transfer of angiogenic microRNAs regulate cancer cell metastasis. *J Biol Chem* (2013) 288:10849–59. doi: 10.1074/jbc.M112.446831
18. Villarroya-Beltri C, Gutiérrez-Vázquez C, Sánchez-Cabo F, Pérez-Hernández D, Vázquez J, Martin-Cofreces N, et al. Sumoylated hnRNPA2B1 controls the sorting of miRNAs into exosomes through binding to specific motifs. *Nat Commun* (2013) 4:2980. doi: 10.1038/ncomms3980

19. Fan Q, Yang L, Zhang X, Peng X, Wei S, Su D, et al. The emerging role of exosome-derived non-coding RNAs in cancer biology. *Cancer Lett* (2018) 414:107–15. doi: 10.1016/j.canlet.2017.10.040
20. Wang M, Yu F, Ding H, Wang Y, Li P, Wang K. Emerging function and clinical values of exosomal microRNAs in cancer. *Mol Ther Nucleic Acids* (2019) 16:791–804. doi: 10.1016/j.omtn.2019.04.027
21. Roato I. Bone metastases: When and how lung cancer interacts with bone. *World J Clin Oncol* (2014) 5(2):149–55. doi: 10.5306/wjco.v5.i2.149
22. Hiraga T. Bone metastasis: Interaction between cancer cells and bone microenvironment. *J Oral Biosci* (2019) 61:95–8. doi: 10.1016/j.job.2019.02.002
23. Taverna S, Pucci M, Giallombardo M, Di Bella MA, Santarpia M, Reclusa P, et al. Amphiregulin contained in NSCLC-exosomes induces osteoclast differentiation through the activation of EGFR pathway. *Sci Rep* (2017) 7:3170. doi: 10.1038/s41598-017-03460-y
24. Xu Z, Liu X, Wang H, Li J, Dai L, Li J, et al. Lung adenocarcinoma cell-derived exosomal miR-21 facilitates osteoclastogenesis. *Gene* (2018) 666:116–22. doi: 10.1016/j.gene.2018.05.008
25. Valencia K, Luis-Ravelo D, Bovy N, Antón I, Martínez-Canarias S, Zandueta C, et al. miRNA cargo within exosome-like vesicle transfer influences metastatic bone colonization. *Mol Oncol* (2014) 8:689–703. doi: 10.1016/j.molonc.2014.01.012
26. Chen X, Wang Z, Duan N, Zhu G, Schwarz EM, Xie C, et al. Osteoblast-osteoclast interactions. *Connect Tissue Res* (2018) 59:99–107. doi: 10.1080/03008207.2017.1290085
27. Li Q, Huang QP, Wang YL, Huang QS. Extracellular vesicle-mediated bone metabolism in the bone microenvironment. *J Bone Miner Metab* (2018) 36:1–11. doi: 10.1007/s00774-017-0860-5
28. Zhao P, Xiao L, Peng J, Qian Y-Q, Huang C-C. Exosomes derived from bone marrow mesenchymal stem cells improve osteoporosis through promoting osteoblast proliferation via MAPK pathway. *Eur Rev Med Pharmacol Sci* (2018) 22:3962–70. doi: 10.26355/eurrev_201806_15280
29. Yang X, Yang J, Lei P, Wen T. LncRNA MALAT1 shuttled by bone marrow-derived mesenchymal stem cells-secreted exosomes alleviates osteoporosis through mediating microRNA-34c/SATB2 axis. *Aging* (2019) 11:8777–91. doi: 10.18632/aging.102264
30. Jiang L-B, Tian L, Zhang C-G. Bone marrow stem cells-derived exosomes extracted from osteoporosis patients inhibit osteogenesis via microRNA-21/SMAD7. *Eur Rev Med Pharmacol Sci* (2018) 22:6221–9. doi: 10.26355/eurrev_201810_16028
31. Liu S, Liu D, Chen C, Hamamura K, Moshaverinia A, Yang R, et al. MSC transplantation improves osteopenia via epigenetic regulation of notch signaling in lupus. *Cell Metab* (2015) 22:606–18. doi: 10.1016/j.cmet.2015.08.018
32. Kuang MJ, Huang Y, Zhao XG, Zhang R, Ma JX, Wang DC, et al. Exosomes derived from Wharton's jelly of human umbilical cord mesenchymal stem cells reduce osteocyte apoptosis in glucocorticoid-induced osteonecrosis of the femoral head in rats via the miR-21-PTEN-AKT signalling pathway. *Int J Biol Sci* (2019) 15:1861–71. doi: 10.7150/ijbs.32262
33. Qi X, Zhang J, Yuan H, Xu Z, Li Q, Niu X, et al. Exosomes secreted by human-induced pluripotent stem cell-derived mesenchymal stem cells repair critical-sized bone defects through enhanced angiogenesis and osteogenesis in osteoporotic rats. *Int J Biol Sci* (2016) 12:836–49. doi: 10.7150/ijbs.14809
34. Zhang J, Liu X, Li H, Chen C, Hu B, Niu X, et al. Exosomes/tricalcium phosphate combination scaffolds can enhance bone regeneration by activating the PI3K/Akt signaling pathway. *Stem Cell Res Ther* (2016) 7:136. doi: 10.1186/s13287-016-0391-3
35. Liu X, Li Q, Niu X, Hu B, Chen S, Song W, et al. Exosomes secreted from human-induced pluripotent stem cell-derived mesenchymal stem cells prevent osteonecrosis of the femoral head by promoting angiogenesis. *Int J Biol Sci* (2017) 13:232–44. doi: 10.7150/ijbs.16951
36. Yang B-C, Kuang M-J, Kang J-Y, Zhao J, Ma J-X, Ma X-L. Human umbilical cord mesenchymal stem cell-derived exosomes act via the miR-1263/Mob1/Hippo signaling pathway to prevent apoptosis in disuse osteoporosis. *Biochem Biophys Res Commun* (2020) 524:883–9. doi: 10.1016/j.bbrc.2020.02.001
37. Qin Y, Wang L, Gao Z, Chen G, Zhang C. Bone marrow stromal/stem cell-derived extracellular vesicles regulate osteoblast activity and differentiation in vitro and promote bone regeneration in vivo. *Sci Rep* (2016) 6:21961. doi: 10.1038/srep21961
38. Furuta T, Miyaki S, Ishitobi H, Ogura T, Kato Y, Kamei N, et al. Mesenchymal Stem Cell-Derived Exosomes Promote Fracture Healing in a Mouse Model. *Stem Cells Transl Med* (2016) 5:1620–30. doi: 10.5966/sctm.2015-0285
39. Zhang L, Jiao G, Ren S, Zhang X, Li C, Wu W, et al. Exosomes from bone marrow mesenchymal stem cells enhance fracture healing through the promotion of osteogenesis and angiogenesis in a rat model of nonunion. *Stem Cell Res Ther* (2020) 11:38. doi: 10.1186/s13287-020-1562-9
40. Liu W, Li L, Rong Y, Qian D, Chen J, Zhou Z, et al. Hypoxic mesenchymal stem cell-derived exosomes promote bone fracture healing by the transfer of miR-126. *Acta Biomater* (2020) 103:196–212. doi: 10.1016/j.actbio.2019.12.020
41. Ge M, Ke R, Cai T, Yang J, Mu X. Identification and proteomic analysis of osteoblast-derived exosomes. *Biochem Biophys Res Commun* (2015) 467:27–32. doi: 10.1016/j.bbrc.2015.09.135
42. Ge M, Wu Y, Ke R, Cai T, Yang J, Mu X. Value of osteoblast-derived exosomes in bone diseases. *J Craniofac Surg* (2017) 28:866–70. doi: 10.1097/SCS.0000000000003463
43. Cui Y, Luan J, Li H, Zhou X, Han J. Exosomes derived from mineralizing osteoblasts promote ST2 cell osteogenic differentiation by alteration of microRNA expression. *FEBS Lett* (2016) 590:185–92. doi: 10.1002/1873-3468.12024
44. Cappariello A, Loftus A, Muraca M, Maurizi A, Rucci N, Teti A. Osteoblast-derived extracellular vesicles are biological tools for the delivery of active molecules to bone. *J Bone Miner Res* (2018) 33:517–33. doi: 10.1002/jbmr.3332
45. Deng L, Peng Y, Jiang Y, Wu Y, Ding Y, Wang Y, et al. Imipramine protects against bone loss by inhibition of osteoblast-derived microvesicles. *Int J Mol Sci* (2017) 18:1013. doi: 10.3390/ijms18051013
46. Pathak JL, Bravenboer N, Klein-Nulend J. The osteocyte as the new discovery of therapeutic options in rare bone diseases. *Front Endocrinol* (2020) 11:405. doi: 10.3389/fendo.2020.00405
47. Qin Y, Peng Y, Zhao W, Pan J, Ksiezak-Reding H, Cardozo C, et al. Myostatin inhibits osteoblastic differentiation by suppressing osteocyte-derived exosomal microRNA-218: A novel mechanism in muscle-bone communication. *J Biol Chem* (2017) 292:11021–33. doi: 10.1074/jbc.M116.770941
48. Huynh N, VonMoss L, Smith D, Rahman I, Felemban MF, Zuo J, et al. Characterization of regulatory extracellular vesicles from osteoclasts. *J Dent Res* (2016) 95:673–9. doi: 10.1177/0022034516633189
49. Sun W, Zhao C, Li Y, Wang L, Nie G, Peng J, et al. Osteoclast-derived microRNA-containing exosomes selectively inhibit osteoblast activity. *Cell Discovery* (2016) 2:16015. doi: 10.1038/celldisc.2016.15
50. Yang J-X, Xie P, Li Y-S, Wen T, Yang X-C. Osteoclast-derived miR-23a-5p-containing exosomes inhibit osteogenic differentiation by regulating Runx2. *Cell Signal* (2020) 70:109504. doi: 10.1016/j.cellsig.2019
51. Ekström K, Omar O, Granéli C, Wang X, Vazirisani F, Thomsen P. Monocyte exosomes stimulate the osteogenic gene expression of mesenchymal stem cells. *PloS One* (2013) 8:e75227. doi: 10.1371/journal.pone.0075227
52. Zhang X. Interactions between cancer cells and bone microenvironment promote bone metastasis in prostate cancer. *Cancer Commun* (2019) 39:76. doi: 10.1186/s40880-019-0425-1
53. Lang J, Zhao Q, He Y, Yu X. Bone turnover markers and novel biomarkers in lung cancer bone metastases. *Biomarkers* (2018) 23:518–26. doi: 10.1080/1354750X.2018.1463566
54. Terpos E, Confavreux CB, Clézardin P. Bone antiresorptive agents in the treatment of bone metastases associated with solid tumours or multiple myeloma. *Bonekey Rep* (2015) 4:744. doi: 10.1038/bonekey.2015.113
55. Sharma T, Hamilton R, Mandal CC. miR-214: a potential biomarker and therapeutic for different cancers. *Future Oncol* (2015) 11:349–63. doi: 10.2217/fon.14.193
56. Zhang K, Zhang M, Jiang H, Liu F, Liu H, Li Y. Down-regulation of miR-214 inhibits proliferation and glycolysis in non-small-cell lung cancer cells via down-regulating the expression of hexokinase 2 and pyruvate kinase isozyme M2. *BioMed Pharmacother* (2018) 105:545–52. doi: 10.1016/j.biopha.2018.06.009

57. Yin Y, Cai X, Chen X, Liang H, Zhang Y, Li J, et al. Tumor-secreted miR-214 induces regulatory T cells: a major link between immune evasion and tumor growth. *Cell Res* (2014) 24:1164–80. doi: 10.1038/cr.2014.121
58. Yanaihara N, Caplen N, Bowman E, Seike M, Kumamoto K, Yi M, et al. Unique microRNA molecular profiles in lung cancer diagnosis and prognosis. *Cancer Cell* (2006) 9:189–98. doi: 10.1016/j.ccr.2006.01.025
59. Qi W, Chen J, Cheng X, Huang J, Xiang T, Li Q, et al. Targeting the Wnt-regulatory protein CTNNBIP1 by microRNA-214 enhances the stemness and self-renewal of cancer stem-like cells in lung adenocarcinomas. *Stem Cells* (2015) 33:3423–36. doi: 10.1002/stem.2188
60. Rabinowits G, Gerçel-Taylor C, Day JM, Taylor DD, Kloecker GH. Exosomal microRNA: a diagnostic marker for lung cancer. *Clin Lung Cancer* (2009) 10:42–6. doi: 10.3816/CLC.2009.n.006
61. Zhang Y, Li M, Hu C. Exosomal transfer of miR-214 mediates gefitinib resistance in non-small cell lung cancer. *Biochem Biophys Res Commun* (2018) 507:457–64. doi: 10.1016/j.bbrc.2018.11.061
62. Wang X, Guo B, Li Q, Peng J, Yang Z, Wang A, et al. miR-214 targets ATF4 to inhibit bone formation. *Nat Med* (2013) 19:93–100. doi: 10.1038/nm.3026
63. Yang L, Ge D, Cao X, Ge Y, Chen H, Wang W, et al. MiR-214 attenuates osteogenic differentiation of mesenchymal stem cells via targeting FGFR1. *Cell Physiol Biochem* (2016) 38:809–20. doi: 10.1159/000443036
64. Ono M, Inkson CA, Kilts TM, Young MF. WISP-1/CCN4 regulates osteogenesis by enhancing BMP-2 activity. *J Bone Miner Res* (2011) 26:193–208. doi: 10.1002/jbmr.205
65. Salingcarnboriboon RA, Pavasant P, Noda M. Cbl-b enhances Runx2 protein stability and augments osteocalcin promoter activity in osteoblastic cell lines. *J Cell Physiol* (2010) 224:743–7. doi: 10.1002/jcp.22176
66. Shi K, Lu J, Zhao Y, Wang L, Li J, Qi B, et al. MicroRNA-214 suppresses osteogenic differentiation of C2C12 myoblast cells by targeting Osterix. *Bone* (2013) 55:487–94. doi: 10.1016/j.bone.2013.04.002
67. Liu J, Li Y, Luo M, Yuan Z, Liu J. MicroRNA-214 inhibits the osteogenic differentiation of human osteoblasts through the direct regulation of baculoviral IAP repeat-containing 7. *Exp Cell Res* (2017) 351:157–62. doi: 10.1016/j.yexcr.2017.01.006
68. Zhao C, Sun W, Zhang P, Ling S, Li Y, Zhao D, et al. miR-214 promotes osteoclastogenesis by targeting Pten/PI3k/Akt pathway. *RNA Biol* (2015) 12:343–53. doi: 10.1080/15476286.2015.1017205
69. Liu J, Li D, Dang L, Lliang C, Guo B, Lu C, et al. Osteoclastic miR-214 targets TRAF3 to contribute to osteolytic bone metastasis of breast cancer. *Sci Rep* (2017) 7:40487. doi: 10.1038/srep40487
70. Sun M, Zhou X, Chen L, Huang S, Leung V, Wu N, et al. The regulatory roles of micrornas in bone remodeling and perspectives as biomarkers in osteoporosis. *BioMed Res Int* (2016) 2016:1652417. doi: 10.1155/2016/1652417
71. Ostrowski M, Carmo NB, Krumeich S, Fanget I, Raposo G, Savina A, et al. Rab27a and Rab27b control different steps of the exosome secretion pathway. *Nat Cell Biol* (2010) 12:19–30; suppp1-13. doi: 10.1038/ncb2000
72. De Rubis G, Rajeev Krishnan S, Bebawy M. Liquid biopsies in cancer diagnosis, monitoring, and prognosis. *Trends Pharmacol Sci* (2019) 40:172–86. doi: 10.1016/j.tips.2019.01.006
73. Sato Y, Matoba R, Kato K. Recent advances in liquid biopsy in precision oncology research. *Biol Pharm Bull* (2019) 42:337–42. doi: 10.1248/bpb.b18-00804
74. Guibert N, Pradines A, Favre G, Mazieres J. Current and future applications of liquid biopsy in nonsmall cell lung cancer from early to advanced stages. *Eur Respir Rev* (2020) 29:190052. doi: 10.1183/16000617.0052-2019
75. Chen D, Xu T, Wang S, Chang H, Yu T, Zhu Y, et al. Liquid biopsy applications in the clinic. *Mol Diagn Ther* (2020) 24:125–32. doi: 10.1007/s40291-019-00444-8
76. Shi ZY, Yang XX, Malichewe C, Li YS, Guo XL. Exosomal microRNAs-mediated intercellular communication and exosome-based cancer treatment. *Int J Biol Macromol* (2020) 158:530–41. doi: 10.1016/j.ijbiomac.2020.04.228
77. Clayton A, Harris CL, Court J, Mason MD, Morgan BP. Antigen-presenting cell exosomes are protected from complement-mediated lysis by expression of CD55 and CD59. *Eur J Immunol* (2003) 33:522–31. doi: 10.1002/immu.200310028
78. Jin X, Chen Y, Chen H, Fei S, Chen D, Cai X, et al. Evaluation of tumor-derived exosomal mirna as potential diagnostic biomarkers for early-stage non-small cell lung cancer using next-generation sequencing. *Clin Cancer Res* (2017) 23:5311–9. doi: 10.1158/1078-0432.CCR-17-0577
79. Hu C, Meiners S, Lukas C, Stathopoulos GT, Chen J. Role of exosomal microRNAs in lung cancer biology and clinical applications. *Cell Prolif* (2020) 53:e12828. doi: 10.1111/cpr.12828
80. Dejima H, Iinuma H, Kanaoka R, Matsutani N, Kawamura M. Exosomal microRNA in plasma as a non-invasive biomarker for the recurrence of non-small cell lung cancer. *Oncol Lett* (2017) 13:1256–63. doi: 10.3892/ol.2017.5569
81. Yuwen DL, Sheng BB, Liu J, Wenyu W, Shu YQ. MiR-146a-5p level in serum exosomes predicts therapeutic effect of cisplatin in non-small cell lung cancer. *Eur Rev Med Pharmacol Sci* (2017) 21:2650–8.
82. Liu Q, Yu Z, Yuan S, Xie W, Li C, Hu Z, et al. Circulating exosomal microRNAs as prognostic biomarkers for non-small-cell lung cancer. *Oncotarget* (2017) 8:13048–58. doi: 10.18632/oncotarget.14369
83. Yang XR, Pi C, Yu R, Fan XJ, Peng XX, Zhang XC, et al. Correlation of exosomal microRNA clusters with bone metastasis in non-small cell lung cancer. *Clin Exp Metastasis* (2020). doi: 10.1007/s10585-020-10062-y
84. Takenaka T, Nakai S, Katayama M, Hirano M, Ueno N, Noguchi K, et al. Effects of gefitinib treatment on cellular uptake of extracellular vesicles in EGFR-mutant non-small cell lung cancer cells. *Int J Pharm* (2019) 572:118762. doi: 10.1016/j.ijpharm.2019.118762
85. Hu W, Ru Z, Xiao W, Xiong Z, Wang C, Yuan C, et al. Adipose tissue browning in cancer-associated cachexia can be attenuated by inhibition of exosome generation. *Biochem Biophys Res Commun* (2018) 506:122–9. doi: 10.1016/j.bbrc.2018.09.139

Conflict of Interest: The authors declare that the research was conducted in the absence of any commercial or financial relationships that could be construed as a potential conflict of interest.

frontiers in Oncology

ORIGINAL RESEARCH
published: 26 February 2021
doi: 10.3389/fonc.2021.608323

The Clinical Characteristics and Prediction Nomograms for Primary Spine Malignancies

Lei Zhou[1,2†], *Runzhi Huang*[3†], *Ziheng Wei*[1,2†], *Tong Meng*[1,2*] *and Huabin Yin*[1,2*]

[1] Department of Orthopedics, Shanghai General Hospital, Shanghai Jiao Tong University School of Medicine, Shanghai, China, [2] Shanghai Bone Tumor Institution, Shanghai, China, [3] Division of Spine, Department of Orthopedics, Tongji Hospital Affiliated to Tongji University School of Medicine, Shanghai, China

OPEN ACCESS

Edited by:
Kotaro Nishida,
University of the Ryukyus, Japan

Reviewed by:
Kuang-Ming Liao,
Chi Mei Medical Center, Taiwan
Jian Liu,
Zhejiang University-University of Edinburgh Institute, China

***Correspondence:**
Tong Meng
mengtong@medmail.com.cn
Huabin Yin
yinhuabin@aliyun.com

[†]These authors have contributed equally to this work and share first authorship

Specialty section:
This article was submitted to Molecular and Cellular Oncology, a section of the journal Frontiers in Oncology

Received: 20 September 2020
Accepted: 25 January 2021
Published: 26 February 2021

Citation:
Zhou L, Huang R, Wei Z, Meng T and Yin H (2021) The Clinical Characteristics and Prediction Nomograms for Primary Spine Malignancies. Front. Oncol. 11:608323. doi: 10.3389/fonc.2021.608323

Background: Primary spine malignancies (PSMs) are relatively rare in bone tumors. Due to their rarity, the clinical characteristics and prognostic factors are still ambiguous. In this study, we aim to identify the clinical features and proposed prediction nomograms for patients with PSMs.

Methods: Patients diagnosed with PSMs including chordoma, osteosarcoma, chondrosarcoma, Ewing sarcoma, and malignant giant cell tumor of bone (GCTB) between 1975 and 2016 were selected from the Surveillance, Epidemiology, and End Results (SEER) database. The patient and tumor characteristics were described based on clinical information. The significant prognostic factors of overall survival (OS) and cancer-specific survival (CSS) were identified by the univariate and multivariate Cox analysis. Then, the nomograms for OS and CSS were established based on the selected predictors and their accuracy was explored by the Cox–Snell residual plot, area under the curve (AUC) of receiver operator characteristic (ROC) and calibration curve.

Results: The clinical information of 1,096 patients with PSMs was selected from the SEER database between 1975 and 2016. A total of 395 patients were identified with full survival and treatment data between 2004 and 2016. Chordoma is the commonest tumor with 400 cases, along 172 cases with osteosarcoma, 240 cases with chondrosarcoma, 262 cases with Ewing sarcoma and 22 cases with malignant GCTB. The univariate and multivariate analyses revealed that older age (Age > 60), distant metastasis, chemotherapy, and Surgery were independent predictors for OS and/or CSS. Based on these results, the nomograms were established with a better applicability (AUC for CSS: 0.784; AUC for OS: 0.780).

Conclusions: This study provides the statistics evidence for the clinical characteristics and predictors for patients with PSMs based on a large size population. Additionally, precise prediction nomograms were also established with a well-applicability.

Keywords: primary spine malignancy, clinical characteristic, prognostic factor, nomogram, survival

INTRODUCTION

Primary spine malignancies (PSMs) are relatively rare in bone tumors with a wide histopathological heterogeneity (1, 2). Chordoma is the most common tumor type, with the predominate sites of fusion segments (3). Besides, chondrosarcoma, Ewing sarcoma, osteosarcoma, and malignant giant cell tumor of the bone (GCTB) can be commonly found in the spine (4, 5). Due to the specific location of the spine, these tumors often result in local pain, neurologic defect, spinal instability and pathological fracture, which significantly decrease the life quality and overall survival (OS) (6). Till now, surgery is still the main therapeutic method for spine malignancies. As for the surgical treatment, the total *en-bloc* spondylectomy (TES) is recommended. However, due to the specific structure of the spine, many cases are unsuitable for TES, thereby leading to poor prognosis. Thus, there is a pressing need for oncologists and orthopedists to identify the epidemiology features and prognostic factors for patients with PSMs.

Many previous studies have focused on the clinical characteristics and OS-associated factors of PSMs, such as age, Karnofsky performance score (KPS), pathological nature, Frankel grading and therapeutic methods (7–9). However, due to their rarity, most of these studies were based on small sample size in one single tumor center, and their epidemiological features are not well known. In addition, although many score systems of spine metastasis have been constructed, few of them can be applied in PSMs (10–12). Thus, their clinical features and predictors should be identified by a large cohort of patients and advanced modeling methods should also be used to establish a well-applied prediction model.

The Surveillance, Epidemiology, and End Results (SEER) database is a widely used database consisting clinical data of cancer patients (13). Previous studies focused on the clinical features and predictors of PSMs in SEER database were only based on one tumor type with a relative short period, which limit their reliability (13–15). The nomogram is a visual statistical predictive tool for identifying clinically relevant prognostic factors. Thus, recent study has utilized this tool to predict the prognosis specific to an individual and achieves satisfying results (13, 16, 17).

In this study, we selected patients with PSMs from the SEER database with a long period (from 1975 to 2016) to explore their clinical characteristics. In addition, patients from 2004 to 2016 with full treatment information were used to identify the prognostic factors. Based on the identified prognostic factors by regression analysis methods, the nomograms were constructed to evaluate the OS and cause specific survival (CSS) of each individual (15). In general, our finding may identify the comprehensive clinical features of patients with PSMs and provide the well applicable nomograms.

METHODS

Patient Selection and Data Extraction

Patients diagnosed with spine malignancy (Osteosarcoma, Chondrosarcoma, Chordoma, Ewing sarcoma, and GCTB) between 1975 and 2016 were selected from the SEER database. Only patients whose tumor diagnosed with the first primary tumor by histopathological evidence were included in the epidemiological analysis. The clinical data included demographics (*i.e.* age, gender and ethnicity), tumor characteristics (*i.e.* histologic subtype, SEER historic stage, and tumor extension), treatment information (*i.e.* surgery, radiation, and chemotherapy). The end events were defined as all-cause death and cause specific death. Thus, the evaluation indicator consisted of OS time, OS status, CSS time, and CSS status. The patients with unknown demographics, tumor and treatment information as well as outcomes were excluded from further survival analysis. Especially, all ICD-O-3 histologic subtypes were combined for five tumor types and different subtypes with similar survival outcomes were also combined for survival analysis.

Statistical Analysis

The epidemiological analysis was described as demographics, tumor characteristics, treatment information and patient outcomes. All of them were presented by integrated bar-plot and heatmap in each ICD-O-3 histologic subtype.

To identify potential variables for prognosis, Kaplan–Meier survival analysis and Cox regression analysis were used and were presented by Kaplan–Meier curve and forest plot, respectively. The significant variables of the univariate analysis were screened out to construct the multivariate Cox regression model for OS and CSS. Despite the non-significant demographic recodes, demographics were all kept for subsequent multivariate analysis because clinical variables require correction of this information. Furthermore, the prognostic nomograms were constructed based on the multivariate Cox models to predict the 3- and 5-year OS and CSS probability of patients with PSMs.

In the multivariate Cox regression model, the formula was used to calculate the risk score for each individual:

$$riskscore_N = \beta 1 \times \text{variable}_1 + \beta 2 \times \text{variable}_2 + \ldots\ldots + \beta M \times \text{variable}_M$$

In the formula, "N" represented the number of each patient; "β" represented coefficient of each variable in the multivariate model; and "M" represented the number of prognostic variables in the multivariate model.

All patients were subsequently divided into high and low risk groups with the median of the risk score. Kaplan–Meier survival analysis and risk scatter/line plot were utilized to evaluate the independent prognosis value of the risk score and risk distribution in patients with PSMs, respectively. In terms of model diagnosis, the good of fitness (GOF), discrimination and calibration of the multivariate Cox regression model was illustrated by the Cox–Snell residual plot, area under the curve (AUC) of receiver operator characteristic (ROC) and calibration curve, respectively.

Statistical Method

Statistical integration started with descriptive statistic: dichotomous variables were summarized as percentages, and continuous variables

were reported as mean (range). Two-sided P value <0.05 was applied to identify the statistically significant variables in this study. In the Cox regression model, the significance was described by hazard ratio (HR) and 95% confidence interval (CI). The R software (version 3.6.2, www.r-project.org, Institute for Statistics and Mathematics, Vienna, Austria) was used for all statistics analysis processes.

RESULTS

Patient Selection and Data Extraction

The flowchart of inclusion and exclusion processes was summarized in **Figure 1**. A total of 1,097 patients diagnosed with PSMs between 1975 and 2016 were selected from the SEER database. After excluding patients who were not diagnosed by histopathological evidence, 1,058 patients were subsequently included in the epidemiological analysis.

Descriptive Epidemiological Statistic

All demographics, tumor information and outcomes of all the 1,058 patients were summarized by integrated bar-plot and heatmap (**Figure 2A**). The total cohort comprised 634 (60%) males and 928 (88%) white patients, with a similar age distribution from 10- and 79-year old (**Figure 2B**). Regional tumors (403, 38%) and localized tumors (353, 33%) are common in those PSMs, and 149 (14%) patients experienced tumor metastasis (**Figure 2B**). As for tumor histology (**Figure 2B**), chordoma was the most common pathological pattern (384, 36%). Ewing sarcoma (355, 24%) and chondrosarcoma (232, 22%) were similarly distributed. Osteosarcoma was found in 166 patients (16%), whereas malignant giant cell tumor of bone (21, 2%) was rarely uncovered.

As the tumor histology is an important clinical data which is significantly associated with patients' prognosis, we further summarized the demographics data of each ICD-O-3 histologic subtype (Osteosarcoma, **Figure S1A**; Ewing sarcoma, **Figure S1B**; Chondrosarcoma, **Figure S1C**; Chordoma, **Figure S1D**; malignant GCTB, **Figure S1E**). As for age, patients with osteosarcoma/chondrosarcoma/malignant GCTB had a similar distribution of age, and few patients were younger than 10-years old (**Figures 3A, C, E**). Patients with Ewing sarcoma were relatively young, with 12% younger than 10-years old and 46% in the second decade (**Figure 3B**). However, most chordoma patients (70%) were older than 50-years old and even 9% patients were older than 80-years old (**Figure 3D**).

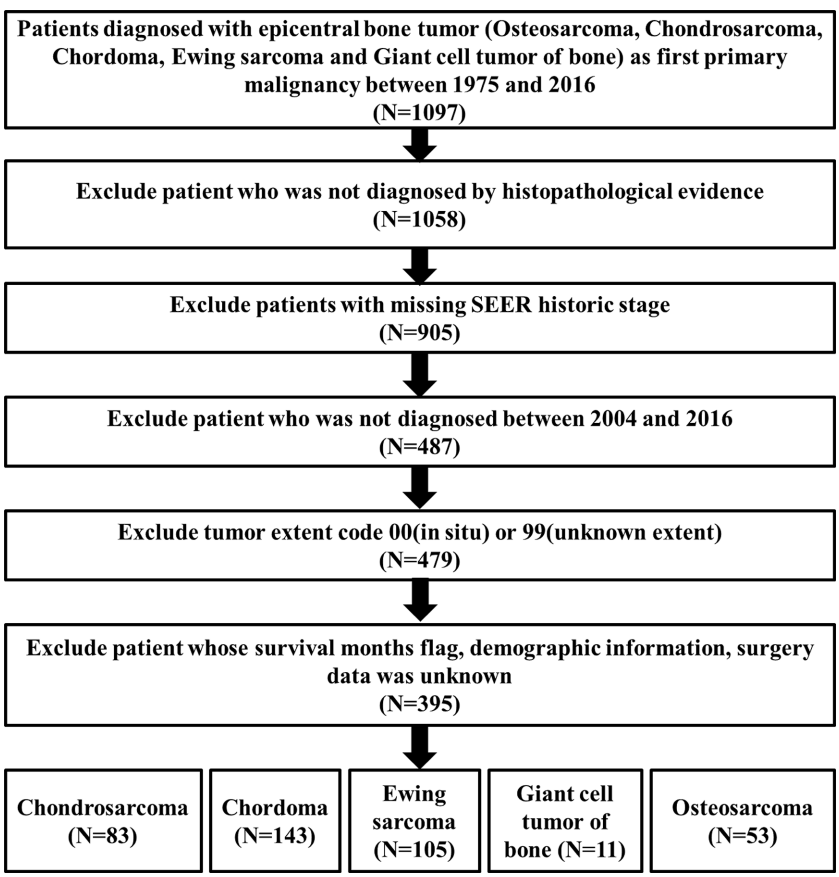

FIGURE 1 | The flowchart of inclusion and exclusion process.

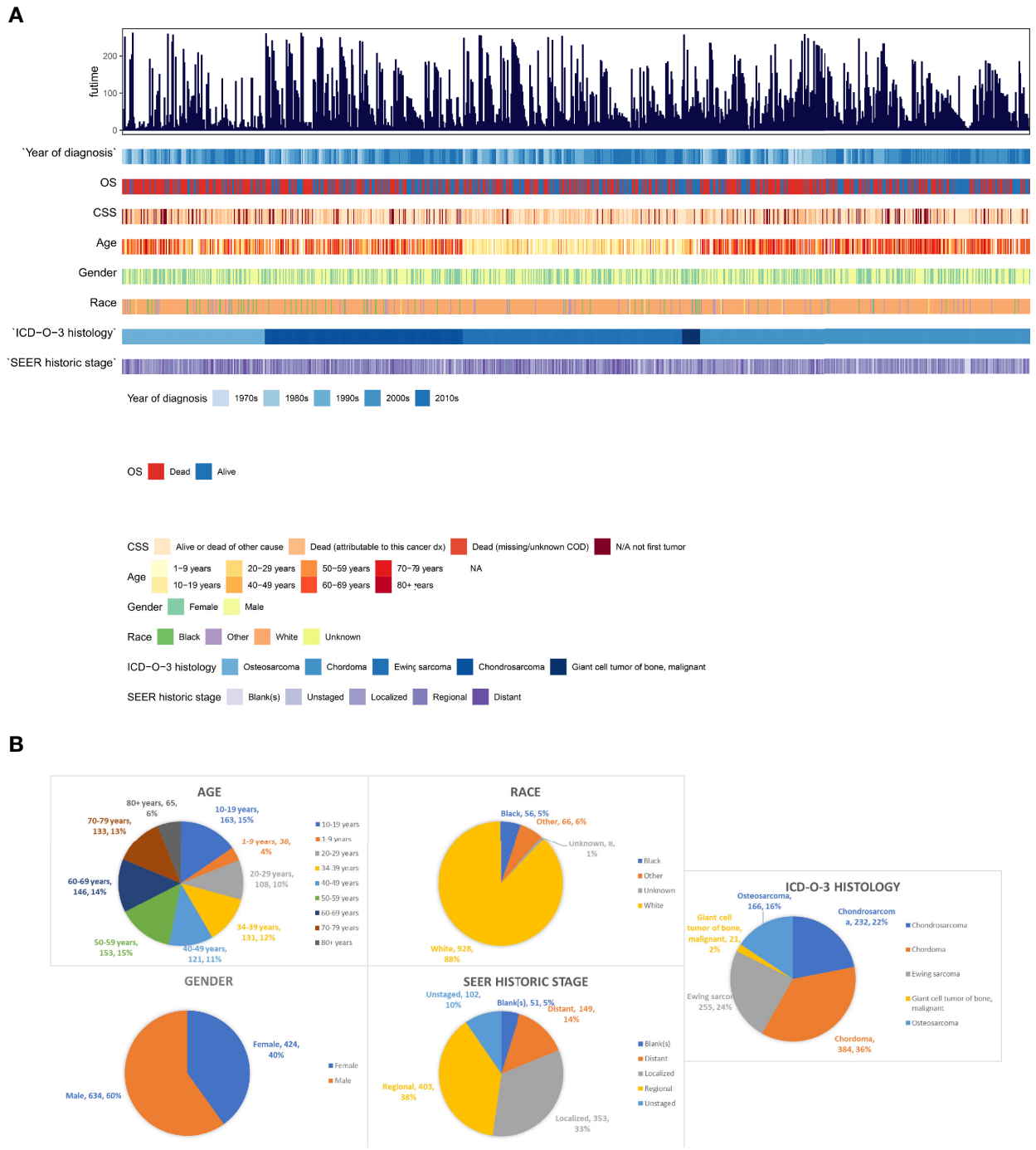

FIGURE 2 | The epidemiological analysis of 1,058 patients with PSMs. **(A)** The integrated bar-plot and heatmap of demographics, tumor information and patient outcomes of patients with PSMs. **(B)** The pie chart of age, race, gender, historic stage and ICD-O-3 histology in the patients with PSMs. PSMs, primary spine malignancies.

Due to the data from the SEER database, most patients of each tumor type were white race (**Figures 3A-E**). In addition, patients with osteosarcoma/Ewing sarcoma/chondrosarcoma/chordoma were male predominance, whereas most malignant GCTB (67%) were female (**Figures 3A–E**). Furthermore, we uncovered that chordoma and malignant GCTB rarely metastasized, while osteosarcoma and Ewing sarcoma had a high tendency of distant metastasis (**Figures 3A, B, D, E**).

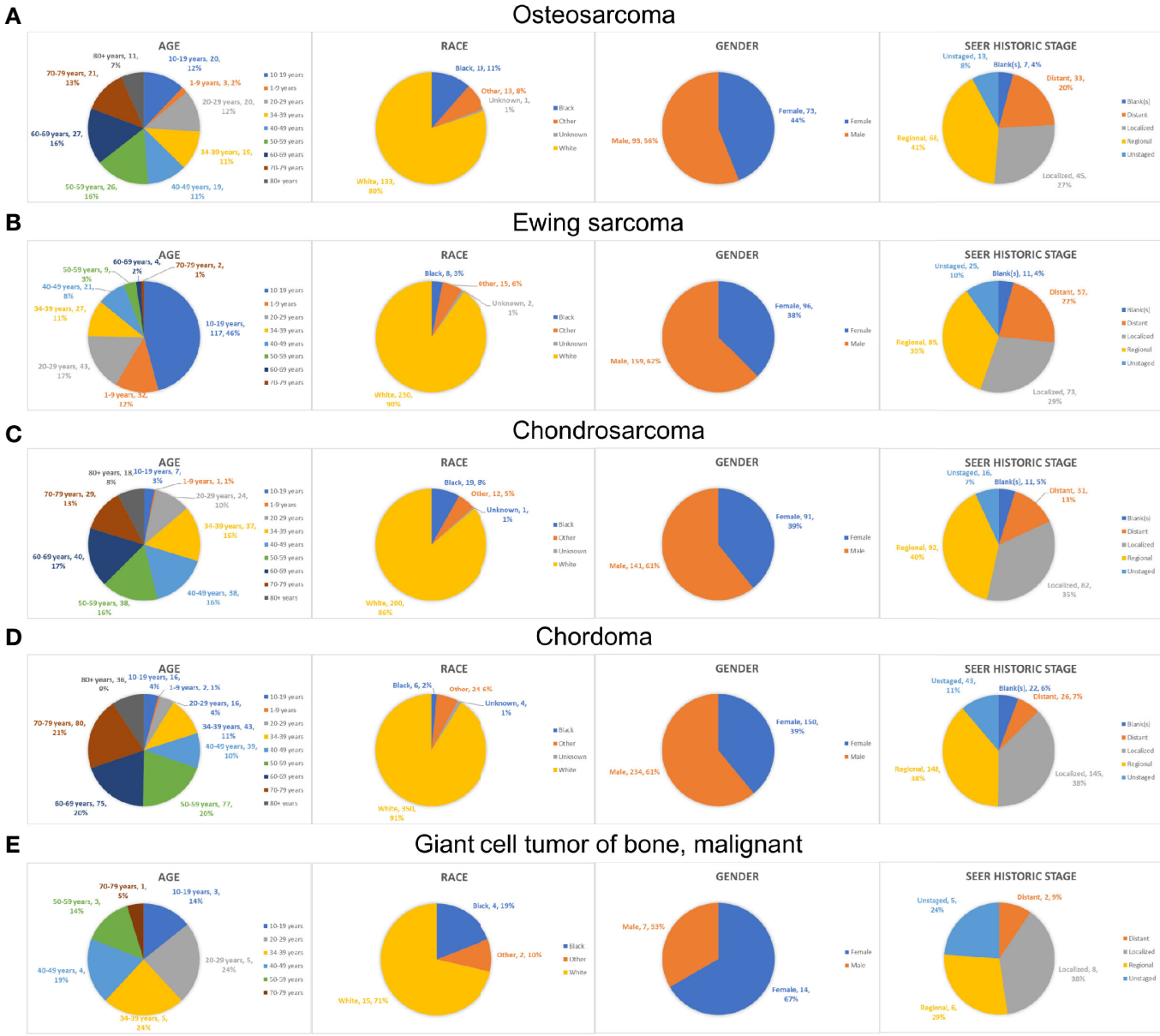

FIGURE 3 | The epidemiological analysis of patients with different types of PSMs. The pie chart of age, race, gender and historic stage in the patients with osteosarcoma **(A)**, Ewing sarcoma **(B)**, chondrosarcoma **(C)**, chordoma **(D)** and malignant GCTB **(E)**. PSMs, primary spine malignancies; GCTB, Giant cell tumor of bone.

Survival Analysis of Selected PSM Patients

To further obtain full treatment data of surgery and adjuvant therapy (radiotherapy and chemotherapy), we selected the chordoma patients treated from 2004 to 2016. Finally, a total of 395 patients with PSMs were identified to decipher the prognostic factors, including 53 osteosarcomas, 83 chondrosarcomas, 143 chordomas, 105 Ewing sarcomas, and 11 malignant giant cell tumors of bone (**Figure 1**). In these 395 patients, 327 underwent surgery, along with 230 having radiotherapy and 143 experiencing chemotherapy. Due to the correlation between tumor type/surgery and adjuvant therapy, we also identified their relation. The results revealed that there was significant difference between patients undergoing radiotherapy with and without surgery (P = 0.516, **Figure S2A** and **Table S1**). More patients treated with chemotherapy and surgery than those undergoing chemotherapy without surgery (P < 0.001, **Figure S2B** and **Table S2**). Besides, more patients with chordoma or Ewing sarcoma were treated with radiotherapy (P < 0.001, **Figure S2C** and **Table S3**) and more patients with Ewing sarcoma or osteosarcoma underwent chemotherapy (P < 0.001, **Figure S2D** and **Table S4**).

The Kaplan–Meier survival analysis was used to evaluate the prognostic values of age (**Figure 4A**, P < 0.001), gender (**Figure 4B**, P = 0.228), race (**Figure 4C**, P = 0.358), extension (**Figure 4D**, P = 0.001), ICD-O-3 histology (Figure 4E, P < 0.001), SEER historic stage (**Figure 4F**, P <0.001), surgery (**Figure 4G**, P < 0.001), chemotherapy (**Figure 4H**, P = 0.006) and radiotherapy (**Figure 4I**, P = 0.202) for CSS. Six prognostic factors were identified and analyzed in the multivariate Cox regression. The results revealed that patients with older age (Age > 60: HR, 4.24; 95% CI, 2.49–7.22; P < 0.001; Reference, Age < 30) and chemotherapy (HR, 2.13; 95% CI, 1.345–3.38; P = 0.001; Reference, No/Unknown) were significant risk variables for CSS. Besides, patients with localized tumor (HR, 0.16; 95% CI, 0.067–0.39; P < 0.001; Reference, Distant) and regional tumor (HR, 0.31; 95% CI, 0.196–0.48; P < 0.001; Reference, Distant) were significant favorable variables for CSS (**Figure 5A**).

Based on the multivariate Cox models, the prognostic nomogram was constructed, which could predict the 3- and 5-year CSS probability of patients with PSMs (**Figure 5B**). The risk score for each patient was calculated by the formula described in the *Methods* section. The risk line and scatterplot illustrated the distribution of risk score among all the patients, respectively (**Figures 5C, D**). In addition, the Kaplan–Meier survival curve showed a significantly prognostic value of the risk score for CSS (**Figure 5E**, P < 0.001). In terms of model diagnosis, the calibration curve, ROC curve (AUC = 0.784) and Cox–Snell residual plot showed acceptable calibration, discrimination and GOF and of the multivariate Cox regression model for CSS (**Figures 5F–I**).

Similar to CSS survival analysis, the Kaplan–Meier method was also used to evaluate the predictors for OS. The same six factors were identified as prognostic ones, namely age (P < 0.001), extension (P = 0.001), ICD-O-3 histology (P < 0.001), SEER historic stage (P < 0.001), surgery (P < 0.001), and chemotherapy (P = 0.072). Their Kaplan–Meier curves for OS were illustrated in **Figure 6**. In the multivariate Cox regression analysis for OS, patients with older age (age > 60: HR, 3.37; 95% CI, 2.255–5.03; P < 0.001; Reference, age < 30) was significant risk variables for OS. In addition, compared with patients with distant tumor, those with localized (HR, 0.18; 95% CI, 0.074–0.43; P < 0.001) or regional tumor (HR, 0.31; 95% CI, 0.203–0.46 P < 0.001) have a favorable prognosis. Furthermore, surgical treatment significantly improved the OS of patients with PSMs (HR, 0.51; 95% CI, 0.353–0.75; P < 0.001; **Figure 7A**).

The prognostic nomogram was also constructed to predict the 3- and 5-year OS probability of patients with PSMs (**Figure 7B**). The risk line and scatterplot of OS illustrated the distribution of risk score among all patients (**Figures 7C, D**). In the Kaplan–Meier survival analysis, risk score for OS revealed a significant prognostic value (**Figure 7E**, P < 0.001). To evaluate the calibration, discrimination, and GOF of the multivariate Cox regression model for OS, calibration curve, ROC curve, and residual plot were used. The former revealed a suitable calibration (**Figures 7F, G**); the AUC of ROC was 0.780 (**Figure 7H**); the latter showed a good GOF (**Figure 7I**).

Subgroup Cox Regression Analysis With Time Frame of Diagnosis

Although some previous epidemiological study comparing SEER areas with non-SEER areas in the United States concluded that the age and sex distributions of these areas were comparable, we could not agree with them about the temporal and spatial heterogeneity of the SEER data any more (18–20). However, to further minimize this temporal and spatial heterogeneity, we also performed four subgroup Cox regression analysis and conducted four nomograms with time frame of diagnosis [(Patients diagnosed between 2004 and 2010 for OS, **Figure S3**); patients diagnosed between 2004 and 2010 for CSS, **Figure S4**); patients diagnosed between 2011 and 2016 for OS, **Figure S5**); patients diagnosed between 2011 and 2016 for CSS, **Figure S6**)]. All models were diagnosed by calibration, time-related ROC and decision curve, suggesting the significant predictors were stable at different times.

DISCUSSION

PSMs are rare tumors with poor prognosis (21). Due to the specific spinal structure, surgery, and radiotherapy may damage the normal function of the spinal cord and result in neurologic defects (22). Thus, their therapeutic options are challenging. Evaluating the clinical features and prognostic factors may assist orthopedists in early diagnosis and treatment decision-making, whereas those have not been explored comprehensively. Based on the SEER database, we found that chordoma is the commonest tumor type with 36% of all the PSMs, followed by Ewing sarcomas (24%) and chondrosarcoma (22%). Patients with Ewing sarcomas had a younger age, whereas chordoma patients were relatively old. Malignant GCTB had a female predominance, and osteosarcoma and Ewing sarcomas had a high tendency to metastasize. In addition, patients with older age (Age > 60) or distant metastasis had poor prognosis for both CSS and OS. Chemotherapy is an unfavorable factor of the patients'

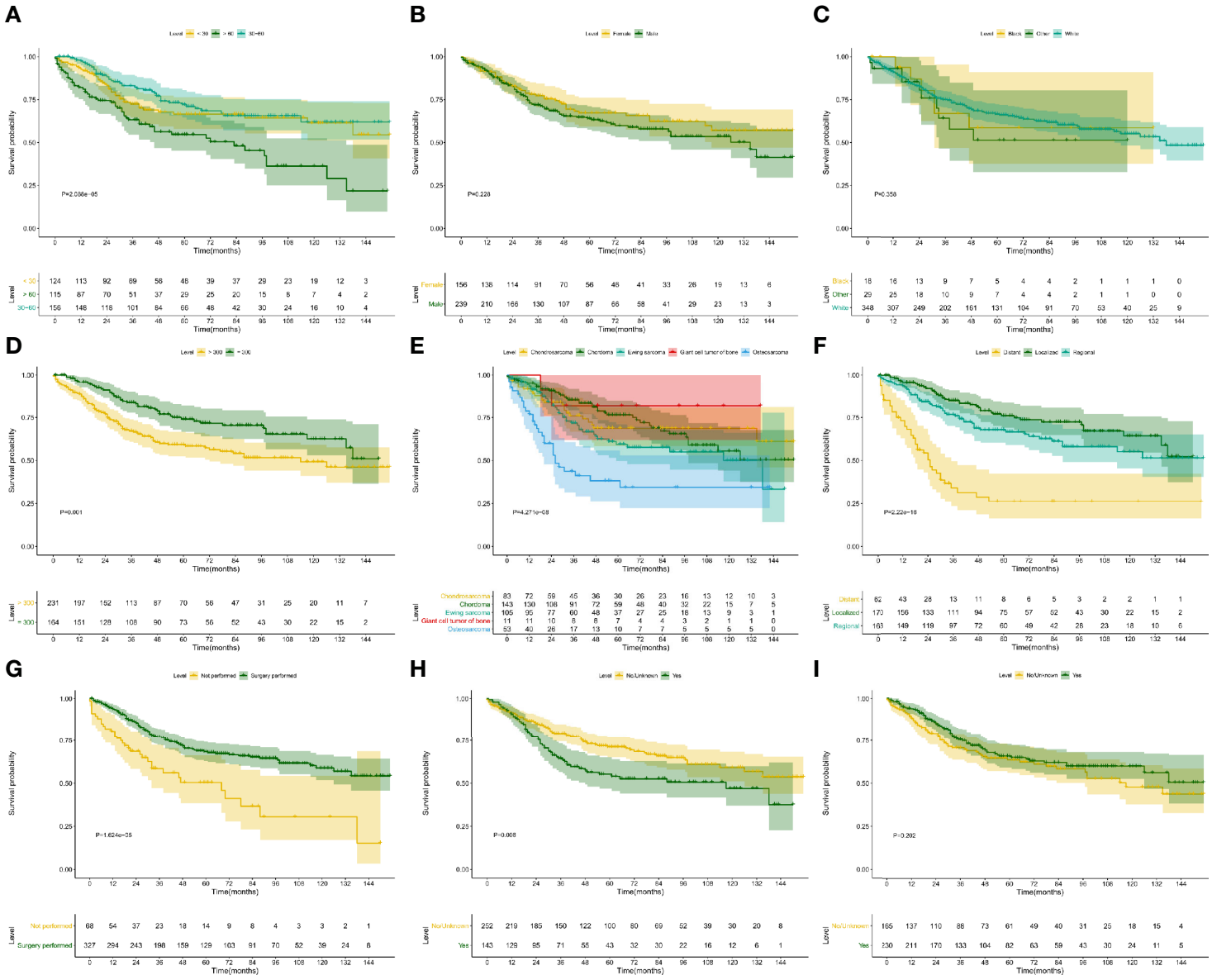

FIGURE 4 | Kaplan–Meier survival analysis for CSS. The Kaplan–Meier survival curves of age (**A**, P < 0.001), gender (**B**, P = 0.228), race (**C**, P = 0.358), extension (**D**, P = 0.001), ICD-O-3 histology (**E**, P < 0.001), SEER historic stage (**F**, P < 0.001), surgery (**G**, P < 0.001), chemotherapy (**H**, P = 0.006) and radiotherapy (**I**, P = 0.202) for CSS. CSS, cancer-specific survival.

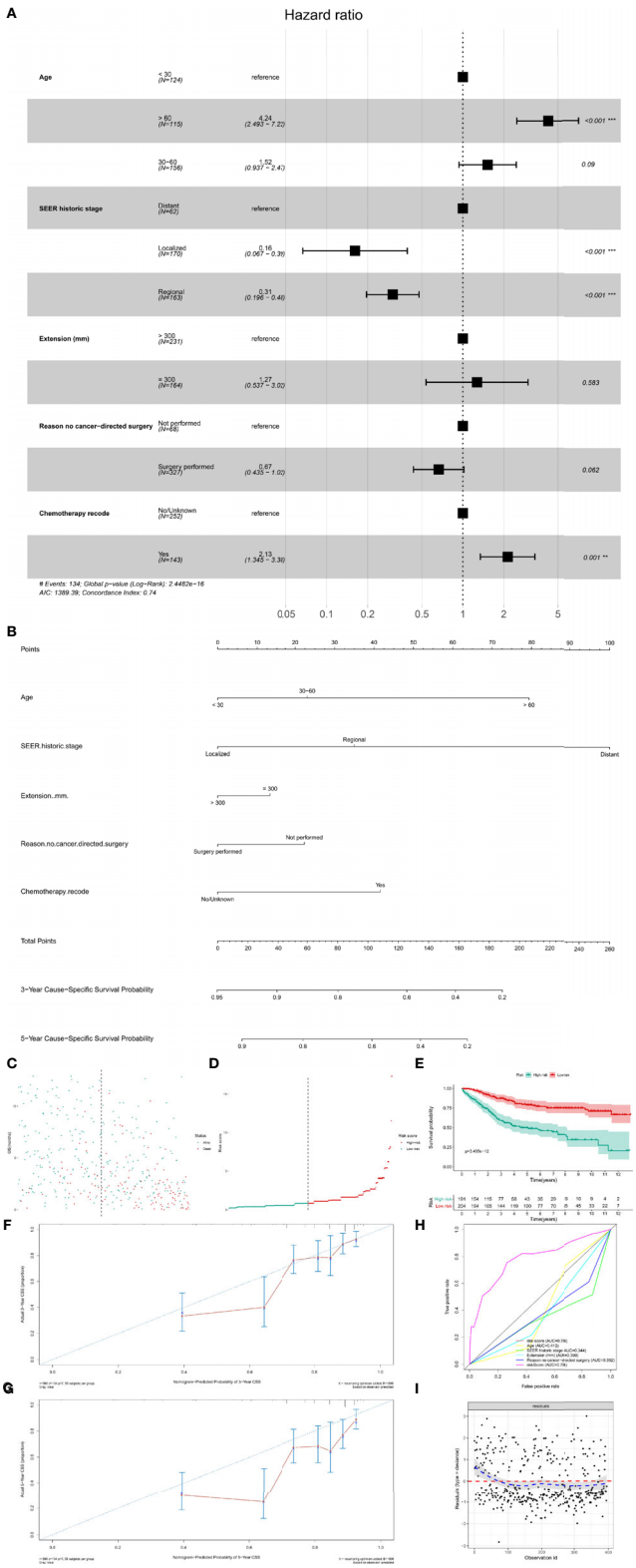

FIGURE 5 | The multivariate Cox regression model and nomogram for CSS. **(A)** The multivariate Cox regression analysis for CSS; **(B)** The prognostic nomogram for CSS. The risk line **(C)** and scatterplot **(D)** of the risk score. The Kaplan–Meier survival curve of the risk score for CSS (**E**, P < 0.001). The calibration curve **(F, G)**, ROC curve **(H)** and Cox–Snell residual plot **(I)** of the multivariate Cox regression model for CSS. CSS, cancer-specific survival; ROC, receiver operator characteristic.

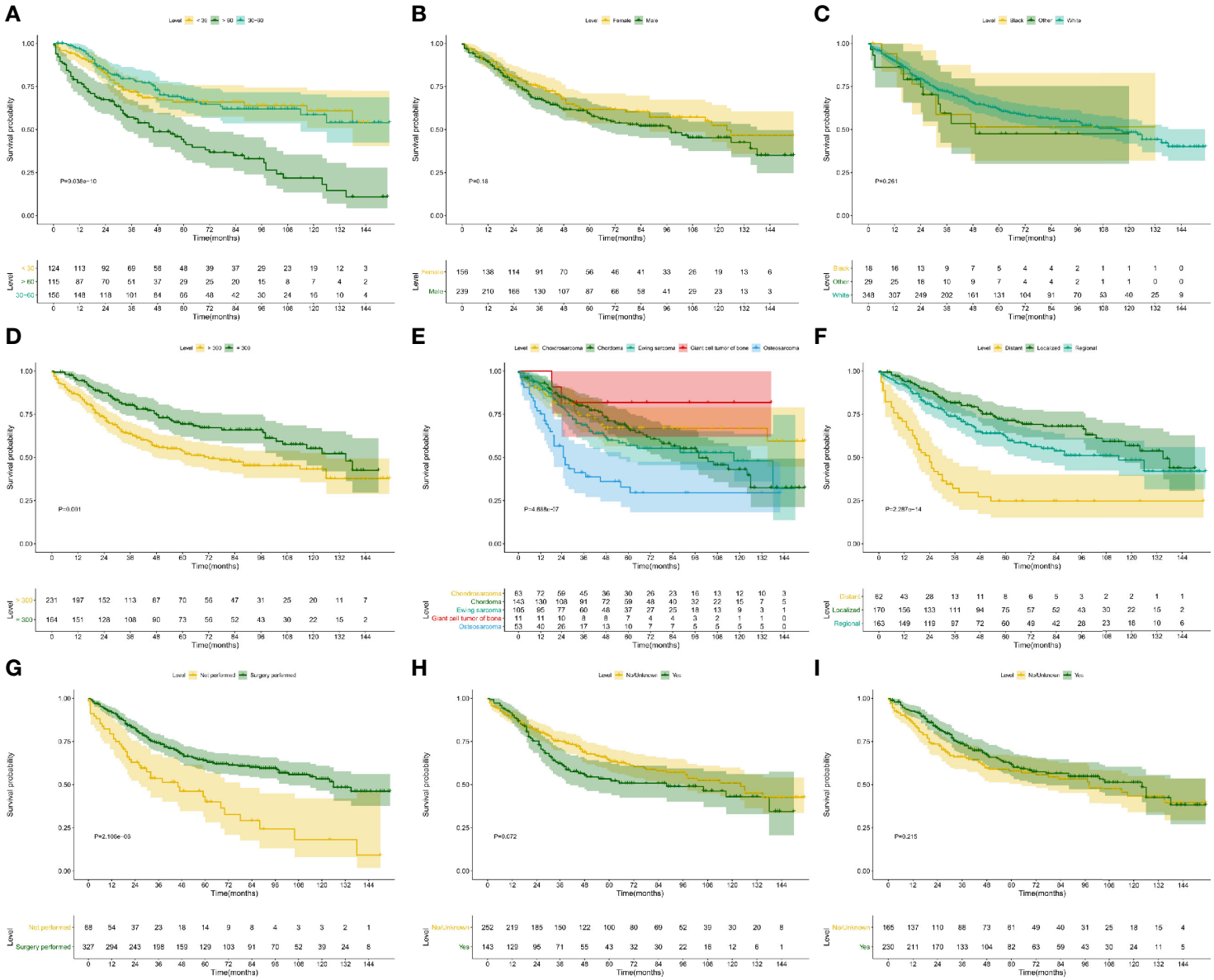

FIGURE 6 | Kaplan–Meier survival analysis for OS. The Kaplan–Meier survival curves of age (**A**, P < 0.001), gender (**B**, P = 0.180), race (**C**, P = 0.261), extension (**D**, P = 0.001), ICD-O-3 histology (**E**, P < 0.001), SEER historic stage (**F**, P < 0.001), surgery (**G**, P < 0.001), chemotherapy (**H**, P = 0.072) and radiotherapy (**I**, P = 0.215) for OS. OS, overall survival.

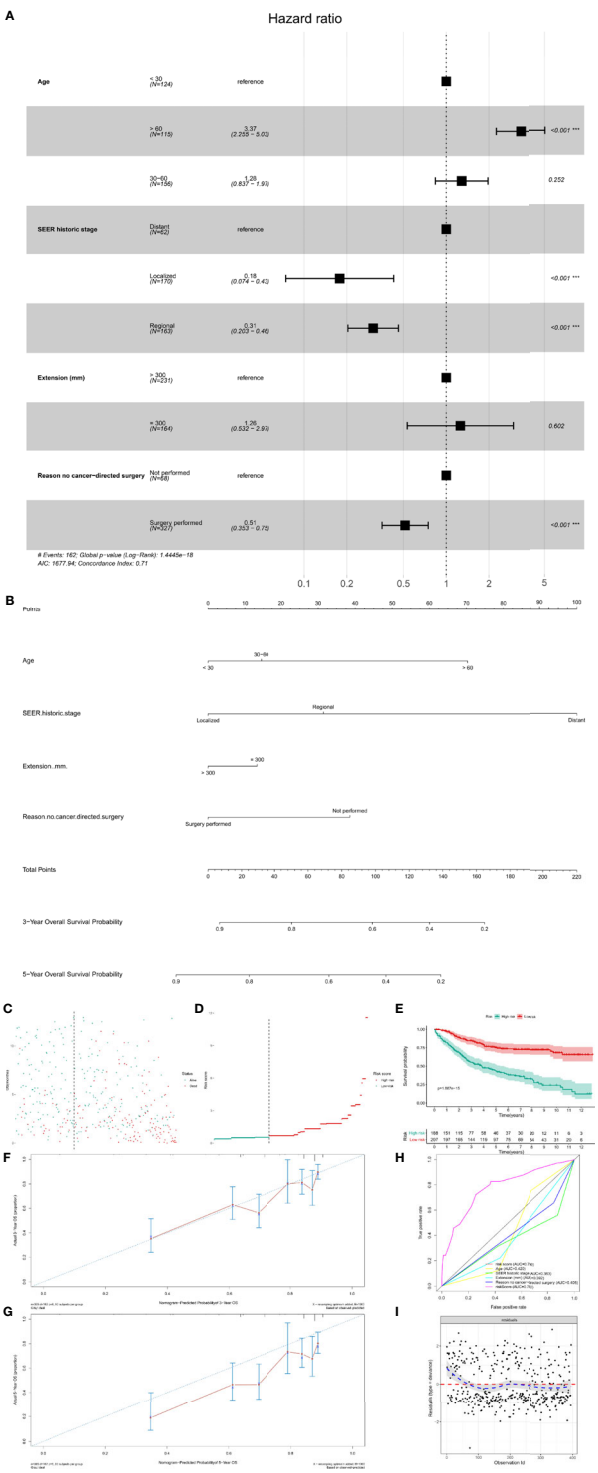

FIGURE 7 | The multivariate Cox regression model and nomogram for OS. **(A)** The multivariate Cox regression analysis for OS; **(B)** The prognostic nomogram for OS. The risk line **(C)** and scatterplot **(D)** of the risk score. The Kaplan–Meier survival curve of the risk score for OS **(E**, $P < 0.001$**)**. The calibration curve **(F, G)**, ROC curve **(H)** and Cox–Snell residual plot **(I)** of the multivariate Cox regression model for OS. OS, overall survival; ROC, receiver operator characteristic.

CSS. Surgery could significantly improve the OS of patients with PSMs.

Generally, the age of PSM patients is not consistent with previous studies, and it is largely associated with the tumor histology (3, 4, 23). In this study, PSM patients had a similar age distribution from 10- and 79-year old, whereas only 10% patients were diagnosed younger than 10-year old or older than 79-year old. In addition, Ewing sarcoma patients were relatively young, and 58% patients were younger than 20-years old. Chordoma patients were relatively old, and most chordoma patients (70%) were older than 50-years old. Furthermore, we also found that old age was an unfavorable predictor for both OS and CSS. This might be due to the poor physical condition of old patients, which could impair the tolerance of operation and subsequently decrease the survival time. With regard to patients' demographics, gender and race are also common features. We uncovered a slight male predominance (60%) in PSM patients. However, most patients with malignant GCTB were female. As the collected data came from SEER database, white was the leading race a matter of course.

There are many tumor types of PSMs, such as bone tumors, soft tissue sarcoma, and neurogenic tumor (6, 24). In this study, we mainly investigated the bone tumors of PSMs, and we identified five histological types in SEER database. Chordoma consisted of 36% PSMs and were regarded as the most common one. Malignant giant cell tumor of the bone was a rare type of PSM, with only 21 patients being identified. Although histological type was not the prognostic factor in the nomogram for CSS and OS, the prognosis of patients with different histological types were varied. Based on the Kaplan–Meier survival analysis, we found that patients with chordoma, chondrosarcoma or Ewing sarcomas had similar prognosis, which was more favorable than osteosarcoma patients and poorer than malignant GCTB patients.

Surgical treatment is the standard treatment strategy for PSMs, and it provides many benefits, such as tumor resection, local pain relief, spinal cord decompression, and spinal reconstruction (21, 25). In this study, we found that surgical treatment could significantly improve the OS of PSM patients, indicating its important roles in the control of PSM. As for tumor resection, the resection method and margin condition are also critical factors in the final outcome of PSM patients (22, 26). Compared to subtotal excision, *en-bloc* tumor resection with wide margins (R0), recommended by many spine surgeons, offers long-term disease control for most PSMs (27–29). However, the treatment information in the SEER database does not include these data which limits the power of similar studies (15, 30).

Both chemotherapy and radiotherapy are widely used as adjuvant therapies for the clinical management of spine malignancies. As for ES and osteosarcoma, chemotherapy is the standard treatment method and recommended to be performed preoperatively and postoperatively (31). Besides, radiotherapy is often used in ES, and unresectable or recurrent OS, chondrosarcoma and malignant GCTB (31). However, both chemotherapy and radiotherapy only provide limited benefits for chordoma (32). In this study, we found the poor prognosis in PSM patients treated with chemotherapy. In the subgroup analysis, most chemotherapy-applied patients were osteosarcoma

and Ewing sarcomas. Thus, we supposed that the poor prognosis of chemotherapy-applied patients may be associated with the tumor histology.

Although this study provides a comprehensive analysis for the clinical features and prognostic factors of PSM patients, there are still some limitations. First, as a population-based study from SEER database, some important data associated with patients' prognosis are missing, such as resection mode, chemotherapy strategy and radiotherapy dose. Second, it has all the limitations inherent in retrospective studies (Retrospective studies have lower level of evidence than prospective studies in the theory of evidence-based medicine). Third, all the cases in this study are from America, thus data from Europe and Asia are still needed to verify our results. Last but not least, due to the limitation of SEER database, surgical margin status, chemotherapy and radiotherapy strategy were incomplete. To ensure the missing values did not impact outcomes, several subgroup analyses were performed based on the dataset separated the missing values. In the future, more important variables would be collected and incorporated into the nomogram. As our future direction, some vital genetic or epigenetic signatures associated with these risk indicators, which has been validated by multi-omics data and wet experimental assays will be integrated to develop a more rigorous nomogram.

CONCLUSION

This study provides the statistics evidence for the clinical characteristics and predictors for patients with PSMs based on a large size population. Additionally, precise prediction nomograms were also established with a well-applicability.

DATA AVAILABILITY STATEMENT

Publicly available datasets were analyzed in this study. This data can be found here: Surveillance, Epidemiology, and End Results (SEER) database (https://seer.cancer.gov/).

AUTHOR CONTRIBUTIONS

LZ: Data collection, Writing - original draft. RH: Data analysis, Writing - original draft. ZW: Data collection, Writing - original draft. HY: Methodology, Software. TM: Conceptualization, Supervision, Writing - review & editing. All authors contributed to the article and approved the submitted version.

FUNDING

This study was supported in part by the National Natural Science Foundation of China (No. 81702659; 81772856; 82073207), The Youth Fund of Shanghai Municipal Health Planning Commission (No. 20174Y0117), Interdisciplinary Program of Shanghai Jiao Tong University (No.YG2017MS26), Shanghai Talent Development Fund (No.2018094).

SUPPLEMENTARY MATERIAL

The Supplementary Material for this article can be found online at: https://www.frontiersin.org/articles/10.3389/fonc.2021.608323/full#supplementary-material

Supplementary Figure 1 | The epidemiological analysis of patients with different types of PSMs. The integrated bar-plot and heatmap of demographics, tumor information, and patient outcomes of patients with osteosarcoma **(A)**, Ewing sarcoma **(B)**, chondrosarcoma **(C)**, chordoma **(D)** and malignant GCTB **(E)**. PSMs, primary spine malignancies; GCTB, Giant cell tumor of bone.

Supplementary Figure 2 | The subgroup analysis between radiotherapy/chemotherapy and surgery/tumor histology. The bar graph revealed the correlation between radiotherapy and surgery **(A)**, between radiotherapy and tumor histology **(B)**, between chemotherapy and surgery **(C)**, between chemotherapy and tumor histology **(D)**.

Supplementary Figure 3 | Construction of the prognostic nomogram with 179 patients diagnosed between 2004 and 2010 for predicting OS. **(A)** The constructed prognostic nomogram based on the multivariate Cox model. **(B)** The calibration curve illustrated decent calibration of the prognostic nomogram. The decision curve **(C)** and time-related ROC **(D)** were also conducted to show the patient benefit and the discrimination of the nomogram.

Supplementary Figure 4 | Construction of the prognostic nomogram with 179 patients diagnosed between 2004 and 2010 for predicting CSS. **(A)** The constructed prognostic nomogram based on the multivariate Cox model. **(B)** The calibration curve illustrated decent calibration of the prognostic nomogram. The decision curve **(C)** and time-related ROC **(D)** were also conducted to show the patient benefit and the discrimination of the nomogram.

Supplementary Figure 5 | Construction of the prognostic nomogram with 216 patients diagnosed between 2004 and 2010 for predicting OS. **(A)** The constructed prognostic nomogram based on the multivariate Cox model. **(B)** The calibration curve illustrated decent calibration of the prognostic nomogram. The decision curve **(C)** and time-related ROC **(D)** were also conducted to show the patient benefit and the discrimination of the nomogram.

Supplementary Figure 6 | Construction of the prognostic nomogram with 216 patients diagnosed between 2004 and 2010 for predicting OS. **(A)** The constructed prognostic nomogram based on the multivariate Cox model. **(B)** The calibration curve illustrated decent calibration of the prognostic nomogram. The decision curve **(C)** and time-related ROC **(D)** were also conducted to show the patient benefit and the discrimination of the nomogram. (Page 14, Lines 14–30; Page 15, Lines 1–6).

REFERENCES

1. Dang L, Liu X, Dang G, Jiang L, Wei F, Yu M, et al. Primary tumors of the spine: a review of clinical features in 438 patients. *J Neurooncol* (2015) 121 (3):513–20. doi: 10.1007/s11060-014-1650-8
2. Donthineni R. Diagnosis and staging of spine tumors. *Orthop Clin North Am* (2009) 40(1):1–7. doi: 10.1016/j.ocl.2008.10.001
3. Meng T, Yin H, Li B, Li Z, Xu W, Zhou W, et al. Clinical features and prognostic factors of patients with chordoma in the spine: a retrospective analysis of 153 patients in a single center. *Neuro Oncol* (2015) 17(5):725–32. doi: 10.1093/neuonc/nou331
4. Yin H, Cheng M, Li B, Li B, Wang P, Meng T, et al. Treatment and outcome of malignant giant cell tumor in the spine. *J Neurooncol* (2015) 124(2):275–81. doi: 10.1007/s11060-015-1835-9

5. Yin H, Zhou W, Meng J, Zhang D, Wu Z, Wang T, et al. Prognostic factors of patients with spinal chondrosarcoma: a retrospective analysis of 98 consecutive patients in a single center. *Ann Surg Oncol* (2014) 21(11):3572–8. doi: 10.1245/s10434-014-3745-z
6. Sundaresan N, Boriani S, Rothman A, Holtzman R. Tumors of the osseous spine. *J Neurooncol* (2004) 69(1-3):273–90. doi: 10.1023/B:NEON.0000041888.33499.03
7. Cloyd JM, Chou D, Deviren V, Ames CP. En bloc resection of primary tumors of the cervical spine: report of two cases and systematic review of the literature. *Spine J* (2009) 9(11):928–35. doi: 10.1016/j.spinee.2009.07.005
8. Song D, Meng T, Lin Z, Fan T, Yin H, Li B, et al. Clinical Features and Prognostic Factors of Pediatric Spine Tumors: A Single-Center Experience With 190 Cases. *Spine (Phila Pa 1976)* (2016) 41(12):1006–12. doi: 10.1097/brs.0000000000001541
9. Chang UK, Lee DH, Kim MS. Stereotactic radiosurgery for primary malignant spinal tumors. *Neurol Res* (2014) 36(6):597–606. doi: 10.1179/1743132814y.0000000381
10. Tomita K, Kawahara N, Kobayashi T, Yoshida A, Murakami H, Akamaru T. Surgical strategy for spinal metastases. *Spine (Phila Pa 1976)* (2001) 26 (3):298–306. doi: 10.1097/00007632-200102010-00016
11. Wibmer C, Leithner A, Hofmann G, Clar H, Kapitan M, Berghold A, et al. Survival analysis of 254 patients after manifestation of spinal metastases: evaluation of seven preoperative scoring systems. *Spine (Phila Pa 1976)* (2011) 36(23):1977–86. doi: 10.1097/BRS.0b013e3182011f84
12. Morgen SS, Fruergaard S, Gehrchen M, Bjorck S, Engelholm SA, Dahl B. A revision of the Tokuhashi revised score improves the prognostic ability in patients with metastatic spinal cord compression. *J Cancer Res Clin Oncol* (2018) 144(1):33–8. doi: 10.1007/s00432-017-2519-y
13. Yan P, Huang R, Hu P, Liu F, Zhu X, Hu P, et al. Nomograms for predicting the overall and cause-specific survival in patients with malignant peripheral nerve sheath tumor: a population-based study. *J Neurooncol* (2019) 143 (3):495–503. doi: 10.1007/s11060-019-03181-4
14. Shi J, Yang J, Ma X, Wang X. Risk factors for metastasis and poor prognosis of Ewing sarcoma: a population based study. *J Orthop Surg Res* (2020) 15(1):88. doi: 10.1186/s13018-020-01607-8
15. Huang R, Xian S, Shi T, Yan P, Hu P, Yin H, et al. Evaluating and Predicting the Probability of Death in Patients with Non-Metastatic Osteosarcoma: A Population-Based Study. *Med Sci Monit* (2019) 25:4675–90. doi: 10.12659/msm.915418
16. Zhou X, Ning Q, Jin K, Zhang T, Ma X. Development and validation of a preoperative nomogram for predicting survival of patients with locally advanced prostate cancer after radical prostatectomy. *BMC Cancer* (2020) 20(1):97. doi: 10.1186/s12885-020-6565-5
17. Huang Z, Tong Y, Tian H, Zhao C. Establishment of a prognostic nomogram for lung adenocarcinoma with brain metastases. *World Neurosurg* (2020) 141: e700–9. doi: 10.1016/j.wneu.2020.05.273
18. Balachandran VP, Gonen M, Smith JJ, DeMatteo RP. Nomograms in oncology: more than meets the eye. *Lancet Oncol* (2015) 16(4):e173–80. doi: 10.1016/s1470-2045(14)71116-7
19. Nattinger AB, McAuliffe TL, Schapira MM. Generalizability of the surveillance, epidemiology, and end results registry population: factors relevant to epidemiologic and health care research. *J Clin Epidemiol* (1997) 50(8):939–45. doi: 10.1016/s0895-4356(97)00099-1
20. Giuffrida AY, Burgueno JE, Koniaris LG, Gutierrez JC, Duncan R, Scully SP. Chondrosarcoma in the United States (1973 to 2003): an analysis of 2890 cases from the SEER database. *J Bone Joint Surg Am* (2009) 91(5):1063–72. doi: 10.2106/jbjs.h.00416
21. Boriani S, Weinstein JN, Biagini R. Primary bone tumors of the spine. Terminology and surgical staging. *Spine (Phila Pa 1976)* (1997) 22(9):1036–44. doi: 10.1097/00007632-199705010-00020
22. Fisher CG, Saravanja DD, Dvorak MF, Rampersaud YR, Clarkson PW, Hurlbert J, et al. Surgical management of primary bone tumors of the spine: validation of an approach to enhance cure and reduce local recurrence. *Spine (Phila Pa 1976)* (2011) 36(10):830–6. doi: 10.1097/BRS.0b013e3181e502e5
23. Orguc S, Arkun R. Primary tumors of the spine. *Semin Musculoskelet Radiol* (2014) 18(3):280–99. doi: 10.1055/s-0034-1375570
24. Flemming DJ, Murphey MD, Carmichael BB, Bernard SA. Primary tumors of the spine. *Semin Musculoskelet Radiol* (2000) 4(3):299–320. doi: 10.1055/s-2000-9340
25. Cahill DW. Surgical management of malignant tumors of the adult bony spine. *South Med J* (1996) 89(7):653–65. doi: 10.1097/00007611-199607000-00002
26. Zileli M. Surgery for Primary Spine Tumors: How Radical Must We Operate? *World Neurosurg* (2017) 100:688–9. doi: 10.1016/j.wneu.2017.01.090
27. Heary RF, Vaccaro AR, Benevenia J, Cotler JM. "En-bloc" vertebrectomy in the mobile lumbar spine. *Surg Neurol* (1998) 50(6):548–56. doi: 10.1016/S0090-3019(98)00078-0
28. Wang X, Eichbaum E, Jian F, Chou D. Two-Stage En Bloc Resection of Multilevel Cervical Chordomas With Vertebral Artery Preservation: Operative Technique. *Oper Neurosurg (Hagerstown)* (2018) 14(5):538–45. doi: 10.1093/ons/opx178
29. Koga T, Shin M, Saito N. Treatment with high marginal dose is mandatory to achieve long-term control of skull base chordomas and chondrosarcomas by means of stereotactic radiosurgery. *J Neurooncol* (2010) 98(2):233–8. doi: 10.1007/s11060-010-0184-y
30. Bohman LE, Koch M, Bailey RL, Alonso-Basanta M, Lee JY. Skull base chordoma and chondrosarcoma: influence of clinical and demographic factors on prognosis: a SEER analysis. *World Neurosurg* (2014) 82(5):806–14. doi: 10.1016/j.wneu.2014.07.005
31. Biermann JS, Chow W, Reed DR, Lucas D, Adkins DR, Agulnik M, et al. NCCN Guidelines Insights: Bone Cancer, Version 2.2017. *J Natl Compr Canc Netw* (2017) 15(2):155–67. doi: 10.6004/jnccn.2017.0017
32. Whelan JS, Davis LE. Osteosarcoma, Chondrosarcoma, and Chordoma. *J Clin Oncol* (2018) 36(2):188–93. doi: 10.1200/jco.2017.75.1743

Conflict of Interest: The authors declare that the research was conducted in the absence of any commercial or financial relationships that could be construed as a potential conflict of interest.

frontiers in Genetics

METHODS
published: 11 March 2021
doi: 10.3389/fgene.2021.634116

A Novel Six-mRNA Signature Predicts Survival of Patients With Glioblastoma Multiforme

Zhentao Liu[1,2†], Hao Zhang[3†], Hongkang Hu[1†], Zheng Cai[1,4], Chengyin Lu[1], Qiang Liang[1], Jun Qian[5], Chunhui Wang[1] and Lei Jiang[1*]*

[1] Department of Neurosurgery, Changzheng Hospital, Naval Medical University, Shanghai, China, [2] Department of Neurosurgery, No. 988 Hospital of Joint Logistic Support Force, Zhengzhou, China, [3] Department of Orthopaedic Oncology, Changzheng Hospital, Naval Medical University, Shanghai, China, [4] Department of Pharmacy, Changhai Hospital, Naval Medical University, Shanghai, China, [5] Department of Neurosurgery, Tongji Hospital, Shanghai Tong Ji University School of Medicine, Shanghai, China

Glioblastoma multiforme (GBM) is a devastating brain tumor and displays divergent clinical outcomes due to its high degree of heterogeneity. Reliable prognostic biomarkers are urgently needed for improving risk stratification and survival prediction. In this study, we analyzed genome-wide mRNA profiles in GBM patients derived from The Cancer Genome Atlas (TCGA) and Gene Expression Omnibus (GEO) databases to identify mRNA-based signatures for GBM prognosis with survival analysis. Univariate Cox regression model was used to evaluate the relationship between the expression of mRNA and the prognosis of patients with GBM. We established a risk score model that consisted of six mRNA (AACS, STEAP1, STEAP2, G6PC3, FKBP9, and LOXL1) by the LASSO regression method. The six-mRNA signature could divide patients into a high-risk and a low-risk group with significantly different survival rates in training and test sets. Multivariate Cox regression analysis confirmed that it was an independent prognostic factor in GBM patients, and it has a superior predictive power as compared with age, IDH mutation status, MGMT, and G-CIMP methylation status. By combining this signature and clinical risk factors, a nomogram can be established to predict 1-, 2-, and 3-year OS in GBM patients with relatively high accuracy.

Keywords: glioblastoma multiforme, six-mRNA signature, LASSO, prognosis, biomarkers

OPEN ACCESS

Edited by:
Dianwen Song,
Shanghai First People's Hospital, China

Reviewed by:
Zhouxiao Li,
Ludwig Maximilian University of Munich, Germany
Linhua Sun,
Peking University, China

****Correspondence:***
Chunhui Wang
wanghi628@163.com
Lei Jiang
jl13jan@126.com

† These authors have contributed equally to this work

Specialty section:
This article was submitted to RNA, a section of the journal Frontiers in Genetics

Received: *27 November 2020*
Accepted: *08 February 2021*
Published: *11 March 2021*

Citation:
Liu Z, Zhang H, Hu H, Cai Z, Lu C, Liang Q, Qian J, Wang C and Jiang L (2021) A Novel Six-mRNA Signature Predicts Survival of Patients With Glioblastoma Multiforme. Front. Genet. 12:634116. doi: 10.3389/fgene.2021.634116

BACKGROUND

Glioblastoma, also known as glioblastoma multiforme (GBM), is the most common primary malignant cancer involving the central nervous system (CNS), characterized by aggressive invasiveness and an infiltrative growth pattern (Lapointe et al., 2018; Lee et al., 2018). According to the Central Brain Tumor Registry of the United States (CBTRUS), GBM accounts for 14.9% of all primary brain tumors and 55.4% of all gliomas (Alexander and Cloughesy, 2017). Current standard treatment for GBM patients comprises maximal safe surgical resection, concurrent

Abbreviations: GBM, Glioblastoma multiforme; OS, Overall survival; L1-LASSO, Least absolute shrinkage and selection operator; TCGA, The Cancer Genome Atlas; GEO, Gene Expression Omnibus; ROC, Receiver operating characteristic; AUC, Area Under Curve; KPS, Karnofsky; WT, wild type; MT, mutant type; IDH1, isocitrate dehydrogenase 1; MGMT, O6-methylguanine DNA-methyltransferase; CIMP, CpG Island Methylator Phenotype.

chemo-radiotherapy, and adjuvant chemotherapy with temozolomide (TMZ) (Laug et al., 2018). Despite recent advances in multi-modality strategies and individualized therapies, GBM patients usually have a dismal prognosis, with a median overall survival (OS) of less than 15 months (Lapointe et al., 2018).

The 2007 World Health Organization (WHO) classification system has been used for glioma classification over the past decade (Fuller and Scheithauer, 2007). This histological classification and grading system was largely based on visual criteria alone and fails to accurately evaluate the clinical outcomes of GBM patients. Actually, GBM patients with indistinguishable histopathological features can have different clinical outcomes. Accordingly, numerous efforts have been undertaken to characterize the underlying pathological molecular mechanisms and identify reliable prognostic markers for a precise prediction in GBM patients. More recently, some biomarkers including loss of 1p19q chromosome, methylation of the O6-methylguanine DNA-methyltransferase (MGMT), and iso-citrate dehydrogenases 1/2 (IDH1/2) have been found to be closely related to the therapy sensitivity and prognosis (Smits and van den Bent, 2017; Feyissa et al., 2019; Radke et al., 2019). MGMT promoter region was recognized to have a predictive value for the efficacy of TMZ-based chemotherapy, and mutations in the genes encoding for iso-citrate dehydrogenases 1/2 (IDH1/2) could predict a relatively long-term survival of GBM patients (Feyissa et al., 2019; Radke et al., 2019). In the 2016 updated version of the WHO classification system, molecular information has been integrated into pathological diagnosis for further subgroup stratification (Louis et al., 2016). However, due to the biological heterogeneity of GBM, individual biomarkers alone are unable to predict the therapy sensitivity and survival of GBM patients. In this regard, there is an urgent need to identify more effective tumor biomarkers for risk stratification and prognosis prediction.

RNA sequencing (RNA-Seq) is the most commonly used high-throughput technology for transcriptome profiling and offers more sensitive and accurate measurement of gene expression as compared with traditional gene expression arrays (Wang et al., 2009). The Cancer Genome Atlas (TCGA) has accrued RNA-Seq-based transcriptome data across various cancer types and thus provides a robust platform to systematically analyze the large-scale RNA-Seq data (Peng et al., 2015). A comprehensive characterization of gene expression changes in GBM will provide a large number of new potential predictive and prognostic molecular markers. In this study, we retrieved mRNA expression profiles from a large number of GBM patients and analyzed them by re-purposing the publicly available TCGA database to identify an effective signature of mRNAs for predicting survival of GBM patients.

METHODS

TCGA GBM and GSE108474 Datasets Download and Processing

The TCGA GBM data (Level 3 RNA-Seq) of 174 individuals with clinical information were extracted from the TCGA (GDC) database, including data from 169 GBM tissues and 5 normal brain tissues. The exclusion criteria are as follows: (1) GBM was ruled out by histological diagnosis, (2) the existence of another malignancy with GBM, and (3) patient death due to unrelated causes. Only patients who were followed up for longer than a month were included in the subsequent analysis. Finally, 152 GBM patients were included in this study. Seventy percent of the TCGA patients were randomly selected as the training set and the remaining 30% of the patients were selected as the test set. As the data were downloaded from the public database, ethical approval was not applicable in this case. The data processing procedures met the policies of TCGA data access and human subject protection[1]. GSE108474 from the GEO database was conducted through GPL (Affymetrix Human Genome U133 Plus 2.0 Array)[2]. A total of 210 GBM samples were selected from the GSE108474 database. The GEO data were also downloaded from the public database platform. Count data from the TCGA set and GSE108474 set were integrated into expression matrix, which were converted to TPM and standardized to Z score data for subsequent model analysis.

Identification of Differentially Expressed mRNAs in GBM

Three bioconductor software analysis packages—Deseq2, limma + voom, and edgerR—are used to analyze the difference of mRNA expression read count data. The expression differences were characterized by logFC (log2 fold change). mRNAs with $|\text{logFC}| > 1$ ($P < 0.05$) were considered differentially expressed mRNAs and selected for further analysis.

Identification of mRNAs Significantly Associated With OS and Prognostic Signature Construction in GBM

The semi-supervised method combining both the gene expression data and clinical data was used to identify candidate mRNAs with a prognostic value. Univariate Cox regression analysis was conducted to identify common mRNAs related to OS within each of the subgroups stratified by the IDH status. Within each group of clinical characteristics, the patient subclasses represented non-overlapping sets. Common mRNAs associated with OS in at least two independent subgroups were selected for the subsequent study, using an HR > 1 or HR < 1 with $P < 0.05$ as the cutoff.

Definition of the Prognostic Risk Model and ROC Curve Analysis

The TCGA dataset "caret" package was randomly divided into a training set and a testing set. An importance score was calculated by the supervised principal component method and assigned to each mRNA. Tenfold cross-validation was used to estimate the optimal feature threshold in supervised principal components and select significant mRNAs. The linear mRNA signature prognostic model was developed based on the supervised principal component method. The mRNA expression

[1]http://cancergenome.nih.gov/publications/publicationguidelines

[2]https://www.ncbi.nlm.nih.gov/geo/

level was expressed as the Z score. The prognostic score was calculated as follows: Prognostic score = (0.058 × Expression AACS) + (0.015 × Expression STEAP1) + (0.009 × Expression STEAP2) + (0.039 × Expression G6PC3) + (0.014 × Expression FKBP9) + (0.067 × Expression LOXL1). Then, the prognostic scores were computed for the 152 patients using our mRNAs prognostic model. The optimal cutoff value of the prognostic score was decided in the ROC (receiver operating characteristic) curve analysis for predicting 1-, 2-, and 3-year survival of the training set. The OS curves were evaluated using the Kaplan–Meier (KM) and log-rank method. Time-dependent ROC curves were used to evaluate the predictive power of the mRNA signature model. All analyses were performed using the R (version 3.5.2) and Bioconductor (version 3.9).

Survival Analysis

The differences in clinical features including sex, age, IDH1, MGMT, and the survival status between the training set, internal testing set, and independent validation set were analyzed using the chi-square test. A univariate Cox model was performed to investigate the relationship between the continuous expression level of each DEmRNA and OS and for preliminary screening of clinical variables that were correlated with OS of the GBM patients. Hazard ratios (HRs) and P-values from univariate Cox regression analysis were used to identify candidate survival-related DEmRNAs. DEmRNAs with HR for death > 1 were defined as high-risk RNAs, and those with HR < 1 were defined as protective RNAs. The common DEmRNAs meeting the criterion of P-value < 0.05 were selected as survival-related DEmRNAs and further analyzed in LASSO regression to identity the most powerful prognostic markers. Finally, a multi-mRNA-based classifier was constructed for predicting OS. To quantify the risk of OS, a standard form of risk score (RS) for each GBM patient was calculated in combination with the relative expression levels of the mRNAs.

Statistical Analysis

Mann–Whitney U-test and χ^2-test were used to compare the correlation between continuous variables and classified variables between the training data and test data, respectively. The independent prognostic variables of OS were screened by univariate and multivariate regression analyses. L1-LASSO penalization was carried out using "glmnet" and "pliable" software packages. KM method was used to draw the survival curve based on survminer software package, and log-rank test was used to compare it. Using "rms" software package, Cox's regression coefficient was calculated to establish the risk assessment formula and mRNA nomogram. Knowing that time-dependent ROC curve analysis is widely used in biomedical reports to evaluate the prediction accuracy of six mRNA signatures, we used the "timeROC" software package to analyze the time-dependent ROC curve. The volcanoes and heat maps were drawn by using the "ggpolt2" software package of the R software. All other statistical tests were carried out with R software version 3.5.2 and the corresponding basic software packages. The value of $P < 0.05$ was determined to be statistically significant.

RESULTS

Baseline Characteristics of the Patients and Analysis Flow

Included in this study were 152 GBM patients from TCGA database and 210 GBM patients from the GEO database (GSE108474). The detailed baseline characteristics of the training set and test set are listed in **Table 1** from the TCGA database. The results showed no significant difference in the baseline characteristics between the two sets (all $P > 0.05$). A total of 210 GBM patients from the GEO database make up an independent validation set. Our research process is shown in **Figure 1**.

Candidate OS-Related mRNAs of GBM Patients in the TCGA Cohort

In the TCGA database, 5754 differentially expressed mRNAs [false detection rate < 0.05 and log2 fold change (Log2fc) ≥ 1] were identified by using the expression profiles of 19,781 mRNAs in 152 cases of GBM and 5 cases of normal brain tissues. These 5754 mRNA volcanoes were visualized through the "ggplot2" package of R software (**Figures 2A–C**). These 5754 differentially expressed mRNAs were considered to be the potential prognostic markers of GBM patients, in which the expression of 3054 mRNAs was up-regulated and that of 2700 mRNAs was down-regulated. To filtrate out the mRNAs associated with OS, the Cox's regression and LASSO regression analyses (lambda parameter selection 1SE) were performed in sequence (**Figures 2D,E**). Finally, six mRNAs related to OS were selected, including AACS, STEAP1, STEAP2, G6PC3, FKBP9, and LOXL1 (**Table 2**).

Development of the Risk Score Formula and Six-mRNA-Based Prognostic Model

To facilitate the application of identified OS-related mRNAs in clinical practice, the risk score of each patient was calculated using the following equation: Risk score = (0.058 × Expression AACS) + (0.015 × Expression STEAP1) + (0.009 × Expression STEAP2) + (0.039 × Expression G6PC3) + (0.014 × Expression FKBP9) + (0.067 × Expression LOXL1). According to the risk score, Youden index (Hughes, 2015) was set to the cutoff value, based on which GBM patients were categorized into a low-risk group and a high-risk group (**Figure 3A**). The survival status of GBM patients in the low- and high-risk groups was obvious in both cohorts (**Figure 3B**). The heat map showed the expression of six mRNAs (AACS, STEAP1, STEAP2, G6PC3, FKBP9, and LOXL1) in the samples (**Figure 3C**). In addition, compared with the low-risk group, KM survival analysis showed that the prognosis of GBM patients in the high-risk group was significantly worse than that in the low-risk group (training and test set in TCGA database $P < 0.00011$, validation set of GEO database $P < 0.0001$) (**Figures 4A,B**). To evaluate the prognostic prediction performance of GBM patients based on the six-mRNA signature model, we compared the AUC values at different time points to draw the survival ROC curve. The AUC value of the primary set and the validation set at 1, 2, and 3 years was

TABLE 1 | Baseline characteristic of study patients.

Variables	Training date	Test date	Overall	*P*-value
No. of patients	107	45	152	
Age (years), *N* (%)				1
Mean (SD)	59.2 (13.4)	59.8 (13.4)	59.6 (13.3)	
Median [Min, Max]	59.0 [21.0, 79.0]	62.0 [21.0, 85.0]	60.0 [21.0, 85.0]	
Age (years), *N* (%)				0.668
< 50	11 (24.4%)	22 (20.6%)	33 (21.7%)	
≥ 50	34 (75.6%)	85 (79.4%)	119 (78.3%)	
Sex, *N* (%)				0.143
Female	20 (44.4%)	34 (31.8%)	54 (35.5%)	
Male	25 (55.6%)	73 (68.2%)	98 (64.5%)	
KPS type, *N* (%)				
<70	9 (20.0%)	23 (21.5%)	32 (21.1%)	0.921
≥70	26 (57.8%)	58 (54.2%)	84 (55.3%)	
Unknown	10 (22.2%)	26 (24.3%)	36 (23.7%)	
IDH1 type, *N* (%)				0.486
MT	2 (4.4%)	7 (6.5%)	9 (5.9%)	
WT	40 (88.9%)	97 (90.7%)	137 (90.1%)	
Unknown	3 (6.7%)	3 (2.8%)	6 (3.9%)	
CIMP type, *N* (%)				0.787
G-CIMP	3 (6.7%)	6 (5.6%)	9 (5.9%)	
Non-G-CIMP	41 (91.1%)	100 (93.5%)	141 (92.8%)	
Unknown	1 (2.2%)	1 (0.9%)	2 (1.3%)	
MGMT type, *N* (%)				0.864
Methylated	18 (40.0%)	38 (35.5%)	56 (36.8%)	
Unmethylated	18 (40.0%)	45 (42.1%)	63 (41.4%)	
Unknown	9 (20.0%)	24 (22.4%)	33 (21.7%)	
Race type, *N* (%)				0.448
Black or African. American	3 (6.7%)	6 (5.6%)	9 (5.9%)	
White	42 (93.3%)	95 (88.8%)	137 (90.1%)	
Asian	0 (0%)	5 (4.7%)	5 (3.3%)	
Unknown	0 (0%)	1 (0.9%)	1 (0.7%)	
Status, *N* (%)				0.825
Alive	9 (20.0%)	20 (18.7%)	29 (19.1%)	
Dead	36 (80.0%)	87 (81.3%)	123 (80.9%)	
OS time				0.883
Mean (SD)	461 (427)	439 (364)	445 (382)	
Median [Min, Max]	394 [64.0, 2680]	382 [33.0, 2130]	383 [33.0, 2680]	

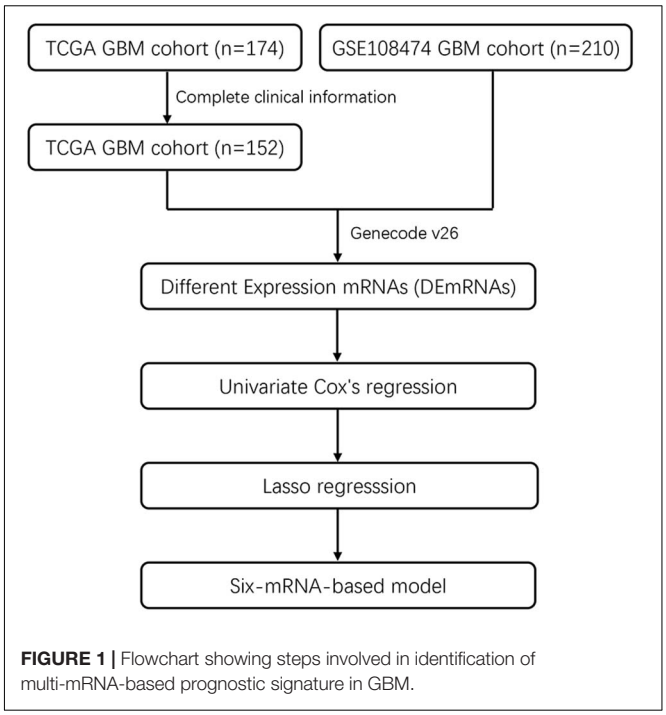

FIGURE 1 | Flowchart showing steps involved in identification of multi-mRNA-based prognostic signature in GBM.

0.660, 0.668, and 0.674, and 0.680, 0.741, and 0.743, respectively (**Figures 4C,D**).

To analyze risk factors affecting the prognosis of GBM patients, univariate Cox's analysis was performed and the result showed that the prognosis of GBM patients was associated with age, IDH1 mutation, MGMT methylation, CIMP methylation, and the six-mRNA signature, but not with gender and KPS (Karnofsky) score. Subsequent multivariate analysis showed that the six-mRNA signature was an independent prognostic survival factor in GBM patients (**Table 3**).

Predictive Ability of the Six-mRNA-Based Model in Different Risk Stratification

To show whether the six-mRNA-based model could predict the OS time of patients, clinical risk factors including age, KPS score, IDH1 mutation status, MGMT methylation status, and CIMP methylation status in GBM patients were stratified. In patients with age ≧ 50 years ($P = 0.006$), age < 50 years ($P = 0.013$), MGMT methylated ($P < 0.005$), KPS ≧ 70 ($P < 0.005$), CIMP unmethylated ($P < 0.005$), and IDH1 WT ($P = 0.015$), OS of GBM patients in the low-risk group was significantly better than that in the high-risk group. However, in patients with KPS < 70 ($P = 0.088$) and MGMT unmethylated ($P = 0139$), there was no significant difference in OS between the low-risk and high-risk groups (**Figures 5A–H**).

To build a convenient and sensitive predictive tool for clinical use, a new prognostic model based on the six-mRNA model was established by combining signature and four clinical risk factors (age, IDH1 status, MGMT status, and CIMP status) to predict 1-, 2-, and 3-years OS in GBM patients. The results showed that the six-mRNA signature and MGMT methylated status contributed most to OS in 1, 2, and 3 years, followed by the CIMP methylated status, patient age, and the IDH1 mutation status in six-mRNA-based nomograms. Each variable obtained a nomogram score on the point scale. By calculating the total score of the nomogram, we easily obtained the nomogram prediction probability of each patient for 1-, 2-, and 3-years OS (**Figure 6**).

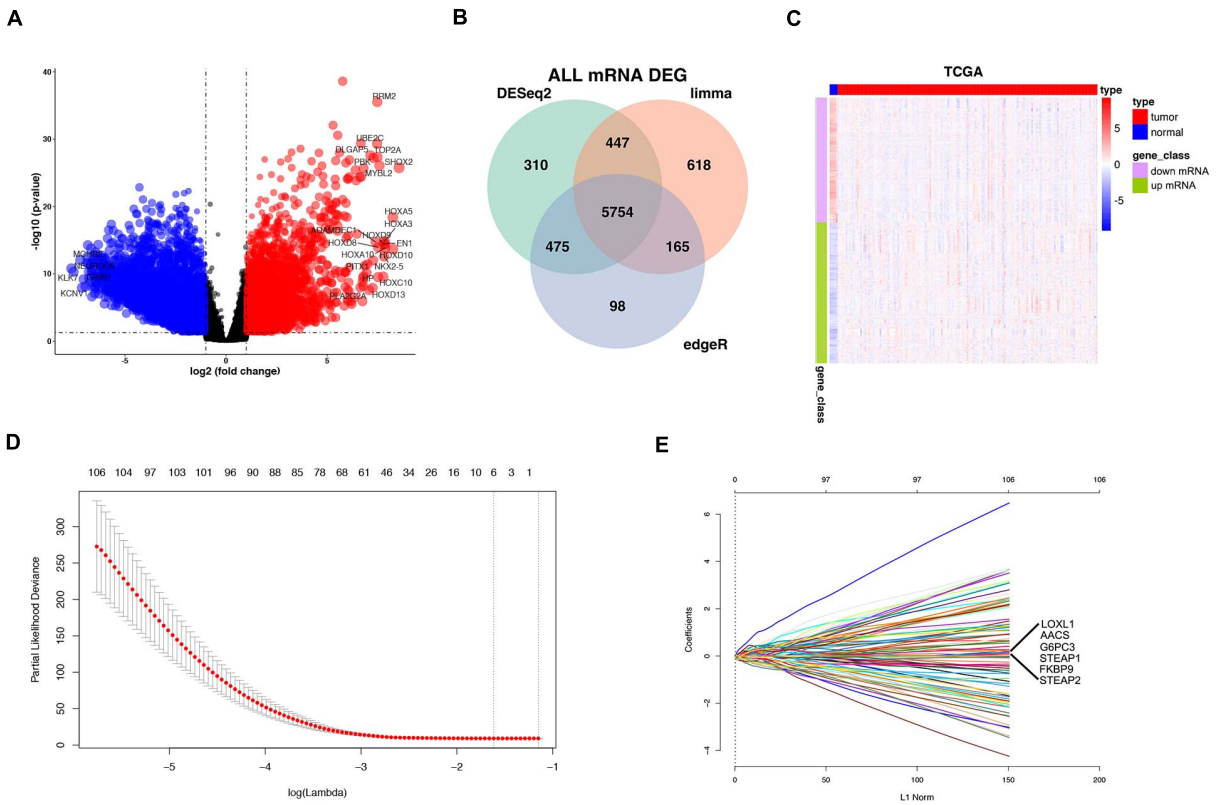

FIGURE 2 | Differentially expressed mRNAs (DEmRNAs) in GBM vs. normal tissues. Volcano Plot: The colorized points in scatter plot represent the DEmRNAs with statistical significance (*P*-value < 0.05, |logFC| > 1) **(A)**. Venn Plot visualizing the DEmRNAs which was screened by limma Deseq2 and edgeR **(B)**. Two-way hierarchical clustering of 152 tumor tissues and 5 normal tissues with the 2114 differentially expressed RNAs using Euclidean distance and average linkage clustering **(C)**. mRNA selection using the least absolute shrinkage and selection operator (LASSO) binary COX regression model. Tuning parameter (λ) selection in the LASSO model **(D)**. LASSO coefficient profiles **(E)**.

Comparison With Other Prognostic Factors

To compare the predictive accuracy of different prognostic factors, ROC analysis showed that the six-miRNA signature had higher prognostic accuracy than mRNA alone (**Figures 7A–C**). More importantly, the accuracy of six-mRNA signature prediction was also significantly better than that of clinical risk factors such as age, IDH1 mutation status, MGMT methylation, and G-CIMP methylation status (**Figure 7D**).

TABLE 2 | Six prognostic mRNAs associated with OS in the training set.

Name	Coefficient	Type	Down/up-regulated	HR	95% CI	*P*-value
AACS	0.058	Risky	Down	1.132	1.028–1.126	0.011*
STEAP1	0.015	Risky	Up	1.012	1.003–1.021	0.012*
STEAP2	0.009	Risky	Down	1.08	1.035–1.126	<0.001*
G6PC3	0.039	Risky	Up	1.012	1.005–1.019	<0.001*
FKBP9	0.014	Risky	Up	1.003	1.001–1.005	0.004*
LOXL1	0.067	Risky	Up	1.009	1.004–1.013	<0.001*

**P < 0.05 was considered statistically significant.*

DISCUSSION

Transcriptional aberrations play a crucial role in the complex regulatory network of glioblastoma and are of great importance for the prognosis of this deadly cancer (Bian et al., 2018). Previous studies mainly focused on the function of individual differently expressed mRNAs, which may not be sufficient to clarify the underlying mechanism of tumorigenesis and predict the prognosis of GBM patients (Stoltz et al., 2015; Hu et al., 2017; Yu et al., 2017). Given the high molecular heterogeneity of GBM, integrating multiple biomarkers into a prediction model could improve the prognostic value as compared with a single biomarker. Such multiple-gene signature can be used in prognosis prediction and personalized therapy due to its great power and superiority of risk stratification in many cancers including GBM (Lai et al., 2019; Zuo et al., 2019). Based on this gene signature, patients can be divided into different risk groups so that more sophisticated or intensive targeted therapies could be selected accordingly.

Currently, many prognostic studies have sought to find GBM-specific genomic signatures based on massive genomic data generated by the large-scale cancer genomics projects such as the TCGA database. Yao et al. (2012) have introduced

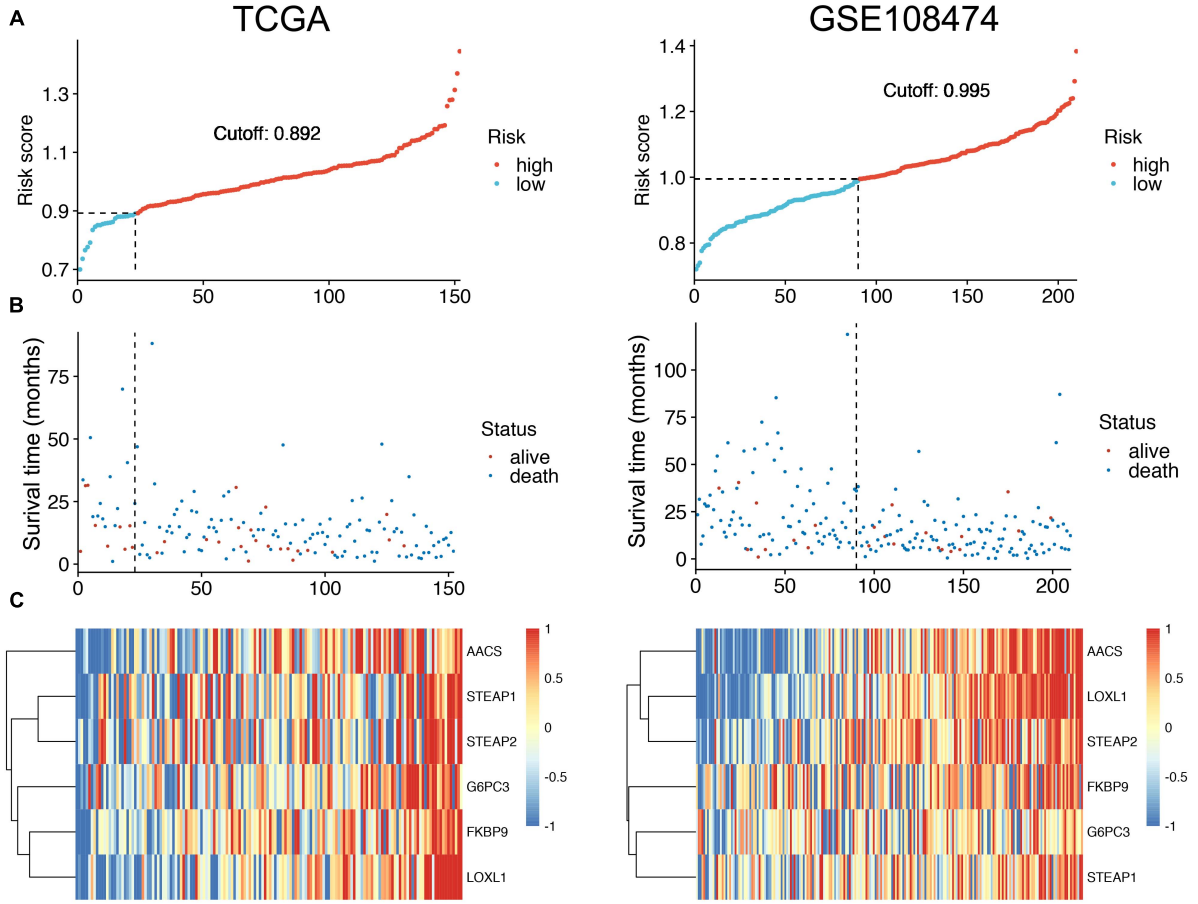

FIGURE 3 | The distribution of risk scores **(A)**. Patient survival time and status. The black dotted line represents the optimum cutoff dividing patients into low-risk and high-risk groups **(B)**. The expression heat map of the mRNAs in a prognostic classifier **(C)**.

an algorithm using Cox proportional hazard regression and random re-sampling to identify functional gene sets linked to patient survival based on microarray gene expression datasets (TCGA and REMBRANDT). Another study conducted by Jing et al. (Han and Puri, 2018) found that the expression of interleukin-13 receptor α1 and α2 genes was associated with poor prognosis in GBM patients by using TCGA data. In addition, Wang et al. (2016) developed a signature with three genes that had prognostic values for patients with MGMT promoter-methylated GBM. However, it should be noted that the predictive power might be limited by the small number of individual mRNAs or specific tumor entities in these studies. Recently, Zuo et al. (2019) built an RNA-Seq-based six-gene signature to predict survival in patients with GBM by analyzing RNA-Seq-based gene expression profiles in the CGGA and TCGA databases. They found that this signature could divide patients into a high-risk or low-risk group with different OS and was independent of other clinicopathological features. However, the mRNAs in Zuo's six-gene signature were not all screened from differentially expressed genes in glioma and normal brain tissues, which may limit its significance in revealing tumor heterogeneity. For this reason, we screened the differentially expressed genes by Cox proportional hazard regression in the present study and only chose GBM survival-related PCGs for further analysis in LASSO regression. Consequently, a six-gene signature was generated using gene expression data from two public databases and was validated in two cohorts of patients.

Various factors may affect the survival of GBM patients, including age, KPS score, extent of surgical removal, MGMT methylated, and the IDH1 mutation status. Our univariate analysis of the TCGA cohort showed that age, IDH1 mutation, MGMT methylated, and CIMP methylated were significantly associated with OS of GBM patients, which is consistent with numerous previous studies (Hegi et al., 2008; Cohen et al., 2013; de Souza et al., 2018). In our study, in GBM patients with age ≧50 years (P = 0.006), age <50 years (P = 0.013), MGMT methylated (P < 0.005), KPS ≧ 70 (P < 0.005), CIMP unmethylated (P < 0.005), and IDH1 WT (P = 0.015), OS of patients in the low-risk group was significantly better than that in the high-risk group. Furthermore, our subsequent multivariate analysis confirmed that this six-gene signature was an independent prognostic predictor of survival for GBM patients.

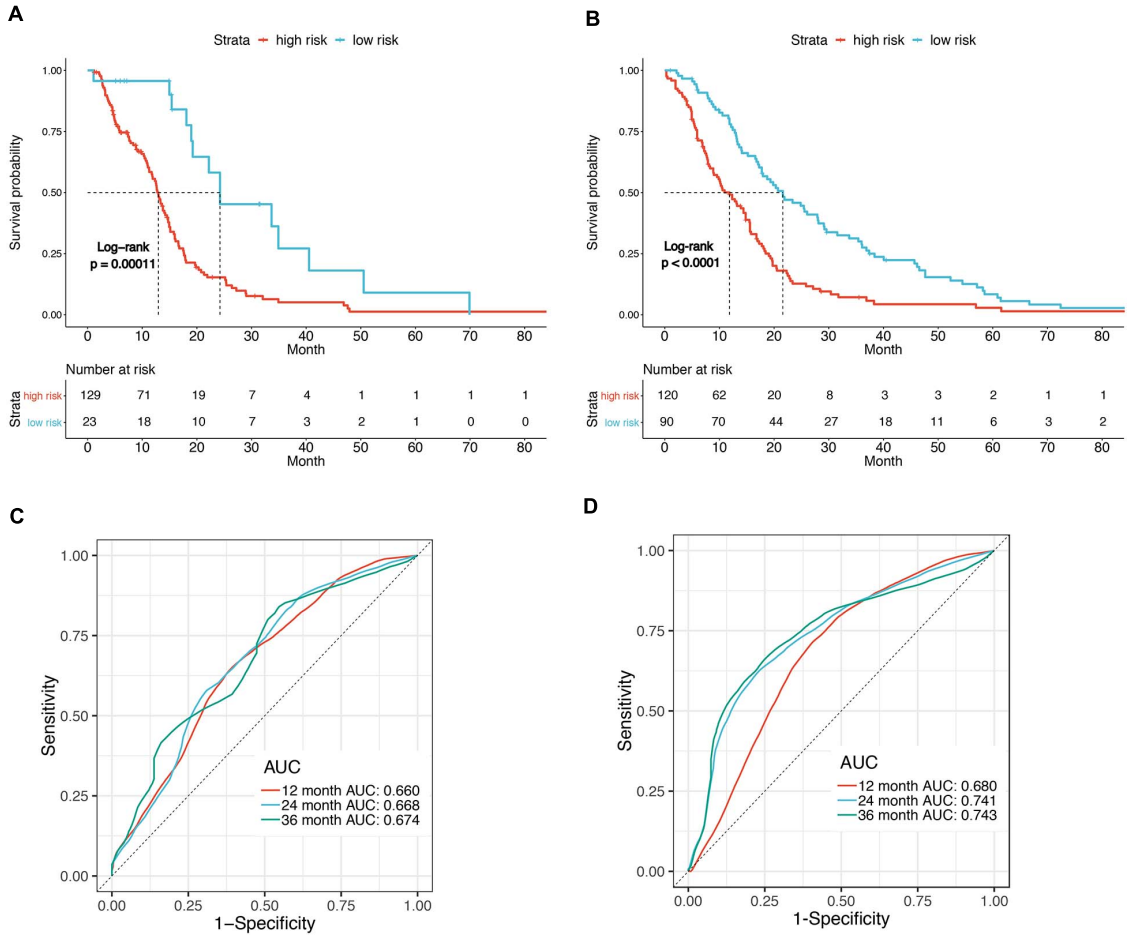

FIGURE 4 | Survival analysis of the patients divided by prognostic mRNA in high and low risk. Kaplan–Meier curves of overall survival in TCGA **(A)** and GSE108474 **(B)** datasets showed poor survival for patients with a high-risk score. ROC curve for 1, 2, and 3 year survival prediction by the six-gene signature in TCGA **(C)** and GSE108474 **(D)** datasets.

TABLE 3 | Univariate and multivariate Cox's regression analyses in the training set.

Variables		Patients (*N*)	Coefficient	Univariate analysis			Multivariate analysis		
				HR	95% CI	*P*-value	HR	95% CI	*P*-value
Age	≥50/<50	119/33	0.579	1.784	1.13–2.818	0.013*	1.143	0.692–5.563	0.601
Gender	Female/Man	54/98	0.062	1.064	0.732–1.547	0.745			
KPS	≥70/<70	108/44	−0.084	0.915	0.611–1.368	0.663			
IDH1	Unknown/Mut	6/9	0.217	1.242	0.176–8.758	0.828			
	WT/Mut	137/9	1.176	3.242	1.317–7.979	0.011*	1.324	0.234–7.493	0.751
MGMT	Methylated/Unknown	33/63	−0.306	0.736	0.458–1.182	0.205			
	Methylated/Unmethylated	56/63	−0.474	0.622	0.408–0.949	0.028*	0.681	0.444–1.045	0.079
CIMP	Unknown/non-G-CIMP	2/141	−17.360	0.000	0–inf	0.995			
	G-CIMP/non-G-CIMP	9/141	−1.196	0.303	0.111–0.822	0.019*	0.835	0.138–5.031	0.844
Six-mRNA signature	High/Low	129/23	1.048	2.850	1.621–5.02	0.00028*	2.901	1.513–5.563	0.001*

**P < 0.05 was considered statistically significant.*

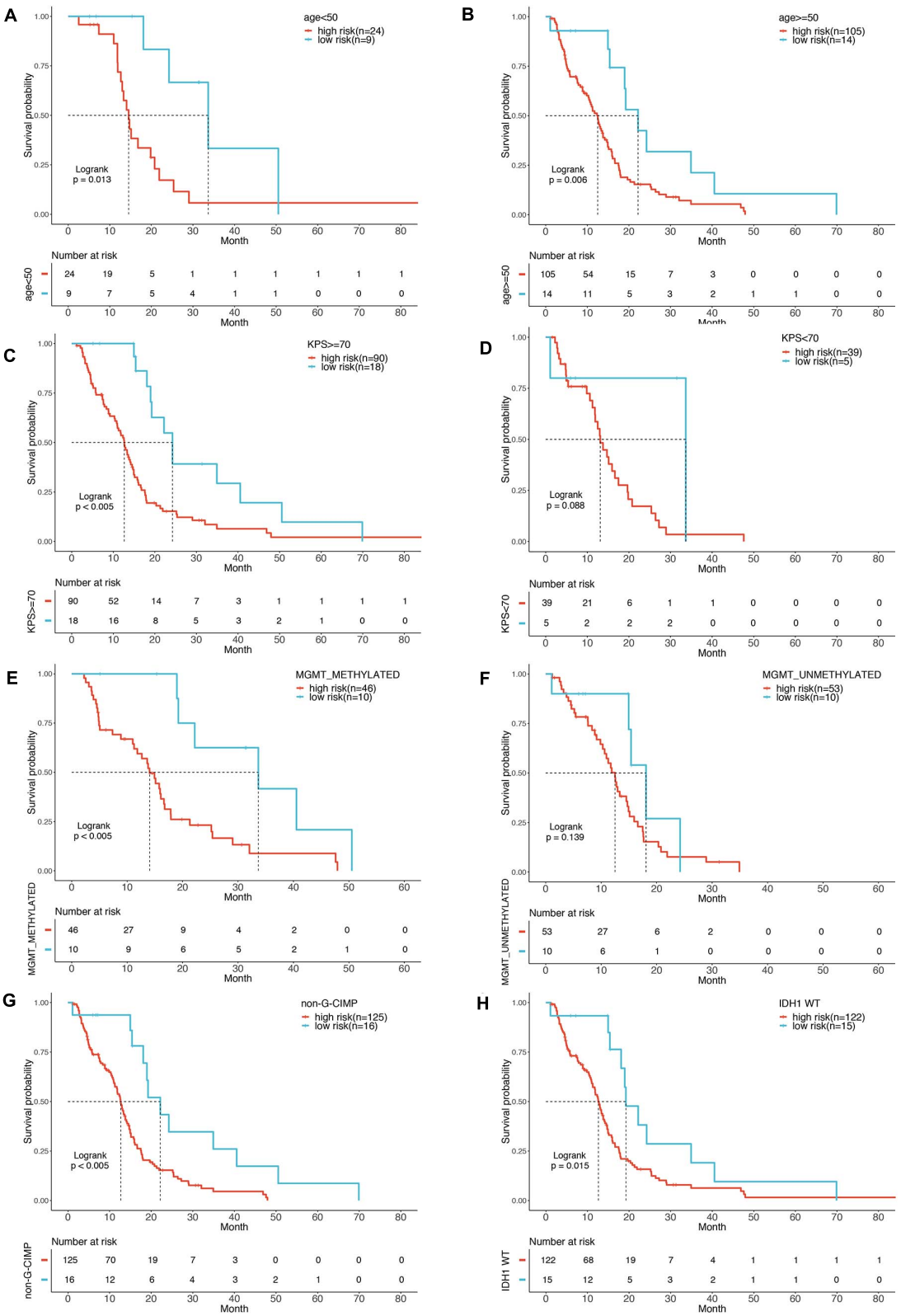

FIGURE 5 | Stratification analysis by different clinical variables. Meier curve analysis of overall survival in high- and low-risk group for younger (age < 50) **(A)** and older patients (age ≥ 50) **(B)**. KPS ≥ 70 **(C)**, and < 70 **(D)**. MGMT methylated status as methylated **(E)** and unmethylated **(F)**. G-CIMP methylated **(G)**. IDH1 mutation status as WT **(H)**.

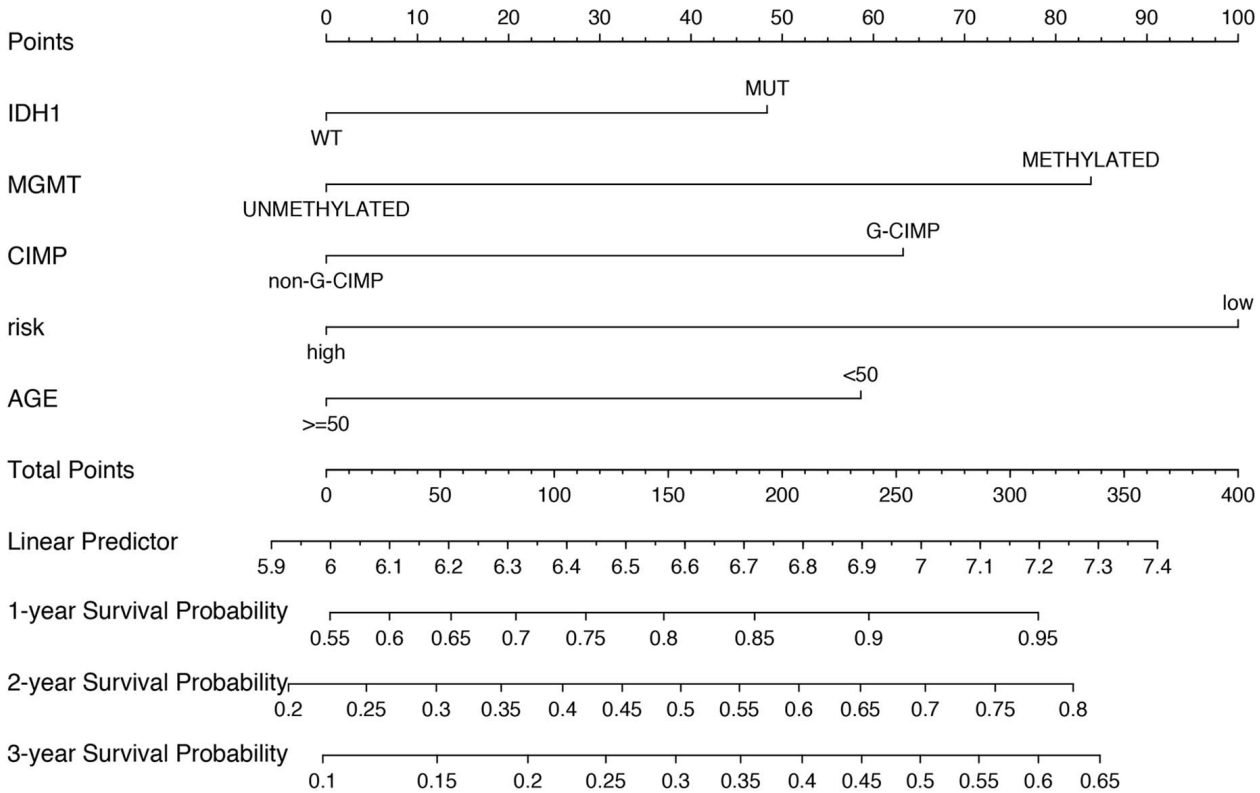

FIGURE 6 | Nomograms to predict 1, 2, and 3 year survival probability in GBM. Total points were obtained by adding up the corresponding points of each individual covariate on the points scale.

The six-mRNA signature identified in this study includes four up-regulated mRNAs (STEAP1, G6PC3, FKBP9, and LOXL1) and two down-regulated mRNAs (STEAP2 and AACS) with respect to their expression levels in GBM tissue samples. Among these genes, a few genes have established roles in cancers, and other genes might be potential new biomarkers for cancers. STEAP1 and STEAP2, the members of the human six-transmembrane epithelial antigen of the prostate (STEAP) protein family, are highly over-expressed in many different cancer entities including prostate, bladder, breast, colon, and lung carcinoma, Ewing's sarcoma, anaplastic thyroid carcinoma, and malignant melanoma (Hubert et al., 1999; Valenti et al., 2009; Gomes et al., 2012). The high rate of co-expression of STEAP1 and 2 has been observed in cancer cell lines. However, the functional role of STEAP1 and STEAP2 in glioma has not yet been established. Acetoacetyl-CoA synthetase (AACS, acetoacetate-CoA ligase) plays an important role in cholesterol homeostasis and normal neuronal development and was found abundant in normal brain tissues (Ohgami et al., 2003). Knockdown of AACS in primary neurons decreased the expression of MAP-2 and NeuN, two known markers of neuronal differentiation (Hasegawa et al., 2012). G6PC3 is known to encode enzymes that have glucose-6-phosphatase activity, which is ubiquitously expressed in various tissues (Hayee et al., 2011). TP53 can reduce gluconeogenesis by down-regulating the expression of G6PC gene in colon and liver cancer cells and *in vivo*, thus implying an important regulatory relationship between TP53 and G6PC gene (Zhang et al., 2014). FKBP9 belongs to the FK506-binding protein (FKBP) family, which has peptidyl–prolyl cis–trans isomerases with the enzymatic function attributable to the FKBP domain (Jo et al., 2001). LOXL1, like other Lysyl oxidase (LOX) family members, has an established role in modifying the tumor microenvironment by crosslinking collagens and elastin in the extracellular matrix (Behmoaras et al., 2008). Increased LOXL1 was found in pancreatic ductal adenocarcinoma (Le Calve et al., 2016). In addition, the expression of LOXL1 was found to be correlated with T invasion, lymph node metastasis, and lymphatic and venous invasion in gastric cancer (Kasashima et al., 2014).

In adopting the prediction model of this study, the following limitations need to be considered. First of all, the biological functions and molecular mechanisms of the six mRNAs in the prediction model in glioma remain unclear and further researches are needed. Second, clinical data of postoperative intervention measures for GBM patients in TCGA and GEO databases are incomplete, such as radiotherapy and chemotherapy, so we cannot conduct a comprehensive analysis of OS. Third, the prediction model cannot effectively predict the patient OS with KPS <70 and MGMT demethylation between the low- and high-risk

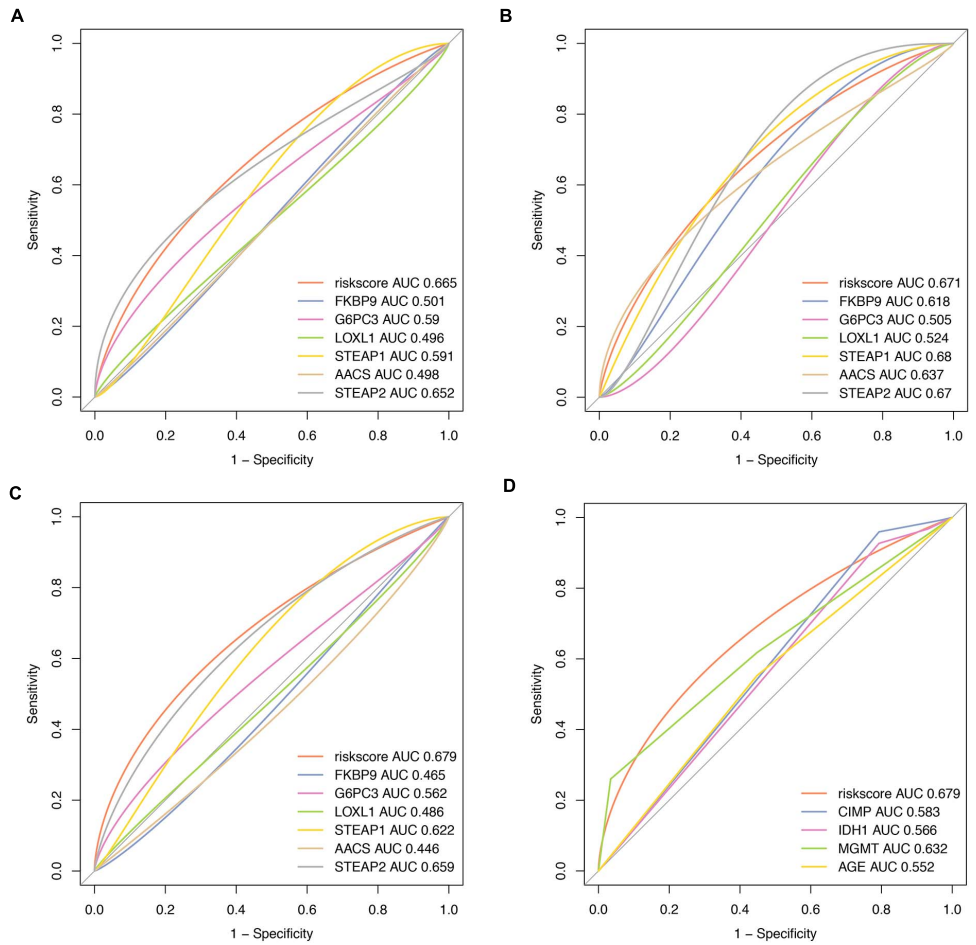

FIGURE 7 | Comparisons of prognostic accuracy at 1 year using the time-dependent receiver operating characteristic curve in the six-mRNA signature with a single mRNA from training date **(A)**, test date **(B)**, TCGA date **(C)** separately, and the six-mRNA-based prognostic model with age, IDH1 status, MGMT methylated status, and G-CIMP methylation in GBM **(D)**.

group. Therefore, multi-center, large-scale, prospective studies are needed to validate the predictive model in clinical practice.

CONCLUSION

In this study, we have identified a six-gene signature for predicting survival of GBM patients by analyzing RNA-Seq gene expression profiles in the TCGA and GEO databases. This multiple-RNA-based signature could effectively stratify GBM patients into low- and high-risk groups with separate survival curves. Our multivariate analysis demonstrated that this six-gene signature is an independent prognostic predictor of survival of GBM patients. To the best of our knowledge, this is the first report about the prognostic value of the six RNAs (STEAP1, G6PC3, FKBP9, STEAP2, AACS, and LOXL1) in GBM, which may serve as new genetic clues for a better understanding about the development, progression, and recurrence of GBM.

DATA AVAILABILITY STATEMENT

Publicly available datasets were analyzed in this study. This data can be found here: http://gepia.cancer-pku.cnGSE108474.

AUTHOR CONTRIBUTIONS

ZL, HZ, and HH analyzed the data and wrote the manuscript. ZC and CL designed the study and performed data. QL and JQ prepared the figures and tables. All authors read and approved the final manuscript.

FUNDING

This work was supported by the National Natural Science Foundation of China (Nos. 81270038 and 81802480), the Shanghai Natural Science Foundation (Nos. 19ZR144890 and 20ZR1457400), and the Scientific Research Initial Funding of Shanghai Tongji Hospital (No. RCQD1704).

REFERENCES

Alexander, B. M., and Cloughesy, T. F. (2017). Adult glioblastoma. *J. Clin. Oncol.* 35, 2402–2409.

Behmoaras, J., Slove, S., Seve, S., Vranckx, R., Sommer, P., and Jacob, M. P. (2008). Differential expression of lysyl oxidases LOXL1 and LOX during growth and aging suggests specific roles in elastin and collagen fiber remodeling in rat aorta. *Rejuvenation Res.* 11, 883–889. doi: 10.1089/rej.2008.0760

Bian, S., Repic, M., Guo, Z., Kavirayani, A., Burkard, T., Bagley, J. A., et al. (2018). Genetically engineered cerebral organoids model brain tumor formation. *Nat. Methods* 15, 631–639. doi: 10.1038/s41592-018-0070-7

Cohen, A. L., Holmen, S. L., and Colman, H. (2013). IDH1 and IDH2 mutations in gliomas. *Curr. Neurol. Neurosci. Rep.* 13:345.

de Souza, C. F., Sabedot, T. S., Malta, T. M., Stetson, L., Morozova, O., Sokolov, A., et al. (2018). A distinct DNA methylation shift in a subset of glioma CpG island methylator phenotypes during tumor recurrence. *Cell Rep.* 23, 637–651. doi: 10.1016/j.celrep.2018.03.107

Feyissa, A. M., Worrell, G. A., Tatum, W. O., Chaichana, K. L., Jentoft, M. E., Guerrero Cazares, H., et al. (2019). Potential influence of IDH1 mutation and MGMT gene promoter methylation on glioma-related preoperative seizures and postoperative seizure control. *Seizure* 69, 283–289. doi: 10.1016/j.seizure.2019.05.018

Fuller, G. N., and Scheithauer, B. W. (2007). The 2007 revised World Health Organization (WHO) classification of tumours of the central nervous system: newly codified entities. *Brain Pathol.* 17, 304–307. doi: 10.1111/j.1750-3639.2007.00084.x

Gomes, I. M., Maia, C. J., and Santos, C. R. (2012). STEAP proteins: from structure to applications in cancer therapy. *Mol. Cancer Res.* 10, 573–587. doi: 10.1158/1541-7786.mcr-11-0281

Han, J., and Puri, R. K. (2018). Analysis of the cancer genome atlas (TCGA) database identifies an inverse relationship between interleukin-13 receptor alpha1 and alpha2 gene expression and poor prognosis and drug resistance in subjects with glioblastoma multiforme. *J. Neurooncol.* 136, 463–474. doi: 10.1007/s11060-017-2680-9

Hasegawa, S., Kume, H., Iinuma, S., Yamasaki, M., Takahashi, N., and Fukui, T. (2012). Acetoacetyl-CoA synthetase is essential for normal neuronal development. *Biochem. Biophys. Res. Commun.* 427, 398–403. doi: 10.1016/j.bbrc.2012.09.076

Hayee, B., Antonopoulos, A., Murphy, E. J., Rahman, F. Z., Sewell, G., Smith, B. N., et al. (2011). G6PC3 mutations are associated with a major defect of glycosylation: a novel mechanism for neutrophil dysfunction. *Glycobiology* 21, 914–924. doi: 10.1093/glycob/cwr023

Hegi, M. E., Liu, L., Herman, J. G., Stupp, R., Wick, W., Weller, M., et al. (2008). Correlation of O6-methylguanine methyltransferase (MGMT) promoter methylation with clinical outcomes in glioblastoma and clinical strategies to modulate MGMT activity. *J. Clin. Oncol.* 26, 4189–4199. doi: 10.1200/jco.2007.11.5964

Hu, X., Martinez-Ledesma, E., Zheng, S., Kim, H., Barthel, F., Jiang, T., et al. (2017). Multigene signature for predicting prognosis of patients with 1p19q co-deletion diffuse glioma. *Neuro Oncol.* 19, 786–795. doi: 10.1093/neuonc/now285

Hubert, R. S., Vivanco, I., Chen, E., Rastegar, S., Leong, K., Mitchell, S. C., et al. (1999). STEAP: a prostate-specific cell-surface antigen highly expressed in human prostate tumors. *Proc. Natl. Acad. Sci. U.S.A.* 96, 14523–14528. doi: 10.1073/pnas.96.25.14523

Hughes, G. (2015). Youden's index and the weight of evidence. *Methods Inf. Med.* 54, 198–199.

Jo, D., Lyu, M. S., Cho, E. G., Park, D., Kozak, C. A., and Kim, M. G. (2001). Identification and genetic mapping of the mouse Fkbp9 gene encoding a new member of FK506-binding protein family. *Mol. Cells* 12, 272–275.

Kasashima, H., Yashiro, M., Kinoshita, H., Fukuoka, T., Morisaki, T., Masuda, G., et al. (2014). Lysyl oxidase-like 2 (LOXL2) from stromal fibroblasts stimulates the progression of gastric cancer. *Cancer Lett.* 354, 438–446. doi: 10.1016/j.canlet.2014.08.014

Lai, J., Wang, H., Pan, Z., and Su, F. (2019). A novel six-microRNA-based model to improve prognosis prediction of breast cancer. *Aging (Albany NY)* 11, 649–662. doi: 10.18632/aging.101767

Lapointe, S., Perry, A., and Butowski, N. A. (2018). Primary brain tumours in adults. *Lancet* 392, 432–446. doi: 10.1016/s0140-6736(18)30990-5

Laug, D., Glasgow, S. M., and Deneen, B. (2018). A glial blueprint for gliomagenesis. *Nat. Rev. Neurosci.* 19, 393–403. doi: 10.1038/s41583-018-0014-3

Le Calve, B., Griveau, A., Vindrieux, D., Marechal, R., Wiel, C., Svrcek, M., et al. (2016). Lysyl oxidase family activity promotes resistance of pancreatic ductal adenocarcinoma to chemotherapy by limiting the intratumoral anticancer drug distribution. *Oncotarget* 7, 32100–32112. doi: 10.18632/oncotarget.8527

Lee, E., Yong, R. L., Paddison, P., and Zhu, J. (2018). Comparison of glioblastoma (GBM) molecular classification methods. *Semin. Cancer Biol.* 53, 201–211. doi: 10.1016/j.semcancer.2018.07.006

Louis, D. N., Perry, A., Reifenberger, G., von Deimling, A., Figarella-Branger, D., Cavenee, W. K., et al. (2016). The 2016 World Health Organization classification of tumors of the central nervous system: a summary. *Acta Neuropathol.* 131, 803–820. doi: 10.1007/s00401-016-1545-1

Ohgami, M., Takahashi, N., Yamasaki, M., and Fukui, T. (2003). Expression of acetoacetyl-CoA synthetase, a novel cytosolic ketone body-utilizing enzyme, in human brain. *Biochem. Pharmacol.* 65, 989–994. doi: 10.1016/s0006-2952(02)01656-8

Peng, L., Bian, X. W., Li, D. K., Xu, C., Wang, G. M., Xia, Q. Y., et al. (2015). Large-scale RNA-Seq transcriptome analysis of 4043 cancers and 548 normal tissue controls across 12 TCGA cancer types. *Sci. Rep.* 5:13413.

Radke, J., Koch, A., Pritsch, F., Schumann, E., Misch, M., Hempt, C., et al. (2019). Predictive MGMT status in a homogeneous cohort of IDH wildtype glioblastoma patients. *Acta Neuropathol. Commun.* 7:89.

Smits, M., and van den Bent, M. J. (2017). Imaging correlates of adult glioma genotypes. *Radiology* 284, 316–331. doi: 10.1148/radiol.2017151930

Stoltz, K., Sinyuk, M., Hale, J. S., Wu, Q., Otvos, B., Walker, K., et al. (2015). Development of a Sox2 reporter system modeling cellular heterogeneity in glioma. *Neuro Oncol.* 17, 361–371. doi: 10.1093/neuonc/\break{}nou320

Valenti, M. T., Dalle Carbonare, L., Donatelli, L., Bertoldo, F., Giovanazzi, B., Caliari, F., et al. (2009). STEAP mRNA detection in serum of patients with solid tumours. *Cancer Lett.* 273, 122–126.

Wang, W., Zhang, L., Wang, Z., Yang, F., Wang, H., Liang, T., et al. (2016). A three-gene signature for prognosis in patients with MGMT promoter-methylated glioblastoma. *Oncotarget* 7, 69991–69999.

Wang, Z., Gerstein, M., and Snyder, M. (2009). RNA-Seq: a revolutionary tool for transcriptomics. *Nat. Rev. Genet.* 10, 57–63.

Yao, J., Zhao, Q., Yuan, Y., Zhang, L., Liu, X., Yung, W. K., et al. (2012). Identification of common prognostic gene expression signatures with biological meanings from microarray gene expression datasets. *PLoS One* 7:e45894. doi: 10.1371/journal.pone.0045894

Yu, Z., Sun, Y., She, X., Wang, Z., Chen, S., Deng, Z., et al. (2017). SIX3, a tumor suppressor, inhibits astrocytoma tumorigenesis by transcriptional repression of AURKA/B. *J. Hematol. Oncol.* 10:115.

Zhang, P., Tu, B., Wang, H., Cao, Z., Tang, M., Zhang, C., et al. (2014). Tumor suppressor p53 cooperates with SIRT6 to regulate gluconeogenesis by promoting FoxO1 nuclear exclusion. *Proc. Natl. Acad. Sci. U.S.A.* 111, 10684–10689.

Zuo, S., Zhang, X., and Wang, L. (2019). A RNA sequencing-based six-gene signature for survival prediction in patients with glioblastoma. *Sci. Rep.* 9:2615.

Conflict of Interest: The authors declare that the research was conducted in the absence of any commercial or financial relationships that could be construed as a potential conflict of interest.

frontiers in Oncology

ORIGINAL RESEARCH
published: 19 March 2021
doi: 10.3389/fonc.2021.601982

Silencing of HuR Inhibits Osteosarcoma Cell Epithelial-Mesenchymal Transition *via* AGO2 in Association With Long Non-Coding RNA XIST

Yongming Liu[1†], Yuan Zhang[2†], Jinxue Zhang[1], Jingchang Ma[3], Xuexue Xu[2], Yuling Wang[3], Ziqing Zhou[3], Dongxu Jiang[3], Shen Shen[3], Yong Ding[1], Yong Zhou[1] and Ran Zhuang[2,3*]*

[1] Orthopedic Department of Tangdu Hospital, The Fourth Military Medical University, Xi'an, China, [2] Institute of Medical Research, Northwestern Polytechnical University, Xi'an, China, [3] Department of Immunology, The Fourth Military Medical University, Xi'an, China

OPEN ACCESS

Edited by:
Dianwen Song,
Shanghai First People's Hospital, China

Reviewed by:
Jie Li,
Nanjing Medical University, China
Gongping Sun,
Shandong University, China
Jianjun Luo,
Chinese Academy of Sciences, China

***Correspondence:**
Ran Zhuang
fmmuzhr@fmmu.edu.cn
Yong Zhou
gukezy@fmmu.edu.cn

[†]These authors have contributed equally to this work

Specialty section:
This article was submitted to Molecular and Cellular Oncology, a section of the journal Frontiers in Oncology

Received: 02 September 2020
Accepted: 01 March 2021
Published: 19 March 2021

Citation:
Liu Y, Zhang Y, Zhang J, Ma J, Xu X, Wang Y, Zhou Z, Jiang D, Shen S, Ding Y, Zhou Y and Zhuang R (2021) Silencing of HuR Inhibits Osteosarcoma Cell Epithelial-Mesenchymal Transition via AGO2 in Association With Long Non-Coding RNA XIST. Front. Oncol. 11:601982. doi: 10.3389/fonc.2021.601982

Background: Osteosarcoma (OS) is a highly malignant and aggressive bone tumor. This study was performed to explore the mechanisms of HuR (human antigen R) in the progression of OS.

Methods: HuR expression levels in OS tissues and cells were detected by immunohistochemistry and western blotting. HuR siRNA was transfected into SJSA-1 OS cells to downregulate HuR expression, and then cell proliferation, migration, and epithelial-mesenchymal transition (EMT) were evaluated. RNA immunoprecipitation was performed to determine the association of the long non-coding RNA (lncRNA) XIST and argonaute RISC catalytic component (AGO) 2 with HuR. Fluorescence *in situ* hybridization analysis was performed to detect the expression of lncRNA XIST. Western blotting and immunofluorescence assays were performed to observe AGO2 expression after HuR or/and lncRNA XIST knockdown.

Results: Knockdown of HuR repressed OS cell migration and EMT. AGO2 was identified as a target of HuR and silencing of HuR decreased AGO2 expression. The lncRNA XIST was associated with HuR-mediated AGO2 suppression. Moreover, knockdown of AGO2 significantly inhibited cell proliferation, migration, and EMT in OS.

Conclusion: Our findings indicate that HuR knockdown suppresses OS cell EMT by regulating lncRNA XIST/AGO2 signaling.

Keywords: osteosarcoma, epithelial-mesenchymal transition, migration, HuR, AGO2, long non-coding RNA XIST

Abbreviations: Ago, Argonaute; AREs, AU-rich elements; CCK-8, cell counting kit-8; DAPI, 4',6-diamidino-2-phenylindole; EdU, 5-ethynyl-2'-deoxyuridine; ELAVL1, ELAV like RNA-binding protein 1; EMT, epithelial-mesenchymal transition; FISH, fluorescence in situ hybridization; HuR, human antigen R; IHC, immunohistochemistry; IP, immunoprecipitation; lncRNA, long noncoding RNA; OS, osteosarcoma; PBS, phosphate-buffered saline; qPCR, quantitative real-time PCR; RISC, RNA-induced silencing complex; siRNA, small interfering RNA; XIST, X-inactive specific transcript.

INTRODUCTION

Osteosarcoma (OS), which mainly occurs in children and young adults, is one of the most prevalent malignant cancers, has a low survival rate, and poor overall prognosis. Despite the introduction of treatments combining surgery, chemotherapy, and radiotherapy, the 5-year survival rate of patients with metastatic OS is 11–30% (1, 2). Thus, studies are needed to explore the underlying molecular mechanisms involved in OS carcinogenesis, progression, and metastasis to find out potential therapeutic targets.

RNA-binding protein HuR (human antigen R), also known as ELAVL1 (ELAV-like RNA-binding protein 1), binds to elements rich in adenylate and uridylate (AU-rich elements) to regulate the stability and translation of various mRNAs (3, 4). Because of its pivotal role in stabilizing the mRNA of key factors involved in carcinogenesis, the effects and therapeutic potential of HuR in cancer have been intensively investigated (5). HuR is overexpressed in various tumors, such as lung cancer, breast cancer, and brain tumors (6–10). Recent studies reported that HuR levels were significantly upregulated in OS tissues compared to that in normal adjacent tissues (11, 12). However, additional studies are required to fully understand the role of HuR in OS.

Long non-coding RNAs (lncRNAs) are a large class of non-protein-coding transcripts with over 200 nucleotides in length (13). lncRNAs contribute to the unrestricted proliferation and invasion of cancer cells (14, 15). lncRNA X-inactive specific transcript (XIST) has emerged as a key regulator of OS. Its expression is significantly increased in OS tissues and cell lines, which is associated with poor prognosis (16, 17). However, the detailed mechanisms of how lncRNA XIST modulates OS progression remain unclear.

Here, we determined the HuR expression level in OS tissues and cell lines. The effects of silencing of HuR on OS proliferation, migration, and epithelial-mesenchymal transition (EMT) processes were examined and its binding partners were predicted.

METHODS

Clinical Samples

A tissue array of patients with malignant OS was purchased from the Alenabio Biological Technology Company (Xi'an, China). Clinical pathological data included age, sex, pathology diagnosis, and TNM grading, which were collected by assessing the medical records of patients with OS who had undergone surgery. No patients had been administered preoperative treatment or had co-occurrence of other diagnosed tumors.

OS Cell Lines

Human OS cell lines were purchased from the American Type Culture Collection (Manassas, VA, USA), whereas the human normal osteoblast cell line hFOB1.19 was obtained from Jennio Biotech Co., Ltd. (Guangzhou, China). Cells were cultured in Dulbecco's modified Eagle's medium (Thermo Fisher Scientific, Waltham, MA, USA) supplemented with 10% fetal bovine serum (Life Technologies, Carlsbad, CA, USA) with 5% CO_2 at 37°C in a humidified incubator. Non-transfected cells were used as a blank group and random small interfering RNA (siRNA)-transfected cells were used as the negative control group. HuR siRNA sequence: GAGGCAATTACCAGTTTCA, lncRNA XIST siRNA sequence: GCTGCAGCCATATTTCTTACT. AGO2 siRNA was obtained from Santa Cruz Biotechnology (Dallas, TX, USA; sc-44409). Lipofectamine™ 3000 (Invitrogen, Carlsbad, CA, USA) was used for cell transfection according to the manufacturer's instructions. Commercially available lentiviral (LV)-HuR constructs (Tianyucheng Biotechnology, Xi'an, Shaanxi, China) were modified to overexpress HuR.

Bioinformatics Analysis

Bioinformatic analysis (http://starbase.sysu.edu.cn/index.php) was performed to predict the potential target of HuR. The UALCAN database was used to analyze argonaute RISC catalytic component 2 (AGO2) gene expression across multiple cancer types (http://ualcan.path.uab.edu/index.html). UALCAN analysis of cancer data was based on The Cancer Genome Atlas database.

Immunohistochemistry (IHC) Staining and Semi-Quantitative Analysis

We used a formalin-fixed paraffin-embedded tissue microarray for IHC analysis. The paraffin sections were deparaffinized, rehydrated, and treated with 3% hydrogen peroxide for 10 min. Antigen retrieval was performed in citrate solution (pH 6.0) in a steamer for 2 min. The sections were washed with phosphate-buffered saline (PBS) and incubated for 30 min in 5% bovine serum albumin. Anti-HuR primary antibody (Santa Cruz Biotechnology) and anti-AGO2 (Affinity Biosciences LTD, Jiangsu, China) were added and incubated overnight at 4°C. The sections were washed with PBS and incubated with horseradish peroxidase-conjugated goat anti-mouse secondary antibody for 30 min at room temperature. A complex of streptavidin-peroxidase and 3,3′-diaminobenzidine substrate was then applied for color development and the slides were counterstained with hematoxylin. A semi-quantitative score was generated based on the IHC staining intensity as described previously (18): +, weak staining; ++, moderate staining; +++, intense staining. The slides were photographed under an optical microscope (BX51, Olympus, Tokyo, Japan).

Quantitative Real-Time PCR (qPCR) Assay

Total RNA was extracted from the cells using TRIzol™ Reagent (Thermo Fisher Scientific), and then reverse-transcribed into cDNA using SuperScript III Reverse Transcriptase from Invitrogen. PCR was performed using the SYBR Green Realtime PCR Master Mix (TAKARA, Shiga, Japan). Relative gene expression was quantified using the comparative Ct ($2^{-\Delta\Delta CT}$) method. β-actin served as an internal reference.

Western Blotting

The cells were washed with cold PBS and lysed using RIPA lysis buffer (Beyotime Biotechnology, Haimen, China) supplemented with a protease inhibitor cocktail (Cell Signaling Technology, Danvers, MA, USA). A nuclear and cytoplasmic isolation kit was purchased from Beyotime Biotechnology and used according to the manufacturer's instructions. Protein concentration was determined with the BCA protein assay kit (Thermo Fisher Scientific). Equal amounts of protein samples (30 μg) were subjected to SDS-PAGE, and then transferred onto polyvinylidene fluoride membranes (Millipore, Billerica, MA, USA). The membranes were blocked with 5% non-fat milk in Tris-buffered saline with 0.1% Tween 20 and blotted with corresponding primary antibodies at 4°C overnight. Proteins were blotted with horseradish peroxidase-conjugated secondary antibody (Cell Signaling Technology) and visualized with an enhanced ECL system (Tanon Science & Technology, Shanghai, China). β-actin was used as whole cell internal loading control. Lamin B1 and tubulin were employed as positive controls for the nuclear and cytoplasmic fractions, respectively.

Cell Proliferation Analysis

Cell Counting Kit (CCK)-8 (Beyotime) was used to analyze cell proliferation after different treatments. The cells were seeded in triplicate into 96-well plates at 3,000 cells/well, followed by culturing for 24 h, 36 h, or 48 h. CCK-8 was added according to the manufacturer's protocol. Absorbance was detected at 450 nm. The effect of HuR on OS cell proliferation was also evaluated in a 5-ethynyl-2′-deoxyuridine (EdU) incorporation assay (RiboBio, Guangzhou, China) according to the manufacturer's instructions. Briefly, 5×10^3 OS cells were plated in triplicate in 96-well plates and cultured for 48 h, followed by exposure to EdU for an additional 4 h at 37°C. The cells were fixed with 4% paraformaldehyde for 15 min and permeabilized with 0.5% Triton X-100 for 20 min at room temperature. After washing three times with PBS, the cells were reacted with Apollo reaction cocktail for 30 min. Nuclei were stained with 4',6-diamidino-2-phenylindole (DAPI; Roche Diagnostics, Basel, Switzerland). EdU-positive cells were visualized under a fluorescent microscope (Olympus).

Cell Cycle and Apoptosis Assay

Flow cytometry was performed to measure the cell cycle and apoptosis in the blank, NC siRNA, and HuR siRNA-transfected groups. After washing with PBS, the cells were fixed in 70% ethanol and precooled at 4°C. Propidium iodide was added to the cell precipitate according to the instructions of the DNA ploidy test kit (Sigma-Aldrich, St. Louis MO, USA). Cell apoptosis was measured using an Annexin V-fluorescein isothiocyanate and propidium iodide staining kit (Beyotime). The cells were evaluated by flow cytometry (Beckman Coulter, Brea, CA, USA). Each experiment was repeated at least three times. FlowJo software VX (FlowJo LLC, Ashland, OR, USA) was used to analyze the data. The degree of apoptosis was also determined using the One Step TUNEL Apoptosis Assay Kit (Beyotime Biotechnology) according to the manufacturer's protocol. Cy3-positive cells were visualized under a fluorescent microscope (Olympus).

Cell Scratch (Wound Healing Migration) and Transwell Migration Assay

OS cells were seeded into six-well plates and treated as described. After 48 h when the cells reached 100% confluence, a scratch was induced in the monolayer. Images of the wound area were captured immediately after the scratch (T0) and 12 h (T12) later to monitor cell migration into the wounded area, and the percentage of the scratch area (% scratch) closed was calculated as (width at T0 − width at T12)/width at T0 × 100. Images of the cells were obtained under an inverted microscope (CX41, Olympus). The experiment was performed three times. The migration assay was performed as described previously (19). A cell culture inserted with a polycarbonate membrane (8 μm pore size) was purchased from Corning Costar, Inc. (Corning, NY, USA).

RNA Immunoprecipitation (RNA IP) Assay

OS cells were lysed with 25 mM of Tris-HCl buffer (pH 7.5) and RNase inhibitor (Sigma-Aldrich). After a pre-clearance procedure, the whole cell lysates were used for IP for 4 h using protein A agarose (Thermo Fisher Scientific) at room temperature in the presence of excess (30 μg) IP antibody (anti-HuR, control mouse IgG). RNA in the IP materials was extracted with TRIzol, followed by detection of *AGO2*, *lncRNA XIST*, and *β-actin* mRNA levels by qPCR. The experiment was repeated at least three times.

Fluorescence *In Situ* Hybridization (FISH) Analysis of lncRNA

The cells were placed on glass chamber slides and cultured. The cells were first fixed with 4% paraformaldehyde in PBS for 30 min, and then permeabilized with 0.1% Triton X-100. Next, the cells were washed and treated with pre-hybridization buffer. The FISH detection kit including probes for lncRNA XIST and U6 was purchased from RiboBio Co., Ltd. (Guangzhou, China). Hybridization was carried out in a humidified chamber for 16 h, followed by staining with DAPI.

Immunofluorescence Assay

The cells were fixed with 4% paraformaldehyde and permeabilized with 0.1% Triton X-100, followed by blocking with 5% bovine serum albumin for 30 min. The cells were incubated with anti-HuR (Santa Cruz Biotechnology) or anti-AGO2 antibodies (Abcam, Cambridge, UK) for 1 h at room temperature. After washing the cells, they were incubated with Cy3-labeled goat anti-mouse secondary antibody and fluorescein isothiocyanate-labeled goat anti-rabbit secondary antibody for 1 h at room temperature, and then stained with DAPI. The images were visualized under a Leica LSM 800 confocal immunofluorescence microscope (Wetzlar, Germany).

Statistical Analysis

All data were statistically analyzed using THE GraphPad Prism version 6 software (La Jolla, CA, USA). All data are presented as means ± standard deviation. Data were analyzed using the independent sample *t*-test for comparison between two groups,

and one-way ANOVA with Tukey multiple comparison test between three or more groups. Statistical analyses for clinical data were performed using SPSS (version 10.0; SPSS, Inc., Chicago, IL, USA). Pearson χ^2 test was used to evaluate the statistical significance of the association between HuR expression and clinical features (n = 30). Statistical significance was defined as $P < 0.05$.

RESULTS

HuR Is Overexpressed in OS Cells

We measured the expression of HuR in different OS tissues and cell lines to evaluate the roles of HuR in OS formation and progression. First, we examined HuR expression in OS tissues by IHC staining. The results showed that HuR is mainly localized in the cell nucleus (**Figure 1A**). Comparisons between HuR expression and the clinicopathological characteristics of OS are shown in **Table 1**. It was shown that the HuR expression had no significant correlation with gender and age of OS patients. All 30 OS samples were in either the N0 stage, in which there was no tumor metastasis to nearby lymph nodes, or M0 stage, indicating the absence of distant organ metastasis. Notably, HuR expression was significantly higher in the T2 stage than that in the T1 stage of OS tumors ($P = 0.001$).

Next, HuR expression was determined in the OS cell lines MG63, SAOS2, U2OS, HOS, and SJSA-1, and normal hFOB1.19. According to our results, HuR was elevated in most OS cell lines, and MG63 and SJSA-1 cells showed a high level of HuR expression (**Figure 1B**). Consistent with the findings of recent studies (11, 12), our results further indicated that HuR is related to the tumor progression in OS.

TABLE 1 | Correlation between HuR and clinical features of patients with OS (n = 30).

Variable		No. of patients	HuR expression			*P*-values
			+	++	+++	
Gender	Male	20 (66.7)	8	9	3	0.885
	Female	10 (33.3)	4	5	1	
Age	>20	20 (66.7)	7	10	3	0.441
	<20	10 (33.3)	5	4	1	
T stage	T1	7 (23.3)	7	0	0	**0.001**
	T2	23 (76.7)	5	14	4	

P-values based on a χ^2 test; bold, statistically significant ($P < 0.05$).

Silencing HuR Increases Sensitivity to Apoptosis of OS Cells

qPCR and western blotting confirmed the knockdown efficiency. siRNA at a concentration of 50 nM was used to knockdown HuR in SJSA-1 cells (**Figures 2A, B**). Because HuR expression was significantly higher in the T2 stage than the T1 stage of the OS tumor, we first determined whether HuR promotes OS cell proliferation. CCK-8 assay was performed to analyze whether HuR expression affects cell proliferation (**Figure 2C**). Consistent with the results of Pan et al. (12), knockdown of HuR inhibited cell viability and proliferation. Additionally, the effects of HuR

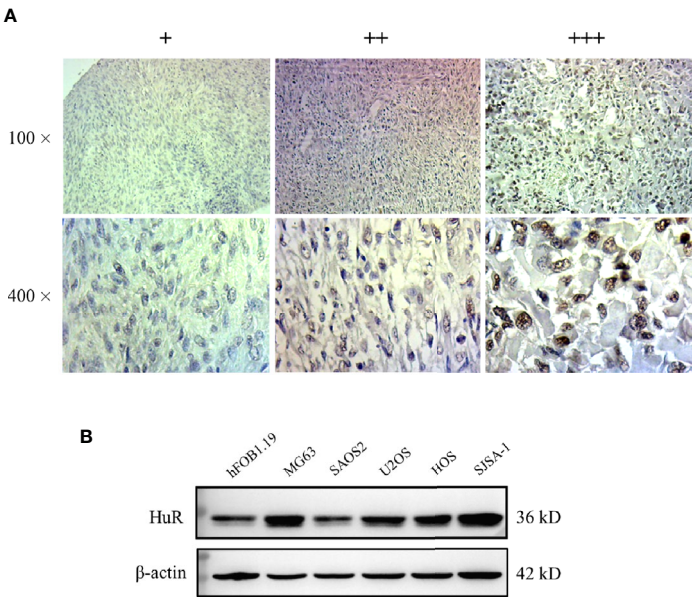

FIGURE 1 | Expression of HuR protein in tissues from patients with osteosarcoma (OS) and in OS cells. **(A)** Representative images of different IHC staining intensities of HuR are shown in OS tissues. Staining patterns were categorized into three groups as follows: weak staining (+), moderate staining (++), and intense staining (+++). Upper panel, original magnification 100x; lower panel, original magnification 400x. **(B)** Western blotting analysis of HuR expression in a human osteoblast cell line (hFOB1.19) and OS cell lines (MG63, SAOS2, U2OS, HOS, and SJSA-1).

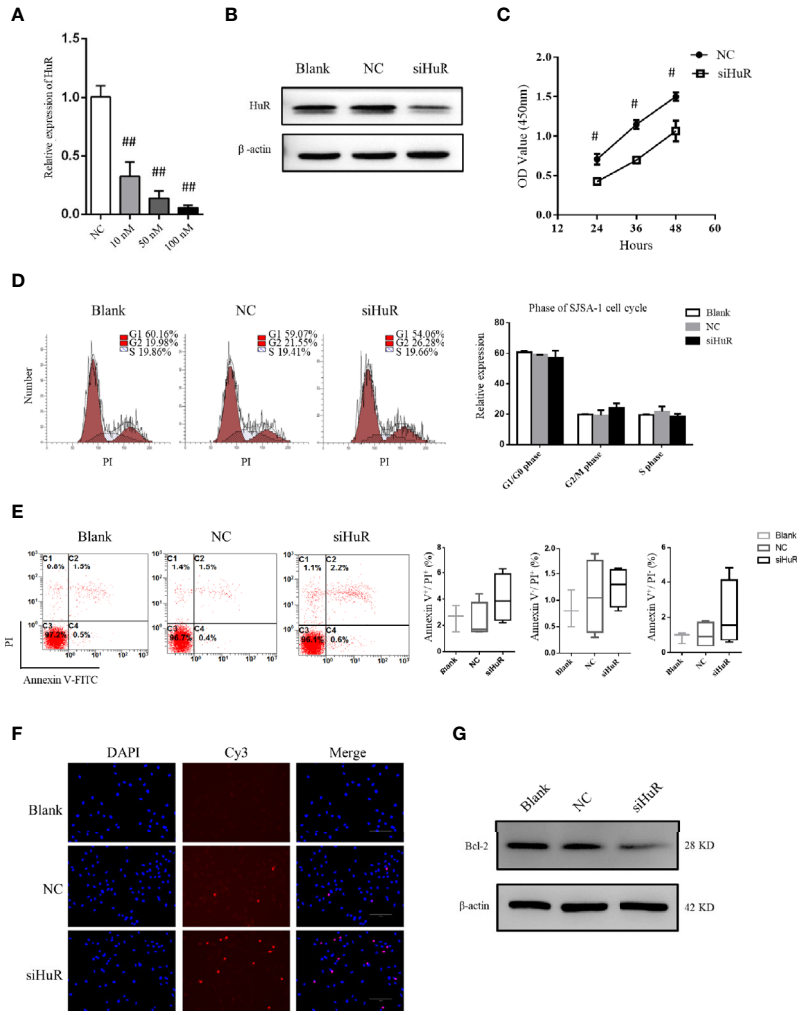

FIGURE 2 | Effect of HuR knockdown on progression of OS cells. **(A)** qPCR analysis for HuR knockdown efficiency at 48 h after siRNA transfection in SJSA-1 OS cells. ## indicates $P < 0.01$ compared to the scramble siRNA negative control (20). **(B)** Western blotting analysis of HuR at 48 h after siRNA transfection in SJSA-1 cells. β-actin was used as an internal control. **(C)** SJSA-1 cells with NC siRNA or HuR siRNA (siHuR) transfection were subjected to a CCK-8 assay to examine cell viability. # indicates $P < 0.05$ compared to the NC group. **(D)** Cell cycle regulation by HuR was detected by propidium iodide staining and flow cytometric analysis in SJSA-1 cells. **(E)** Cell apoptosis was detected by Annexin-V/PI staining and flow cytometric analysis in SJSA-1 cells. Results are representative of at least three independent experiments. **(F)** TUNEL staining in the SJSA-1 cells harvested from blank, negative control, and siHuR groups. Very few TUNEL-positive cells were detected in the blank and NC groups. Scale bar = 125 μm. **(G)** Representative image of western blotting for Bcl-2. β-actin served as an internal loading control.

knockdown on cell cycle and apoptosis were examined by flow cytometric analysis. The assay showed a tendency that silencing of HuR decreased the SJSA-1 cells in G1/G0 and increased G2/M cell cycle progression of the cells, but with no significance (**Figure 2D**). No significant difference in apoptosis was observed between each group through flow cytometric analysis (**Figure 2E**). As shown in **Figure 2F**, there were slightly more TUNEL-positive OS cells in the siHuR group when compared with the blank and NC groups. Furthermore, there was a lower expression of Bcl-2, an apoptotic suppressor, in HuR siRNA-transfected OS cells (**Figure 2G**). Altogether, the mentioned results suggest that knocking down HuR could make OS cells more sensitive to apoptotic stimuli.

We further used a lentiviral construct to overexpress HuR. The results showed that the expression level of HuR was significantly higher in the HuR overexpression (OE HuR) group; whereas the expression levels in HuR siRNA-transfected OS cells were almost undetectable. These results showed that lentiviral infection was efficient. As shown in **Supplementary Figures 1A, B**, western blotting analysis for Bcl-2 and the TUNEL assay indicated that HuR overexpression decreased apoptosis level in OS cells. Besides, to further confirm the biological function of HuR overexpression in OS cells, a rescue experiment was performed with HuR siRNA in HuR overexpressed OS cells. The expression of HuR was significantly downregulated in the siRNA + OE group

compared with OE HuR group. Meanwhile, Bcl-2 level and the TUNEL assay indicated that rescue experiments increased the sensitivity of apoptosis level compared with that in HuR overexpressed OS cells.

Silencing of HuR Inhibites OS Cell Migration and EMT

Next, wound healing and transwell migration assays were performed to detect the migration ability of SJSA-1 cells after different treatments. There was no difference in scratch closure in the NC-siRNA group compared to the blank group. However, there was a significant decrease in the percentage of scratch closure in cells lacking HuR compared to that in the NC-siRNA or blank group (**Figures 3A, B**). Additionally, the transwell migration assay revealed that HuR silencing reduced the number of migrated OS cells compared to that in the control groups (**Figure 3C**). The results showed that HuR knockdown significantly inhibited OS cell migration.

We next investigated the role of HuR knockdown in EMT of OS cells. The protein levels of the EMT markers vimentin, E-cadherin, and N-cadherin, as well as related key transcriptional factors (Twist1, Snail, and Slug) were examined by western blotting. The results showed that silencing of HuR decreased the levels of vimentin, Twist1, and Snail in SJSA-1 OS cells, while increased the level of E-cadherin. However, the levels of N-cadherin, Slug, HMGB-1, and ZO1 were not significantly changed after silencing HuR compared to the control groups in SJSA-1 cells (**Figure 3D**).

HuR Binds to lncRNA XIST and Decreases Its Expression

We further explored the regulatory mechanisms involved in HuR-related OS cell EMT. Numerous studies have reported lncRNAs can interact with RNA-binding proteins in cancer. Recently, lncRNA XIST was demonstrated to promote the progression of OS (16, 21). To gain insight into the precise mechanism and potential interaction of HuR with XIST, we first examined its subcellular localization by FISH with or without HuR siRNA transfection. XIST was distributed in the both nucleus and cytoplasmic regions of OS cells, indicating that

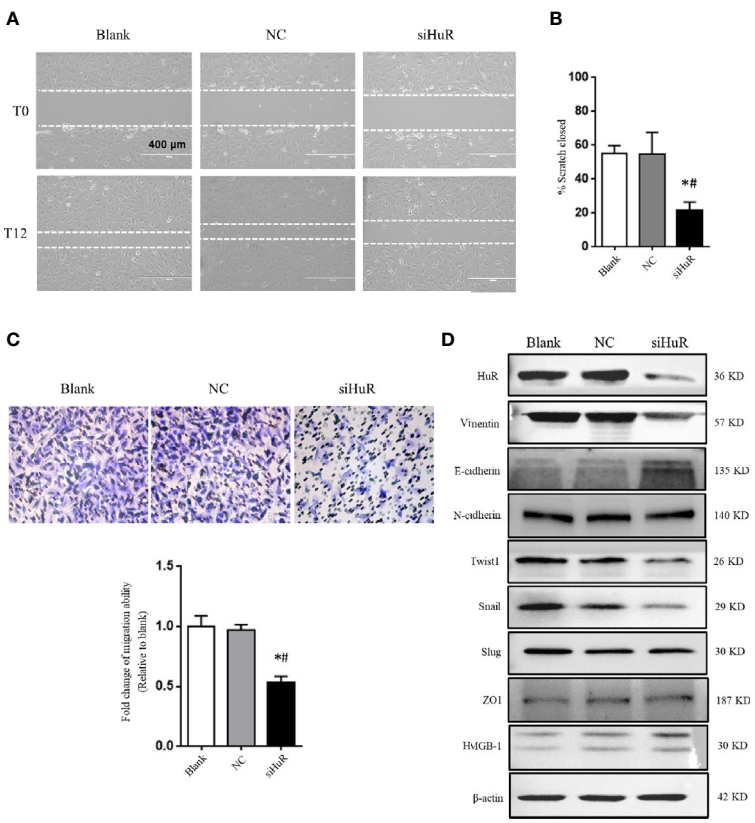

FIGURE 3 | Silencing of HuR inhibits the migration and EMT of OS cells. **(A)** Photographs of cells in scratch assay. Untreated SJSA-1 cells (blank), their corresponding scramble siRNA (20), and HuR siRNA (siHuR) transfected cells were seeded into six-well plates. Images were obtained at 0 and 12 h after scratch to monitor cell migration for wound closure. **(B)** Statistical results of the scratch assay at 12 h. * indicates $P < 0.05$ compared to the blank group. # indicates $P < 0.05$ compared to the NC group. Representative images from three separate experiments are shown. **(C)** Representative images of transwell migration assay of SJSA-1 cells with HuR knockdown and respective blank control and NC siRNA. Lower panel shows the statistical graph of the transwell migration assay. * indicates $P < 0.05$ compared to the blank group. # indicates $P < 0.05$ compared to the NC siRNA. **(D)** Representative images of western blotting for EMT markers and related transcriptional factors. β-actin served as an internal loading control.

XIST acts as a regulatory RNA to influence target mRNAS. After silencing of HuR in OS cells, the level of XIST was downregulated (**Figure 4A**). U6, which is mainly localized in the cell nucleus, was used as an internal reference for staining, as observed in **Figure 4B**. qPCR analysis further demonstrated that lncRNA XIST expression was decreased in OS cells after HuR knockdown (**Figure 4C**). Additionally, the RNA IP assay revealed that lncRNA XIST was highly expressed in the RNA-protein complex that had been precipitated by the anti-HuR antibody (**Figure 4D**).

Considering that lncRNA-mRNA typically forms a regulatory network, we hypothesized that repression of XIST by HuR involved other factors associated with XIST. We searched starbase and predicted that both HuR and XIST could bind to AGO2, which is an integral component of the RNA-induced silencing complex (RISC). The results revealed high levels of AGO2 in the RNA-protein complex immune-precipitated by the anti-HuR antibody (**Figure 4E**). The results indicate that HuR binds to the lncRNA XIST and AGO2 in OS cells.

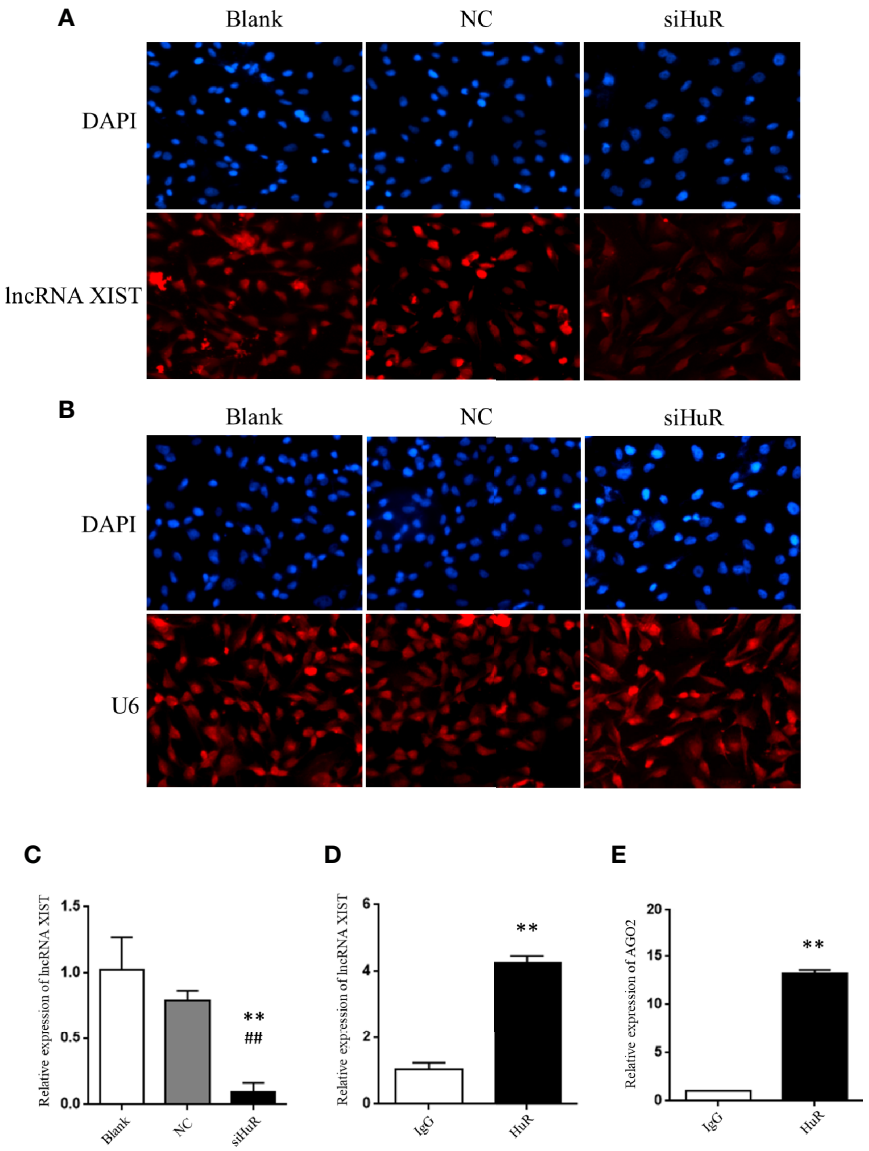

FIGURE 4 | Silencing of HuR represses lncRNA XIST expression in OS cells. **(A)** RNA fluorescence *in situ* hybridization (FISH) analysis of lncRNA XIST with a specific probe in SASJ-1 OS cells. **(B)** U6, a ribonucleoprotein, served as the endogenous control for FISH analysis; the nucleus was stained with DAPI. **(C)** The mRNA level of lncRNA XIST was detected by qPCR in cells after different treatments. ** indicates $P < 0.01$ compared to the blank group. ## indicates $P < 0.01$ compared to the NC group. qPCR was used to measure the lncRNA XIST **(D)** and AGO2 **(E)** abundance in the HuR-IP complex following the RIP assay. ** indicates $P < 0.01$ compared to the mouse IgG group.

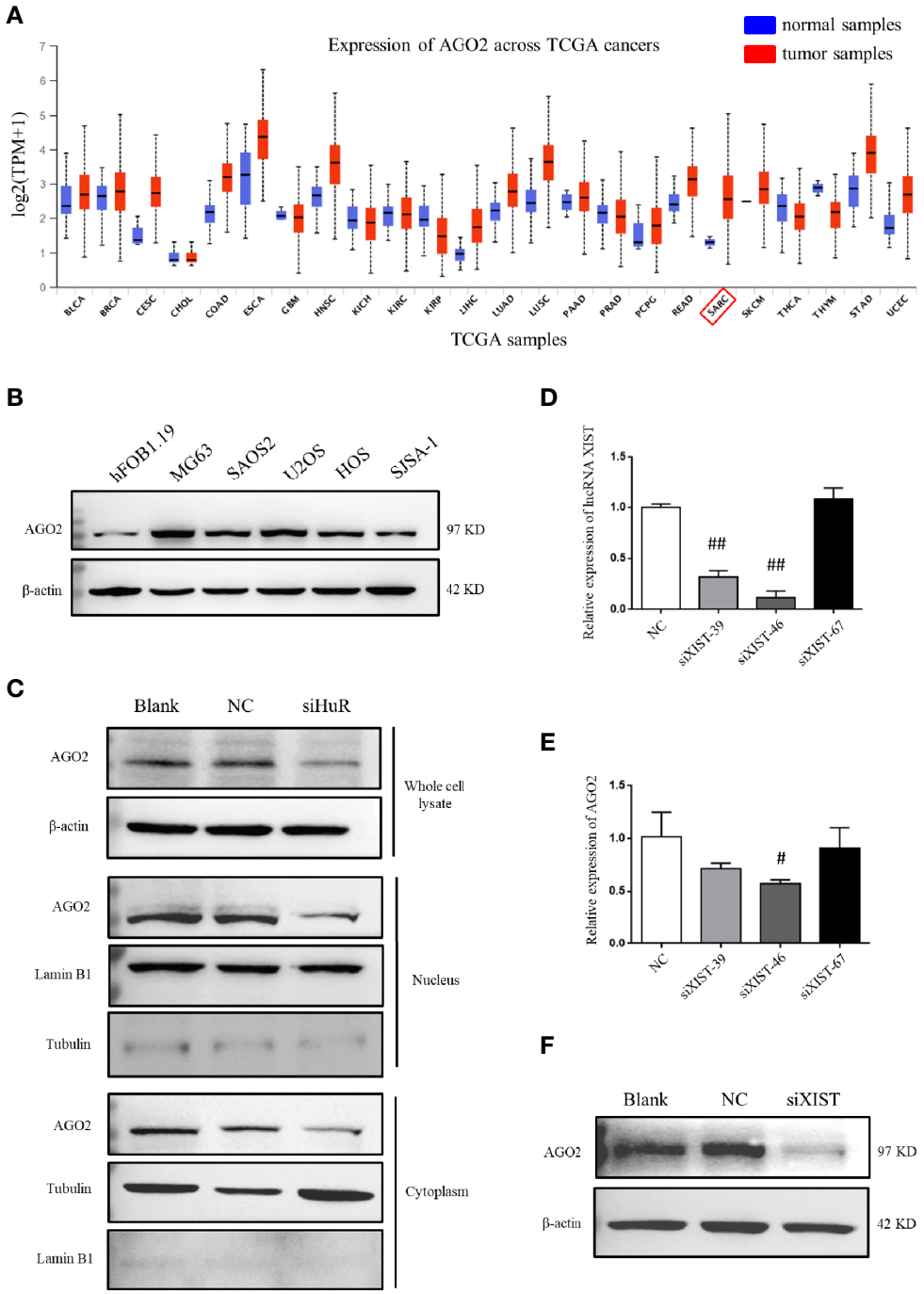

FIGURE 5 | AGO2 expression was regulated by HuR and lncRNA XIST in OS cells. **(A)** Expression levels of AGO2 in multiple cancers and normal samples using data from TCGA database. SARC: sarcoma cancer. **(B)** Western blotting analysis of AGO2 expression in a human osteoblast cell line (hFOB1.19) and OS cell lines (MG63, SAOS2, U2OS, HOS, and SJSA-1). The blots in **Figure 1B** were stripped and re-probed for AGO2 protein. **(C)** Western blotting analysis of AGO2 expression in cell fractions after HuR knockdown. Whole cell lysate and nuclear and cytoplasmic fractions of cells with different treatment were isolated. Protein concentrations were measured by the Bradford assay, and equal amounts of protein were analyzed. β-actin, lamin B1, and tubulin served as loading controls for the whole cell lysate, nuclear fraction, and cytoplasmic fraction, respectively. **(D)** Expression of XIST in SJSA-1 cells transfected with NC siRNA or different siRNA against XIST was confirmed by qPCR analysis. $^{\#\#}$ indicates $P < 0.01$ compared to the NC group. **(E)** mRNA levels of AGO2 in SJSA-1 cells transfected with NC siRNA or different siRNAs against XIST. $^{\#}$ indicates $P < 0.05$ compared to the NC group. **(F)** Protein level of AGO2 in SJSA-1 cells transfected with NC siRNA or siRNA-46 against XIST and blank group without transfection.

AGO2 Is Regulated by HuR and lncRNA XIST

Analysis by UALCAN showed that AGO2 was expressed at different levels in cases with multiple types of tumors, with a relatively large difference between normal tissues and tumors tissues in sarcoma cancer compared to other cancer types, indicating that a high AGO2 level is correlated with sarcoma progression (**Figure 5A**). AGO2 expression was determined in the OS cell lines MG63, SAOS2, U2OS, HOS, and SJSA-1, and normal hFOB1.19 cells. OS cells showed a significantly high level of AGO2 expression compared to that in normal osteoblast cells (**Figure 5B**). RISC is assembled by Dicer, argonaute protein, siRNA, and other biological macromolecules. Although AGO2-mediated RNA silencing mainly functions in the cytoplasm, western blotting revealed that knockdown of HuR diminished AGO2 protein levels both in the cell nucleus and cytoplasm (**Figure 5C**). Tubulin and lamin B1 levels were checked in the nucleus and cytoplasm to ensure that there was no contamination in the nucleus fraction and cytoplasm fraction.

To investigate the role of lncRNA XIST on AGO2, we designed three siRNAs specific to XIST. RNAi has been widely and effectively used to study lncRNA XIST deficiency (22, 23). qPCR demonstrated that siXIST-46 is the most effective siRNA for lncRNA XIST knockdown with an interference efficiency of over 80% (**Figure 5D**). qPCR and western blotting assays revealed that silencing of XIST significantly downregulated AGO2 at both mRNA and protein levels in OS cells (**Figures 5E, F**).

Immunofluorescence staining and confocal analysis were conducted to observe the expression and subcellular localization of AGO2, which is regulated by HuR and lncRNA XIST. As shown in **Figure 6A**, most HuR was localized in the nucleus of SJSA-1 OS cells, whereas AGO2 was mainly distributed in the cytoplasm. siRNAs for both HuR and lncRNA XIST inhibited AGO2 expression; in contrast, siRNA for XIST did not influence the level and distribution of HuR (**Figures 6B, C**). The combination of HuR and lncRNA XIST siRNA strongly suppressed AGO2 protein expression (**Figure 6D**).

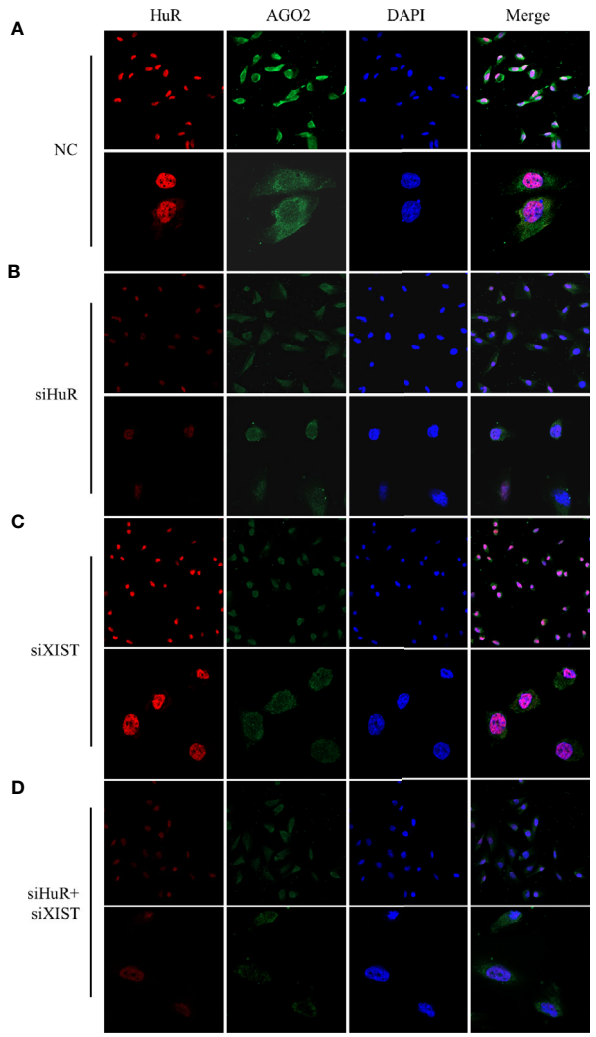

FIGURE 6 | Confocal microscopic analysis of AGO2 expression in OS cells. Representative immunofluorescence analysis results for regulation of AGO2 by HuR and lncRNA XIST. SJSA-1 cells with different treatments were fixed with 1% paraformaldehyde and stained with anti-HuR (red) and anti-AGO2 (green) antibodies. Nuclei of cells appeared as blue because of DAPI nuclear staining. **(A)** Cells were transfected with an NC siRNA for 48 h. **(B)** Cells were transfected with a HuR siRNA for 48 h. **(C)** Cells were transfected with an lncRNA XIST siRNA for 48 h. **(D)** Cells were co-transfected with both HuR and lncRNA XIST siRNAs for 48 h. Stained cells were examined under a Leica confocal immunofluorescence microscope. Upper panel: original magnification 200x; lower panel, original magnification 630x.

AGO2 Is Involved in OS Cell Progression

Considering that AGO2 was significantly regulated by HuR/lncRNA XIST, we further evaluated the role of AGO2 in OS cells. First, a specific siRNA effectively downregulated AGO2 expression at the mRNA and protein levels (**Figures 7A, B**). As shown in **Figure 7C**, the CCK-8 assay demonstrated that knockdown of AGO2 significantly inhibited OS cell viabilty compared to that in the NC siRNA control. The EdU incorporation assay for immunochemical detection of the nucleotide analog incorporated into replicated DNA showed consistent results with the CCK-8 assay (**Figures 7D, E**, $P < 0.05$).

Moreover, western blotting analysis indicated that silencing of AGO2 inhibited the level of the EMT-related molecule vimentin and Snail in OS cells (**Figure 7F**). Compared to cells transfected with NC siRNA, OS cells transfected with AGO2 siRNA exhibited lower levels of migration ability (**Figure 7G**) as detected in the transwell assay. Furthermore, we examined AGO2 expression in OS tissues by IHC staining. The results showed that AGO2 is localized in the both cell nucleus and cytoplasm (**Figure 7H**). Comparisons between AGO2 expression and the clinicopathological characteristics of OS are shown in **Table 2**. However, it was shown that AGO2 expression has no significant correlation with gender, age, and different stages of OS tumors. Taken together, these results suggest that HuR

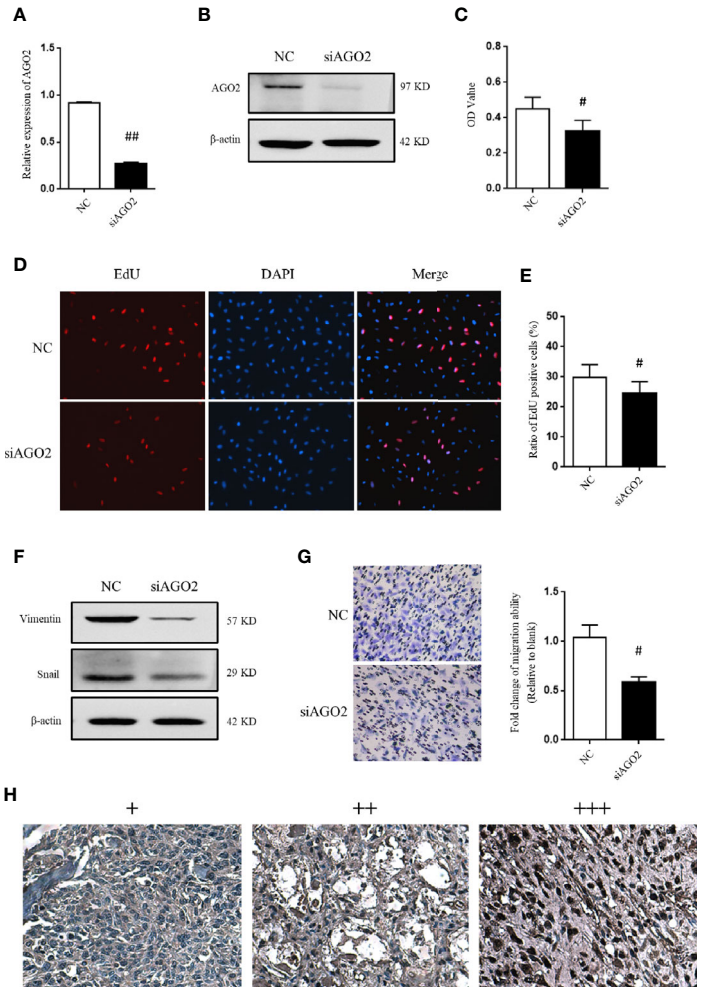

FIGURE 7 | AGO2 regulates OS cell progression and migration. **(A)** qPCR and **(B)** western blotting analysis were performed to detect the efficiency of AGO2 siRNA. ## indicates $P < 0.01$ compared to the NC group. **(C)** SJSA-1 cells with NC siRNA or AGO2 siRNA transfection were subjected to a CCK-8 assay to examine cell viability. # indicates $P < 0.05$ compared to the NC group. **(D)** EdU proliferation assay analysis was performed 48 h after AGO2 siRNA or NC siRNA transfection in SJSA-1 cells. Cell nucleus was stained with DAPI. Original magnification 200x. **(E)** Statistical graph of EdU assay. # indicates $P < 0.05$ compared to the NC group. **(F)** Representative images of western blotting for EMT markers vimentin and transcriptional factor Snail. β-actin served as an internal loading control. **(G)** Representative images of transwell migration assay of SJSA-1 cells with AGO2 knockdown and NC siRNA control. Statistical graph of transwell migration assay is shown. # indicates $P < 0.05$ compared to the NC group. Representative images from three separate experiments are shown. **(H)** Expression of AGO2 protein in OS tissues from patients with osteosarcoma. Representative images of different IHC staining intensities of AGO2 are shown in OS tissues. Staining patterns were categorized into three groups as follows: weak staining (+), moderate staining (++), and intense staining (+++). Original magnification 200x.

TABLE 2 | Correlation between AGO2 and clinical features of patients with OS (n = 34).

Variable		No. of patients	AGO2 expression			*P*-values
			+	++	+++	
Gender	Male	22 (64.7)	10	4	8	0.483
	Female	12 (35.3)	7	3	2	
Age	>20	24 (70.6)	12	4	8	0.596
	<20	10 (29.4)	5	3	2	
T stage	T1	8 (23.5)	6	1	1	0.265
	T2	26 (76.5)	11	6	9	

P-values based on a χ^2 test.

regulates OS cell tumorigenesis and progression by targeting AGO2 with the assistance of lncRNA XIST.

DISCUSSION

Overexpression of HuR occurs during tumorigenesis and cancer progression in various cancer types (9). Thus, inhibition of HuR biological function is an attractive goal in cancer research. Recently, the HuR small molecule inhibitor MS-444 was developed and shown to attenuate the invasion of glioblastoma cells and growth of colorectal cancer cells (20, 24). The CMLD-2

inhibitor exhibited antitumor effects *via* MAD2 in thyroid cancer cells (25).

Recently, Pan et al. showed that knockdown of HuR inhibited MG63 OS cell viability and EMT and promoted cell apoptosis by suppressing the miR-142-3p and high mobility group AT-hook 1 axis (12). Xu et al. demonstrated that HuR suppresses OS cell migration, invasion, and EMT by inhibiting YAP activation, which is a key executor in the Hippo signaling pathway (11). These studies demonstrate that HuR expression was significantly increased in OS tissues compared to that in adjacent normal tissues. Here, we found that HuR expression significantly differed between the T1 and T2 stages of OS tumors. In this study, both the IHC staining and immunofluorescence assays showed that HuR is mainly localized in the OS cell nucleus. This is not consistent with the consensus that HuR is mostly localized in the nucleus of normal cells, but typically translocated to the cytoplasmic region of malignant cells (9). An increased nuclear HuR expression pattern was more frequently observed in invasive epithelial tumors than that in low malignant potential ovarian tumors (26). However, according to this observation, some molecules likely help HuR to carry out its function in OS cells.

Aberrant expression of lncRNAs has been detected in multiple cancers and may be useful as diagnostic and prognostic markers in cancer progression (27). Moreover, lncRNAs have been investigated as key modulators that regulate many biological processes in human cancers *via* diverse mechanisms and may act as decoys, scaffolds, and enhancer RNAs (28). LncRNA was reported to regulate gene expression and function by cooperating with HuR in different manners, such as sponges or by recruiting HuR/miRNA, competitively/blocking binding to HuR, and stabilizing HuR protein (29–31).

LncRNA XIST expression was significantly upregulated in OS tissues, and high XIST expression is associated with tumor size, advanced clinical stage, and distant metastasis (17, 21). The mechanisms have been investigated previously, including the involvement of XIST in NK-κB/PUMA signaling (32), repression of P21 expression to regulate the cell cycle by binding EZH2 (33), targeting of YAP *via* miR-195-5p (34), regulation of miR-21-5p/PDCD4 or miR-193a-3p (35, 36), or sponging of miRNA-137 (37). In the current study, we demonstrated that XIST directly binds to the HuR protein and is regulated by HuR in OS cells, suggesting that XIST is associated with HuR-mediated OS tumor progression.

Furthermore, HuR may stabilize target mRNAs and increase the translation of numerous mRNAs while repressing the translation of other mRNAs (e.g., IGF-IR). Therefore, we investigated the target modulated by HuR in OS cells. As an important enzyme in the RNA interference pathway, AGO2 is differentially expressed in many tumors and is related to the clinical stage and pathological grading (38, 39). However, our results showed no significant correlation between AGO2 expression and typical clinical characteristics (like gender, age, and stages) of OS tumors, which may result from the limited sample amount of OS cases, so the studies of larger sample sizes are needed to verify these findings. AGO2 protein is widely expressed in organisms; as a regulatory element, it may play a role in inhibiting or promoting tumors, depending on the miRNA to which it binds. Kim et al. reported that HuR is associated with AGO2 in an RNA-dependent manner according to co-IP analyses, and HuR is necessary for the AGO2/let7 interaction with *c-Myc* mRNA in HeLa cells (40). Here, we found that HuR bound to AGO2, and further demonstrated that lncRNA XIST may function as a mediator of HuR-induced AGO2 modulation. Thus, the inhibition effect of AGO2 on OS migration and EMT by downregulating lncRNA XIST expression is a new function for the RNA-binding protein HuR.

In conclusion, mechanistic studies indicated that downregulation of HuR significantly inhibited OS cell migration and EMT by regulating the lncRNA XIST/AGO2 signaling pathway.

DATA AVAILABILITY STATEMENT

The raw data supporting the conclusions of this article will be made available by the authors, without undue reservation.

ETHICS STATEMENT

Ethical approval was not required for the commercialized OS tissue array samples in accordance with the institutional requirements.

AUTHOR CONTRIBUTIONS

YD, YZho, RZ designed the study. YL, YZha, JZ performed the *in vitro* experiments. JM, XX, and YW prepared the figures. ZZ, DJ, and SS collected and analyzed the data. YZho, RZ wrote the manuscript. All authors contributed to the article and approved the submitted version.

FUNDING

This investigation was supported by the Natural Science Foundation of China (No. 81871258 and No. 81671575).

SUPPLEMENTARY MATERIAL

The Supplementary Material for this article can be found online at: https://www.frontiersin.org/articles/10.3389/fonc.2021.601982/full#supplementary-material

Supplementary Figure 1 | Effect of HuR overexpression on apoptosis of OS cells. **(A)** Representative image of western blotting for HuR and Bcl-2. β-actin served as an internal loading control. **(B)** TUNEL staining in the SJSA-1 cells harvested from the HuR overexpression (OE) group and HuR siRNA + OE group. Scale bar = 125 μm.

REFERENCES

1. Otoukesh B, Boddouhi B, Moghtadaei M, Kaghazian P, Kaghazian M. Novel molecular insights and new therapeutic strategies in osteosarcoma. *Cancer Cell Int* (2018) 18:158. doi: 10.1186/s12935-018-0654-4
2. Gill J, Ahluwalia MK, Geller D, Gorlick R. New targets and approaches in osteosarcoma. *Pharmacol Ther* (2013) 137(1):89–99. doi: 10.1016/j.pharmthera.2012.09.003
3. Zhang W, Vreeland AC, Noy N. RNA-binding protein HuR regulates nuclear import of protein. *J Cell Sci* (2016) 129(21):4025–33. doi: 10.1242/jcs.192096
4. Brennan CM, Steitz JA. HuR and mRNA stability. *Cell Mol Life Sci CMLS* (2001) 58(2):266–77. doi: 10.1007/PL00000854
5. Yuan Z, Sanders AJ, Ye L, Jiang WG. HuR, a key post-transcriptional regulator, and its implication in progression of breast cancer. *Histol Histopathol* (2010) 25(10):1331–40. doi: 10.14670/HH-25.1331
6. Zhang Y, Yang L, Ling C, Heng W. HuR facilitates cancer stemness of lung cancer cells via regulating miR-873/CDK3 and miR-125a-3p/CDK3 axis. *Biotechnol Lett* (2018) 40(4):623–31. doi: 10.1007/s10529-018-2512-9
7. Zhang Z, Huang A, Zhang A, Zhou C. HuR promotes breast cancer cell proliferation and survival via binding to CDK3 mRNA. *Biomed Pharmacother = Biomed Pharmacother* (2017) 91:788–95. doi: 10.1016/j.biopha.2017.04.063
8. Levidou G, Kotta-Loizou I, Tasoulas J, Papadopoulos T, Theocharis S. Clinical Significance and Biological Role of HuR in Head and Neck Carcinomas. *Dis Markers* (2018) 2018:4020937. doi: 10.1155/2018/4020937
9. Kotta-Loizou I, Giaginis C, Theocharis S. Clinical significance of HuR expression in human malignancy. *Med Oncol (Northwood London England)* (2014) 31(9):161. doi: 10.1007/s12032-014-0161-y
10. Nabors LB, Gillespie GY, Harkins L, King PH. HuR, a RNA stability factor, is expressed in malignant brain tumors and binds to adenine- and uridine-rich elements within the 3' untranslated regions of cytokine and angiogenic factor mRNAs. *Cancer Res* (2001) 61(5):2154–61.
11. Xu W, Chen C, Xu R, Li Y, Hu R, Li Z, et al. Knockdown of HuR represses osteosarcoma cells migration, invasion and stemness through inhibition of YAP activation and increases susceptibility to chemotherapeutic agents. *Biomed Pharmacother = Biomed Pharmacother* (2018) 102:587–93. doi: 10.1016/j.biopha.2018.03.098
12. Pan W, Pang J, Ji B, Wang Z, Liu C, Cheng Y, et al. RNA binding protein HuR promotes osteosarcoma cell progression via suppressing the miR-142-3p/HMGA1 axis. *Oncol Lett* (2018) 16(2):1475–82. doi: 10.3892/ol.2018.8855
13. Ponting CP, Oliver PL, Reik W. Evolution and functions of long noncoding RNAs. *Cell* (2009) 136(4):629–41. doi: 10.1016/j.cell.2009.02.006
14. Wang C, Jing J, Cheng L. Emerging roles of non-coding RNAs in the pathogenesis, diagnosis and prognosis of osteosarcoma. *Invest New Drugs* (2018) 36(6):1116–32. doi: 10.1007/s10637-018-0624-7
15. Lin C, Yang L. Long Noncoding RNA in Cancer: Wiring Signaling Circuitry. *Trends Cell Biol* (2018) 28(4):287–301. doi: 10.1016/j.tcb.2017.11.008
16. Lv GY, Miao J, Zhang XL. Long Noncoding RNA XIST Promotes Osteosarcoma Progression by Targeting Ras-Related Protein RAP2B via miR-320b. *Oncol Res* (2018) 26(6):837–46. doi: 10.3727/096504017X14920318811721
17. Li GL, Wu YX, Li YM, Li J. High expression of long non-coding RNA XIST in osteosarcoma is associated with cell proliferation and poor prognosis. *Eur Rev Med Pharmacol Sci* (2017) 21(12):2829–34.
18. Li J PW, Yang P, Chen R, Gu Q, Qian W, Ji D, et al. MicroRNA-1224-5p Inhibits Metastasis and Epithelial-Mesenchymal Transition in Colorectal Cancer by Targeting SP1-Mediated NF-κB Signaling Pathways. *Front Oncol* (2020) 10:294. doi: 10.3389/fonc.2020.00294
19. Luo L, Ye G, Nadeem L, Fu G, Yang BB, Honarparvar E, et al. MicroRNA-378a-5p promotes trophoblast cell survival, migration and invasion by targeting Nodal. *J Cell Sci* (2012) 125(Pt 13):3124–32. doi: 10.1242/jcs.096412
20. Blanco FF, Preet R, Aguado A, Vishwakarma V, Stevens LE, Vyas A, et al. Impact of HuR inhibition by the small molecule MS-444 on colorectal cancer cell tumorigenesis. *Oncotarget* (2016) 7(45):74043–58. doi: 10.18632/oncotarget.12189
21. Wang W, Shen H, Cao G, Huang J. Long non-coding RNA XIST predicts poor prognosis and promotes malignant phenotypes in osteosarcoma. *Oncol Lett* (2019) 17(1):256–62. doi: 10.3892/ol.2018.9596
22. Liu H, Deng H, Zhao Y, Li C, Liang Y. LncRNA XIST/miR-34a axis modulates the cell proliferation and tumor growth of thyroid cancer through MET-PI3K-AKT signaling. *J Exp Clin Cancer Res CR* (2018) 37(1):279. doi: 10.1186/s13046-018-0950-9
23. Matoba S, Inoue K, Kohda T, Sugimoto M, Mizutani E, Ogonuki N, et al. RNAi-mediated knockdown of Xist can rescue the impaired postimplantation development of cloned mouse embryos. *Proc Natl Acad Sci U S A* (2011) 108 (51):20621–6. doi: 10.1073/pnas.1112664108
24. Wang J, Hjelmeland AB, Nabors LB, King PH. Anti-cancer effects of the HuR inhibitor, MS-444, in malignant glioma cells. *Cancer Biol Ther* (2019) 20 (7):979–88. doi: 10.1080/15384047.2019.1591673
25. Allegri L, Baldan F, Roy S, Aube J, Russo D, Filetti S, et al. The HuR CMLD-2 inhibitor exhibits antitumor effects via MAD2 downregulation in thyroid cancer cells. *Sci Rep* (2019) 9(1):7374. doi: 10.1038/s41598-019-43894-0
26. Yi X, Zhou Y, Zheng W, Chambers SK. HuR expression in the nucleus correlates with high histological grade and poor disease-free survival in ovarian cancer. *Aust New Z J Obstet Gynaecol* (2009) 49(1):93–8. doi: 10.1111/j.1479-828X.2008.00937.x
27. Fang Y, Fullwood MJ. Roles, Functions, and Mechanisms of Long Non-coding RNAs in Cancer. *Genomics Proteomics Bioinf* (2016) 14(1):42–54. doi: 10.1016/j.gpb.2015.09.006
28. Bach DH, Lee SK. Long noncoding RNAs in cancer cells. *Cancer Lett* (2018) 419:152–66. doi: 10.1016/j.canlet.2018.01.053
29. Dou Q, Xu Y, Zhu Y, Hu Y, Yan Y, Yan H. LncRNA FAM83H-AS1 contributes to the radioresistance, proliferation, and metastasis in ovarian cancer through stabilizing HuR protein. *Eur J Pharmacol* (2019) 852:134–41. doi: 10.1016/j.ejphar.2019.03.002
30. Zhang F, Ni H, Li X, Liu H, Xi T, Zheng L. LncRNA FENDRR attenuates adriamycin resistance via suppressing MDR1 expression through sponging HuR and miR-184 in chronic myelogenous leukaemia cells. *FEBS Lett* (2019). 593(15):1993–2007. doi: 10.1002/1873-3468.13480
31. Shen L, Han J, Wang H, Meng Q, Chen L, Liu Y, et al. Cachexia-related long noncoding RNA, CAAlnc1, suppresses adipogenesis by blocking the binding of HuR to adipogenic transcription factor mRNAs. *Int J Cancer* (2019) 145 (7):1809–21. doi: 10.1002/ijc.32236
32. Gao W, Gao J, Chen L, Ren Y, Ma J. Targeting XIST induced apoptosis of human osteosarcoma cells by activation of NF-kB/PUMA signal. *Bioengineered* (2019) 10(1):261–70. doi: 10.1080/21655979.2019.1631104
33. Xu T, Jiang W, Fan L, Gao Q, Li G. Upregulation of long noncoding RNA Xist promotes proliferation of osteosarcoma by epigenetic silencing of P21. *Oncotarget* (2017) 8(60):101406–17. doi: 10.18632/oncotarget.20738
34. Yang C, Wu K, Wang S, Wei G. Long non-coding RNA XIST promotes osteosarcoma progression by targeting YAP via miR-195-5p. *J Cell Biochem* (2018) 119(7):5646–56. doi: 10.1002/jcb.26743
35. Zhang R, Xia T. Long non-coding RNA XIST regulates PDCD4 expression by interacting with miR-21-5p and inhibits osteosarcoma cell growth and metastasis. *Int J Oncol* (2017) 51(5):1460–70. doi: 10.3892/ijo.2017.4127
36. Wu D, Nie X, Ma C, Liu X, Liang X, An Y, et al. RSF1 functions as an oncogene in osteosarcoma and is regulated by XIST/miR-193a-3p axis. *Biomed Pharmacother = Biomed Pharmacother* (2017) 95:207–14. doi: 10.1016/j.biopha.2017.08.068
37. Li H, Cui J, Xu B, He S, Yang H, Liu L. Long non-coding RNA XIST serves an oncogenic role in osteosarcoma by sponging miR-137. *Exp Ther Med* (2019) 17(1):730–8. doi: 10.3892/etm.2018.7032
38. Shen J, Xia W, Khotskaya YB, Huo L, Nakanishi K, Lim SO, et al. EGFR modulates microRNA maturation in response to hypoxia through phosphorylation of AGO2. *Nature* (2013) 497(7449):383–7. doi: 10.1038/nature12080
39. Huang JT, Wang J, Srivastava V, Sen S, Liu SM. MicroRNA Machinery Genes as Novel Biomarkers for CancerFrontiers in oncology. *Front Oncol* (2014) 4:113. doi: 10.3389/fonc.2014.00113
40. Kim HH, Kuwano Y, Srikantan S, Lee EK, Martindale JL, Gorospe M. HuR recruits let-7/RISC to repress c-Myc expression. *Genes Dev* (2009) 23(15):1743–8. doi: 10.1101/gad.1812509

Conflict of Interest: The authors declare that the research was conducted in the absence of any commercial or financial relationships that could be construed as a potential conflict of interest.

frontiers in Oncology

ORIGINAL RESEARCH
published: 19 March 2021
doi: 10.3389/fonc.2021.641184

Identification and Validation of the Prognostic Stemness Biomarkers in Bladder Cancer Bone Metastasis

Yao Kang[1,2†], *Xiaojun Zhu*[3,4,5†], *Xijun Wang*[4,5,6†], *Shiyao Liao*[1,2], *Mengran Jin*[1,2], *Li Zhang*[1,2], *Xiangyang Wu*[1,2], *Tingxiao Zhao*[1,2], *Jun Zhang*[1,2*], *Jun Lv*[1,2*] *and Danjie Zhu*[1,2*]

[1] Department of Orthopedics, Zhejiang Provincial People's Hospital, Hangzhou, China, [2] Department of Orthopedics, Hangzhou Medical College People's Hospital, Hangzhou, China, [3] Department of Musculoskeletal Oncology, Sun Yat-Sen University Cancer Center, Guangzhou, China, [4] State Key Laboratory of Oncology in South China, Guangzhou, China, [5] Collaborative Innovation Center for Cancer Medicine, Guangzhou, China, [6] Department of Head and Neck Surgery, Sun Yat-Sen University Cancer Center, Guangzhou, China

OPEN ACCESS

Edited by:
Dianwen Song, Shanghai First People's Hospital, China

Reviewed by:
Xudong Yao, Tongji University, China
Zongqiang Huang, First Affiliated Hospital of Zhengzhou University, China

***Correspondence:**
Jun Zhang
spinezhangjun@163.com
Jun Lv
13858010120@163.com
Danjie Zhu
zhudj@126.com

[†]*These authors have contributed equally to this work and share first authorship*

Specialty section:
This article was submitted to Molecular and Cellular Oncology, a section of the journal Frontiers in Oncology

Received: *13 December 2020*
Accepted: *29 January 2021*
Published: *19 March 2021*

Citation:
Kang Y, Zhu X, Wang X, Liao S, Jin M, Zhang L, Wu X, Zhao T, Zhang J, Lv J and Zhu D (2021) Identification and Validation of the Prognostic Stemness Biomarkers in Bladder Cancer Bone Metastasis. Front. Oncol. 11:641184. doi: 10.3389/fonc.2021.641184

Background: Bladder urothelial carcinoma (BLCA) is one of the most common urinary system malignancies with a high metastasis rate. Cancer stem cells (CSCs) play an important role in the occurrence and progression of BLCA, however, its roles in bone metastasis and the prognostic stemness biomarkers have not been identified in BLCA.

Method: In order to identify the roles of CSC in the tumorigenesis, bone metastasis and prognosis of BLCA, the RNA sequencing data of patients with BLCA were retrieved from The Cancer Genome Atlas (TCGA) databases. The mRNA expression-based stemness index (mRNAsi) and the differential expressed genes (DEGs) were evaluated and identified. The associations between mRNAsi and the tumorigenesis, bone metastasis, clinical stage and overall survival (OS) were also established. The key prognostic stemness-related genes (PSRGs) were screened by Lasso regression, and based on them, the predict model was constructed. Its accuracy was tested by the area under the curve (AUC) of the receiver operator characteristic (ROC) curve and the risk score. Additionally, in order to explore the key regulatory network, the relationship among differentially expressing TFs, PSRGs, and absolute quantification of 50 hallmarks of cancer were also identified by Pearson correlation analysis. To verify the identified key TFs and PSRGs, their expression levels were identified by our clinical samples *via* immunohistochemistry (IHC).

Results: A total of 8,647 DEGs were identified between 411 primary BLCAs and 19 normal solid tissue samples. According to the clinical stage, mRNAsi and bone metastasis of BLCA, 2,383 stage-related DEGs, 3,680 stemness-related DEGs and 716 bone metastasis-associated DEGs were uncovered, respectively. Additionally, compared with normal tissue, mRNAsi was significantly upregulated in the primary BLCA and also associated with the prognosis ($P = 0.016$), bone metastasis ($P < 0.001$) and AJCC clinical stage ($P < 0.001$) of BLCA patients. A total of 20 PSRGs were further screened by Lasso regression, and based on them, we constructed the predict model with a relatively high accuracy (AUC: 0.699). Moreover, we found two key TFs (EPO, ARID3A), four key

PRSGs (CACNA1E, LINC01356, CGA and SSX3) and five key hallmarks of cancer gene sets (DNA repair, myc targets, E2F targets, mTORC1 signaling and unfolded protein response) in the regulatory network. The tissue microarray of BLCA and BLCA bone metastasis also revealed high expression of the key TFs (EPO, ARID3A) and PRSGs (SSX3) in BLCA.

Conclusion: Our study identifies mRNAsi as a reliable index in predicting the tumorigenesis, bone metastasis and prognosis of patients with BLCA and provides a well-applied model for predicting the OS for patients with BLCA based on 20 PSRGs. Besides, we also identified the regulatory network between key PSRGs and cancer gene sets in mediating the BLCA bone metastasis.

Keywords: bladder urothelial carcinoma, bone metastasis, cancer stem cell, mRNAsi, prediction model

INTRODUCTION

Bladder urothelial carcinoma (BLCA) is the most common urinary system malignancies, with a high mortality and male predominance (1). With regard to localized disease, surgical treatment, or radiotherapy can be used with a favorable prognosis (2). However, as for metastatic BLCA, these therapeutic options often achieve limited effects in controlling the disease progression (3). Bone is a common metastatic site of BLCA, and the osteolytic destruction often induces skeletal-related events (SREs), such as local pain, pathologic fracture and even spinal cord compression (4). Thus, distant metastasis, in especial bone metastasis, has become the main cause which decreases the overall survival (OS) of patients with BLCA. Facing this clinical dilemma, it is important to investigate the potential tumorigenic and metastatic mechanism of BLCA, and subsequently identify its prognostic biomarkers and therapeutic targets.

The cancer cell population includes various tumor cells, cancer stem cells (CSCs) and microenvironment cells which make the heterogeneity (5). CSCs are specific cell types of malignancies and exhibit stem-like properties, such as self-renewal and initiating other types of cells (6). They are regarded as the main drivers of tumorigenicity, metastatic dissemination and treatment resistance (7). In BLCA, the relationship between molecular biology and CSCs has been addressed, and CSCs are regarded as an important factor inducing tumor recurrence and chemotherapeutic agents resistance (8). However, their roles in the distant metastasis of BLCA, especially bone metastasis, are still unclear.

With the development of bioinformatics, the features of CSC can be identified by deep learning methods which assist scientists in evaluating oncogenic dedifferentiation (9). Two indices have been proposed, namely mRNA expression-based stemness index (mRNAsi) and DNA methylation-based stemness index (mDNAsi). The former reflects the stemness gene expression and the latter shows the stemness epigenetic characteristics. Both of them have been proved to be associated with CSCs activity, along with tumor dedifferentiation and pathological grade (10). However, its roles in BLCA have not been identified, neither is bone metastasis.

In this study, RNA-seq data and clinical information of BLCA samples were collected from The Cancer Genome Atlas (TCGA) databases and the differential expressed genes (DEGs) were identified, along with the association between mRNAsi and tumorigenesis, bone metastasis and patients' OS. The prognostic stemness-related genes (PSRGs) were also found and based on them, we constructed the predict model. Moreover, the regulatory mechanism of PSRGs and downstream signaling pathway were also explored to provide the prognostic biomarkers and therapeutic targets which may assist oncologists in the prediction of BLCA occurrence and bone metastasis, along with the clinical treatment.

METHOD

Data Extraction

In formats of raw-counts and Fragments Per Kilobase per Million (FPKM), RNA sequencing data of 411 primary BLCA samples and 19 normal solid tissue samples were downloaded from The Cancer Genome Atlas (TCGA) (https://tcga-data.nci.nih.gov). Bone metastasis diagnosis was specifically concerned, and other selected potential factors include demographics data (i.e., age at diagnosis, race, and gender), tumor information (i.e., histologic grade, AJCC clinical stage, TNM classification), and endpoint data (i.e., OS status and OS time). All of them were extracted in eXtensible Markup Language (XML) files from the database.

The Estimation of mRNAsi

In the current study, the normalized gene expression profiles of each sample were used to estimate the mRNAsi by the algorithm named one-class logistic regression machine learning (OCLR). In the original article of mRNAsi, Malta, T.M., et al. reported mRNAsi as an index between 0 and 1, which could evaluate the activity of CSCs, dedifferentiation of malignant cells (9).

Differential Expression Analysis and Functional Enrichment Analysis

Statistical analysis began with four different groups of DEGs analysis by edgeR algorithm. $|\log2$ Fold Change (FC)$| > 1.0$ and False Discovery Rate (FDR) value < 0.05 were used as the

screening criteria in the identification of DEGs. The groups of DEGs were as follows: primary BLCA vs normal solid tissue; Stage I/II BLCA vs Stage III/IV BLCA; low mRNAsi BLCA vs high mRNAsi BLCAs (divided by the median mRNAsi); BLCA without bone metastasis vs BLCA with bone metastasis.

The Gene Ontology (GO), Kyoto Encyclopedia of Genes and Genomes (KEGG) enrichment analysis as well as Gene Set Enrichment Analysis (GSEA) were used to explore the potential signaling pathways in the tumorigenesis, progression and metastasis (11). Both of them were conducted in our study. GO analysis can illuminate the biological processes (BPs), cellular components (CCs), and molecular functions (MFs) of enriched DEGs, and KEGG analysis describes the pathophysiologic pathways while 50 hallmarks of cancer gene sets were retrieved from Molecular Signatures Database (MSigDB) v7.0 (https://www.gsea-msigdb.org/gsea/msigdb/index.jsp) for GSEA (12).

The Identification of PRSGs

The intersection of identified DEGs in these four groups were integrated into the univariate Cox regression analysis. Genes with $p<0.05$ in the univariate Cox regression analysis were defined as PRSGs. Next, all the PRSGs were included in the multivariate Cox analysis. The Least Absolute Shrinkage and Selection Operator (LASSO) regression analysis were utilized to ensure no overfitting of the final multivariate Cox model and the five-fold cross-validation was performed. In terms of model diagnosis, the discrimination and goodness of fit (GOF) of the multivariate model were illustrated by the area under curve (AUC) of receiver operator characteristic (ROC) curve for five-year OS and the Cox-Snell residual plot, respectively.

The Calculation of Prognostic Index (PI) and Independent Prognosis Analysis

The formula of the multivariate Cox model (as followed) was used to calculate the PI for each BLCA patient.

$$PI_m = \beta 1 \times PRSG_1 + \beta 2 \times PRSG_2 + \beta 3 \times PRSG_3 \ldots \ldots + \beta n \times PRSG_n$$

In the formula, "m" represented the number of each BLCA patient; "n" represented the number of prognostic PRSG in the multivariate model; "β" represented the coefficient of each PRSG in the multivariate model. In addition, all BLCA patients were divided into the high-risk group or low-risk group according to the median of PI. Moreover, the independent prognosis value of the PI in BLCA was evaluated by Kaplan-Meier survival analysis, univariate Cox analysis and multivariate Cox analysis corrected by age at diagnosis, gender and AJCC clinical stage.

The Construction of the Prognostic Nomogram

The Cox models including PI were used to construct the prognostic nomogram, which could predict the 3-, 5- and 8-year OS probability of BLCA patients. The calibration plot was used to illuminate the calibration of the prognostic nomogram. The decision curve and time-related ROC with 95% confidence interval were also conducted to illustrate the patient benefit and the discrimination of the nomogram.

The Identification of Transcription Factors (TFs) and Signaling Pathways Co-Expressed With PRSGs

First of all, official gene symbol of 318 cancer related TFs, 50 hallmarks of cancer gene sets were retrieved from Cistrome database (http://cistrome.org/) and Molecular Signatures Database (MSigDB) v7.0 (https://www.gsea-msigdb.org/gsea/msigdb/index.jsp), respectively (12, 13). Absolute quantification of the 50 hallmark of cancer gene sets in all the samples were quantified as continuous variables by Gene Set Variation Analysis (GSVA) (14). Then, the co-expression analysis was performed among differential expressed TFs, PRSGs and absolute quantification of 50 hallmarks of cancer. Interaction pairs between TFs and PRSGs with $|\text{correlation coefficient}| > 0.40$ and P value < 0.05 along with interaction pairs between PRSGs and hallmarks of cancer with $|\text{correlation coefficient}| > 0.25$ and P value < 0.05 were used to construct the regulatory network among TFs, PRSGs, and hallmarks of cancer.

Immunohistochemistry (IHC) Validation

The IHC slides and information were obtained from the Human Protein Atlas. Immunostaining on each slide was assessed by experienced pathologists to examine the percentage of EPO, ARID3A, CGA, and SSX3 positive tumor cells (11).

ATAC-Seq

Assay for Targeting Accessible-Chromatin with high-throughout sequencing (ATAC-seq) data available from TCGA GDC (https://gdc.cancer.gov/about-data/publications/ATACseq-AWG) were used to validated the regulation mechanism of key PRSGs (15). Gviz package of Bio-conductor were used to visualize the accessible peaks (16).

Statistics Analysis

Discontinuous variables should be presented as percentages while continuous variables in normal distribution should be described as mean ± standard deviation (SD) or else reported as median (Range). Variance homogeneous and normal distributed continuous variables could be compared by student t-test, otherwise, the Mann-Whitney U-test or Kruskal-Wallis H-test should be used. In this study, only two-sided P value < 0.05 was considered as statistically significant for all analysis process. The R software (www.r-project.org; version 3.6.1; Institute for Statistics and Mathematics, Vienna, Austria) were used for all statistics analysis processes.

RESULTS

DEGs Analysis and Functional Enrichment Analysis

The analysis process of the current study was summarized in the flowchart (**Figure 1**). In DEG analysis, all RNA-seq data were from

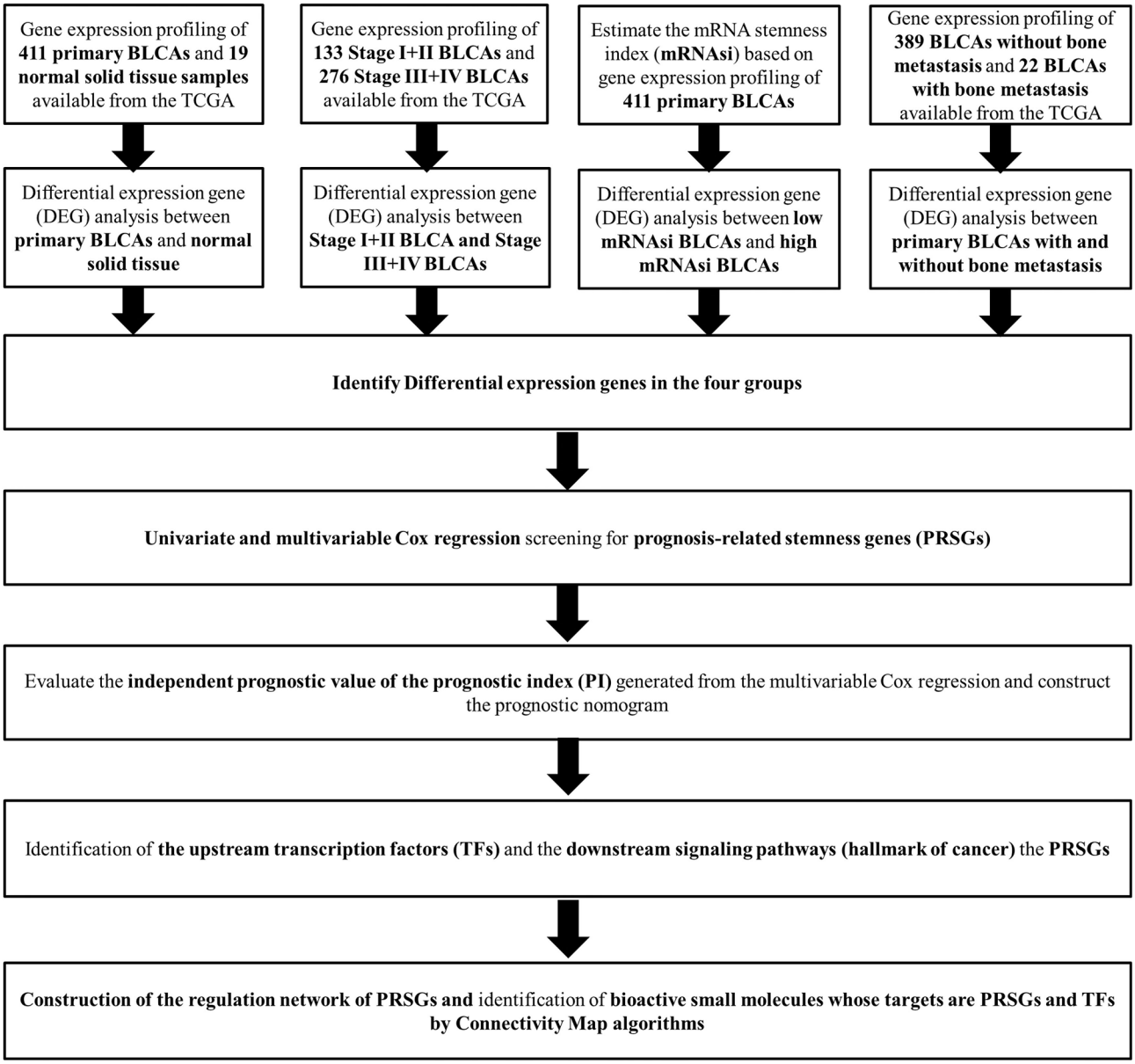

FIGURE 1 | The flowchart of all analysis processes.

primary BLCA samples or normal solid tissues, not distant metastasis tumors. All samples with missing grouping information (normal or tumor; stage I/II or stage III/IV; low mRNAsi or high mRNAsi; primary BLCAs without bone metastasis or primary BLCAs with bone metastasis) were deleted. A total of 8,647 genes (2,949 downregulated genes and 5,698 upregulated genes) were identified as DEGs between 411 primary BLCAs and 19 normal solid tissue samples in the heatmap (**Figure 2A**). The volcano plot of these DEGs were presented in **Figure 2B**. In order to explore the features of identified DEGs, GO, and KEGG analysis were used. The significant enrichment items of biological processes (BPs), cellular components (CCs), molecular functions (MFs) were muscle system process, collagen-containing extracellular matrix, and receptor ligand activity, respectively (**Figure 2C**). The KEGG pathways identified neuroactive ligand-receptor interaction, PI3K-Akt signaling pathway, MAPK signaling pathway. and cytokine-cytokine receptor interaction as the key enriched signaling pathways (**Figure 2D**). And the enrichment plots of top five significant Hallmark gene set in GSEA were shown in **Figure 2E**, illustrating that DNA repair, myc targets, E2F targets

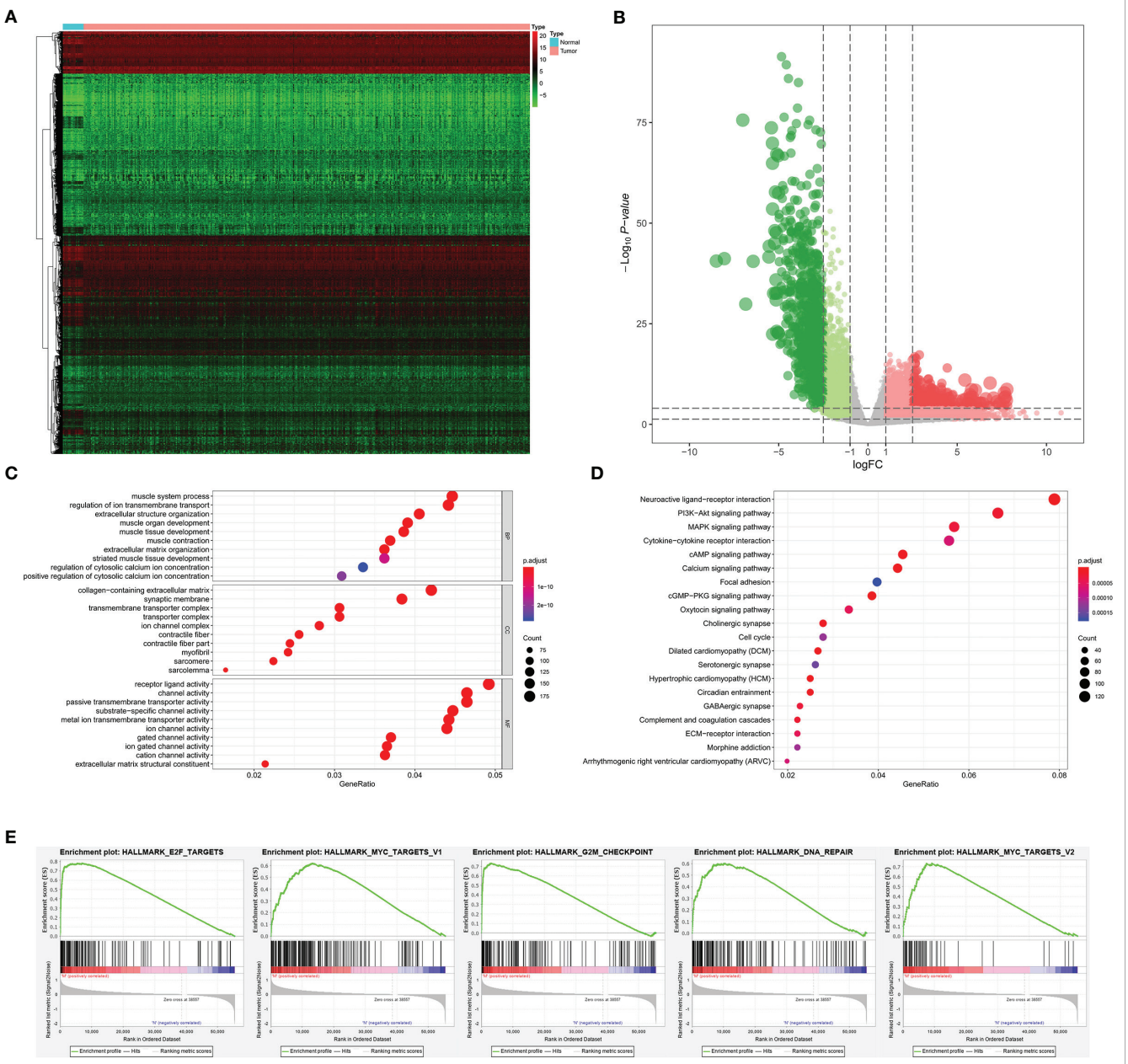

FIGURE 2 | The results of differential expression genes analysis and functional enrichment analysis between primary BLCAs and normal solid tissue samples: The heatmap **(A)** and volcano plot **(B)** of the differential expressed genes. The GO **(C)**, KEGG **(D)**, and **(E)** top five GSEA enriched terms for the differential expressed genes.

and G2M checkpoint were the most significant enrichment items.

Among 389 primary BLCA samples, 113 Stage I/II BLCAs were identified, along with 276 Stage III/IV BLCAs. A total of 2,383 DEGs (700 downregulated ones and 1,683 upregulated ones) were uncovered between Stage I/II and III/IV BLCAs. The heatmap and volcano plot were shown in **Figures 3A, B**. The GO enrichment items included skin development, collagen-containing extracellular matrix, receptor ligand activity (**Figure 3C**). KEGG analysis uncovered the roles of neuroactive ligand-receptor interaction, PI3K-Akt signaling pathway and Ras signaling pathway (**Figure 3D**). And the GSEA results suggested that myogenesis, epithelial-mesenchymal transition (EMT), apical junction, angiogenesis, and KRAS targets were the most significant enrichment items with the progression of tumor stages (**Figure 3E**).

The stemness DEGs was identified by low mRNAsi BLCAs and high mRNAsi BLCAs (divided by the median mRNAsi). Then, a total of 3,680 stemness DEGs including 1,403

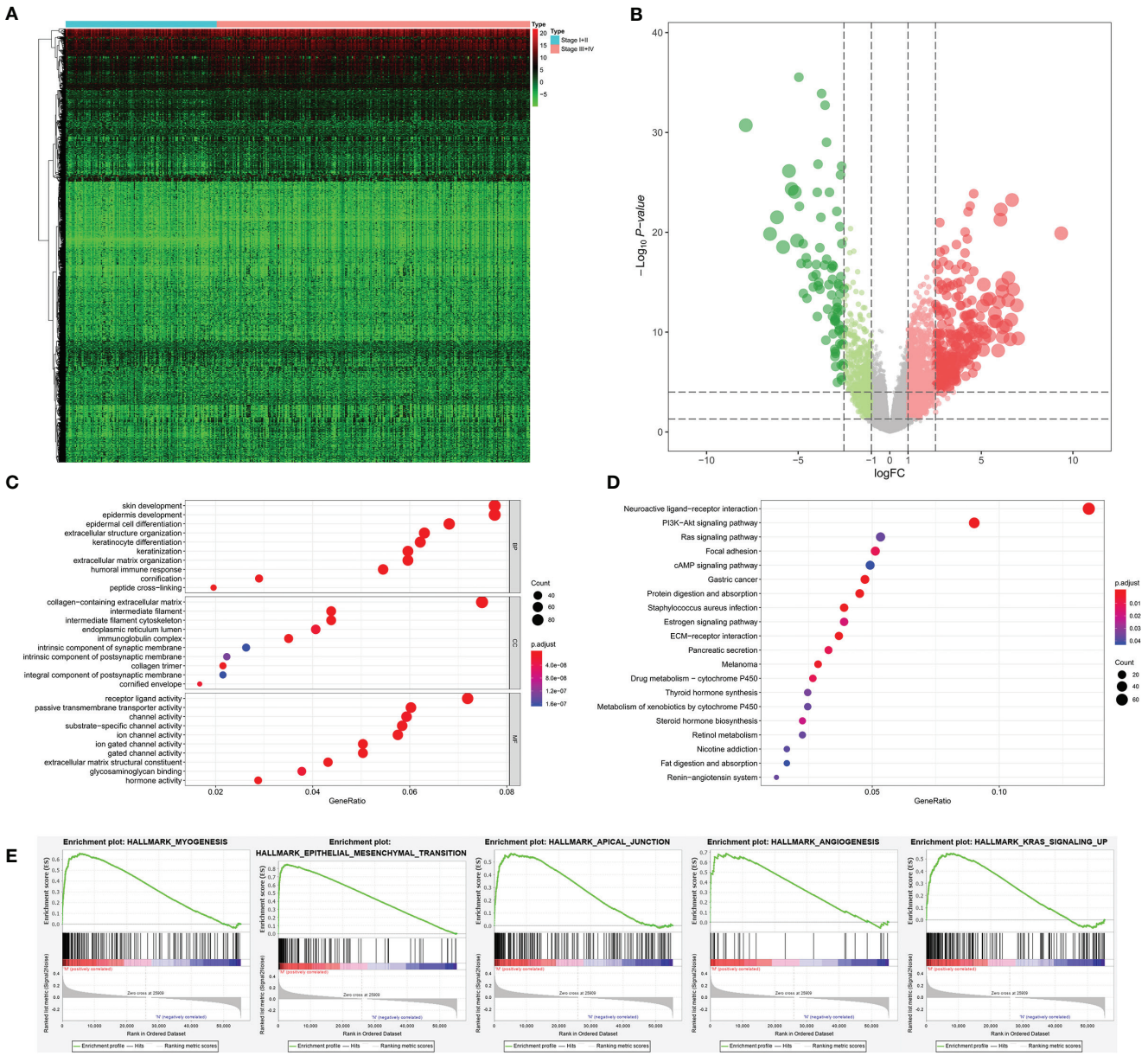

FIGURE 3 | The results of differential expression genes analysis and functional enrichment analysis between Stage I or II BLCAs and Stage III or IV BLCAs: The heatmap **(A)** and volcano plot **(B)** of the differential expressed genes. The GO **(C)**, KEGG **(D)**, and **(E)** top five GSEA enriched terms for the differential expressed genes.

downregulated ones and 2,277 upregulated ones were found (**Figures 4A, B**). Extracellular structure organization, collagen-containing extracellular matrix, receptor ligand activity were the most significant enrichment items of BPs, CCs, MFs associated with stemness (**Figure 4C**). Neuroactive ligand-receptor interaction, PI3K-Akt signaling pathway and calcium signaling pathway were stemness-associated KEGG pathways (**Figure 4D**). Similarly, the myogenesis, epithelial-mesenchymal transition (EMT), apical junction, and KRAS targets were also identified as most significant enrichment items related to mRNAsi in GSEA (**Figure 4E**).

As for bone metastasis, the dataset consisted of 389 primary BLCAs without bone metastasis and 22 primary BLCAs with bone metastasis. The DEGs were also explored between them and we identified a total of 716 bone metastasis-associated DEGs including 143 downregulated genes and 573 upregulated genes. The heatmap and volcano plot were shown in **Figures 5A, B**. The bone metastasis-associated DEGs enriched in the GO items of

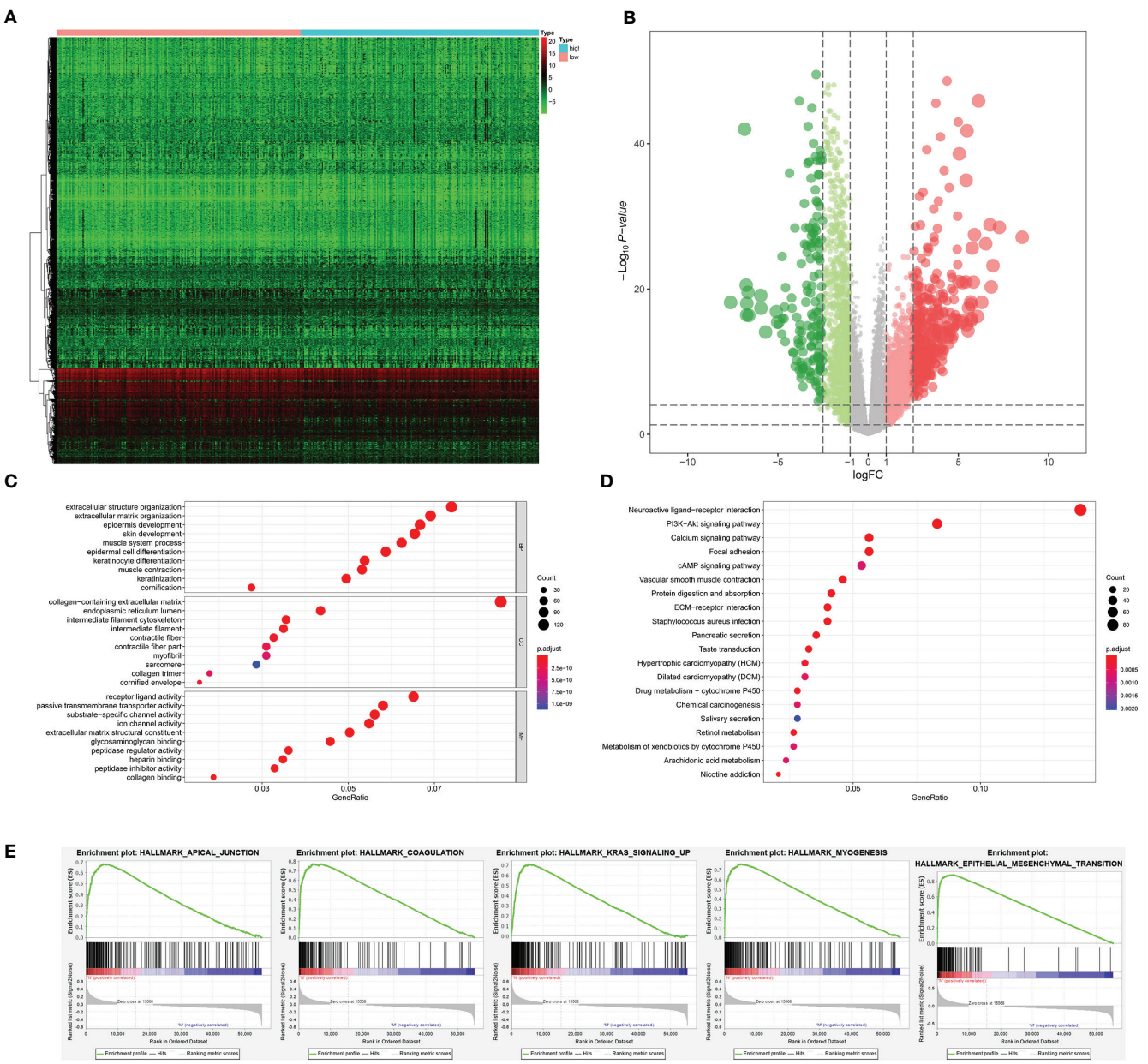

FIGURE 4 | The results of differential expression genes analysis and functional enrichment analysis between low mRNAsi BLCAs and high mRNAsi BLCAs: The heatmap **(A)** and volcano plot **(B)** of the differential expressed genes. The GO **(C)**, KEGG **(D)**, and **(E)** top five GSEA enriched terms for the differential expressed genes.

signal release, synaptic membrane and substrate-specific channel activity (**Figure 5C**). KEGG items of neuroactive ligand-receptor interaction and cytokine-cytokine receptor interaction were also significantly enriched in the bone metastasis-specific DEGs (**Figure 5D**). And the enrichment plots of top five significant Hallmark gene set in GSEA were shown in **Figure 5E**, showing that TNFA targets, IL6-JAK-STAT3 signaling, coagulation, complement, and P53 targets were the most significant enrichment items related to bone metastasis of BLCA.

The Clinic Correlation of mRNAsi

Totally, 66 genes in the four groups of DEGs analysis were intersected by Venn plot and 13 genes were significantly up-regulated in the four DEG group (**Figure 6A**). The results of non-parametric tests (Mann-Whitney U-test or Kruskal-Wallis H-test) and Kaplan-Meier survival analysis suggested that compared with the normal solid tissue, mRNAsi was abnormally upregulated in the primary BLCA ($P < 0.001$, **Figure 6B**) and significantly associated with the prognosis of

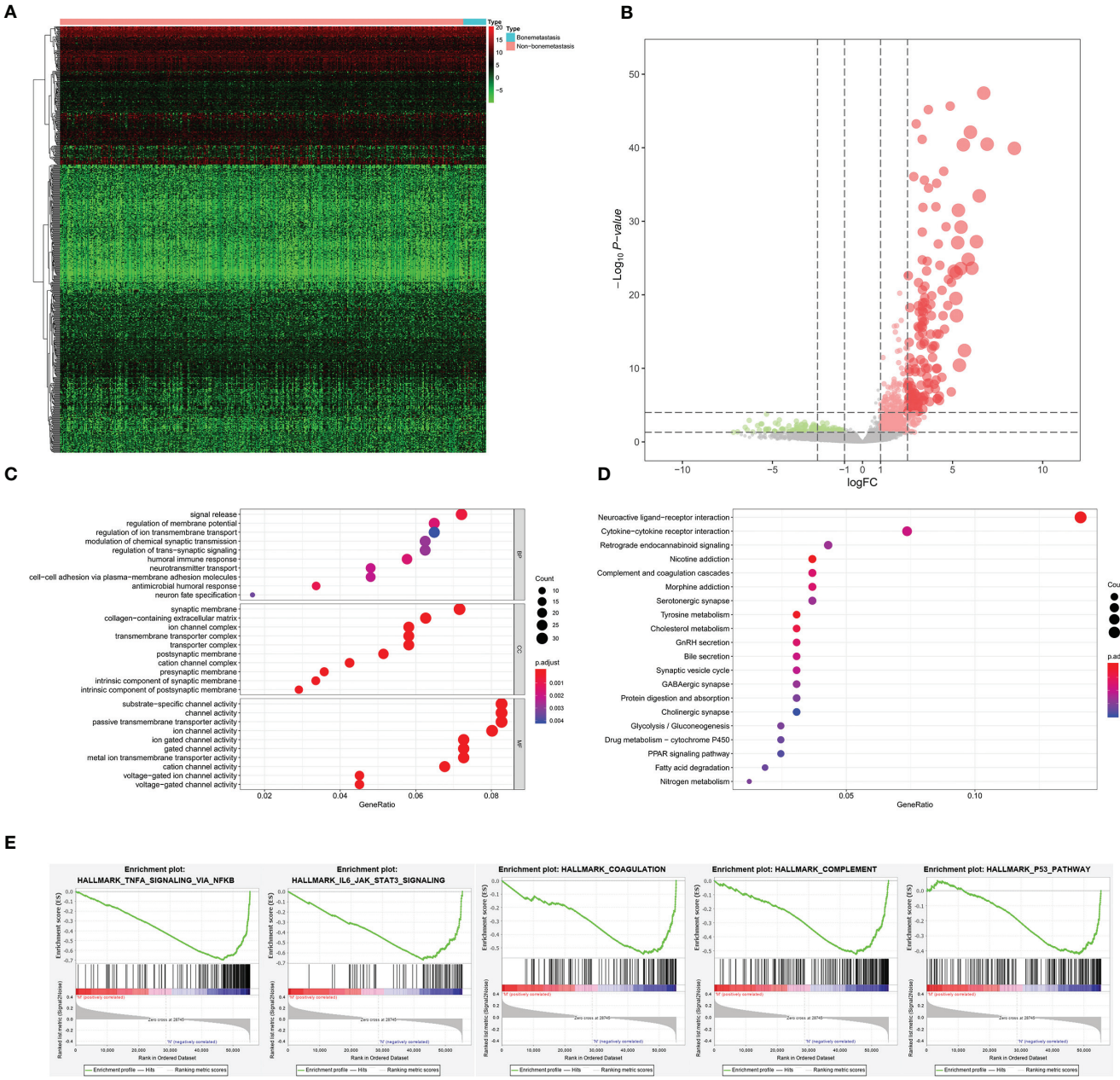

FIGURE 5 | The results of differential expression genes analysis and functional enrichment analysis between BLCAs with and without bone metastasis: The heatmap **(A)** and volcano plot **(B)** of the differential expressed genes. The GO **(C)**, KEGG **(D)**, and **(E)** top five GSEA enriched terms for the differential expressed genes.

BLCA patients (P = 0.016, **Figure 6C**), bone metastasis diagnosis (P < 0.001, **Figure 6D**) and AJCC clinical stage (P < 0.001, **Figure 6E**). Besides, the expression levels of these 66 genes were presented in the heatmap (**Figure 6F**).

The Identification of PRSGs and Independent Prognosis Analysis

First of all, 66 DEGs intersected by Venn plot were incorporated into the univariate Cox regression analysis. Then, 20 genes with prognostic values in the univariate Cox regression analysis were defined as PRSGs integrated into the LASSO regression analysis (**Figures 7A, B**), suggesting that only 13 PRSGs (NTSR1, PRRG3, CGA, UNC5C, LINC00922, SSX3, CHRND, MYBPH, ROS1, TNN, SPANXB1, CASC22, and C6orf15) were essential for model fitting (**Figure 7C**).

The PI for each BLCA patient was calculated by the formula described in the methodology. The distribution of PI among all BLCA patients were shown by the risk line and risk scatterplot

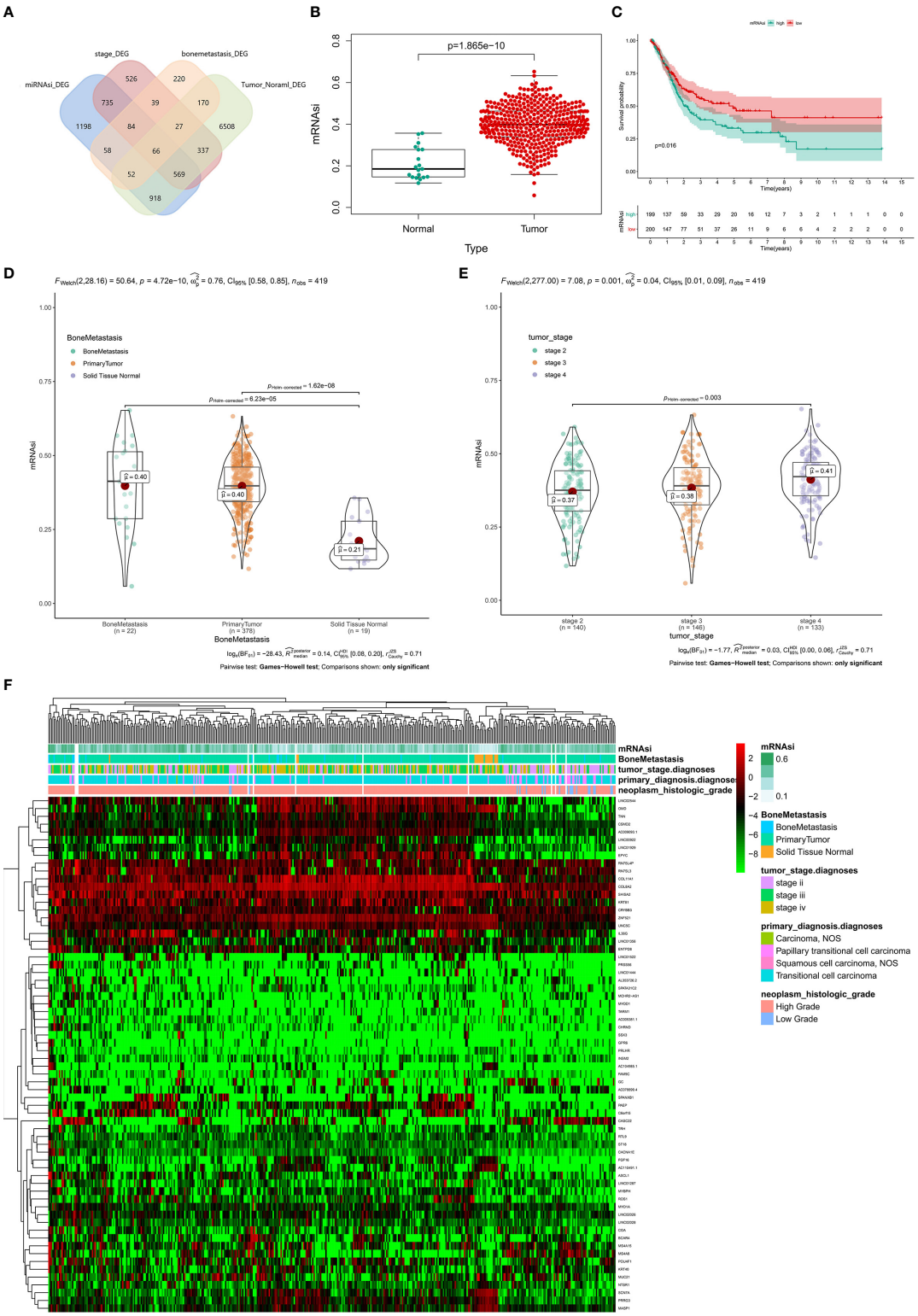

FIGURE 6 | The clinical relevance of mRNAsi and identification of stemness-related genes. **(A)** The Venn plot of the tumorigenesis-, stemness-, stage- and bone metastasis-related differential expressed genes. **(B)** The difference of mRNAi between normal and tumor group. **(C)** Kaplan-Meier survival analysis of mRNAsi between normal and tumor group. **(D)** The difference of mRNAi among normal, tumor and bone metastasis. **(E)** The difference of mRNAi among different clinical stage. **(F)** The heatmap of mRNAsi, bone metastasis, tumor stage, primary diagnosis and neoplasm histologic grade.

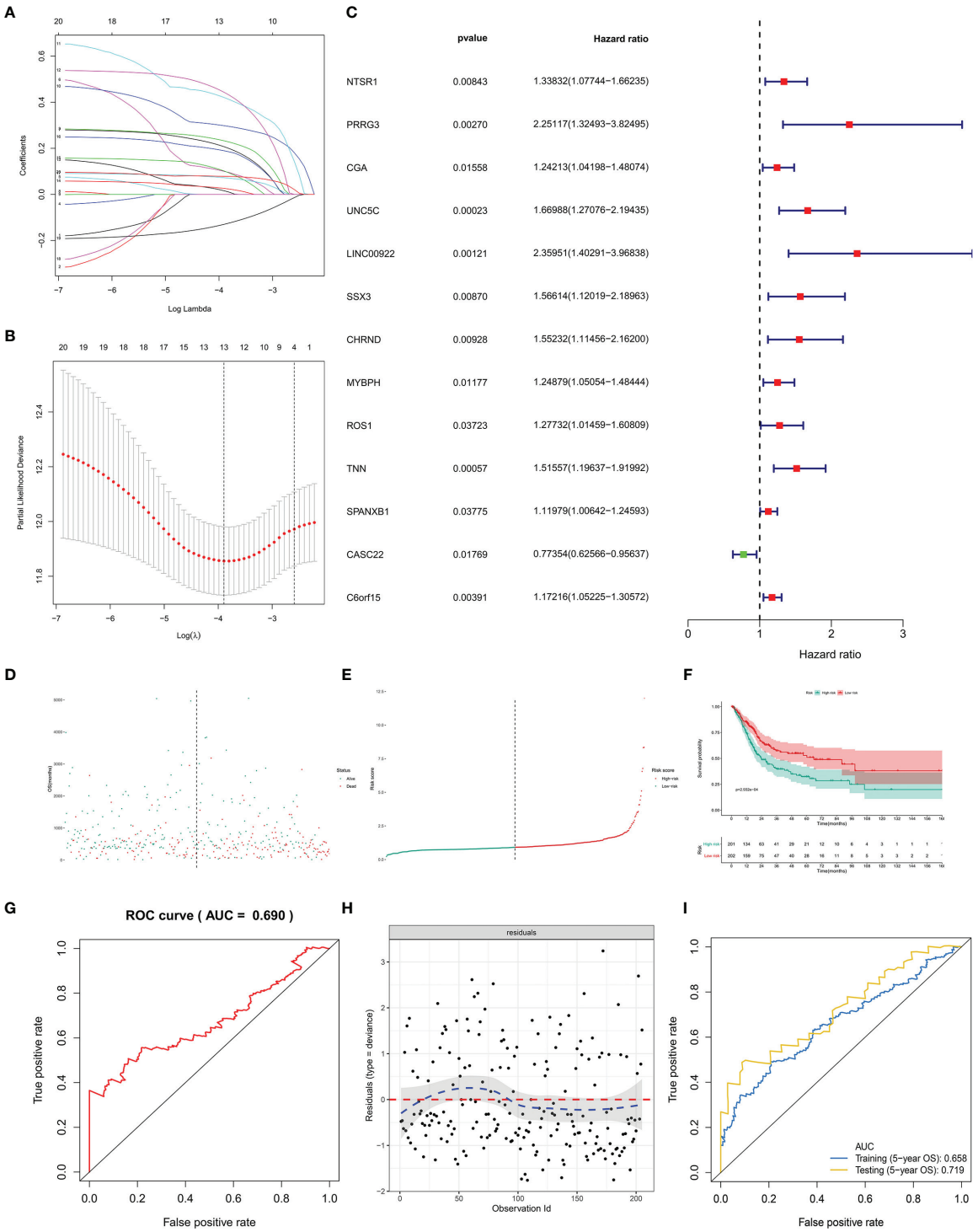

FIGURE 7 | The model diagnosis of multivariate Cox model including prognostic stemness-related genes. **(A)** The final multivariate model of the 20 prognostic stemness-related genes. **(B–E)** The LASSO regression analysis of the model. **(F)** The Kaplan-Meier analysis of the risk score. The ROC curve **(G)** and residual plot **(H)** of the multivariate model. **(I)** And the five-fold cross-validation of the multivariate Cox model was performed, also showing similar discriminations to the original model (AUC of training dataset (5–year OS) = 0.658; AUC of testing dataset (5–year OS) = 0.719).

(**Figures 7D, E**). The Kaplan-Meier survival curve suggested that PI had prognostic value for BLCA patients (**Figure 7F**, P < 0.001). Moreover, the ROC of five-year of OS (AUC = 0.699, **Figure 7G**) and the residual plot (**Figure 7H**) illustrated an acceptable discrimination and GOF of the multivariate Cox regression model. And the five-fold cross-validation of the multivariate Cox model was performed, also showing similar discriminations to the original model (AUC of training dataset (5−year OS) = 0.658; AUC of testing dataset (5−year OS) = 0.719) (**Figure 7I**).

Construction of the Prognostic Nomogram

PI was then tested in the univariate and multivariate Cox model corrected by demographics and AJCC clinical stage. The results revealed that PI was an independent factor for predicting prognosis of BLCA in the univariate (HR = 60.735, 95%CI (17.376–212.289), P < 0.001, **Figure 8A**) and multivariate (HR = 1.412, 95%CI (1.256–1.558), P < 0.001, **Figure 8B**) Cox model. Besides, T stage and tumor grade were also integrated into univariate and multivariate Cox analyses to correct the PI, illustrating that PI was still an independent factor for predicting prognosis of BLCA in the univariate (HR = 1.456, 95%CI (1.315-1.612), P < 0.001, **Figure S1A**) and multivariate (HR = 1.480, 95%CI (1.324-1.654), P < 0.001, **Figure S1B**) Cox model.

Based on the Cox model, the prognostic nomogram was constructed to predict the 3-, 5-, and 8-year OS probability of BLCA patients (**Figure 8C**). The calibration curve illustrated acceptable calibration of the prognostic nomogram (**Figure 8D**). Additionally, the decision curve and time-related ROC with 95% confidence interval were also conducted to illustrate the patient benefit and the discrimination of the nomogram (When threshold probability of the nomogram was greater than 0.42, all patients could benefit from this model) (**Figures 8E, F**). Especially, as a clinical bioinformatics study, the gene expression levels should be corrected by demographics in multivariate regression models and age should to be treated as a categorical variable in the perspectives of some researchers. However, as age and gender were not significant in the multivariate Cox analysis, these two factors were inappropriate for nomogram construction. And to preserve more modeling samples, some other important clinicopathological features such as histology subtype, grade, pathologic T/N/M classification, and primary diagnosis were not included in the multivariate regression model. To further reduce these biases, the other five multivariate regression models were also constructed and diagnosed by calibration, time-related ROC and decision curve (**Figure S2**: modeling with 205 objectives same to **Figure 8** and treating age as a categorical variable) (**Figure S3**: modeling with all 403 objectives with all available variables and missing values) (**Figure S4**: modeling with all 403 objectives with all missing values and available variables except for age and gender) (**Figure S5**: modeling with 164 objectives with all available variables and excluding all missing values) (**Figure S6**: modeling with 164 objectives with all available variables except for age and gender and excluding all missing values). Especially, some paradoxical results could be found in these five multivariate regression models (e.g., malignant clinicopathological features achieved lower points in **Figure S3**; N1 achieved lower points than N0 in **Figure S3**). These problems might be caused by the several reasons. First, some missing values affected the fitting of the regression models, showing in the residual plots. Second, some clinicopathological features had endogenous interaction such as the AJCC stage was evaluated by T/N/M classification. Last but not least, although some variables contradicted to the clinical experiences in nomograms, these variables were not showing significant results in the multivariate regression models. Therefore, these variables could not be regarded as independent prognostic factors for BLCA patients, and were not suitable to illustrate in the nomograms. In order to distinguish the significant variables from the others, asterisks were used to annotate the statistical significance of each variables (***: P < 0.001; **: P < 0.01; **: P < 0.05). In sum, these five multivariate regression models and nomograms had limited clinical significance of predicting BLCA patients. However, PI was an independent factor in each multivariate regression model for predicting prognosis of BLCA.

Identification of the PRSGs Co-Expressed Upstream TFs and the Downstream Signaling Pathways

A total of 86 differentially expressed TFs were identified between primary BLCAs and normal solid tissue samples. Their association with mRNAi, bone metastasis, tumor stage diagnoses, primary diagnosis, and neoplasm histologic grade were shown in the heatmaps (**Figure 9A**). The differentially expressed TFs were also presented in the volcano plots (**Figure 9B**). The relationships between 50 hallmarks of cancer gene sets and mRNAi, bone metastasis, tumor stage diagnoses, primary diagnosis, and neoplasm histologic grade were also shown in the heatmaps (**Figure 9C**). The volcano plots also described their expressions between primary BLCAs and normal solid tissue samples (**Figure 9D**). Among the above-mentioned 20 PRSGs, only four genes (CACNA1E, LINC01356, CGA, and SSX3) have consistent tendency in the four DEG group. Furthermore, point to point co-expression analysis were conducted among these four PRSGs, 86 TFs and absolute quantification of 50 hallmarks of cancer. Interaction pairs between TFs and PRSGs with | correlation coefficient| > 0.30 and P value < 0.05 along with interaction pairs between PRSGs and hallmarks of cancer with P value < 0.05 were used to construct the regulation network among TFs, four key PRSGs (CACNA1E, LINC01356, CGA, and SSX3) and hallmarks of cancer. In the heatmap of key hallmarks of cancer gene sets, we found the enrichment of oxidative phosphorylation, DNA repair, peroxisome, myc targets, E2F targets, mTORC1 signaling, unfolded protein response, cholesterol homeostasis, glycolysis, and UV response in the groups of tumorigenesis and bone metastasis. A total of 48 co-expression interaction pairs between TFs and PRSGs, and two co-expression interaction pairs between PRSGs and hallmarks of cancer passed the criteria and were used to construct the regulation network (**Figures 9E, F**). The regulation networks implied the correlation among CACNA1E, SSX3, LINC01356, DNA repair, myc targets, E2F targets, mTORC1 signaling, and

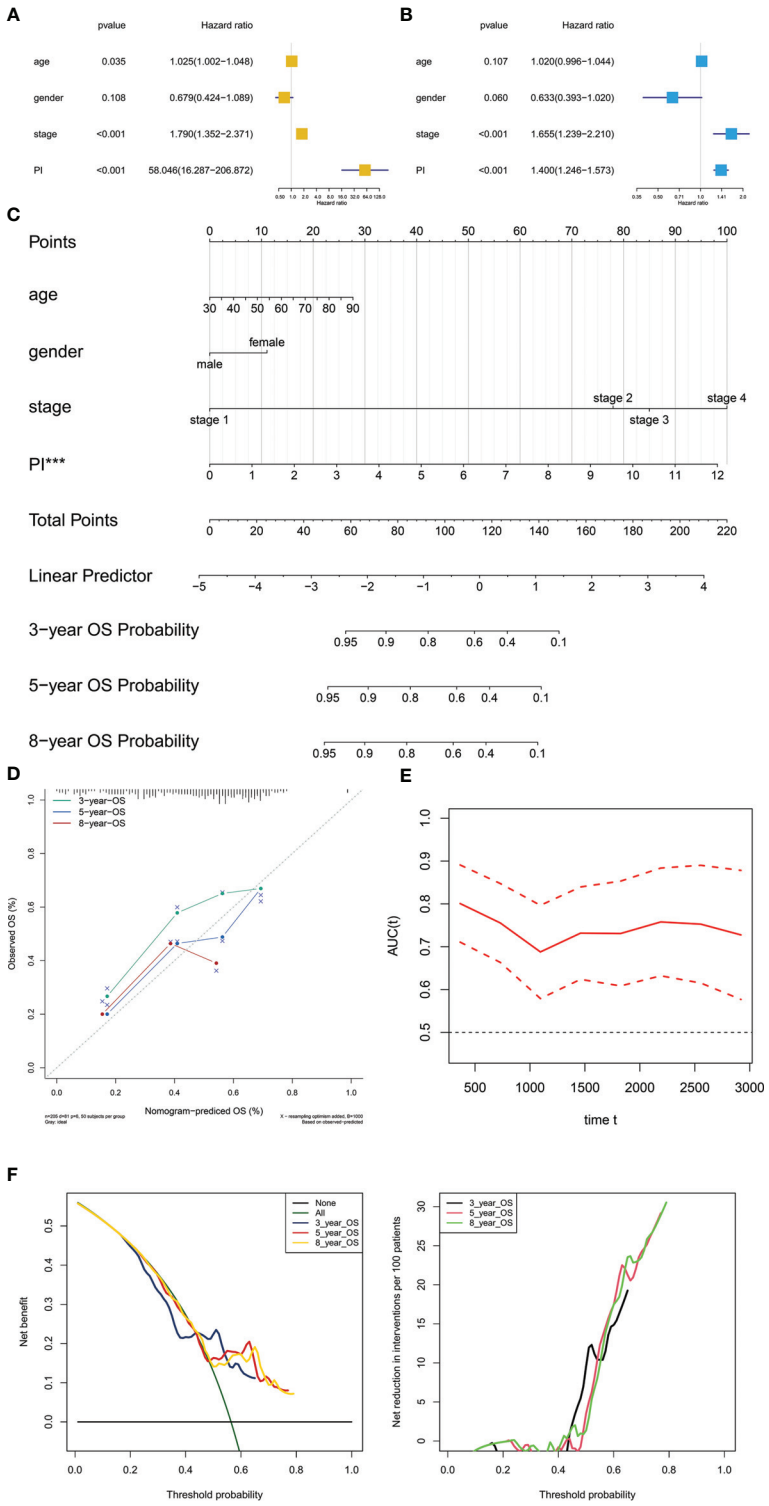

FIGURE 8 | Independent prognosis analysis and construction of the prognostic nomogram. The univariate **(A)** and multivariate **(B)** Cox regression model corrected by demographics and stage. The constructed prognostic nomogram based on the multivariate Cox model **(C)**. The calibration curve illustrated acceptable calibration of the prognostic nomogram **(D)**. Additionally, the decision curve and time-related ROC with 95% confidence interval were also conducted to illustrate the patient benefit and the discrimination of the nomogram **(E, F)**. (***P < 0.001; **P < 0.01; **P < 0.05).

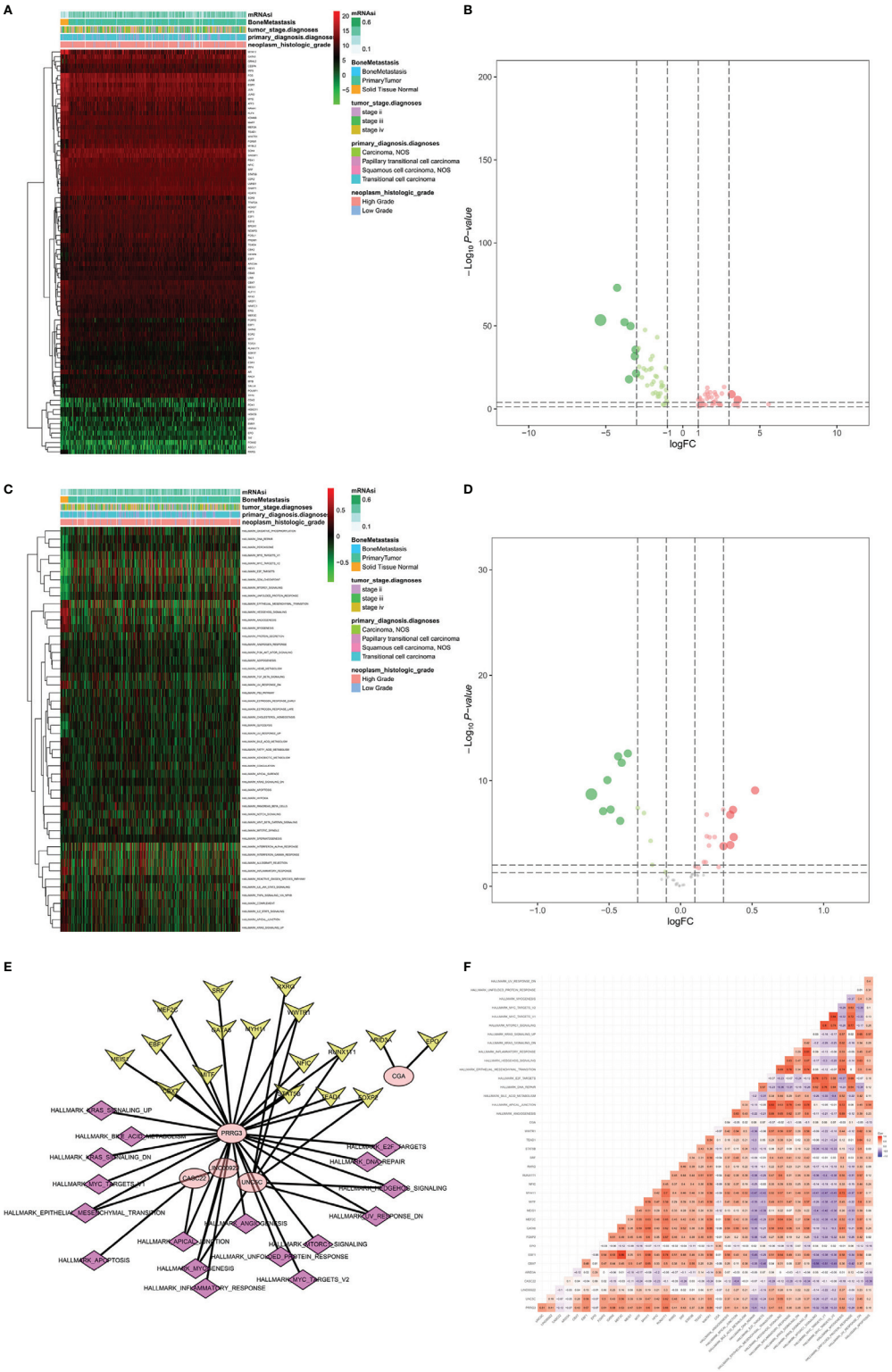

FIGURE 9 | Identification of the PRSGs co-expressed upstream TFs, the downstream hallmarks of cancer gene sets. The heatmap **(A)** and volcano plot **(B)** of differentially expressed TFs between primary BLCAs and normal solid tissue samples. The heatmap **(C)** and volcano plot **(D)** of differentially expressed hallmarks of cancer gene sets between primary BLCAs and normal solid tissue samples. The point to point co-expression analysis **(E)** and co-expression interaction pairs **(F)** between TFs, PRSGs, and hallmarks of cancer.

unfolded protein response, which may regulate the tumorigenesis and bone metastasis of BLCA.

The protein levels of key TFs and PRSGs were further validated by IHC. The representative images of IHC revealed that the four proteins were highly expressed in BLCA by our samples (**Figure 10**). In the Human Protein Atlas, EPO was significantly higher in BLCA than that in normal urinary bladder (**Figure S7A**). The ARID3A and SSX3 highly expressed in BLCA, but barely found in normal urinary bladder (**Figure S7B, C**). The CGA was found in neither BLCA nor normal urinary bladder tissues (**Figure S7D**).

The ATAC-seq data of BLCA were further used to validate the regulation mechanism of four key PRSGs (ARID3A, **Figure 11A**; CGA, **Figure 11B**; EPO, **Figure 11C**; SSX3, **Figure 11D**), illustrating their accessible peaks in the chromatin.

DISCUSSION

Bladder cancer is a heterogeneous group of tumors with more than 40 histological subtypes of pathological patterns (2). BLCA is the common subtype, with a high metastasis rate (17). CSCs are considered responsible for many important aspects of tumors, such as tumorigenesis, progression and treatment recurrence, however, their roles in the tumorigenesis and metastasis have not been identified clearly in the BLCA. In this study, we identified mRNAsi as a reliable index for the tumorigenesis, prognosis, AJCC clinical stage and bone metastasis of BLCA. In addition, we found 20 key PRSGs which were associated with the tumorigenesis, clinical stage and bone metastasis. Based on them, a well-applied predict model was constructed which may assist urological surgeons in predicting the prognosis and bone metastasis of BLCA. Furthermore, based on multivariate Cox model and correlation analysis, CACNA1E, LINC01356, CGA, and SSX3 were inferred as potential diagnostic biomarkers and therapeutic targets for BLCA and its bone metastasis.

As a population of cancer cells, CSCs are regarded as the tumor initiating cells and therapeutic refractoriness cells (18). Nowadays, single-cell sequencing was used to identify the human bladder cancer stem cells (BCSCs) and uncovered 21 key altered genes in BCSCs (8). Many other studies also focused on the CSCs regulation in BLCA to investigate the potential mechanism and candidate targets (19–21). For example, CD24 could maintain

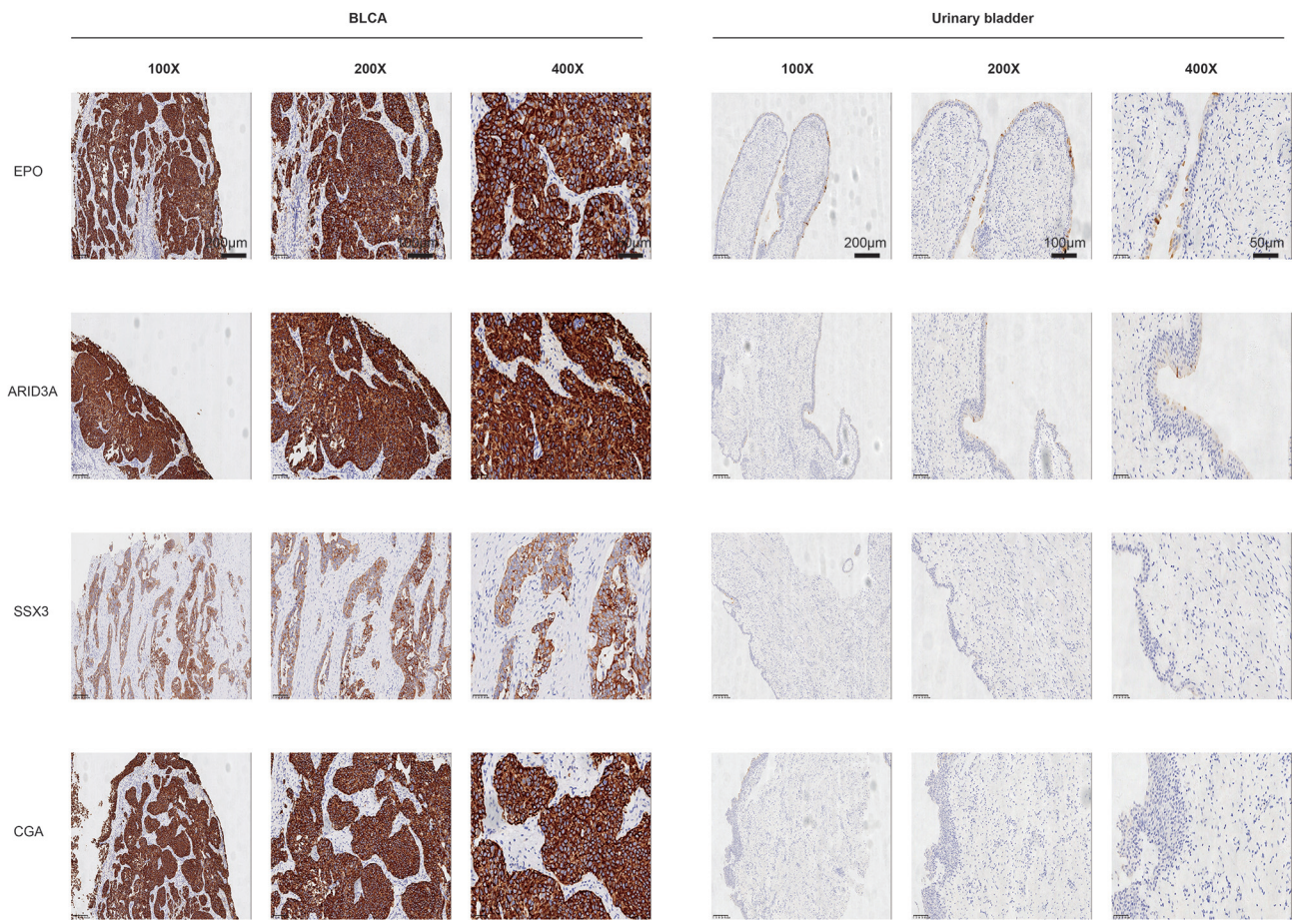

FIGURE 10 | The protein levels of key TFs and PRSGs in BLCA and normal urinary bladder.

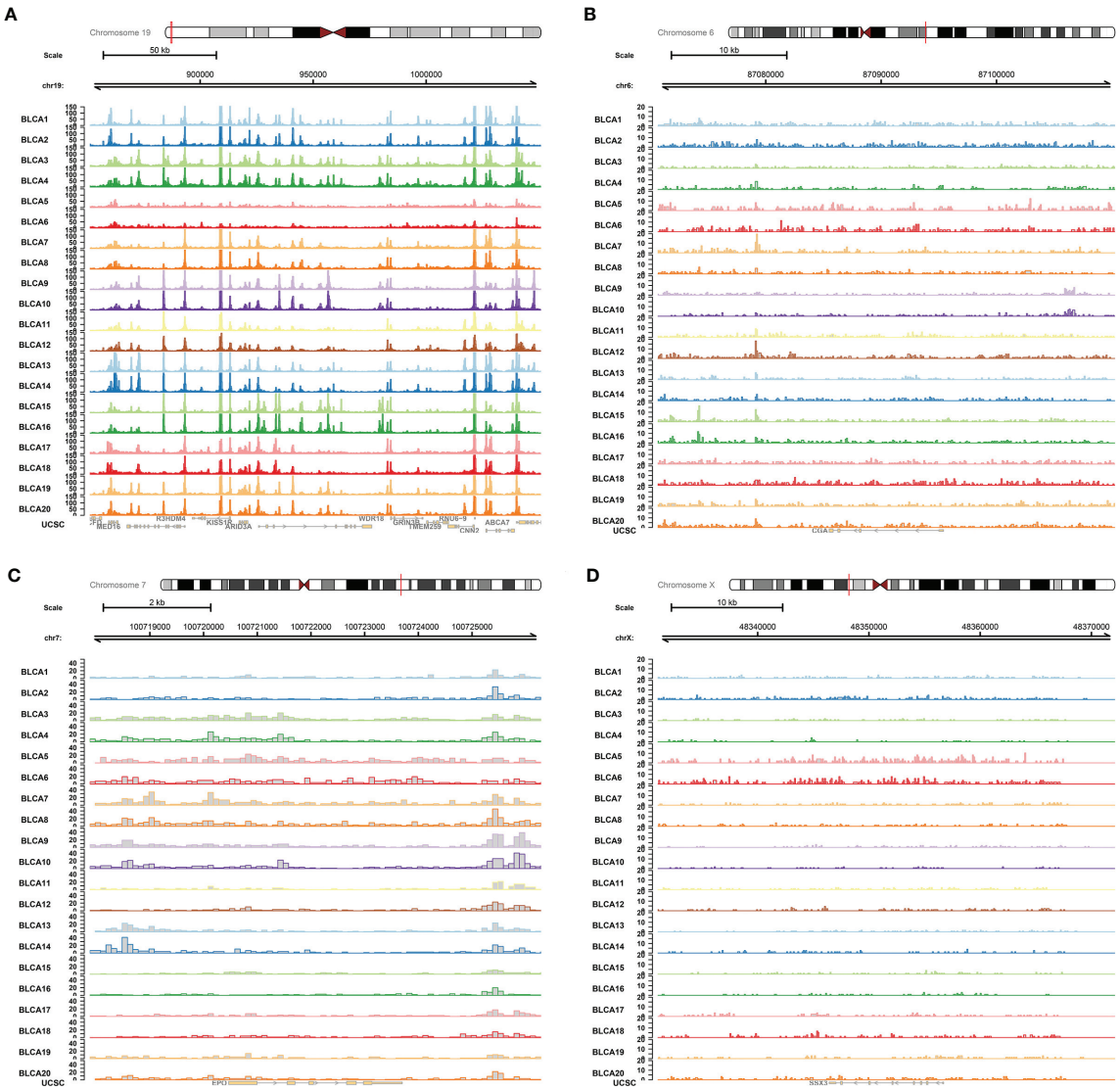

FIGURE 11 | ATAC-seq validation. ATAC-seq data of BLCA were used to validated the regulation mechanism of four key PRSGs [ARID3A **(A)**, CGA **(B)**, EPO **(C)**, SSX3 **(D)**], illustrating their accessible peaks in the chromatin.

the urothelial cancer stem-like traits and serve as a potential urinary biomarker for non-invasive BLCA (19). YAP was also regarded as a cancer stem cell regulator and a promising therapy target for patients with bladder cancer (20). Targeting COX2 and YAP1 pathways combined with systemic chemotherapy could also improve the clinical management of BLCA (21). However, the roles of CSCs in regulating the metastasis of BLCA, in especial bone metastasis, have not been described clearly.

In this study, we used the mRNAsi to identify the CSCs features in BLCA and found that it was significantly associated with the tumorigenesis, prognosis, AJCC clinical stage and bone metastasis in BLCA patients. It provided evidences for the roles of CSCs in the bone metastasis of BLCA, thus detecting and targeting key PRSGs may provide novel strategy for bone metastasis monitor and targeted therapy for patients with BLCA. In the multivariate Cox model and correlation analysis, we identified four key PRSGs, namely CACNA1E, LINC01356, CGA, and SSX3.

CACNA1E, the voltage-gated calcium channels (VGCCs) family member, often mediates the tumor evolution and heterogeneity formation *via* MAPK signaling pathway (22). Its amplification and overexpression were also found to be associated with the recurrence of Wilms' tumors (23). CGA is the alpha-subunit of glycoprotein hormones. Its level was found to be elevated in many cancers and it could also participate in the process of tumor metastasis (24, 25). SSX3, one of the cancer/testis antigens, is also a well-known oncogene in many tumors. It was significantly associated with the poor outcome in patients with pancreatic ductal adenocarcinoma (PDAC) and could serve as a predictor of metastatic outcome in breast cancer patients

(26, 27). Besides, SSX family can also serve as the vaccine targets for the treatment of sarcoma tumors (28).

Based on 20 PRSGs, we constructed a prediction model for the OS of patients with BLCA and the model achieved a good accuracy and applicability (AUC: 0.699). The construction of prediction model can assist oncologists in clinical decision-marking, thus many previous studies have focused on the identification of prognostic biomarkers in patients with BLCA (29–31). A lot of statistical methods, such as deep learning, Cox regression and LASSO regression analysis, have been used in the identification of the prognostic factors including the clinical information (age, clinical stage, and lymphovascular invasion), laboratory examination (C-reactive protein); molecular features (competing endogenous RNA, immune infiltration) (29, 30, 32–34). Although these results revealed the feasibility of personalized risk factors identification in predicting the prognosis of BLCA, none of them included the CSC-related signatures and PSRGs. Thus, the present research is a supplemental to the existing studies about the prognosis evaluation in patients with BLCA.

Due to the significant association between CSCs characteristics and TFs activity, epigenetic state, chromatin regulators and microenvironment cell networks (35), exploring the upstream TFs and downstream signaling pathways may offer more information of tumorigenesis and bone metastasis of BLCA. In this study, we identified the regulation networks between the abovementioned PRSGs and key TFs (EPO, ARID3A), hallmarks of cancer gene sets (DNA repair, myc targets, E2F targets, mTORC1 signaling, and unfolded protein response). EPO and its receptor have been reported to promote the tumor growth and invasion *via* an angiogenic effect (36). In tumor metastasis, EPO also plays an important role and may regulate the JAK/STAT and ERK1/2 pathways (37). ARID3A, a member of ARID family of DNA-binding proteins, serves as an independent predictor for prognosis in various cancers (38). It could control the tumor growth in a p53-dependent manner and promote esophageal squamous cell carcinoma invasion and metastasis (38, 39).

These five hallmarks of cancer gene sets generally took part in the tumor occurrence and development. DNA damage repair genes may be associated with the tumorigenesis and metastasis of prostate cancer (40). Besides, overexpression of c-MYC also leads to many cancers and it could be used as a possible target for therapeutic intervention in metastatic cancers (41). mTORC1, a well-known signaling pathway influenced by nutrients and growth factors, is significantly linked with metabolic diseases including cancer (5). Therapeutically, inhibition of mTOR signaling with rapamycin have been reported to attenuate the migration and invasion of colorectal cancer (42). Thus, we supposed that these identified signaling pathways may take part in the regulation of BLCA bone metastasis.

Although our data provide a reliable prediction model for BLCA and identify the potential mechanism for BLCA bone metastasis, this study still possessed some limitations that warrant consideration. Firstly, the samples involved in this study are from America, and thus the applicability of prediction model in European and Asian still needs further validation. Second, the sequencing data rely on one single cohort and the sample size is relatively limited. Third, the potential mechanism is based on bioinformation analysis and has not been verified by molecular and animal experiments. Thus, the future study will be conducted to verify these potential mechanisms *via* molecular experiments.

CONCLUSION

Our study identifies mRNAsi as a reliable index in predicting the tumorigenesis, bone metastasis and prognosis of patients with BLCA and provides a well-applied model for predicting the OS for patients with BLCA. Besides, we also inferred the potential regulatory network between key PSRGs and cancer gene sets in mediating the BLCA bone metastasis.

DATA AVAILABILITY STATEMENT

The code and datasets generated and/or analyzed during the current study are available in the **Supplementary Material** and TCGA program (https://portal.gdc.cancer.gov).

AUTHOR CONTRIBUTIONS

YK, XZ, and XJW designed and performed the research, analyzed and interpreted the data, and drafted the manuscript. SL, MJ, LZ, XYW, and TZ collected the data and designed the methodology. JZ, JL, and DZ reviewed the manuscript. All authors contributed to the article and approved the submitted version.

FUNDING

This study was supported by grants from the Zhejiang Provincial Health Bureau Science Foundation of China (NO. 2018KY017 and 2020KY408) and the Medical Health Science and Technology Project of Zhejiang Provincial Health Commission (NO. 2020ky040).

ACKNOWLEDGMENTS

We thank The Cancer Genome Atlas (TCGA) team for using their data.

SUPPLEMENTARY MATERIAL

The Supplementary Material for this article can be found online at: https://www.frontiersin.org/articles/10.3389/fonc.2021.641184/full#supplementary-material

Supplementary Figure 1 | Independent prognosis analysis with T stage and tumor grade integrated into univariate and multivariate Cox analyses. T stage and

tumor grade were also integrated into univariate and multivariate Cox analyses to correct the PI in the univariate (HR = 1.456, 95%CI (1.315-1.612), P < 0.001, **A**) and multivariate (HR = 1.480, 95%CI (1.324-1.654), P < 0.001, **B**) Cox model.

Supplementary Figure 2 | Construction of the prognostic nomogram with 205 objectives and treating age as a categorical variable. **(A)** The constructed prognostic nomogram based on the multivariate Cox model. **(B)** The calibration curve illustrated acceptable calibration of the prognostic nomogram. The time-related ROC with 95% confidence interval **(C)**, decision curve **(D)** and residual plot **(E)** were also conducted to illustrate the patient benefit and the discrimination of the nomogram. Note: (***P < 0.001; **P < 0.01; **P < 0.05).

Supplementary Figure 3 | Construction of the prognostic nomogram with all 403 objectives with all available variables and missing values. **(A)** The constructed prognostic nomogram based on the multivariate Cox model. **(B)** The calibration curve illustrated acceptable calibration of the prognostic nomogram. The time-related ROC with 95% confidence interval **(C)**, decision curve **(D)** and residual plot **(E)** were also conducted to illustrate the patient benefit and the discrimination of the nomogram. (***P < 0.001; **P < 0.01; **P < 0.05).

Supplementary Figure 4 | Construction of the prognostic nomogram with all 403 objectives with all missing values and available variables except for age and gender. **(A)** The constructed prognostic nomogram based on the multivariate Cox model. **(B)** The calibration curve illustrated acceptable calibration of the prognostic nomogram. The time-related ROC with 95% confidence interval **(C)**, decision curve **(D)** and residual plot **(E)** were also conducted to illustrate the patient benefit and the discrimination of the nomogram. (***P < 0.001; **P < 0.01; **P < 0.05).

Supplementary Figure 5 | Construction of the prognostic nomogram with 164 objectives with all available variables and excluding all missing values **(A)** The constructed prognostic nomogram based on the multivariate Cox model. **(B)** The calibration curve illustrated acceptable calibration of the prognostic nomogram. The time-related ROC with 95% confidence interval **(C)**, decision curve **(D)** and residual plot **(E)** were also conducted to illustrate the patient benefit and the discrimination of the nomogram. Note: (***P < 0.001; **P < 0.01; **P < 0.05).

Supplementary Figure 6 | Construction of the prognostic nomogram with 164 objectives with all available variables except for age and gender and excluding all missing values **(A)** The constructed prognostic nomogram based on the multivariate Cox model. **(B)** The calibration curve illustrated acceptable calibration of the prognostic nomogram. The time-related ROC with 95% confidence interval **(C)**, decision curve **(D)** and residual plot **(E)** were also conducted to illustrate the patient benefit and the discrimination of the nomogram. (***P < 0.001; **P < 0.01; **P < 0.05).

Supplementary Figure 7 | The protein levels of key TFs and PRSGs in BLCA and normal urinary bladder in the Human Protein Atlas. The representative IHC images of EPO **(A)**, ARID3A **(B)**, SSX3 **(C)** and CGA **(D)** in BLCA and normal urinary bladder tissues.

REFERENCES

1. Dobruch J, Daneshmand S, Fisch M, Lotan Y, Noon AP, Resnick MJ, et al. Gender and Bladder Cancer: A Collaborative Review of Etiology, Biology, and Outcomes. *Eur Urol* (2016) 69(2):300–10. doi: 10.1016/j.eururo.2015.08.037
2. Alifrangis C, McGovern U, Freeman A, Powles T, Linch M. Molecular and histopathology directed therapy for advanced bladder cancer. *Nat Rev Urol* (2019) 16(8):465–83. doi: 10.1038/s41585-019-0208-0
3. Nadal R, Bellmunt J. Management of metastatic bladder cancer. *Cancer Treat Rev* (2019) 76:10–21. doi: 10.1016/j.ctrv.2019.04.002
4. Biehler-Gomez L, Giordano G, Cattaneo C. The overlooked primary: bladder cancer metastases on dry bone. A study of the 20th century CAL Milano Cemetery Skeletal Collection. *Int J Paleopathol* (2019) 24:130–40. doi: 10.1016/j.ijpp.2018.10.005
5. Deng L, Meng T, Chen L, Wei W, Wang P. The role of ubiquitination in tumorigenesis and targeted drug discovery. *Signal Transduct Target Ther* (2020) 5:11. doi: 10.1038/s41392-020-0107-0
6. De Francesco EM, Sotgia F, Lisanti MP. Cancer stem cells (CSCs): metabolic strategies for their identification and eradication. *Biochem J* (2018) 475 (9):1611–34. doi: 10.1042/bcj20170164
7. Clarke MF. Clinical and Therapeutic Implications of Cancer Stem Cells. *N Engl J Med* (2019) 380(23):2237–45. doi: 10.1056/NEJMra1804280
8. Yang Z, Li C, Fan Z, Liu H, Zhang X, Cai Z, et al. Single-cell Sequencing Reveals Variants in ARID1A, GPRC5A and MLL2 Driving Self-renewal of Human Bladder Cancer Stem Cells. *Eur Urol* (2017) 71(1):8–12. doi: 10.1016/j.eururo.2016.06.025
9. Malta TM, Sokolov A, Gentles AJ, Burzykowski T, Poisson L, Weinstein JN, et al. Machine Learning Identifies Stemness Features Associated with Oncogenic Dedifferentiation. *Cell* (2018) 173(2):338–54.e15. doi: 10.1016/j.cell.2018.03.034
10. Pan S, Zhan Y, Chen X, Wu B, Liu B. Identification of Biomarkers for Controlling Cancer Stem Cell Characteristics in Bladder Cancer by Network Analysis of Transcriptome Data Stemness Indices. *Front Oncol* (2019) 9:613. doi: 10.3389/fonc.2019.00613
11. Meng T, Huang R, Zeng Z, Huang Z, Yin H, Jiao C, et al. Identification of Prognostic and Metastatic Alternative Splicing Signatures in Kidney Renal Clear Cell Carcinoma. *Front Bioeng Biotechnol* (2019) 7:270. doi: 10.3389/fbioe.2019.00270
12. Liberzon A, Birger C, Thorvaldsdóttir H, Ghandi M, Mesirov JP, Tamayo P. The Molecular Signatures Database (MSigDB) hallmark gene set collection. *Cell Syst* (2015) 1(6):417–25. doi: 10.1016/j.cels.2015.12.004
13. Zheng R, Wan C, Mei S, Qin Q, Wu Q, Sun H, et al. Cistrome Data Browser: expanded datasets and new tools for gene regulatory analysis. *Nucleic Acids Res* (2019) 47(D1):D729–d735. doi: 10.1093/nar/gky1094
14. Hanzelmann S, Castelo R, Guinney J. GSVA: gene set variation analysis for microarray and RNA-seq data. *BMC Bioinf* (2013) 14:7. doi: 10.1186/1471-2105-14-7
15. Corces MR, Granja JM, Shams S, Louie BH, Seoane JA, Zhou W, et al. The chromatin accessibility landscape of primary human cancers. *Science* (2018) 362(6413):eaav1898. doi: 10.1126/science.aav1898
16. Hahne F, Ivanek R. Visualizing Genomic Data Using Gviz and Bioconductor. *Methods Mol Biol* (2016) 1418:335–51. doi: 10.1007/978-1-4939-3578-9_16
17. Vetterlein MW, Karabon P, Dalela D, Jindal T, Sood A, Seisen T, et al. Impact of Baseline Characteristics on the Survival Benefit of High-Intensity Local Treatment in Metastatic Urothelial Carcinoma of the Bladder. *Eur Urol Focus* (2018) 4(4):568–71. doi: 10.1016/j.euf.2016.12.003
18. Feng YH, Su YC, Lin SF, Lin PR, Wu CL, Tung CL, et al. Oct4 upregulates osteopontin via Egr1 and is associated with poor outcome in human lung cancer. *BMC Cancer* (2019) 19(1):791. doi: 10.1186/s12885-019-6014-5
19. Ooki A, VandenBussche CJ, Kates M, Hahn NM, Matoso A, McConkey DJ, et al. CD24 regulates cancer stem cell (CSC)-like traits and a panel of CSC-related molecules serves as a non-invasive urinary biomarker for the detection of bladder cancer. *Br J Cancer* (2018) 119(8):961–70. doi: 10.1038/s41416-018-0291-7
20. Zhao AY, Dai YJ, Lian JF, Huang Y, Lin JG, Dai YB, et al. YAP regulates ALDH1A1 expression and stem cell property of bladder cancer cells. *Onco Targets Ther* (2018) 11:6657–63. doi: 10.2147/ott.S170858
21. Ooki A, Del Carmen Rodriguez Pena M, Marchionni L, Dinalankara W, Begum A, Hahn NM, et al. YAP1 and COX2 Coordinately Regulate Urothelial Cancer Stem-like Cells. *Cancer Res* (2018) 78(1):168–81. doi: 10.1158/0008-5472.Can-17-0836
22. Zhang X, Zhang M, Hou Y, Xu L, Li W, Zou Z, et al. Single-cell analyses of transcriptional heterogeneity in squamous cell carcinoma of urinary bladder. *Oncotarget* (2016) 7(40):66069–76. doi: 10.18632/oncotarget.11803
23. Natrajan R, Little SE, Reis-Filho JS, Hing L, Messahel B, Grundy PE, et al. Amplification and overexpression of CACNA1E correlates with relapse in favorable histology Wilms' tumors. *Clin Cancer Res* (2006) 12(24):7284–93. doi: 10.1158/1078-0432.Ccr-06-1567
24. Cai H, Liu W, Feng T, Li Z, Liu Y. Clinical Presentation and Pathologic Characteristics of Pituitary Metastasis from Breast Carcinoma: Cases and a Systematic Review of the Literature. *World Neurosurg* (2019) S1878–8750 (18):32949–8. doi: 10.1016/j.wneu.2018.12.126
25. Conteduca V, Scarpi E, Salvi S, Casadio V, Lolli C, Gurioli G, et al. Plasma androgen receptor and serum chromogranin A in advanced prostate cancer. *Sci Rep* (2018) 8(1):15442. doi: 10.1038/s41598-018-33774-4
26. Haider S, Wang J, Nagano A, Desai A, Arumugam P, Dumartin L, et al. A multi-gene signature predicts outcome in patients with pancreatic ductal

adenocarcinoma. *Genome Med* (2014) 6(12):105. doi: 10.1186/s13073-014-0105-3
27. Yau C, Esserman L, Moore DH, Waldman F, Sninsky J, Benz CC. A multigene predictor of metastatic outcome in early stage hormone receptor-negative and triple-negative breast cancer. *Breast Cancer Res* (2010) 12(5):R85. doi: 10.1186/bcr2753
28. Smith HA, McNeel DG. The SSX family of cancer-testis antigens as target proteins for tumor therapy. *Clin Dev Immunol* (2010) 2010:150591. doi: 10.1155/2010/150591
29. Woerl AC, Eckstein M, Geiger J, Wagner DC, Daher T, Stenzel P, et al. Deep Learning Predicts Molecular Subtype of Muscle-invasive Bladder Cancer from Conventional Histopathological Slides. *Eur Urol* (2020) 78(2):256–64. doi: 10.1016/j.eururo.2020.04.023
30. Harmon SA, Sanford TH, Brown GT, Yang C, Mehralivand S, Jacob JM, et al. Multiresolution Application of Artificial Intelligence in Digital Pathology for Prediction of Positive Lymph Nodes From Primary Tumors in Bladder Cancer. *JCO Clin Cancer Inform* (2020) 4:367–82. doi: 10.1200/cci.19.00155
31. Miyake M, Matsuyama H, Teramukai S, Kinoshita F, Yokota I, Matsumoto H, et al. A new risk stratification model for intravesical recurrence, disease progression, and cancer-specific death in patients with non-muscle invasive bladder cancer: the J-NICE risk tables. *Int J Clin Oncol* (2020) 25(7):1364–76. doi: 10.1007/s10147-020-01654-5
32. Jiang J, Bi Y, Liu XP, Yu D, Yan X, Yao J, et al. To construct a ceRNA regulatory network as prognostic biomarkers for bladder cancer. *J Cell Mol Med* (2020) 24(9):5375–86. doi: 10.1111/jcmm.15193
33. Necchi A, Raggi D, Gallina A, Ross JS, Farè E, Giannatempo P, et al. Impact of Molecular Subtyping and Immune Infiltration on Pathological Response and Outcome Following Neoadjuvant Pembrolizumab in Muscle-invasive Bladder Cancer. *Eur Urol* (2020) 77(6):701–10. doi: 10.1016/j.eururo.2020.02.028
34. Tamalunas A, Buchner A, Kretschmer A, Jokisch F, Schulz G, Eismann L, et al. Impact of Routine Laboratory Parameters in Patients Undergoing Radical Cystectomy for Urothelial Carcinoma of the Bladder: A Long-Term Follow-Up. *Urol Int* (2020) 104(7–8):551–8. doi: 10.1159/000506263
35. Tirosh I, Suvà ML. Dissecting human gliomas by single-cell RNA sequencing. *Neuro Oncol* (2018) 20(1):37–43. doi: 10.1093/neuonc/nox126
36. Farrell F, Lee A. The erythropoietin receptor and its expression in tumor cells and other tissues. *Oncologist* (2004) 9(Suppl 5):18–30. doi: 10.1634/theoncologist.9-90005-18
37. Mirmohammadsadegh A, Marini A, Gustrau A, Delia D, Nambiar S, Hassan M, et al. Role of erythropoietin receptor expression in malignant melanoma. *J Invest Dermatol* (2010) 130(1):201–10. doi: 10.1038/jid.2009.162
38. Song M, Kim H, Kim WK, Hong SP, Lee C, Kim H. High expression of AT-rich interactive domain 3A (ARID3A) is associated with good prognosis in colorectal carcinoma. *Ann Surg Oncol* (2014) 21(Suppl 4):S481–9. doi: 10.1245/s10434-013-3435-2
39. Ma J, Zhan Y, Xu Z, Li Y, Luo A, Ding F, et al. ZEB1 induced miR-99b/let-7e/miR-125a cluster promotes invasion and metastasis in esophageal squamous cell carcinoma. *Cancer Lett* (2017) 398:37–45. doi: 10.1016/j.canlet.2017.04.006
40. Wu B, Lu X, Shen H, Yuan X, Wang X, Yin N, et al. Intratumoral heterogeneity and genetic characteristics of prostate cancer. *Int J Cancer* (2020) 146(12):3369–78. doi: 10.1002/ijc.32961
41. Fatma H, Siddique HR. Role of long non-coding RNAs and MYC interaction in cancer metastasis: A possible target for therapeutic intervention. *Toxicol Appl Pharmacol* (2020) 399:115056. doi: 10.1016/j.taap.2020.115056
42. Gulhati P, Bowen KA, Liu J, Stevens PD, Rychahou PG, Chen M, et al. mTORC1 and mTORC2 regulate EMT, motility, and metastasis of colorectal cancer via RhoA and Rac1 signaling pathways. *Cancer Res* (2011) 71(9):3246–56. doi: 10.1158/0008-5472.Can-10-4058

Conflict of Interest: The authors declare that the research was conducted in the absence of any commercial or financial relationships that could be construed as a potential conflict of interest.

frontiers in Oncology

ORIGINAL RESEARCH
published: 21 May 2021
doi: 10.3389/fonc.2021.609548

p62 Overexpression Promotes Bone Metastasis of Lung Adenocarcinoma out of LC3-Dependent Autophagy

Dongqi Li[1†], Chuanchun He[1†], Fan Ye[1], En Ye[2], Hao He[1], Gong Chen[1] and Jing Zhang[1]*

[1] Department of Orthopaedics, Bone and Soft Tissue Tumors Research Center of Yunnan Province, The Third Affiliated Hospital of Kunming Medical University, Tumor Hospital of Yunnan Province, Kunming, China, [2] Department of Pathology, The Third Affiliated Hospital of Kunming Medical University, Tumor Hospital of Yunnan Province, Kunming, China

p62 protein has been implicated in bone metastasis and is a multifunctional adaptor protein usually correlated with autophagy. Herein, we investigated p62 expression and its prognostic significance in bone metastasis of lung adenocarcinoma, and analyzed whether the mechanism involved depends on autophagy. mRNA and protein expression of p62, LC3B and Beclin 1 were detected by reverse transcription-quantitative PCR and western blotting, respectively, in fresh bone metastasis tissues (n=6 cases) and normal cancellous bone tissues (n=3 cases). The association between p62 and LC3B expression and patient prognosis was subsequently analyzed in 62 paraffin-embedded bone metastasis specimens by immunohistochemistry assay. Small interfering RNA (siRNA) was employed to downregulate p62 expression in SPC-A-1 and A549 cells. Cell proliferation and migration ability were tested by CCK8, CCF and Transwell assays respectively. Autophagy was induced by Rapamycin or inhibited by Atg 7 knockout/Chloroquine in A549 cells and p62 and LC3II/I expression were analyzed. After subcutaneous inoculation or intracardial injection of A549 cells into nude mice, the effect of p62 downregulation *in vivo* was analyzed by histopathological examination. The results showed that p62, LC3B and Beclin 1 mRNA and protein were all overexpressed in bone metastasis tissues (all P<0.01). Patient samples with high p62 expression levels were significantly associated with more bone lesions (>3), shorter overall survival rates and shorter progression free survival rates compared with patients having lower p62 expression (P=0.014, P=0.003, P=0.048, respectively). Cox regression analysis identified p62 expression as an independent prognostic indicator of overall survival of patients with bone metastasis (P=0.007). *In vitro* p62 downregulation inhibited SPC-A-1 and A549 cells migration but had no effect on cell proliferation. After autophagy induction or inhibition, p62 expression involved in autophagy flux and changed inconsistently according to the switch of LC3I to LC3II in different autophagy conditions. *In vivo* p62 downregulation had no effect on growth of subcutaneous tumor. Lung or bone metastasis lesion was not found in all mice model. These findings suggested that p62 overexpression promotes tumor cell invasion out of LC3-dependent autophagy, which could be used a

OPEN ACCESS

Edited by:
Kotaro Nishida,
University of the Ryukyus, Japan

Reviewed by:
Fuming Li,
University of Pennsylvania, United States
Paola Costelli,
University of Turin, Italy

****Correspondence:***
Jing Zhang
nmlimit@sina.com

[†]These authors have contributed equally to this work

Specialty section:
This article was submitted to Molecular and Cellular Oncology, a section of the journal Frontiers in Oncology

Received: *23 September 2020*
Accepted: *06 April 2021*
Published: *21 May 2021*

Citation:
Li D, He C, Ye F, Ye E, He H, Chen G and Zhang J (2021) p62 Overexpression Promotes Bone Metastasis of Lung Adenocarcinoma out of LC3-Dependent Autophagy. Front. Oncol. 11:609548. doi: 10.3389/fonc.2021.609548

potential prognostic biomarker and therapeutic target for bone metastasis of lung adenocarcinoma.

Keywords: p62/sequestosome 1, bone metastasis, lung cancer, prognosis, autophagy, LC3

INTRODUCTION

Lung cancer presents the most morbidity and mortality among malignant tumors in China, and lung adenocarcinoma accounts for about 39.7% of cases (1). In recent years, the treatment of lung cancer has made great progress, but once distant metastases occur, the 5-year survival rate drops below 5% (2). About 30-65% of cases will experience different degrees of bone metastasis, followed by severe pain, hypercalcemia, pathological fractures, nerve or spinal cord compression, and other bone related adverse events, the quality of life is seriously decreased (3, 4). Recent studies have shown that tumor cell proliferation and bone metabolism disorders may be two key factors causing bone metastasis, but the key regulatory factors involved are not clear (5).

p62 (also known as sequestosome-1, SQSTM-1 or A170) is a multifunctional adaptor protein, which is generally considered to be a key player in autophagy similar to LC3 and Beclin 1 proteins (6). p62 serves as a link between LC3 protein and ubiquitinated substrates, which incorporate into the completed autophagosome and are degraded in autolysosomes, thus serving as an index of autophagic degradation (7). p62 is highly expressed in many solid tumors and is closely related to tumor proliferation, invasion and metastasis (8, 9). Furthermore, p62 protein is a key regulator of cellular bone metabolism (10). p62 gene mutations are considered to be the main cause of Paget's disease of bone, which is a skeletal disorder characterized by excessive activation of osteoclasts (11). In primary bone tumors like osteosarcoma (12), giant cell tumor of bone (13), and myeloma (14), p62 overexpression promotes tumor cell invasion and activation of osteoclasts. But its role in bone metastasis is unknown.

In a previous review, we speculated that p62 proteins might be an emerging regulator of bone metastasis (15). The aim of this study was to investigate p62 expression and its prognostic significance in bone metastasis of lung adenocarcinoma, and to analyze whether the related mechanism depends on autophagy.

MATERIALS AND METHODS

Tissue Specimens and Patients

For RT-qPCR and western blotting assays, 6 cases of fresh bone metastasis tissues from lung adenocarcinoma and 3 cases of normal cancellous bone tissues (from amputation limbs) were collected during surgery between May 2017 and July 2018. In addition, 62 paraffin-embedded specimens of bone metastasis tissues were collected between January 2015 and December 2018 for immunohistochemical testing. All cases were histologically and clinically diagnosed at The Third Affiliated Hospital of Kunming Medical University, Tumor Hospital of Yunnan Province (China). The median follow–up time of the patients was 10 months (ranging from 3–26 months). The protocol for the present study was approved by the Medical Institutional and Clinical Research Ethics Committee of Tumor Hospital of Yunnan Province. All patients included in the present study provided informed verbal consent for participation in the study.

RT–qPCR

Total RNA was extracted using TRIzol (Thermo Fisher Scientific, Inc., USA) from fresh bone metastasis tissues. Real-time quantitative polymerase reaction (RT–qPCR) was performed using the All–in–One™ First–Strand cDNA Synthesis kit (GeneCopoeia, Inc., USA). The temperature protocol was as follows: 37°C for 15 min, 50°C for 5 min, 98°C for 5 min. The primer sequences used for qPCR of p62 and GAPDH were as follows: p62 forward, 5'-CTGGGACTGAGAAGGCTCAC–3' and reverse, 5'-GCAGCTGATGGTTTGGAAAT-3'; and GAPDH forward, 5'-CTTAGCACCCCTGGCCAAG-3' and reverse, 5'-ATGTTCTGGAGAGCCCCG-3'. RT-qPCR sequencing was performed using the SYBR Green Master with Rox kit (GeneCopoeia, Inc., USA). The reaction conditions for qPCR were 95°C for 10 min, followed by 35 cycles of 95°C for 15 sec, 60°C for 30 sec and 72°C for 30 sec. The mRNA expression levels in each group were quantified using the $2^{-\Delta\Delta Cq}$ method (16).

Western Blot Assay

Fresh bone metastasis tissues were harvested using RIPA lysis buffer (Beyotime Institute of Biotechnology, Inc., CHN). Protein concentrations were measured using the bicinchoninic acid protein assay kit (Beyotime Institute of Biotechnology, Inc., CHN). The total protein of each specimen (30 mg/lane) was separated by SDS-PAGE (10% gels), and then transferred onto a polyvinylidene difluoride membrane (EMD Millipore, Inc., USA). B-actin was used as a loading control. The membrane was blocked with 5% bovine serum albumin (BSA, Beijing Solarbio Science & Technology Co., Ltd., CHN) at room temperature for 40 min, and subsequently incubated with mouse anti-p62 (1:1,500; cat. no. ab56416; Abcam), rabbit anti- LC3B (1:1,000; cat. no. ab48394; Abcam, Inc., UK), rabbit anti-Beclin1 (1:1,000; cat. no. ab207612; Abcam, Inc., UK) and mouse anti-β-actin (1:5,000; cat. no. ab6276; Abcam, Inc., UK) primary antibodies overnight at 4°C. The membranes were then incubated with peroxidase-conjugated goat anti-mouse IgG (1:20,000; cat. no. A4416; Sigma-Aldrich; Merck KGaA, Inc., GER) at room temperature for 1 h. Protein bands were visualized using SuperSignal™ West Femto Maximum Sensitivity Substrate reagents (Thermo Fisher Scientific, Inc., USA). The relative gray value of the immune reactive bands was compared using ImageJ software (version 1.46, National Institutes of Health, USA).

Immunohistochemistry Assay

In brief, bone metastasis tissues were fixed in 10% formaldehyde for 12 h at room temperature. Then paraffin-embedded specimens of bone metastasis tissues were cut into 4-μm sections and baked at 65°C for 30 min. The sections were washed with xylene and rehydrated with 70, 80, 90 and 100% graded ethanol solutions. Tissue sections were submerged for 2 min in an EDTA buffer at 95°C and 90 kPa for antigen retrieval. Subsequently, the sections were treated with 3% hydrogen peroxide in methanol, followed by incubation with 1% rabbit serum albumin (Cell Signaling Technology, Inc., GER) at room temperature for 10 min. The specimens were incubated overnight at 4°C with an anti-p62 antibody (1:800; cat. no. 16177S; Cell Signaling Technology, Inc., GER) or anti- LC3B (1:500; cat. no. ab48394; Abcam., UK). The specimens were then incubated with SignalStain® Boost IHC Detection Reagent (1:1000; cat. no. 8114P; Cell Signaling Technology, Inc., GER) at 37°C for 30 min. The degree of immunostaining of sections was reviewed by light microscope and scored by two independent pathologists. p62 and LC3B staining was scored semi-quantitatively as negative (<10% positively stained cells; score 0), weak (10–25% positively stained cells; score 1), moderate (26–50% positively stained cells; score 2), or strong (more than 50% positively stained cells; score 3). For statistical analysis, scores 0 and 1 together were considered low expression, while scores 2 and 3 together were considered high expression (17).

Cell Culture and Cell Transfection

SPC-A-1 and A549 cells were purchased from the American Type Culture Collection (ATCC, Rockville, USA). All cells were cultured in Dulbecco's modified Eagle's medium (DMEM) (Gibco, Grand Island, USA) supplemented with 10% fetal bovine serum, 100 U/ml penicillin and 100 μg/ml streptomycin (BioWest, Nuaillé, FRA), at 37°C in a humidified atmosphere containing 5% CO_2. The medium is replaced every 48h. Small interfering RNA (siRNA) targeting p62 and negative control scrambled siRNA were both designed and synthesized by GeneCopoeia Co., Ltd, USA (siRNA-p62, cat. no. HSH021660-LVRU6GP; scrambled siRNA-p62, cat. no. SHCTR001-LVRU6GP). The sequences of the siRNAs were as follows: siRNA-p62, 5'-CCATCCAGTATTCAAAGCATC-3' and scrambled siRNA, 5'-gcttcgcgccgtagtctta-3'. Atg7 knockout (Atg-/-) by siRNA was purchased from Cell Signaling Technology, Inc., GER (cat. no. #6604). Transfections of SPC-A-1 and A549 cells with siRNA (50 nm) were performed using a Lipofectamine® 3000 kit (Gibco; Thermo Fisher Scientific, Inc., USA), according to the manufacturer's protocols. Cell density was 10^6 cells/25 cm dishes. Puromycin (1 μg/ml) was used to kill any cells that were not successfully transfected. A549 cells silenced for p62 or Atg7 were constructed. Subsequent experimentation was conducted after transfection for 48 h.

Cell Proliferation Assay

Transfected and control SPC-A-1 and A549 cells were plated in 96-well plates in DMEM with 10% FBS (both Gibco; Thermo Fisher Scientific, Inc., USA) at a density of 5000 cells/well. To quantify cell viability, cultures were stained after 24, 48, and 72 hours; 10 μl Cell Counting Kit-8 (CCK-8, Dojindo Molecular Technologies, Inc., JPN) working solution was then added into the wells for 2 h at 37°C according to the manufacturer's instructions, after which the absorbance was measured at 450 nm using an Epoch Multi-Volume Spectrophotometer system (BioTek Instruments, Inc., USA). Cell colony formation (CCF) assay was conducted as follows. Briefly, transfected and control A549 cells were seeded in 12-well plates at a density of 500 cells per well and cultured with RPMI-1640 containing 10% FBS (Gibco, Grand Island, USA). After 8–10 days of culture, supernatants were discarded, and cells were washed with PBS, fixed with 4% paraformaldehyde for 30 min, and stained with 1% crystal violet (Solarbio, Beijing, China) for 20 min and then counted. The colony numbers were quantified using ImageJ software. Cell survival was calculated relative to that of control cells.

Transwell Migration Assay

Cells (1×10^5), suspended in DMEM containing 0.1% BSA were added to the top of the Boyden chamber (EMD Millipore, Inc., USA) at 37°C for 2h. The lower chamber contained 10% serum-supplemented medium. After incubation for 24 h at 37°C, a Transwell chamber (EMD Millipore, Inc., USA) was used to determine cell migration ability. A total of 1×10^5 siRNA-p62 transfected A549 cells were suspended in DMEM containing 10% FBS at a density of 5000 cells/well. Cells were subsequently placed onto the top of each chamber. Medium containing 10% FBS was added to the bottom of the chamber. The cells were incubated for 24 h, and then cells on the upside of the membrane were wiped off to remove the non-migrated cells. Cells that had migrated to the underside of the membrane were stained with crystal violet at room temperature for 20 min and visualized under Nikon Eclipse TE2000-U microscope. A total of 4 random fields (magnification, ×100) were scanned and analyzed using the aforementioned ImageJ software.

GFP-LC3B Expression Assay

pmCherry-EGFP-LC3B-h plasmid was purchased from Ke Lei Biological Technology Co., Ltd, CHN (cat. no. kl-zl-0999). SPC-A-1 and A549 cells were placed on coverslips and transfected with pmCherry-EGFP-LC3B particles (30 viral particles per cell) using the Lipofectamine® 3000 kit (Gibco; Thermo Fisher Scientific, Inc., USA), according to the manufacturer's protocols. After 18 h, cells were treated with DMSO or D-limonene for 30 min and then fixed with formalin solution, containing 4% paraformaldehyde. Coverslips were mounted with ProLong® Gold antifade mountant containing 4′, 6-diamidino-2-phenylindole, DAPI (Molecular Probes) to visualize nuclei. Images were acquired by confocal microscopy using a 63× objective (Leica TCS SPE Confocal System, Leica Microsystems, GER).

Experiment *In Vivo*

All animal experiments were approved by the Institutional Animal Care and Use Committee at the Kunming Medical University. Male BABL/c nude mice (6 weeks of age, 20g–22 g) were purchased from Shanghai SLAC Laboratory Animal Co. (Shanghai, China). Mice were maintained in a specific pathogen-free facility. To assess the

effect of p62 downregulation on tumor growth *in vivo*, the stably transfected A549 cells (shR-P62 and scrambled control) were 10^6/100 μl injected subcutaneously into the opposite flanks of mice (n = 5). Tumor volumes were measured with a micrometer caliper and calculated as (length × width^2)/2 every 2 days from the fifth day after injection. At the end of the experiment, mice were anesthetized with isoflurane and euthanized on the 14th day, and tumor tissues were collected, photographed and weighed. To assess the effect of p62 downregulation on tumor metastasis, intracardial injection of cells as described above (n = 5), the mice were dissected on the 28th day to search metastasis lesion in lung and bone by histopathological examination.

Statistics Analysis

Statistical analyses of immunohistochemistry assay were performed using the SPSS 17.0 software package (SPSS, Inc., USA). The significance of the differences between groups was estimated using the χ^2 test. The significance of the correlation between groups was estimated using Pearson correlation analysis. Progression-free or overall survival curves were plotted according to the Kaplan-Meier method, and compared using the log-rank test. The significance of survival variables was evaluated using a multivariate Cox proportional hazards regression analysis. Statistical graphs were drawn using GraphPad Prism v.6.0 (GraphPad Software, Inc., USA). The differences of p62, LC3B, and Beclin1 mRNA and protein expression levels between two groups of fresh bone metastasis tissues and normal cancellous bone tissues were tested with a Student's t-test. The differences of p62 and LC3II/I protein expression levels, cell proliferation rates and migration cell numbers between multiple groups were tested by one-way ANOVA with post-hoc Tukey's test. All data are presented as the mean ± standard deviation of three independent experiments. P<0.05 was considered to indicate a statistically significant difference.

RESULTS

p62 and Autophagic Protein Was Overexpressed in Bone Metastasis Tissues

In 6 cases of fresh bone metastasis tissues and 3 cases of normal cancellous bone tissues, p62 mRNA and protein were overexpressed in tumor tissues compared with normal tissues, as determined by RT-qPCR and western blot assays, respectively (**Figures 1A, B**). Both LC3B protein and Beclin 1 protein are overexpressed in tumor tissues compared with normal tissues (**Figures 1C, D**). The western blot results was provides in **Figure S1** for quantification. There was a positive correlation between p62 protein and LC3B protein expression (R2 = 0.66, P = 0.005, **Figure 1E**). There was no correlation between p62 protein and beclin1 protein expression, LC3II/I protein and beclin1 protein expression (**Figure S2**). Thus, our subsequent experiments mainly focus on p62 and LC3B expression to explore the role of p62 in autophagy.

p62 Overexpression Was Associated With Poor Prognosis of Patients With Bone Metastasis of Lung Adenocarcinoma

As shown in **Figures 2A–D**, and as evidenced by the mostly cytoplasmic and limited cytomembrane staining, p62 and LC3B protein were widely expressed in lung adenocarcinoma cells. To assess the association between p62/LC3B expression levels and clinicopathological features, the tumor specimens were classified into a high expression level group and a low expression level group (**Table 1**). High p62 expression levels were significantly associated with greater than 3 bone metastasis lesions (P = 0.014), and not with age (P = 0.636), sex (P = 0.914), or pathological fractures (P = 0.35). Furthermore, patients in the high p62 expression group had shorter overall survival rates and shorter progression free survival rates compared with patients in the low p62 expression group (P=0.003, P = 0.048, respectively; **Figures 2E, F**). In three serial specimens of lung tumor, lymph node metastasis and bone metastasis tissues, p62 staining gradually increased (**Figures S3**). But high LC3B expression levels showed no association with any clinicopathological characteristics (**Table 1**). Correlation analysis showed that there was no correlation between p62 protein and LC3B protein (R^2 = 0.06, P = 0.15). Cox regression analysis identified p62 expression as an independent prognostic indicator of overall survival in patients with bone metastasis of lung adenocarcinoma (P = 0.007, **Table 2**).

p62 Downregulation Inhibited Migration but Not Proliferation of Lung Adenocarcinoma Cells

The expression of p62 was downregulated by small interfering RNA transfection in SPC-A-1 and A549 cells. After 48h, p62 mRNA expression was inhibited as assessed by RT-qPCR assay (**Figures 3A–C**). Western blot assay also showed p62 protein

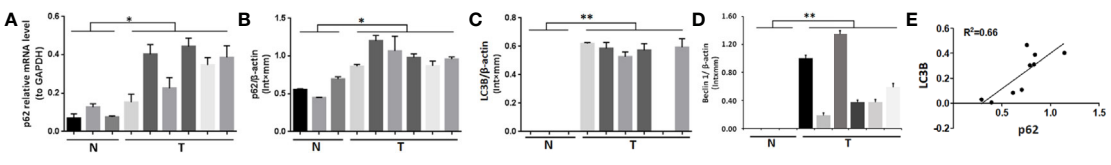

FIGURE 1 | Expression of p62, LC3B and Beclin 1 in bone metastasis tissues of lung adenocarcinoma. **(A, B)** Both p62 mRNA and protein expression levels were higher in tumor tissues (T) than in normal cancellous bone tissues (N). **(C)** LC3B and **(D)** Beclin 1 protein expression levels were higher in tumor tissues (T) than in normal cancellous bone tissues (N). **(E)** Positive correlation between p62 protein expression and LC3B protein expression (P=0.005). T, bone metastasis tissues; N, normal cancellous bone tissues. **P < 0.05, **P < 0.01*.

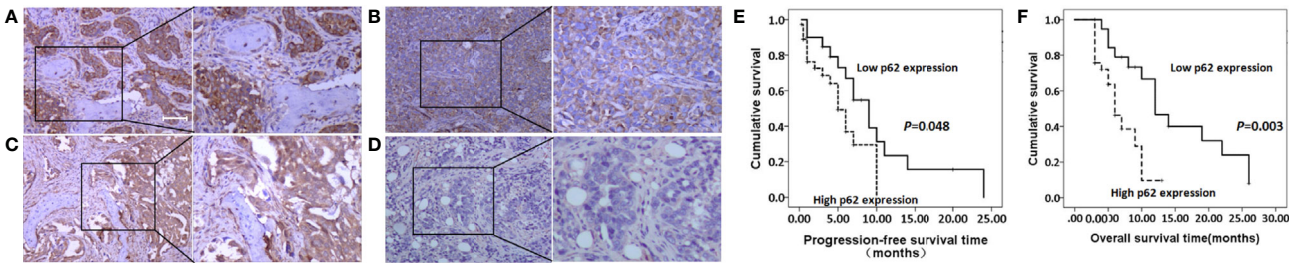

FIGURE 2 | p62 and LC3B protein expression as determined by immunohistochemistry assay. **(A, B)** High p62 (A, scale bar 100μm) and LC3B **(B)** expression at magnification ×100 (left) and ×200 (right). **(C, D)** Low p62 **(C)** and LC3B **(D)** expression at magnification ×100 (left) and ×200 (right). **(E, F)** High p62 expression was associated with shorter progression-free survival rates **(E)** and overall survival rates **(F)** in patients with bone metastasis of lung adenocarcinoma.

TABLE 1 | Association of p62 and LC3B protein expression with clinicopathological features of patients with lung adenocarcinoma bone metastasis.

	p62		P	LC3B		P
	Low expression	High expression		Low expression	High expression	
Age						
(years)	52.68±8.71	53.92±10.51	0.636	52.51±10.229	55.13±9.172	0.316
Sex						
Male	27	13	0.914	27	13	0.230
Female	12	10		12	10	
Number of bone metastasis						
≤3	16	16	0.014	17	13	0.235
>3	6	24		22	10	
Pathologic fracture						
Yes	14	22	0.350	22	14	0.471
No	8	18		17	9	

TABLE 2 | Cox regression analysis of overall survival in 62 patients with lung adenocarcinoma bone metastasis.

Clinicopathological features	B	SE	Wald	df	Sig.	Exp (B)	95.0% CI for Exp (B)	
							Lower	Upper
p62	-1.317	0.490	7.229	1	0.007	0.268	0.103	0.700
LC3B	-0.615	0.365	2.838	1	0.092	0.541	0.264	1.106
Age	0.030	0.021	1.967	1	0.161	1.031	0.988	1.075
Sex	0.190	0.363	0.273	1	0.601	1.209	0.594	2.460
Number of bone metastasis	0.377	0.393	0.919	1	0.338	1.458	0.675	3.150
Pathologic fracture	0.076	0.403	0.036	1	0.850	1.079	0.490	2.379

B, regression coefficient; SE, standard error; Wald, χ^2 value; df, degree of freedom; Sig, significance; Exp(B), odds ratio; CI, confidence interval.

expression was downregulated in siR-p62 transfected cells than scrambled control cells (**Figure 3D**). The differences between the silenced p62 gene cells (siRp62 group) and the scrambled control (siR-NC) group were analyzed. The difference in proliferation measured by relative optical density (OD) values between the two groups was not statistically significant between 0h to 72h (**Figures 3E, F**). The same results showed p62 downregulation had no effect on cell colony formation by CCF assay (**Figures 3G, H**). However, the downregulation of p62 led to the inhibition of migration of SPC-A-1 and A549 cells (**Figure 4**). *In vivo* assays, the volumes of subcutaneous tumor were 602.4 mm^3, 550.9 mm^3 in control group (n = 2), 608.3 mm^3, 560.8 mm^3 in scrambled control group (n = 2) and 596.4 mm^3, 564.8 mm^3, 598.2 mm^3 in silenced p62 group (n = 3). The difference was not statistically significant between three groups (**Figure 5A**). Lung or bone metastasis lesion was not found in all mice model by histopathological examination (**Figures 5B, C**).

p62 Expression Was Independent of Autophagy

In SPC-A-1 and A549 cells, autophagy was induced by rapamycin, which increased the number of positive GFP-LC3 cells as detected by confocal microscopy (**Figures 6A–C**). We used A549 cells for subsequent experiments because of the more obvious autophagic puncta in these cells. The consistent results showed LC3II/I expression level was increased after Rapamycin treatment by western blot assay. Furthermore, there was not a clear correlation between the increases in LC3II/I expression and

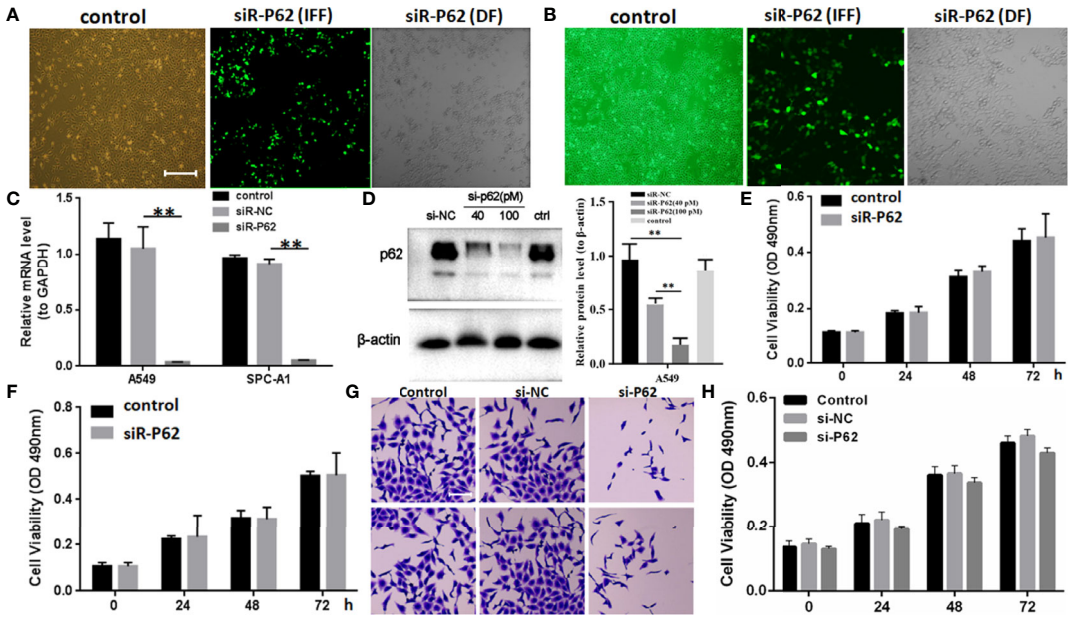

FIGURE 3 | p62 downregulation using small interfering RNA transfection did not inhibit tumor proliferation in SPC-A-1 and A549 cells. **(A)** Small interfering p62 RNA (siR-p62) plasmid was successfully transfected in A549 cells. The left control indicates untreated tumor cells. The middle siR-p62 (IFF) indicates small interfering p62 RNA-transfected tumor cells in immunofluorescence field. The right siR-p62 (DF) indicates small interfering p62 RNA-transfected tumor cells in dark field (scale bar 200μm). **(B)** siR-p62 plasmid was successfully transfected in SPC-A-1 cells. **(C)** After 48h p62 mRNA expression level was downregulated in siR-p62 transfected cells than scrambled control cells (siR-NC). **(D)** p62 protein expression level was downregulated in siR-p62 transfected cells than scrambled control cells (siR-NC). **(E, F)** The difference in proliferation between siR-p62 transfected group and scrambled control group (siR-NC) of A549 **(E)** and SPC-A-1 **(F)** cells was found to be not significant between 0 h to 72 h. **(G, H)** Cell colony formation assay showed the difference in proliferation between siR-p62 transfected group and scrambled control group (siR-NC) of A549 cells was not significant between 0 h to 72 h (scale bar 50μm). control, untreated A549 or SPC-A-1 cells; siR-p62, small interfering p62 RNA transfected cells; siR-NC, siR-p62 scrambled control; IFF, immunofluorescence field; DF, dark field; ***P < 0.01*.

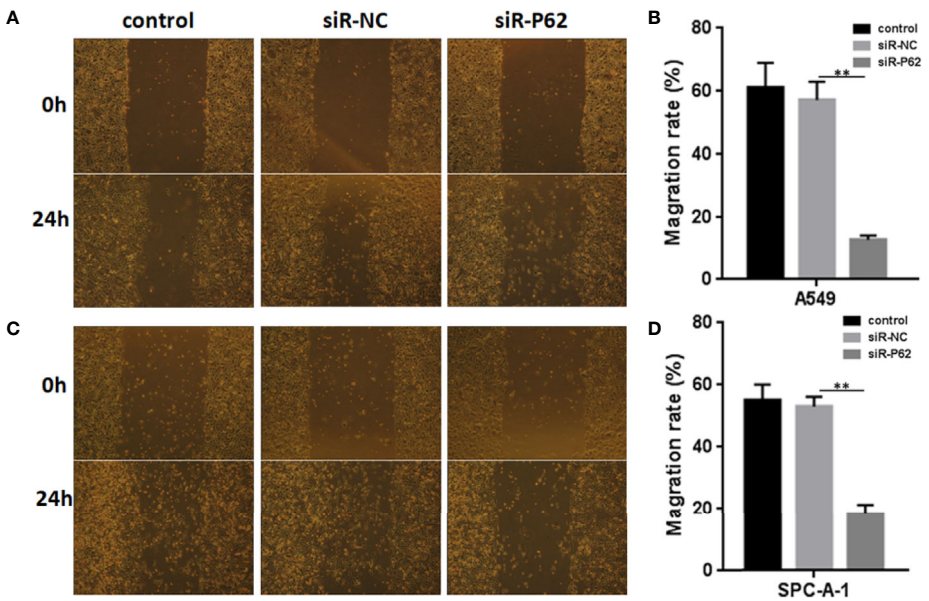

FIGURE 4 | p62 downregulation inhibits the migration of A549 and SPC-A-1 cells. **(A)** Migration of A549 cells with different p62 expression. **(B)** p62 downregulation inhibited the migration of A549 cells. **(C)** Migration of SPC-A-1 cells with different p62 expression. **(D)** p62 downregulation inhibited the migration of SPC-A-1 cells. control, untreated A549 or SPC-A-1 cells; siR-p62, small interfering p62 RNA transfected cells; siR-NC, siR-p62 scrambled control. ***P < 0.01*.

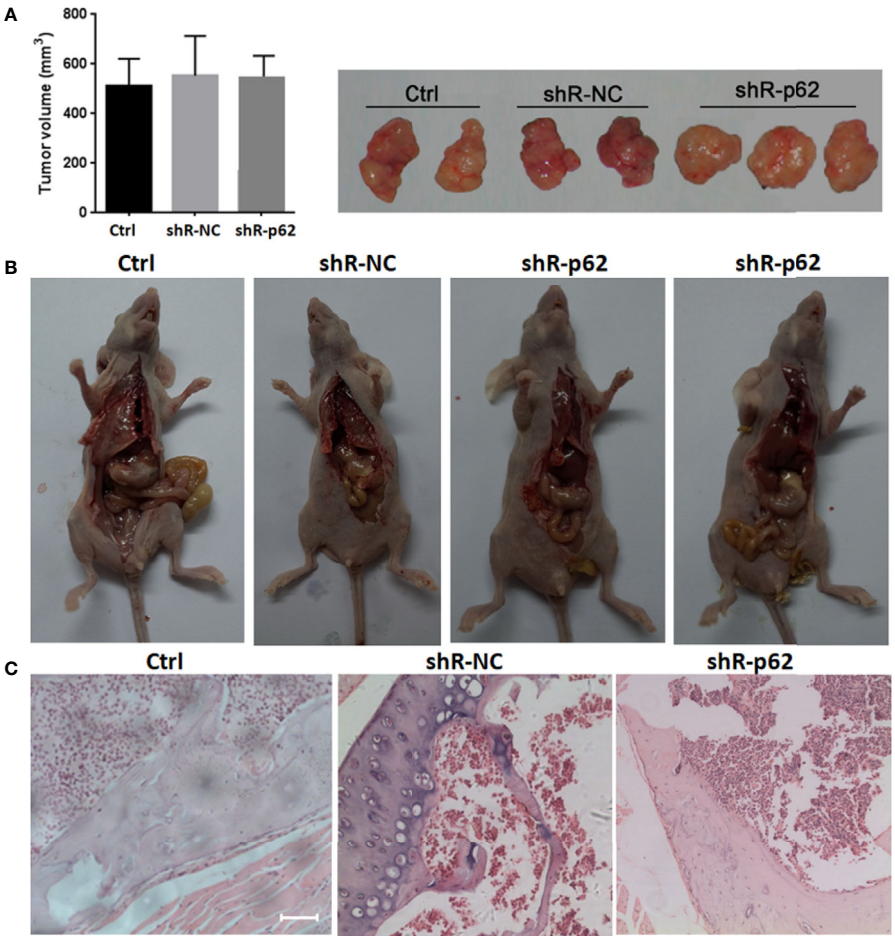

FIGURE 5 | *In vivo* p62 downregulation had no effect on growth of subcutaneous tumor. **(A)** The difference of tumor volumes between silenced p62 group (n = 3), scrambled control group (n = 2) and control group (n = 2) was not statistically significant. **(B)** All mice model was dissected on the 28th day, and lung or bone metastasis lesion was not found. **(C)** Bone metastasis lesion of limb or spine was not found under microscope (scale bar 200μm). Ctrl, untreated A549 cells; shR-p62, stably transfected A549 cells; shR-NC, shR-p62 scrambled control.

the decrease in p62 expression (**Figures 6D, E**). Following autophagy inhibition by Atg 7 gene knockout, LC3II/I expression almost disappeared but p62 expression decreased slightly following treatment with Rapamycin (**Figures 6F, G**). In A549 cells treated with lysosomal proteolysis inhibitors, p62 expression increased but only partly colocalized with LC3 protein (**Figure 7A**). As classic substrate of autophagy degradation, p62 expression changed inconsistently according to the switch of LC3I to LC3II in different autophagy conditions (**Figure 7B**). These results demonstrated that p62 expression involved in autophagy flux, which was independent of LC3 expression. In brief, p62 expression might function out of LC3-dependent autophagy.

DISCUSSION

According to the "seed and soil" hypothesis, bone metastasis is dependent on the interactions between tumor cells and the bone microenvironment including the fenestrated capillaries in bone, bone matrix, and cells in the bone marrow (BM) stroma, such as osteoblasts and osteoclasts (18). Identification of key regulators between tumor cells and the bone microenvironment could clarify molecular mechanism involved and will improve clinical treatment of bone metastasis. Our results showed there was a higher mRNA and protein expression of p62 in bone metastasis of lung adenocarcinoma compared with normal cancellous bone tissue, suggesting p62 may be involved in tumor formation or metastasis during gene transcription and protein translation. p62 is not only overexpressed in early-stage lung cancer (19), but it is also associated with poor prognosis of patients with lung adenocarcinoma (17, 20). Our results were consistent with previous research (21). Furthermore, we found p62 expression gradually increased when transitioning from lung tumor, lymph node metastasis and bone metastasis tissues, which suggested that p62 protein might promote tumor invasion of lung adenocarcinoma. We also confirmed p62 downregulation

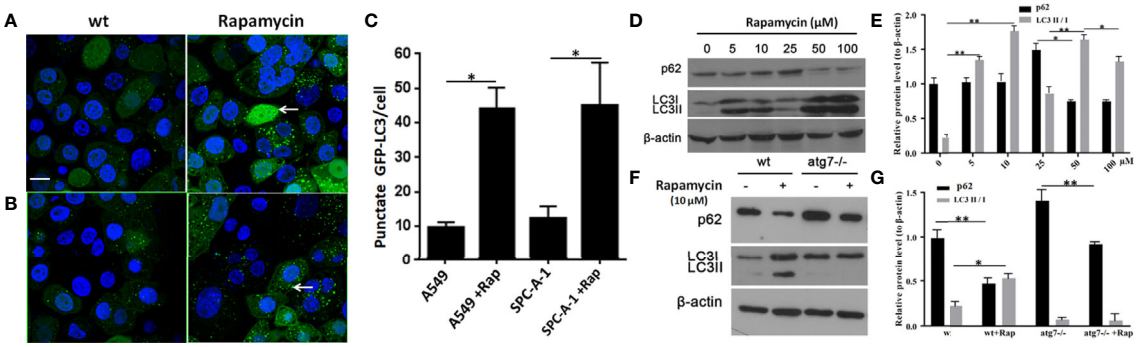

FIGURE 6 | Changes in detection of p62 and LC3 II/I protein upon induction or inhibition of autophagy. **(A)** In untreated wild type A549 cells, punctate GFP-LC3 (white arrow) was rare (left image) but increased significantly after exposure to rapamycin (10 μM/L) for 24 h (right image) by GFP-LC3 immunofluorescence microscopy. **(B)** Similar to wild type SPC-A-1 cells, punctate GFP-LC3 increased slightly after treatment with rapamycin. **(C)** Punctate GFP-LC3 positive cells were increased after rapamycin exposure both in A549 and SPC-A-1 cells. **(D)** p62 and LC3 II/I protein expression upon different concentrations of exposure to rapamycin for 24h. **(E)** Densitometric analysis of protein bands showing LC3 II/I protein expression increased from 5μM/L to 10μM/L and decreased from 50 μM/L to 100 μM/L, but p62 protein expression changes were not obvious. **(F)** Changes in detection of p62 and LC3 II/I protein upon autophagic gene 7 knockout (Atg7-/-). **(G)** Densitometric analysis of protein bands showing LC3 II/I protein expression almost disappeared after Atg7-/- knockout, but p62 protein expression decreased obviously both after autophagy induction by Rapamycin and autophagy inhibition by Atg7-/- knockout. Scale bar was 20 μm. wt, wild type A549 or SPC-A-1 cells; Rap, Rapamycin. *$P < 0.05$, **$P < 0.01$.

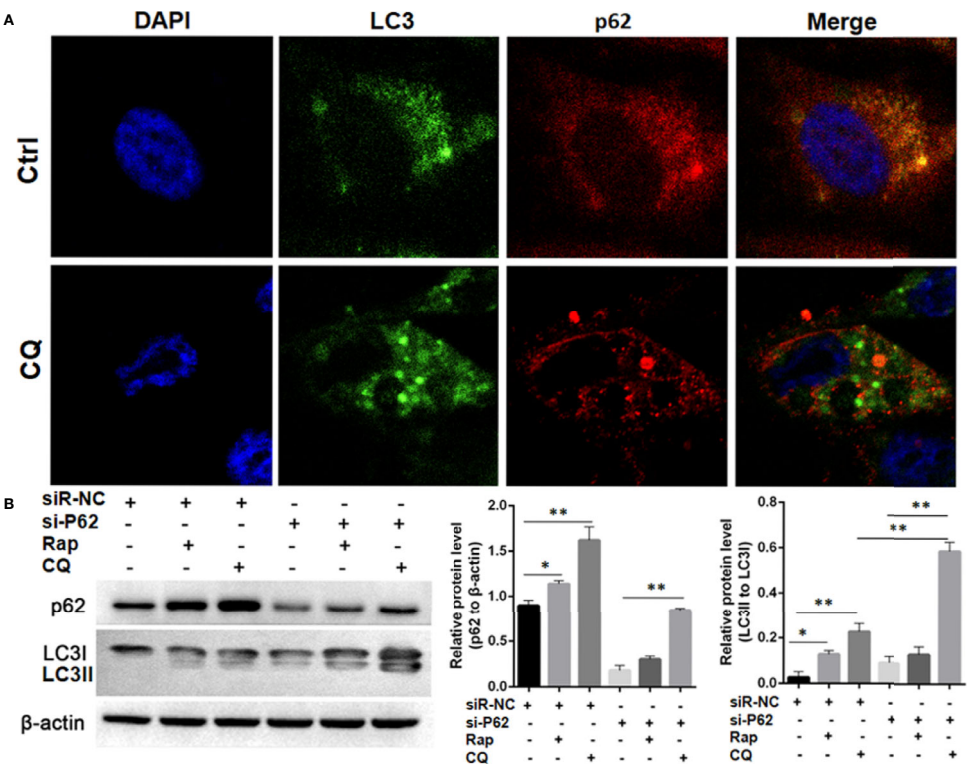

FIGURE 7 | Autophagy flux detection upon treating with Chloroquine (CQ) or Rapamycin (Rap) in wild type and p62 silencing A549 cells. **(A)** Double immunofluorescent staining of p62 and LC3 protein in A549 cells treated with CQ (20μM/L for 48h). Punctate GFP-LC3 emits green fluorescence, and punctuate mCherry-p62 emits red fluorescence. In merged panel p62 protein only partly colocalized with LC3 protein. **(B)** Changes of p62 and LC3 protein was detected upon Rap or CQ in different A549 cells. Significant switch of LC3 I to LC3 II was detected in different A549 cells treated with CQ or Rap, which demonstrates that autophagy flux is activated. Meanwhile, increased p62 expression is induced instead of degradation as autophagy substrate. In p62 silencing A549 cells, Significant switch of LC3 I to LC3 II was detected upon treating with CQ but not with Rap. Ctrl, untreated A549 cells; siR-p62, small interfering p62 RNA transfected cells; siR-NC, siR-p62 scrambled control; CQ, Chloroquine; Rap, Rapamycin. *$P < 0.05$, **$P < 0.01$.

inhibited lung adenocarcinoma cells invasion *in vitro*. In addition, p62 overexpression also showed a stronger association with bone metastasis lesions, which also suggested p62 overexpression played a key role in the bone microenvironment and metabolism (10). The ability of p62 to modulate tumor cells and osteoclasts suggested that it may be a feasible target for bone metastasis and especially for osteolytic metastasis (15).

p62 is considered a key autophagy-associated protein like LC3B and Beclin1 (7). Targeting autophagy is a promising therapeutic strategy to overcome bone tumor and metastasis (22, 23). Our results showed that LC3B and Beclin1 were also overexpressed in bone metastasis tissues, but only LC3B expression had positive correlation with p62 expression by western blot assay. Nonetheless, there was no obvious correlation between p62 expression and LC3B expression by immunohistochemistry, which was not consistent with western blot assay. So we continue to focus on both p62 and LC3B in next studies.

We further verified whether p62 protein could regulate bone metastasis of lung adenocarcinoma by participating in autophagy. p62 and LC3B proteins are the most common markers of autophagic activity. The LC3B protein precursor is processed to excise the carboxyl terminal to produce LC3I protein, which in turn covalently binds to phospholipids on the autophagosome membrane to generate LC3II protein (24). As a substrate for autophagy ubiquitination, p62 protein binds LC3II protein and translocates to the autophagosome for degradation. Therefore, the expression of p62 protein and LC3II/I protein are generally negatively correlated, which dynamically reflects the dynamic changes in autophagy (7). In our study, p62 expression involved autophagy flux activation, but p62 protein did not vary along with changes in LC3II/I protein in different autophagy conditions, which suggests that p62 could function out of LC3-dependent autophagy. Previous study revealed that oligomerized p62 targeted to the autophagosome formation site independent of LC3 (25). A recent study showed that p62 protein expression was not associated with autophagy under specific conditions (26), while p62 protein has also been shown to promote tumor cell survival by activation of the NF-κb pathway (27). The latest study revealed that p62 expression might target PD-L1, and p62 signaling axis could be useful to suppress the EGFR-TKI-resistant lung cancer (28). Thus, p62 may play versatile role in different cells or in different microenvironments (6).

In vivo assay our data showed p62 downregulation did not inhibit tumor growth, which was consistent with the data *in vitro*. But no metastasis lesion was found in mice model, which did not support the results *in vitro*. The reasons may include the amount of samples was small. We will repeat the experiment and change other highly metastatic lung cancer HARA-B, 95d cells in future. Another reason maybe that p62 regulates metastasis in different ways (not overexpression), like inducing Epithelial-Mesenchymal Transition (29). This was a preliminary study, next we will foucs on p62 signaling of promoting metastasis beside autophagy pathway.

In conclusion, our findings confirmed that the overexpression of the autophagic protein p62 promotes bone metastasis of lung adenocarcinoma, although the associated mechanism may be out of LC3-dependent autophagy. p62 could be used a potential prognostic biomarker and therapeutic target for bone metastasis of lung adenocarcinoma. New promising research investigating a p62 vaccine treatment received good response in advanced solid tumors (30, 31) and neurodegenerative disease (32). We propose that this new therapeutic strategy may improve clinical treatment of bone metastasis of lung adenocarcinoma.

DATA AVAILABILITY STATEMENT

The raw data supporting the conclusions of this article will be made available by the authors, without undue reservation, to any qualified researcher.

ETHICS STATEMENT

The studies involving human participants were reviewed and approved by Medical Institutional and Clinical Research Ethics Committee of Yunnan Tumor Hospital of China. Written informed consent for participation was not required for this study in accordance with the national legislation and the institutional requirements. The animal study was reviewed and approved by The Institutional Animal Care and Use Committee at the Kunming Medical University.

AUTHOR CONTRIBUTIONS

JZ designed this research and revised the manuscript. DL and CH performed the western blot analysis, RT−qPCR assays and cell experiments, and wrote the manuscript. FY performed the p62 and atg7 siRNA assays. EY performed immunohistochemistry assays and HH analyzed the data. GC collected the experiment tissues and followed up the patients. All authors contributed to the article and approved the submitted version.

FUNDING

This work was supported by the National Nature Science Foundation of China (grant no. 81760486), and Science and Technology Plan of Yunnan province (grant no. 2018FB133).

SUPPLEMENTARY MATERIAL

The Supplementary Material for this article can be found online at: https://www.frontiersin.org/articles/10.3389/fonc.2021.609548/full#supplementary-material

Supplementary Figure 1 | Expression of p62, LC3B and Beclin 1 in bone metastasis tissues of lung adenocarcinoma by western blot assay.

Supplementary Figure 2 | There was no correlation between p62 protein and beclin1 protein expression. There was no correlation between LC3II/I protein and beclin1 protein expression.

Supplementary Figure 3 | p62 staining became more and more intense in tumor tissues from lung adenocarcinoma, lymph node metastasis to bone metastasis by immunohistochemistry assay. **(A)** Faint staining in lung adenocarcinoma tissues at magnification ×200 (left, scale bar 100μm) and ×400 (right). **(B)** Moderate staining in lymph node metastasis tissues at magnifications of ×200 (left) and ×400 (right). **(C)** Strong staining in bone metastasis tissues at magnifications of ×200 (left) and ×400 (right).

REFERENCES

1. Chen W, Zheng R, Baade PD, Zhang S, Zeng H, Freddie B, et al. Cancer Statistics in China, 2015. *CA Cancer J Clin* (2016) 66:115–32. doi: 10.3322/caac.21338
2. Siegel RL, Miller KD, Jemal A. Cancer Statistics, 2020. *CA Cancer J Clin* (2020) 70:7–30. doi: 10.3322/caac.21590
3. Fornetti J, Welm AL, Stewart SA. Understanding the Bone in Cancer Metastasis. *J Bone Miner Res* (2018) 33:2099–113. doi: 10.1002/jbmr.3618
4. Croucher PI, Mcdonald MM, Martin TJ. Bone Metastasis: The Importance of the Neighbourhood. *Nat Rev Cancer* (2016) 16:373. doi: 10.1038/nrc.2016.44
5. Zhang W, Bado I, Wang H, Lo HC, Zhang XH. Bone Metastasis: Find Your Niche and Fit in. *Trends Cancer* (2019) 5:95–110. doi: 10.1016/j.trecan.2018.12.004
6. Sánchez MP, Saito T, Komatsu M. p62/SQSTM1: 'Jack of All Trades' in Health and Cancer. *FEBS J* (2019) 286:8–23. doi: 10.1111/febs.14712
7. Klionsky DJ, Abdelmohsen K, Abe A, Abedin MJ, Abeliovich H, Arozena AA, et al. Guidelines for the Use and Interpretation of Assays for Monitoring Autophagy (3rd Edition). *Autophagy* (2016) 12:1–222. doi: 10.1080/15548627
8. Wu Q, Xiang M, Wang K, Chen Z, Lu L, Ya T, et al. Overexpression of p62 Induces Autophagy and Promotes Proliferation, Migration and Invasion of Nasopharyngeal Carcinoma Cells Through Promoting ERK Signaling Pathway. *Curr Cancer Drug Targets* (2020) 20:624–37. doi: 10.2174/1568009620666200424145122
9. Tao M, Liu T, You Q. Jiang ZY.p62 as a Therapeutic Target for Tumor. *Eur J Med Chem* (2020) 193:112231. doi: 10.1016/j.ejmech.2020.112231
10. Usategui-Martín R, Gestoso-Uzal N, Calero-Paniagua I, Pereda JM, Pino-Montes J, González-Sarmiento R. A Mutation in p62 Protein (P. R321C), Associated to Paget's Disease of Bone, Causes a Blockade of Autophagy and an Activation of NF-kB Pathway. *Bone* (2020) 133:115265. doi: 10.1016/j.bone.2020.115265
11. Shaw B, Burrel CL, Green D, Navarro-Martinez A, Scott D, Daroszewska A, et al. Molecular Insights Into an Ancient Form of Paget's Disease of Bone. *Proc Natl Acad Sci USA* (2016) 116:10463–72. doi: 10.1073/pnas.1820556116
12. Lu Y, Wang Q, Zhou Y, Sun L, Hu B, Xue H, et al. Overexpression of p62 is Associated With Poor Prognosis and Aggressive Phenotypes in Osteosarcoma. *Oncol Lett* (2018) 15:9889–95. doi: 10.3892/ol.2018.8579
13. Liu S, Ye F, Li D, He C, He H, Zhang J. p62 Overexpression Promotes Neoplastic Stromal Cell Proliferation and Is Associated With the Recurrence of Giant Cell Tumor of Bone. *Oncol Lett* (2020) 20:86. doi: 10.3892/ol.2020.11947
14. Sha Z, Schnell HM, Ruoff K, Goldberg A. Rapid Induction of p62 and GABARAPL1 Upon Proteasome Inhibition Promotes Survival Before Autophagy Activation. *J Cell Biol* (2018) 217:1757–76. doi: 10.1083/jcb.201708168
15. Zhang J, Yang Z, Dong J. P62: An Emerging Oncotarget for Osteolytic Metastasis. *J Bone Oncol* (2016) 5:30–7. doi: 10.1016/j.jbo.2016.01.003
16. Livak KJ, Schmittgen TD. Analysis of Relative Gene Expression Data Using Real-Time Quantitative PCR and the 2-ΔΔCT Method. *Methods* (2001) 25:402–8. doi: 10.1006/meth.2001.1262
17. Chen Y, Schnitzler KL, Ma Y, Nenkov M, Theis B, Peterson I. The Clinical Influence of Autophagy-Associated Proteins on Human Lung Cancer. *Dis Markers* (2018) 2018:1–9. doi: 10.1155/2018/8314963
18. Wang M, Xia F, Wei Y, Wei X. Molecular Mechanisms and Clinical Management of Cancer Bone Metastasis. *Bone Res* (2020) 8:30. doi: 10.1038/s41413-020-00105-1
19. Anna MS, Olivia A, José AG, Mathias G, Spasenija S, Lukas B, et al. Prognostic Value of the Autophagy Markers LC3 and p62/SQSTM1 in Early-Stage Non-Small Cell Lung Cancer. *Oncotarget* (2016) 7:39544–55. doi: 10.18632/oncotarget.9647
20. Inoue D, Suzuki T, Mitsuishi Y, Miki Y, Suzuki S, Sugawara S, et al. Accumulation of p62/SQSTM1 Is Associated With Poor Prognosis in Patients With Lung Adenocarcinoma. *Cancer Sci* (2012) 103:760–6. doi: 10.1111/j.1349-7006.2012.02216.x
21. Wang C, Li Y, Li Y, Gong H, Zhang H, Yuan Y, et al. Expression and Clinical Significance of LC-3 and P62 in Non-Small Cell Lung Cancer. *Zhongguo Fei Ai Za Zhi* (2018) 21:445–50. doi: 10.3779/j.issn.1009-3419.2018.06.04
22. Niu J, Yan T, Guo W, Wang W, Zhao Z. Insight Into the Role of Autophagy in Osteosarcoma and Its Therapeutic Implication. *Front Oncol* (2019) 9:1232. doi: 10.3389/fonc.2019.01232
23. Liao YX, Yu HY, Lv JY, Cai YR, Liu F, He ZM, et al. Targeting Autophagy is a Promising Therapeutic Strategy to Overcome Chemoresistance and Reduce Metastasis in Osteosarcoma. *Int J Oncol* (2019) 55:1213–22. doi: 10.3892/ijo.2019.4902
24. Loos F, Xie W, Sica V, Bravo-San Pedr JM, Souquère S, Pierron G, et al. Artificial Tethering of LC3 or p62 to Organelles is Not Sufficient to Trigger Autophagy. *Cell Death Dis* (2019) 10:771. doi: 10.1038/s41419-019-2011-5
25. Itakura E, Mizushima N. P62 Targeting to the Autophagosome Formation Site Requires Self-Oligomerization But Not LC3 Binding. *J Cell Biol* (2011) 192:17–27. doi: 10.1083/jcb.201009067
26. Chen Y, Li Q, Li Q, Xing SS, Liu Y, Liu YJ, et al. p62/SQSTM1, a Central But Unexploited Target: Advances in Its Physiological/Pathogenic Functions and Small Molecular Modulators. *J Med Chem* (2020) 63:10135–57. doi: 10.1021/acs.jmedchem.9b02038
27. Ha J, Kim M, Seo D, Park JS, Lee J, Lee J, et al. The Deubiquitinating Enzyme USP20 Regulates the Tnfα-Induced Nf-κb Signaling Pathway Through Stabilization of P62. *Int J Mol Sci* (2020) 21:3116. doi: 10.3390/ijms21093116
28. Park HS, Lee DH, Kang DH, Yeo MK, Bae G, Lee D, et al. Targeting YAP-p62 Signaling Axis Suppresses the EGFR-TKI-Resistant Lung Adenocarcinoma. *Cancer Med* (2021) 10(4):1405–17. doi: 10.1002/cam4.3734
29. Zheng Y, Xu B, Zhao Y, Yang S, Wang S, Ma L, et al. Dead-Box Helicase 3 X-Linked Promotes Metastasis by Inducing Epithelial-Mesenchymal Transition Via P62/Sequestosome-1. *Dig Dis Sci* (2021) 1. doi: 10.1007/s10620-020-06735-z
30. Ponomarenko DM, Klimova ID, Chapygina YA, Dvornichenko VV, Zhukova NV, Orlova RV, et al. Safety and Efficacy of P62 DNA Vaccine ELENAGEN in a First-in-Human Trial in Patients With Advanced Solid Tumors. *Oncotarget* (2017) 8:53730–9. doi: 10.18632/oncotarget.16574
31. Ponomarenko DM, Gabai VL, Sufianov AA, Kolesnikov SI, Shneider AM. Response of a Chemo-Resistant Triple-Negative Breast Cancer Patient to a Combination of p62-Encoding Plasmid, Elenagen, and CMF Chemotherapy. *Oncotarget* (2020) 11:294–9. doi: 10.18632/oncotarget.27323
32. Cecarini V, Bonfili L, Gogoi O, Lawrence SE, Venanzi FM, Azevedo V, et al. Neuroprotective Effects of p62(SQSTM1)-Engineered Lactic Acid Bacteria in Alzheimer's Disease: A Pre-Clinical Study. *Aging* (2020) 12:15995–6020. doi: 10.18632/aging.103900

Conflict of Interest: The authors declare that the research was conducted in the absence of any commercial or financial relationships that could be construed as a potential conflict of interest.

frontiers in Oncology

ORIGINAL RESEARCH
published: 24 June 2021
doi: 10.3389/fonc.2021.629823

Nomogram for Predicting the Postoperative Venous Thromboembolism in Spinal Metastasis Tumor: A Multicenter Retrospective Study

Hao-ran Zhang[1†], Ming-you Xu[1†], Xiong-gang Yang[2], Feng Wang[1], Hao Zhang[1], Li Yang[1], Rui-qi Qiao[1], Ji-kai Li[1], Yun-long Zhao[1], Jing-yu Zhang[1] and Yong-cheng Hu[1*]*

[1] Department of Bone Tumor, Tianjin Hospital, Tianjin, China, [2] Department of Orthopedics, Huashan Hospital, Fudan University, Shanghai, China

OPEN ACCESS

Edited by:
Kotaro Nishida,
University of the Ryukyus, Japan

Reviewed by:
Jian-feng Zhang,
The Second Hospital of Tangshan, China
Deng-xing Lun,
Weifang People's Hospital, China

***Correspondence:**
Yong-cheng Hu
13820287567@163.com
Jing-yu Zhang
zhangjingyu2010@163.com

[†]These authors have contributed equally to this work

Specialty section:
This article was submitted to Molecular and Cellular Oncology, a section of the journal Frontiers in Oncology

Received: 16 November 2020
Accepted: 14 June 2021
Published: 24 June 2021

Citation:
Zhang H-r, Xu M-y, Yang X-g, Wang F, Zhang H, Yang L, Qiao R-q, Li J-k, Zhao Y-l, Zhang J-y and Hu Y-c (2021) Nomogram for Predicting the Postoperative Venous Thromboembolism in Spinal Metastasis Tumor: A Multicenter Retrospective Study. Front. Oncol. 11:629823. doi: 10.3389/fonc.2021.629823

Introduction: Venous thromboembolism can be divided into deep vein thrombosis and pulmonary embolism. These diseases are a major factor affecting the clinical prognosis of patients and can lead to the death of these patients. Unfortunately, the literature on the risk factors of venous thromboembolism after surgery for spine metastatic bone lesions are rare, and no predictive model has been established.

Methods: We retrospectively analyzed 411 cancer patients who underwent metastatic spinal tumor surgery at our institution between 2009 and 2019. The outcome variable of the current study is venous thromboembolism that occurred within 90 days of surgery. In order to identify the risk factors for venous thromboembolism, a univariate logistic regression analysis was performed first, and then variables significant at the P value less than 0.2 were included in a multivariate logistic regression analysis. Finally, a nomogram model was established using the independent risk factors.

Results: In the multivariate logistic regression model, four independent risk factors for venous thromboembolism were further screened out, including preoperative Frankel score (OR=2.68, 95% CI 1.78-4.04, P=0.001), blood transfusion (OR=3.11, 95% CI 1.61-6.02, P=0.041), Charlson comorbidity index (OR=2.01, 95% CI 1.27-3.17, P=0.013; OR=2.29, 95% CI 1.25-4.20, P=0.017), and operative time (OR=1.36, 95% CI 1.14-1.63, P=0.001). On the basis of the four independent influencing factors screened out by multivariate logistic regression model, a nomogram prediction model was established. Both training sample and validation sample showed that the predicted probability of the nomogram had a strong correlation with the actual situation.

Conclusion: The prediction model for postoperative VTE developed by our team provides clinicians with a simple method that can be used to calculate the VTE risk of patients at the bedside, and can help clinicians make evidence-based judgments on when

to use intervention measures. In clinical practice, the simplicity of this predictive model has great practical value.

Keywords: venous thromboembolism, deep vein thrombosis, pulmonary embolism, spinal metastasis, prediction model

INTRODUCTION

Venous thromboembolism (VTE) can be divided into deep vein thrombosis (DVT) and pulmonary embolism (PE). These diseases are a major factor affecting the clinical prognosis of patients and can lead to the death of these patients. Unfortunately, cancer patients have a higher risk of VTE than other patients (1, 2). In addition, spinal surgery is also considered an independent risk factor for VTE (3, 4). Patients with spinal metastases have both the characteristics of cancer patients and the need for spinal surgery. Therefore, it is reasonable to believe that this patient population has a higher prevalence of VTE. A recent retrospective study showed that 11% of patients with spinal metastases undergoing spinal surgery were observed to have symptomatic VTE (5). Accurately identifying risk factors related to VTE can help clinicians and patients determine which high-risk groups can be treated with interventions as soon as possible, which is very helpful for reducing perioperative mortality and improving postoperative survival time and quality of life.

For the risk factors of VTE after spinal surgery, some studies have reported the corresponding results, and some risk scores have been established (6–8). However, it is still unclear whether these conclusions are equally applicable to spinal metastasis surgery, because the treatment measures and prognostic characteristics of patients with spinal metastases are very specific (5). Therefore, it is very necessary to identify the risk factors of VTE in patients with spinal metastases. Unfortunately, the literature on the risk factors of VTE after surgery for spine metastatic bone lesions are rare (5, 9), and no predictive model has been established. Groot et al. found that longer duration of surgery was independently associated with an increased risk of symptomatic VTE (5). Kaewborisutsakul et al. found that patients who underwent surgery for extramedullary spinal tumors showed a 2.9% incidence of DVT and risk factors associated with DVT occurrence were operative time ≥8 h and plasma transfusion (9).

Nomogram model has been widely used in prognostic research and risk assessment of cancer patients (10–12). This prediction method transforms the traditional regression model into a visual risk assessment for each patient by creating a user-friendly graph, which is undoubtedly convenient and accurate. And compared with the traditional scoring table, the nomogram has proven to be more reliable than other systems, so it has been suggested as an alternative or even a new standard (13). Through the nomogram model, clinicians can show patients their predictions of future events more vividly, instead of roughly reporting corresponding risk factors, which also has a positive effect on improving patient compliance.

Therefore, in this study, we try to determine the risk factors related to VTE in patients undergoing spinal metastasis surgery and establish a nomogram prediction model.

Abbreviations: VTE, venous thromboembolism; DVT, deep vein thrombosis; PE, pulmonary embolism; AUC, area under the curve; ROC, receiver operating characteristic.

PATIENTS AND METHODS

Participants

We retrospectively analyzed 411 cancer patients who underwent metastatic spinal tumor surgery at our institution between October 2009 and April 2019. The indications for surgery were worsening neurological function, existing or potential spinal instability, pain that cannot be alleviated, or a combination of these factors. The exclusion criteria were as follows: minimally invasive surgery for spinal metastases, revision procedures, a VTE within 2 weeks before surgery, patients with coagulopathy, and surgery for sacral metastases. This study received ethical approval from the institutional review board and each patient obtained informed consent.

Description of Study Population

Among all patients, 230 (56.0%) were male patients and 181 (44.0%) were female patients. 49 (11.9%) patients had tumors in the cervical region, 206 (50.1%) patients had tumors in the thoracic region, and 156 (38.0%) patients had tumors in the lumbar area. 250 (60.8%) patients had more than one spinal metastasis. 246 (59.9%) patients and 239 (58.2%) patients received preoperative radiotherapy and chemotherapy, respectively. 302 (73.5%) patients were able to walk with or without aids before surgery. In order to better validate the model, we divided the entire study population into training sample and validation sample, and the two samples maintained similarity between various indicators (**Table 1**).

Outcome and Variables

This study was completed according to the "Transparent Reporting of a multivariable prediction model for Individual Prognosis or Diagnosis" statement (14). The outcome variable of the current study is PE or DVT that occurred within 90 days of surgery. The patient presented with calf swelling or tenderness, acute dyspnea, deoxygenation or unexplained shock. DVT is diagnosed by leg ultrasonography, and PE is diagnosed by pulmonary angiography or chest CT in patients with symptoms of pulmonary embolism.

The recorded data included demographic characteristics, primary tumor type, tumor location, number of spinal

TABLE 1 | Baseline characteristics of the study population.

Characteristics	All patients	Training sample	Validation sample	P value
Number	411	288	123	
Gender, N (%)				0.492
male	230 (56.0%)	158 (54.9%)	72 (58.5%)	
female	181 (44.0%)	130 (45.1%)	51 (41.5%)	
Age, mean ± SD	58.4 ± 10.6	58.8 ± 10.2	57.4 ± 11.4	0.239
Type of tumor, N (%)				0.667
rapid	191 (46.5%)	138 (47.9%)	53 (43.1%)	
moderate	164 (39.9%)	112 (38.9%)	52 (42.3%)	
slow	56 (13.6%)	38 (13.2%)	18 (14.6%)	
Tumor location, N (%)				0.906
cervical	49 (11.9%)	33 (11.5%)	16 (13.0%)	
thoracic	206 (50.1%)	145 (50.3%)	61 (49.6%)	
lumbar	156 (38.0%)	110 (38.2%)	46 (37.4%)	
Number of spinal metastases, N (%)				0.356
single	161 (39.2%)	117 (40.6%)	44 (35.8%)	
multiple	250 (60.8%)	171 (59.4%)	79 (64.2%)	
BMI (kg/m^2), N (%)				0.991
< 18.5	13 (3.2%)	9 (3.1%)	4 (3.3%)	
18.5-30	349 (84.9%)	245 (85.1%)	104 (84.6%)	
> 30	49 (11.9%)	34 (11.8%)	15 (12.2%)	
Surgical procedure, N (%)				0.351
type 1	68 (16.5%)	43 (14.9%)	25 (20.3%)	
type 2	319 (77.6%)	229 (79.5%)	90 (73.2%)	
type 3	24 (5.8%)	16 (5.6%)	8 (6.5%)	
Preoperative radiotherapy, N (%)				0.426
yes	246 (59.9%)	176 (61.1%)	70 (56.9%)	
no	165 (40.1%)	112 (38.9%)	53 (43.1%)	
Preoperative chemotherapy, N (%)				0.441
yes	239 (58.2%)	171 (59.4%)	68 (55.3%)	
no	172 (41.8%)	117 (40.6%)	55 (44.7%)	
Visceral metastases, N (%)				0.462
no	100 (24.3%)	73 (25.3%)	27 (22.0%)	
yes	311 (75.7%)	215 (74.7%)	96 (78.0%)	
Blood loss (liters), mean ± SD	1.3 ± 1.1	1.2 ± 0.9	1.3 ± 1.3	0.497
Preoperative Frankel score, N (%)				0.693
A-C	109 (26.5%)	78 (27.1%)	31 (25.2%)	
D-E	302 (73.5%)	210 (72.9%)	92 (74.8%)	
Blood transfusion, N (%)				0.194
yes	177 (43.1%)	130 (45.1%)	47 (38.2%)	
no	234 (56.9%)	158 (54.9%)	76 (61.8%)	
Charlson comorbidity index, N (%)				0.131
6	63 (15.3%)	42 (14.6%)	21 (17.1%)	
7	117 (28.5%)	75 (26.0%)	42 (34.1%)	
≥8	231 (56.2%)	171 (59.4%)	60 (48.8%)	
Operative time (hours), mean ± SD	4.0 ± 1.4	4.0 ± 1.3	4.1 ± 1.6	0.759

metastases, BMI, surgical procedure, preoperative radiotherapy, preoperative chemotherapy, visceral metastases, blood loss, preoperative Frankel score, blood transfusion, Charlson comorbidity index, and operative time.

Primary tumor type was divided into 3 groups according to Tomita and colleagues, including rapid group (lung and stomach), moderate group (kidney, liver, uterus, unidentified, and others) and slow group (thyroid, prostate, breast, and rectum) (15). Tumor location included cervical spine, thoracic spine and lumbar spine. The number of spinal metastases was divided into single spinal metastases and multiple spinal metastases. The surgical methods we used varied according to the location and size of metastatic tumors, and can be divided into three categories in general: palliative instrumentation and decompression (type 1), subtotal corpectomy (type 2), and total en bloc spondylectomy (type 3) (10). Reconstruction and stabilization procedures were performed *via* pedicle screws, titanium mesh, bone cement, and bone graft fusion alone or with various combinations. The intraoperative blood loss was obtained from the anesthetist's medical records and records of intraoperative fluid management. The neurological status of cancer patient before surgery was evaluated according to the Frankel score: patients with A-C grade were considered to be nonambulatory, and patients with D-E grade retained walking function (16). The comorbidity was measured and calculated according to the modified Charlson Comorbidity Index (17).

Statistical Analysis

Using a computer program, the study population was randomly divided into training sample and validation sample, with a ratio

of 7:3. Continuous variables were described as mean ± standard deviation, and categorical variables were described as proportions. The Student's t-tests (continuous variables) and chi-square tests (categorical variables) were used to confirm any statistical differences between means and proportions.

In order to identify the risk factors for VTE, a univariate logistic regression analysis was performed first, and then variables significant at the P value less than 0.2 were included in a multivariate logistic regression analysis to screen for independent risk factors. A forest plot was used to visualize the results of univariate and multivariate regression analyses. Finally, a nomogram model was established using the independent risk factors screened out by multivariate logistic regression.

Discrimination of the prediction model was validated using the area under the curve (AUC) and the consistence was validated using the calibration curves. The calibration curve plot is a curve fitting graph of the actual occurrence rate and the predicted occurrence rate. The calibration curve is the fitting line between the predicted and actual incidences, and y=x means that the predicted and actual incidences are exactly the same. The closer the two lines are, the closer the predicted and actual occurrence rates are, which further shows that the consistence of the model is better. The prediction model was established and validated according to the study published by Iasonos and colleagues (18). Statistical analysis was performed using R version 3.5.2 for Windows (R Foundation for Statistical Computing, Vienna, Austria), GraphPad Prism 8 Software (GraphPad Software Inc., San Diego, CA), and SPSS 22.0 software (SPSS Inc., Chicago, Illinois, USA). $P \leq 0.05$ (two-sided) was considered statistically significant.

RESULTS

Clinical Status

There were 49 patients (11.9%) diagnosed with VTE within 90 days after spinal metastasis surgery, of which 42 patients (10.2%) had DVT and seven patients (1.7%) had PE. The mean age of 49 patients was 58.5 years, and there were 20 female patients (40.8%). Among the seven patients with PE, five patients were observed to be accompanied by DVT, and one patient died of PE. For patients with VTE, the mean intraoperative blood loss was 1.4 ± 0.9 liters, the mean operative time was 4.6 ± 0.8 hours, and 33 patients (67.3%) received blood transfusion.

Risk Factors Associated With VTE

Univariate logistic regression analysis showed that gender (P=0.628), age (P=0.903), primary tumor type (P=0.329, P=0.817), tumor location (P=0.296, P=0.937), number of spinal metastases (P=0.880), BMI (P=0.466, P=0.566), surgical procedure (P=0.672, P=0.223), preoperative radiotherapy (P=0.345), and preoperative chemotherapy (P=0.880) were not statistically significant. These factors did not enter the next statistical test. According to the test level we set, a total of six factors were put into the multivariate logistic regression model, including visceral metastases, blood loss, preoperative Frankel score, blood transfusion, Charlson comorbidity index, and operative time (**Table 2** and **Figure 1**).

In the multivariate logistic regression model, four independent risk factors for VTE were further screened out, including preoperative Frankel score (OR=2.68, 95% CI 1.78-4.04, P=0.001), blood transfusion (OR=3.11, 95% CI 1.61-6.02, P=0.041), Charlson comorbidity index (OR=2.01, 95% CI 1.27-3.17, P=0.013; OR=2.29, 95% CI 1.25-4.20, P=0.017), and operative time (OR=1.36, 95% CI 1.14-1.63, P=0.001). The remaining factors (visceral metastases and blood loss) did not show significant statistical significance (**Table 2** and **Figure 1**).

Establishment and Validation of the Nomogram

On the basis of the four independent influencing factors screened out by multivariate logistic regression model, a nomogram prediction model was established (**Figure 2**). Assign these independent influencing factors in the nomogram to line segments of different lengths. The length of line segment represented the weight of the predictive factor. For each independent patient, each influencing factor was scored according to the actual situation, and then the points were added to get a total point. According to the final total point, the estimated risk probability of postoperative VTE for this patient can be obtained. The nomogram showed that the higher the patient's score, the higher the risk of postoperative VTE.

The receiver operating characteristic (ROC) curves were drawn in the training sample and the validation sample, and AUC was calculated to determine the discrimination of the prediction model. The results showed that the model had a high discrimination ability (**Figure 3**). The AUCs of the training sample and the validation sample were 0.852 and 0.843, respectively. In addition, the calibration curves were drawn to show the agreement between the predicted value and the true value. Both training sample and validation sample showed that the predicted probability of the nomogram had a strong correlation with the actual situation (**Figure 4**).

DISCUSSION

As cancer patients live longer and various diagnostic measures continue to improve, the incidence of metastatic spinal disease in the population is increasing. The spine is the third most common site of cancer metastases, second only to the lung and liver (19–21). The treatment of spinal metastases requires multidisciplinary collaboration, including surgery, radiotherapy and chemotherapy. The purposes of surgery are to relieve the symptoms of spinal cord compression, restore and maintain spinal stability, and improve the life expectancy and quality of life of cancer patients as much as possible.

However, there have been several literature proving that cancer and spinal surgery are two major risk factors for postoperative VTE, and VTE is associated with poor prognosis (22–24). Therefore, accurately identifying the risk factors of VTE

TABLE 2 | Logistic regression assessing risk factors for venous thromboembolism.

Factor	Univariable analysis			Multivariable analysis		
	OR	95% CI	P value	OR	95% CI	P value
Gender						NI
male	0.86	0.47-1.58	0.628			
female	Ref	Ref	Ref			
Age	1.00	0.97-1.03	0.903			NI
Type of tumor						NI
rapid	Ref	Ref	Ref			
moderate	0.72	0.37-1.40	0.329			
slow	1.11	0.47-2.61	0.817			
Tumor location						NI
cervical	Ref	Ref	Ref			
thoracic	0.61	0.24-1.54	0.296			
lumbar	1.04	0.42-2.59	0.937			
Number of spinal metastases						NI
single	Ref	Ref	Ref			
multiple	0.97	0.65-1.44	0.880			
BMI (kg/m^2)						NI
<18.5	1.51	0.50-4.76	0.466			
18.5-30	Ref	Ref	Ref			
>30	1.43	0.42-4.88	0.566			
Surgical procedure						NI
type 1	Ref	Ref	Ref			
type 2	1.18	0.56-2.49	0.672			
type 3	3.70	0.45-3.03	0.223			
Preoperative radiotherapy						NI
yes	Ref	Ref	Ref			
no	0.83	0.55-1.23	0.345			
Preoperative chemotherapy						NI
yes	Ref	Ref	Ref			
no	0.97	0.65-1.44	0.880			
Visceral metastases						
no	Ref	Ref	Ref			
yes	1.39	0.88-2.20	0.163	1.61	0.23-11.14	0.629
Blood loss (liters)	2.00	1.26-3.15	0.003	1.54	0.74-3.21	0.252
Preoperative Frankel score						
A-C	5.56	3.03-11.11	0.001	2.68	1.78-4.04	0.001
D-E	Ref	Ref	Ref			
Blood transfusion						
yes	8.33	4.00-19.23	0.010	3.11	1.61-6.02	0.041
no	Ref	Ref	Ref			
Charlson comorbidity index						
6	Ref	Ref	Ref			
7	3.33	0.72-15.52	0.125	2.01	1.27-3.17	0.013
≥8	5.82	1.36-24.84	0.017	2.29	1.25-4.20	0.017
Operative time (hours)	1.56	1.30-1.87	0.020	1.36	1.14-1.63	0.001

NI, not included.

helps clinicians adjust clinical decisions in a timely manner to adapt to the different conditions of patients. For non-tumor spinal surgery, there have been some studies that discussed the incidence and risk factors of VTE in detail (7, 8, 25), and a predictive score had been established (6). However, for spinal metastasis surgery, the current research results are far from enough. In daily clinical practice, orthopedic oncologists need a predictive model for the postoperative VTE in patients with spinal metastases to assess the patients' risks and make corresponding interventions. Therefore, the purpose of this study is to screen out independent risk factors for VTE after spinal metastasis surgery and establish a user-friendly predictive model.

The lack of walking function will lead to a high risk of VTE has been proven by several studies. Dermody et al. followed 174 asymptomatic, non-ambulatory neurosurgical patients and found that the incidence of postoperative DVT was 23% (26). Tominaga et al. retrospectively studied the data of patients who underwent spinal surgery and developed postoperative VTE to identify risk factors related to postoperative VTE. Multivariate logistic regression analysis showed that the independent risk factors were preoperative walking disorder and age (7). In patients undergoing surgery for spinal metastases, Zacharia et al. have demonstrated that non-ambulatory status is an independent risk factor for positive finding on preoperative DVT screening. 24% of non-ambulatory patients suffer from

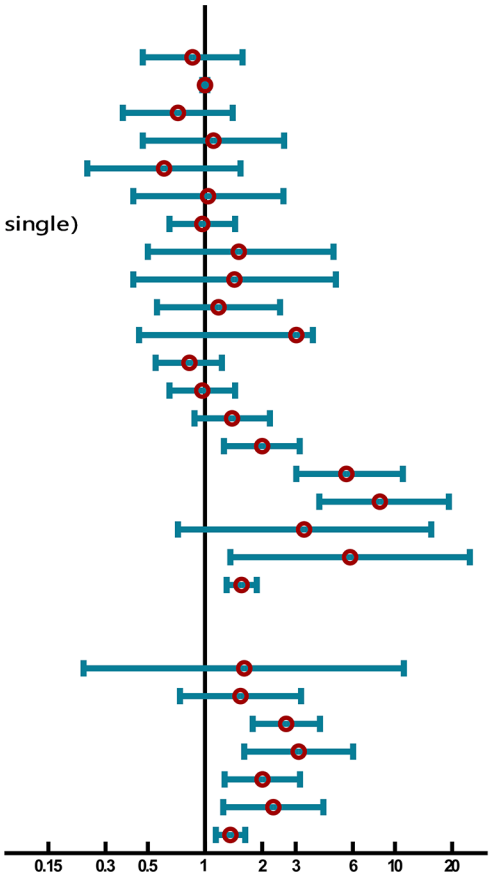

FIGURE 1 | The forest plot shows the results of univariate and multivariate analyses. In the multivariate logistic regression model, four independent risk factors for VTE were further screened out, including preoperative Frankel score (OR=2.68, 95% CI 1.78-4.04, P=0.001), blood transfusion (OR=3.11, 95% CI 1.61-6.02, P=0.041), Charlson comorbidity index (OR=2.01, 95% CI 1.27-3.17, P=0.013; OR=2.29, 95% CI 1.25-4.20, P=0.017), and operative time (OR=1.36, 95% CI 1.14-1.63, P=0.001).

DVT, and this incidence of DVT is 4 times higher than that of ambulatory patient population (27). These conclusions indicate that early gait training is important to prevent VTE, although it may take a long time for the muscle strength to reach the level required for walking. The use of robotic suits for neurological rehabilitation may help patients with walking difficulties. Aach et al. reported that the use of hybrid assistive limb exoskeleton can effectively improve the ability to walk on the ground (28).

Blood transfusion is associated with a high risk of VTE in cancer patients (29). One possible explanation may be that a tissue-factor-initiated pathway of coagulation activation on tumor cells appears to trigger coagulation activation in malignancy (30). Regarding the specific components of blood products, most evidence shows that VTE is closely related to red blood cell transfusion, and there is also some evidence that VTE is associated with platelet transfusion (31). In addition, in the study conducted by Kaewborisutsakul and colleagues (9), multivariate regression analysis found that there was a statistical correlation between the infusion of fresh frozen plasma and the high risk of VTE (9). The current study supports the above conclusions, patients who have blood transfusion have three times the risk of suffering from VTE, compared with patients without blood transfusion.

Age-adjusted Charlson Comorbidity Index is a widely used comorbidity scoring system. This score quantifies comorbidities based on the number and severity of the diseases that the patient has endured, and can be used to predict the patient's risk of death (17). Groot and colleagues introduced the Charlson Comorbidity Index into the study to assess the risk of postoperative VTE in patients with spinal metastases, although the final statistical analysis showed that there was no significant statistical association between the index and the risk of VTE (5). The current research showed that Charlson Comorbidity Index is an independent risk factor for postoperative VTE in patients with spinal metastases, and as the index increases, the risk tends to increase. Certain indicators in the Charlson Comorbidity Index have been proven to be high-risk factors for postoperative VTE, including age (7), diabetes (32), cerebrovascular disease (33), solid tumors (22), and hemiplegia (6, 7). Therefore, we can completely believe that the Charlson Comorbidity Index can predict the arrival of VTE.

Some studies have explored the association between operative time and postoperative VTE. Tominaga et al. found that 20 of 80

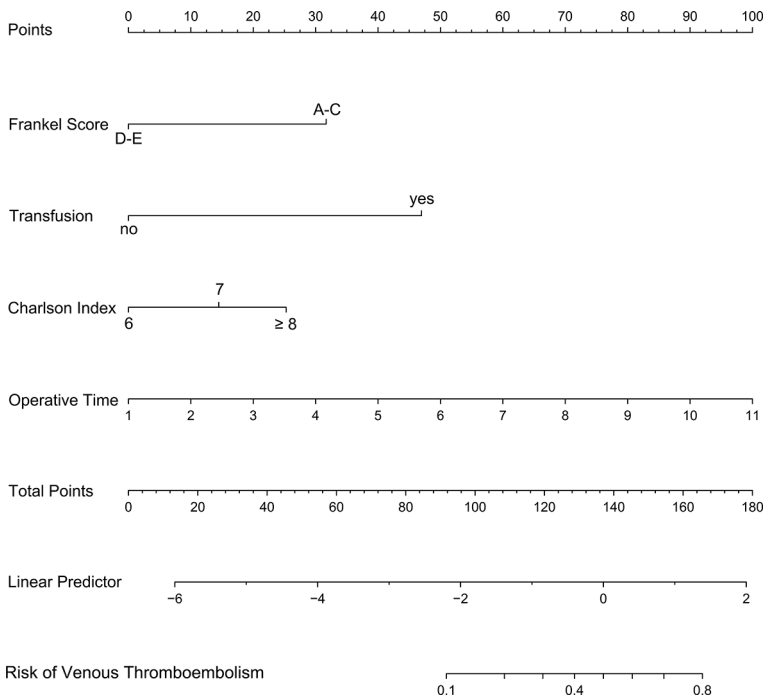

FIGURE 2 | A nomogram model was established using independent risk factors screened out by multivariate regression analysis. The corresponding score for each factor is based on the condition of the patient, which can be determined by making a vertical line upwards (e.g., a patient with blood transfusion will receive between 40 and 50 scores). Add all the scores to get the total score, then find the corresponding point on the total points axis and make a vertical line down to predict the risk of the VTE within 90 days after spinal metastasis surgery.

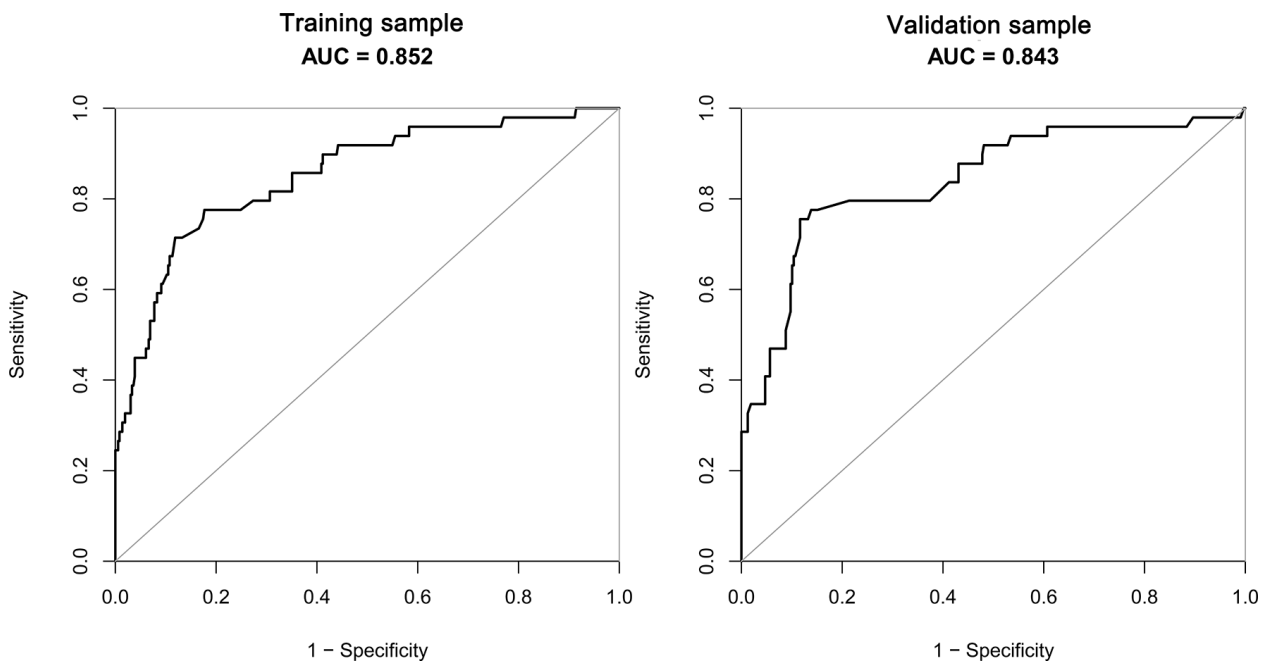

FIGURE 3 | The AUC of training sample (AUC=0.852) and validation sample (AUC=0.843) showed that the model had a high discrimination ability.

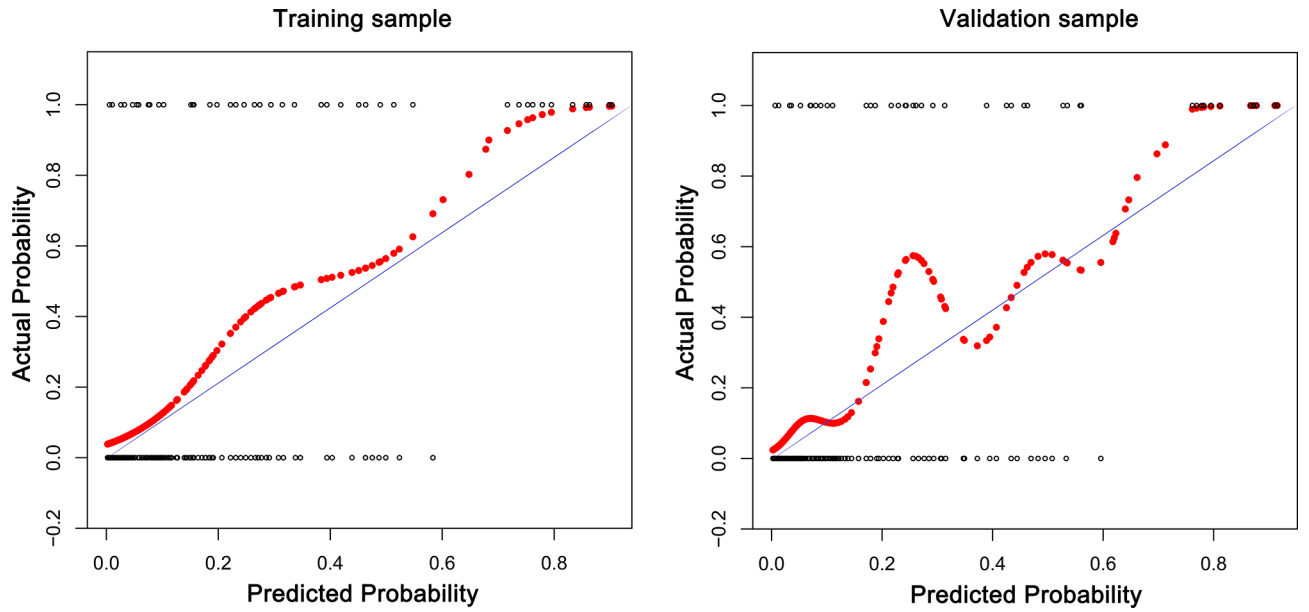

FIGURE 4 | The calibration curves for assessing the consistency between the predicted and the actual risk of postoperative VTE. Favorable consistencies between the predicted and the actual risk evaluation are presented.

patients had VTE after spinal surgery. The median operative time for patients with VTE and without VTE were 212.5 minutes and 177.5 minutes, respectively (7). A large-scale retrospective study showed that longer operative time was independently associated with an increased risk of postoperative symptomatic VTE. The risk of VTE will increase by 15% for every additional hour of surgery (5). They explained that this may require clinicians to consider more measures to prevent symptomatic VTE, such as chemoprophylaxis. Schoenfeld et al. (34) and Piper et al. (6) also determined that operative time > 261 minutes and operative time ≥ 4 hours were independent predictors of VTE after spinal surgery. In the current study, univariate and multivariate regression analyses showed that operative time is an independent prognostic factor affecting postoperative VTE. As the operative time increases by 1 hour, the risk of postoperative VTE will increase by 36%. Our explanation for this phenomenon is: maintaining a supine posture for a long time during the operation will cause part of the venous return to be blocked and blood will be in a hypercoagulable state, which could easily cause blood clots.

In the current study, we are trying to determine the risk factors of VTE after spinal metastasis surgery and further stratify and predict the future condition of patients. This predictive model can help clinicians make evidence-based decisions on when to use chemoprophylaxis, thereby further reducing the incidence of VTE and related medical expenses in patients undergoing spinal metastasis surgery.

There are several limitations in this study. First of all, any retrospective analysis may cause errors due to selection bias and recall bias; however, we reduce the selection bias by expanding the number of hospitals participating in the database construction. Secondly, due to the limitations of the database, we have not been able to analyze the potential predictive value of some indicators for postoperative VTE, such as D-dimer, preoperative hemoglobin, and blood oxygen saturation. Finally, we conducted internal validation, but did not complete external validation, which would have a certain adverse effect on the applicability of the model. Future studies should further evaluate the applicability of this model in other spinal metastasis cohorts and make possible modifications. The external validation can be accomplished by repeating the analyses of various risk factors using data from databases in other countries or regions.

The prediction model for postoperative VTE developed by our team provides clinicians with a simple method that can be used to calculate the VTE risk of patients at the bedside, and can help clinicians make evidence-based judgments on when to use intervention measures. In clinical practice, the simplicity of this predictive model has great practical value. For the pathogenesis and significance of various risk factors of VTE after surgery, further researches are needed.

DATA AVAILABILITY STATEMENT

The raw data supporting the conclusions of this article will be made available by the authors, without undue reservation.

ETHICS STATEMENT

The studies involving human participants were reviewed and approved by Medical ethics review committee of Tianjin Hospital. The patients/participants provided their written informed consent to participate in this study.

AUTHOR CONTRIBUTIONS

H-rZ and M-yX analyzed and interpreted the patient data and were the major contributors in writing this manuscript. R-qQ, Y-cH, and X-gY checked and revised the manuscript. J-kL collected the data and sorted out the material. LY and HZ participated in the conception of the study and manuscript revision. FW, J-yZ, and Y-lZ helped finalizing the manuscript. All authors contributed to the article and approved the submitted version.

ACKNOWLEDGMENTS

We thank all participating patients and their families.

REFERENCES

1. Blom JW, Doggen CJ, Osanto S, Rosendaal FR. Malignancies, Prothrombotic Mutations, and the Risk of Venous Thrombosis. *JAMA* (2005) 293(6):715–22. doi: 10.1001/jama.293.6.715
2. Heit JA, Silverstein MD, Mohr DN, Petterson TM, O'Fallon WM, Melton LJ3rd. Risk Factors for Deep Vein Thrombosis and Pulmonary Embolism: A Population-Based Case-Control Study. *Arch Internal Med* (2000) 160(6):809–15. doi: 10.1001/archinte.160.6.809
3. Nicolaides AN, Fareed J, Kakkar AK, Comerota AJ, Goldhaber SZ, Hull R, et al. Prevention and Treatment of Venous Thromboembolism–International Consensus Statement. *Int Angiol* (2013) 32(2):111–260. doi: 10.1177/1076029612474840
4. Greenall R. Prevention, Diagnosis and Treatment of Venous Thromboembolism. *Nurs Older People* (2017) 29(1):21–5. doi: 10.7748/nop.2017.e872
5. Groot OQ, Ogink PT, Paulino Pereira NR, Ferrone ML, Harris MB, Lozano-Calderon SA, et al. High Risk of Symptomatic Venous Thromboembolism After Surgery for Spine Metastatic Bone Lesions: A Retrospective Study. *Clin Orthopaedics Related Res* (2019) 477(7):1674–86. doi: 10.1097/corr.0000000000000733
6. Piper K, Algattas H, DeAndrea-Lazarus IA, Kimmell KT, Li YM, Walter KA, et al. Risk Factors Associated With Venous Thromboembolism in Patients Undergoing Spine Surgery. *J Neurosurg Spine* (2017) 26(1):90–6. doi: 10.3171/2016.6.spine1656
7. Tominaga H, Setoguchi T, Tanabe F, Kawamura I, Tsuneyoshi Y, Kawabata N, et al. Risk Factors for Venous Thromboembolism After Spine Surgery. *Medicine* (2015) 94(5):e466. doi: 10.1097/md.0000000000000466
8. Xin WQ, Xin QQ, Ming HL, Gao YL, Zhao Y, Gao YK, et al. Predictable Risk Factors of Spontaneous Venous Thromboembolism in Patients Undergoing Spine Surgery. *World Neurosurg* (2019) 127:451–63. doi: 10.1016/j.wneu.2019.04.126
9. Kaewborisutsakul A, Tunthanathip T, Yuwakosol P, Inkate S, Pattharachayakul S. Postoperative Venous Thromboembolism in Extramedullary Spinal Tumors. *Asian J Neurosurg* (2020) 15(1):51–8. doi: 10.4103/ajns.AJNS_279_19
10. Yang XG, Feng JT, Wang F, He X, Zhang H, Yang L, et al. Development and Validation of a Prognostic Nomogram for the Overall Survival of Patients Living With Spinal Metastases. *J Neurooncol* (2019) 145(1):167–76. doi: 10.1007/s11060-019-03284-y
11. Zhang HR, Zhang JY, Yang XG, Qiao RQ, Li JK, Hu YC. Predictive Value of the Nomogram Model in Patients With Megaprosthetic Failure Around the Knee: A Retrospective Analysis. *J Arthroplasty* (2020) 35(10):2944–51. doi: 10.1016/j.arth.2020.05.016
12. Zhang HR, Wang F, Yang XG, Xu MY, Qiao RQ, Li JK, et al. Establishment and Validation of a Nomogram Model for Aseptic Loosening After Tumor Prosthetic Replacement Around the Knee: A Retrospective Analysis. *J Orthopaedic Surg Res* (2019) 14(1):352. doi: 10.1186/s13018-019-1423-3
13. Sternberg CN. Are Nomograms Better Than Currently Available Stage Groupings for Bladder Cancer? *J Clin Oncol* (2006) 24(24):3819–20. doi: 10.1200/jco.2006.07.1290
14. Collins GS, Reitsma JB, Altman DG, Moons KG. Transparent Reporting of a Multivariable Prediction Model for Individual Prognosis or Diagnosis (TRIPOD): The TRIPOD Statement. *BMJ* (2015) 350:g7594. doi: 10.1136/bmj.g7594
15. Tomita K, Kawahara N, Kobayashi T, Yoshida A, Murakami H, Akamaru T. Surgical Strategy for Spinal Metastases. *Spine* (2001) 26(3):298–306. doi: 10.1097/00007632-200102010-00016
16. van Middendorp JJ, Goss B, Urquhart S, Atresh S, Williams RP, Schuetz M. Diagnosis and Prognosis of Traumatic Spinal Cord Injury. *Global Spine J* (2011) 1(1):1–8. doi: 10.1055/s-0031-1296049
17. Quan H, Li B, Couris CM, Fushimi K, Graham P, Hider P, et al. Updating and Validating the Charlson Comorbidity Index and Score for Risk Adjustment in Hospital Discharge Abstracts Using Data From 6 Countries. *Am J Epidemiol* (2011) 173(6):676–82. doi: 10.1093/aje/kwq433
18. Iasonos A, Schrag D, Raj GV, Panageas KS. How to Build and Interpret a Nomogram for Cancer Prognosis. *J Clin Oncol* (2008) 26(8):1364–70. doi: 10.1200/jco.2007.12.9791
19. Luksanapruksa P, Buchowski JM, Zebala LP, Kepler CK, Singhatanadgige W, Bumpass DB. Perioperative Complications of Spinal Metastases Surgery. *Clin Spine Surg* (2017) 30(1):4–13. doi: 10.1097/bsd.0000000000000484
20. Atkinson RA, Jones A, Ousey K, Stephenson J. Management and Cost of Surgical Site Infection in Patients Undergoing Surgery for Spinal Metastasis. *J Hosp Infection* (2017) 95(2):148–53. doi: 10.1016/j.jhin.2016.11.016
21. Quraishi NA, Rajabian A, Spencer A, Arealis G, Mehdian H, Boszczyk BM, et al. Reoperation Rates in the Surgical Treatment of Spinal Metastases. *Spine J* (2015) 15(3 Suppl):S37–43. doi: 10.1016/j.spinee.2015.01.005
22. Donnellan E, Khorana AA. Cancer and Venous Thromboembolic Disease: A Review. *Oncologist* (2017) 22(2):199–207. doi: 10.1634/theoncologist.2016-0214
23. Bergqvist D, Arcelus JI, Felicissimo P. Evaluation of the Duration of Thromboembolic Prophylaxis After High-Risk Orthopaedic Surgery: The ETHOS Observational Study. *Thromb Haemostasis* (2012) 107(2):270–9. doi: 10.1160/th11-07-0463
24. Sørensen HT, Mellemkjaer L, Olsen JH, Baron JA. Prognosis of Cancers Associated With Venous Thromboembolism. *New Engl J Med* (2000) 343(25):1846–50. doi: 10.1056/nejm200012213432504
25. Wang T, Yang SD, Huang WZ, Liu FY, Wang H, Ding WY. Factors Predicting Venous Thromboembolism After Spine Surgery. *Medicine* (2016) 95(52):e5776. doi: 10.1097/md.0000000000005776
26. Dermody M, Alessi-Chinetti J, Iafrati MD, Estes JM. The Utility of Screening for Deep Venous Thrombosis in Asymptomatic, Non-Ambulatory Neurosurgical Patients. *J Vasc Surg* (2011) 53(5):1309–15. doi: 10.1016/j.jvs.2010.10.115
27. Zacharia BE, Kahn S, Bander ED, Cederquist GY, Cope WP, McLaughlin L, et al. Incidence and Risk Factors for Preoperative Deep Venous Thrombosis in 314 Consecutive Patients Undergoing Surgery for Spinal Metastasis. *J Neurosurg Spine* (2017) 27(2):189–97. doi: 10.3171/2017.2.spine16861
28. Aach M, Cruciger O, Sczesny-Kaiser M, Höffken O, Meindl R, Tegenthoff M, et al. Voluntary Driven Exoskeleton as a New Tool for Rehabilitation in Chronic Spinal Cord Injury: A Pilot Study. *Spine J* (2014) 14(12):2847–53. doi: 10.1016/j.spinee.2014.03.042
29. Douros A, Jobski K, Kollhorst B, Schink T, Garbe E. Risk of Venous Thromboembolism in Cancer Patients Treated With Epoetins or Blood Transfusions. *Br J Clin Pharmacol* (2016) 82(3):839–48. doi: 10.1111/bcp.13019
30. Zacharski LR. Hypercoagulability Preceding Cancer. The Iron Hypothesis. *J Thromb Haemostasis: JTH* (2005) 3(3):585–8. doi: 10.1111/j.1538-7836.2005.01178.x
31. Khorana AA, Francis CW, Blumberg N, Culakova E, Refaai MA, Lyman GH. Blood Transfusions, Thrombosis, and Mortality in Hospitalized Patients With Cancer. *Arch Internal Med* (2008) 168(21):2377–81. doi: 10.1001/archinte.168.21.2377
32. Christensen DH, Horváth-Puhó E, Thomsen RW, Knudsen ST, Dekkers O, Prandoni P, et al. Venous Thromboembolism and Risk of Cancer in Patients

With Diabetes Mellitus. *J Diabetes Its Complications* (2016) 30(4):603–7. doi: 10.1016/j.jdiacomp.2016.01.011
33. Tsuda Y, Goto T, Ikegami M, Yamada N, Yamakawa K, Hozumi T, et al. Incidence of, and Risk Factors for, Postoperative Venous Thromboembolism in Patients With Benign or Malignant Musculoskeletal Tumors. *J Orthopaedic Sci* (2013) 18(4):613–7. doi: 10.1007/s00776-013-0401-6
34. Schoenfeld AJ, Herzog JP, Dunn JC, Bader JO, Belmont PJ. Patient-Based and Surgical Characteristics Associated With the Acute Development of Deep Venous Thrombosis and Pulmonary Embolism After Spine Surgery. *Spine* (2013) 38(21):1892–8. doi: 10.1097/BRS.0b013e31829fc3a0

Conflict of Interest: The authors declare that the research was conducted in the absence of any commercial or financial relationships that could be construed as a potential conflict of interest.

frontiers in Oncology

ORIGINAL RESEARCH
published: 25 June 2021
doi: 10.3389/fonc.2021.640933

Surgical Treatment of Sacral Metastatic Tumors

Mengxiong Sun, Dongqing Zuo, Hongsheng Wang, Jiakang Sheng, Xiaojun Ma, Chongren Wang, Pengfei Zan, Yingqi Hua, Wei Sun and Zhengdong Cai*

Department of Orthopedics, Shanghai General Hospital, Shanghai, China

Objective: This study intends to retrospectively analyze the data of patients with sacral metastases in our center, and analyze the treatment methods and therapeutic effects of sacral metastases.

Methods: 73 patients with sacral metastases treated in our hospital from June 2013 to June 2019 were retrospectively analyzed. There were 54 cases of neurological symptoms, 42 cases of sacroiliac joint instability, 24 cases of lower limb muscle weakness and 19 cases of abnormal urination and defecation. Four patients with tumors below S3 underwent complete tumor resection, 23 patients with tumors above S3 and without sacroiliac joint instability underwent tumor curettage and nerve root lysis, 34 patients with tumors above S3 and sacroiliac joint instability underwent tumor curettage, nerve root release and screw rod reconstruction. 12 patients with multiple metastases underwent percutaneous radiofrequency ablation and sacroplasty. VAS was used to evaluate the preoperative and postoperative pain scores, and the postoperative pain relief, neurological function, bowel function, wound healing and complications were evaluated.

Results: There were no perioperative death, 8 cases of poor wound healing, 5 cases of nerve injury, postoperative sensory and motor loss of lower limbs. Cerebrospinal fluid (CSF) leak in 7 cases. The patients were followed up for 6-25 months (mean 12 months). The VAS scores of patients with pain symptoms were 7 points before operation and 1.44 points after operation, In 19 patients with abnormal urination and defecation function, 12 patients recovered to normal 3-6 months after operation, 5 cases had no significant change compared with preoperative, and 2 cases had aggravated symptoms; 17 cases of patients with lower limb muscle strength were significantly recovered after operation, and the average muscle strength was increased by 2 grades; 30 cases of patients with unstable sacroiliac joint got internal fixation had significantly pain relief. Pain symptoms of 9 patients were significantly relieved after percutaneous radiofrequency ablation.

Conclusion: the operation of sacral metastases mainly adopts a relatively conservative surgical method, which can effectively improve the quality of life of patients with sacral metastases by retaining the nerve function and relieving the pain of patients, combining with radiofrequency ablation, sacroplasty and targeted drugs.

Keywords: sacral metastasis, bone tumor, surgery, radiofrequency ablation, sacroplasty

OPEN ACCESS

Edited by:
Dianwen Song,
Shanghai First People's Hospital, China

Reviewed by:
Talib Hassan Ali,
University of ThiQar, Iraq
Li Min,
Sichuan University, China

****Correspondence:***
Wei Sun
viv-sun@163.com

Specialty section:
This article was submitted to Molecular and Cellular Oncology, a section of the journal Frontiers in Oncology

Received: *12 December 2020*
Accepted: *25 May 2021*
Published: *25 June 2021*

Citation:
Sun M, Zuo D, Wang H, Sheng J, Ma X, Wang C, Zan P, Hua Y, Sun W and Cai Z (2021) Surgical Treatment of Sacral Metastatic Tumors. Front. Oncol. 11:640933. doi: 10.3389/fonc.2021.640933

INTRODUCTION

With the development of tumor treatment, many solid tumor patients can get effective treatment and obtain long-term survival. Some patients have bone metastasis in the late stage of treatment (1). Sacrum is also the site of bone metastases in tumor patients (2, 3). Because of the special anatomical position and abundant blood supply of sacrum (4), the treatment of sacral metastatic tumors is relatively difficult. At present, there is no unified standard and guideline for the treatment of sacral metastatic tumors in the world.

Most of the traditional treatments for sacral metastases are local radiotherapy or palliative treatment (2, 5). However, radiotherapy can alleviate the symptoms of patients with sacral metastases, but also has some limitations. For example, radiotherapy may bring wound complications, and due to the special location of the sacrum, radiotherapy may sometimes bring intestinal damage, resulting in radiation enteritis, and so on, and some tumors, due to multiple metastases, cannot solve all the problems through radiotherapy. At the same time, because of the low incidence rate, most cases reported sacral metastases are few (6). At present, the treatment and complications of sacral metastases are still not very clear.

In this study, the data of patients with sacral metastases in our center were analyzed retrospectively, including gender, age, primary tumor, symptoms, treatment methods, symptom remission, improvement of VAS score and complications.

MATERIALS AND METHODS

Data of 73 patients with sacral metastases from June 2013 to June 2019 were collected. The whole project was approved by the ethics committee of Shanghai General Hospital, and all patients signed informed consent. The general information of patients, primary tumor, local and systemic symptoms, treatment methods, pain relief, nerve function, defecation and other data were collected. VAS score system was used for pain relief before treatment, 1 month and 3 months after treatment, and ECoG score system was used for general condition of patients. According to the time nodes (3 months, 6 months, 9 months, 12 months, 24 months), the local control rate and overall survival time were collected. All patients were operated from the posterior approach. Subtotal resection is mainly used when the tumor invades the surrounding nerve seriously and needs to preserve the sacral nerve. It mainly uses curettage or piece-meal resection to preserve the sacral nerve to the maximum extent. En bloc resection is mainly used for complete resection of tumors, mainly for tumors below S3, and complete resection of tumors along the tumor edge.

Sub-total Resection

When the tumor is located in S1-S2, in order to preserve the S1-S2 nerve root of the patient, we used sub-total resection. The specific implementation steps are to open the sacral lamina, decompress the nerve root, scrape off the tumor in the sacral vertebra, and further decompress the nerve root.

En-Bloc Resection

When the tumor is located below S3, we used en-bloc resection. The specific implementation steps are: after exposing the tumor, we start en-bloc resection of the sacrum from the sacrum above the tumor to completely remove the tumor. During the operation, we should pay attention not to injure the intestine in front.

Reconstruction

For patients with stable sacroiliac joint, we usually use bone cement sacroplasty for reconstruction after tumor resection, while for patients with unstable sacroiliac joint, we usually use spinal internal fixation screw rod for fixation.

Statistical Analysis

All statistical analyses were performed using SPSS software package version 16.0 (SPSS Inc., Chicago, IL, USA). Paired t tests were used to assess the significance of the difference between the preoperative, 1-month postoperative and 3-month postoperative scores. The Kaplan–Meier method was used to estimate local control rates and overall survival rates. The log–rank test was used to compare the factors affecting local control. A p value < 0.05 was considered statistically significant.

RESULTS

A total of 73 patients were enrolled, including 33 males (45.2%) and 40 females (54.8%). The average age was 63 years old. 52 patients (71.2%) were over 60 years old and 21 patients (28.8%) were under 60 years old. The average follow-up time was 12 months (range, 6-25 months) (**Table 1**). In the early stage of the disease, 54 patients had lower limb pain, 42 patients had

TABLE 1 | Patients information about the 73 sacral metastasis.

Characteristics	N (%)
Gender	
Male	33 (45.2)
Female	40 (54.8)
Age	
≥60	52 (71.2)
<60	21 (28.8)
Sacral site	
S1-S3	69 (94.5)
S4-SS	4 (5.5)
Primary tumor	
Lung cancer	13 (17.8)
Breast cancer	9 (12.3)
thyroid cancer	7 (9.6)
prostate cancer	9 (12.3)
renal cancer	16 (21.9)
haematological malignancy	3 (4.1)
nasopharyngeal carcinoma	1 (1.14)
rectal cancer	15 (20.5)

Abbreviation: VAS, Visual Analogue Scale; ECOG, Eastern Cooperative Oncology Group; CSF, Cerebrospinal fluid.

sacroiliac joint instability, 24 patients had lower limb muscle strength decline, 12 patients had urination dysfunction, and 7 patients had bowel dysfunction. The average duration of preoperative symptoms was 3 months (1-20 months) (**Table 2**). Among the 19 patients with abnormal urination or bowel function, 12 cases recovered to normal 3-6 months after operation, 5 cases had no obvious change compared with that before operation, and 2 cases had aggravation of symptoms; 17 cases of patients with lower limb muscle strength were significantly recovered after operation, and the average muscle strength was increased by 2 grades.

Among the primary tumor diseases, clear cell renal cell carcinoma was the most common, 16 cases in total, accounting for 21.9%. Among the remaining cancers, 13 cases were lung cancer (17.8%), 9 cases were breast cancer (12.3%), 7 cases were thyroid cancer (9.6%), 9 cases were prostate cancer (12.3%), 3 cases were hematological system tumor (4.1%), 1 case was nasopharyngeal carcinoma (1.4%), and 15 cases were rectal cancer (20.5%) (**Table 1**). Except for rectal cancer, the rest of the tumors were hematogenous metastasis, and most of the rectum was considered as local implantation or infiltration because of its anatomical location close to the sacrum. In all patients, 39 cases (53.4%) had single metastasis, while 34 cases (46.5%) had multiple systemic metastasis. 37 patients had not been treated with primary disease before operation, 10 patients received surgery and chemotherapy at the primary site, 5 patients received surgery at the primary site and radiotherapy at the sacrum, 14 patients received surgery and targeted drug therapy at the primary site, 4 patients received immunotherapy, and 3 patients received local perfusion chemotherapy at the metastatic site.

In 69 patients, tumors were located at S1-S3 (94.5%), and in 4 patients, tumors were located at S4-S5 (5.5%) (**Table 1**). In the treatment, 4 patients with tumors below S3 were treated with en bloc resection. 23 patients with tumors above S3 and without sacroiliac joint instability underwent tumor curettage and neurolysis, 34 patients with tumors above S3 and sacroiliac joint instability underwent tumor curettage, nerve root release and Pedicle screw reconstruction (6), and 12 patients with multiple metastases underwent percutaneous radiofrequency ablation and sacroplasty (**Table 3**). 27 patients underwent preoperative embolization of tumor blood vessels (7). All operations were performed in prone position. Modified Galveston technology was used for internal fixation of sacroiliac joint.(**Figure 1**). Lung cancer and renal cancer patients continue to take targeted drugs after surgery (8, 9), and patients with nasopharyngeal carcinoma continue to receive radiotherapy (10). A patient with renal cell carcinoma recurred many times after resection of the sacral tumor for the first time. After the first operation, percutaneous radiofrequency ablation was used in the later several times due to the rich blood supply (11). The local swelling and pain symptoms of the patient were relieved after radiofrequency ablation. The pain of 30 patients with sacroiliac joint instability and lumbosacral internal fixation was significantly relieved, and the pain symptoms of 9 patients after percutaneous radiofrequency ablation and sacroplasty were significantly relieved.

TABLE 2 | Symptoms and signs of the 73 patients.

Symptoms and signs	N (%)
Leg pain or buttock pain	54 (73.9)
sacroiliac joint instability	42 (57.5)
Lower limb muscle weakness	24 (32.8)
neurogenic bladder dysfunction	12 (16.4)
neurogenic bowel dysfunction	7 (9.6)

TABLE 3 | Treatment modality of the 73 patients.

Treatment modality	N (%)
Gross-total resection	4 (5.5)
Subtotal resection without fixation	23 (31.5)
Subtotal resection with fixation	34 (46.6)
percutaneous radiofrequency ablation + sacroplasty	12 (16.4)

None of the patients died during the perioperative period. There were 8 cases of poor wound healing, 5 cases healed after the first debridement, 2 cases healed after the second debridement, 1 case of wound sinus formation, 5 cases of nerve injury, postoperative sensory and motor loss of lower limbs, 1 case of partial recovery of nerve function during the follow-up period, and the remaining 4 cases did not recover significantly. Cerebrospinal fluid leakage occurred in 7 cases and healed after bed rest, head down and foot high position and wound pressure (12). Two cases of venous thrombosis of lower extremity were relieved after anticoagulation for 2 weeks (13). There were 3 cases of transient urinary retention, 2 cases of urinary tract infection, 1 case of rectal injury and 1 case of long-term internal fixation loosening. (**Table 4**)

The VAS scores of all patients were 7 points before operation, 1.44 points at 1 month after operation, and 1.51 points at 3 months after operation ($P < 0.0001$) (**Figure 2**). The average score of ECoG was 2.52 before operation, 1.33 at 1 month after operation and 0.93 at 3 months after operation ($P < 0.0001$) (**Figure 3**).

The local control time was 18 months (95% CI 0.72-12.36 months), and the local control rate was 75% and 50% at 9 months and 24 months, respectively. The average local control time of sub total resection group was 6 months (95% CI 0.81-1.37 months). The local control rates at 3 months, 6 months, 9 months, 12 months, 18 months and 24 months were 70.2%, 45.6%, 38.6%, 26.3%, 22.8% and 19.3%, respectively. There was no significant difference in the local control rate between the two surgical methods ($P = 0.1515$, log rank test). However, it can be seen from the survival curve that the two methods have a certain trend. En bloc resection seems to be more effective for local control (**Figure 4**). The overall survival rate of patients in en-bloc resection was 18 months (95% CI 0.46-4.82 months), and the overall survival rates of 9 months, 12 months and 24 months were 75%, 50% and 24.6%, respectively. The overall survival time of patients in sub total resection group was 12 months (95% CI 0.21-2.14 months). The overall survival rates of 3 months, 6 months, 9 months, 12 months, 18 months, 25 months were 82.5%, 66.7%, 61.4%, 28.1%, 24.6%, 16.4%, respectively. There

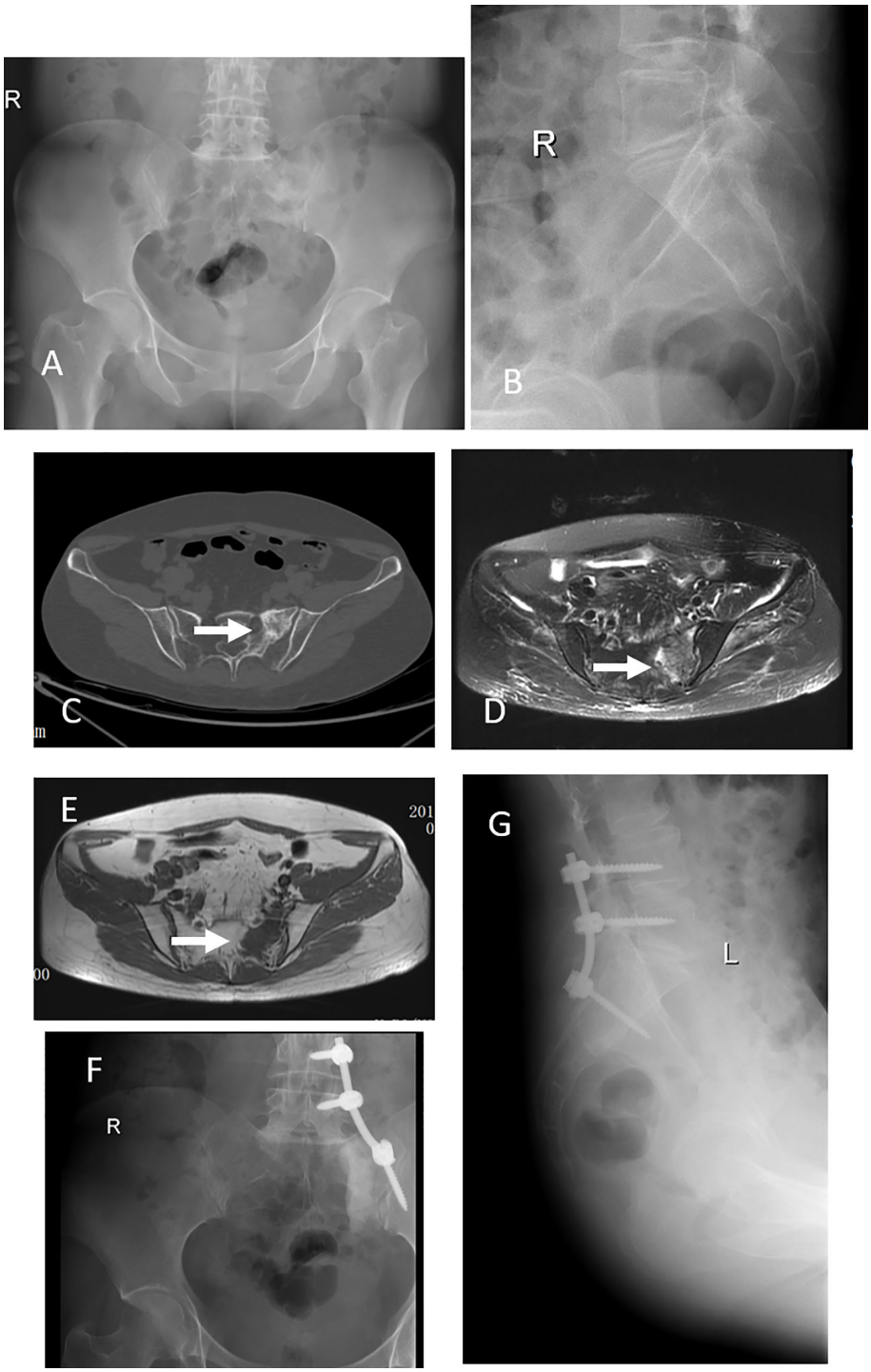

FIGURE 1 | This 42 years old woman had severe back pain after breast cancer treatment for 7 years. X-ray and CT scan showed a tumor at left S1-2 **(A–C)**, an arrow indicate the lesion. MRI scan, both T1 and T2, indicated the tumor occurred in the left S1-2 **(D, E)**. This patient got a subtotal resection and pedicle screw fixation **(F, G)**.

TABLE 4 | Complications of the 73 patients.

Complications	N
Poor wound healing	8
Wound infection	3
sinus tract	1
CSF leak	7
peripheral nerve injury	5
transient urinary retention	3
urinary tract infection	2
Internal fixation loosing	1
rectal injury	1
DVT	2

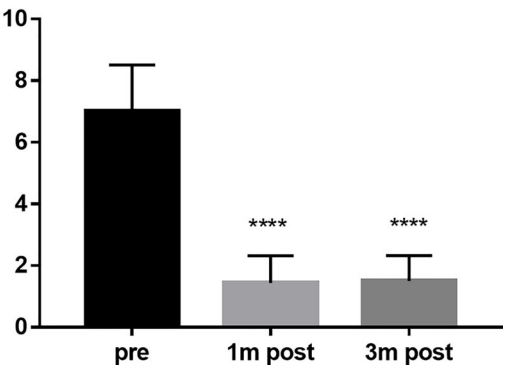

FIGURE 2 | VAS score compared the scores of the patients pre, 1 month post and 3 months post operation. ****P < 0.0001.

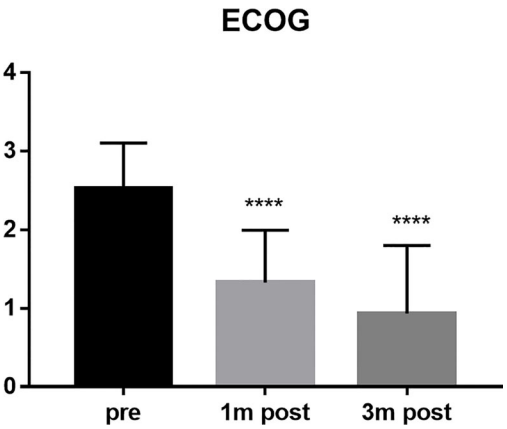

FIGURE 3 | ECOG score compared the scores of the patients pre, 1 month post and 3 months post operation. ****P < 0.0001 and indicated the ECOG scores decreased after surgery.

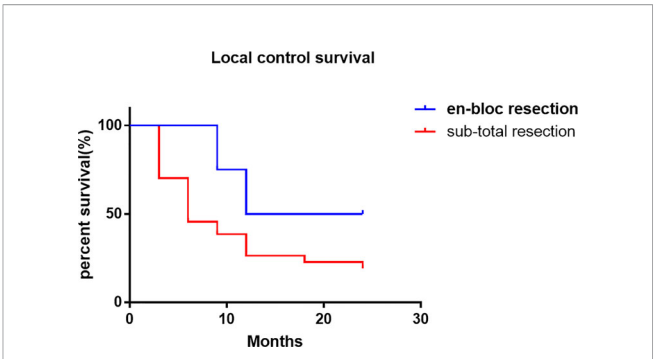

FIGURE 4 | Local control survival rate compared the en-bloc resection and sub-total resection.

was no significant difference in the overall survival rate between the two methods (P = 0.6653, log rank test) (**Figure 5**).

DISCUSSION

Sacral metastases are common tumors of the sacrum, but due to the existence of systemic diseases, the treatment of this metastatic site does not have a decisive impact on the overall survival time of patients. At present, palliative treatment is often used for the treatment of sacral metastases (14). The main purpose of palliative treatment is to relieve local symptoms, including pain and neurological dysfunction. The main treatment methods include some systemic medication and local radiotherapy. If a patient has a pathological sacral fracture and a risk of spinal cord compression, surgical intervention is often required in the case of local non-invasive treatment failure. In these cases, such as sacroiliac joint instability and pain, surgical intervention is particularly important. The contraindications of sacral metastases also include that the tumor situation of the whole body can not tolerate surgery or treatment. The multiple metastatic lesions of the whole body are often treated mainly by internal medicine, and the patients refuse surgery and other situations are not suitable for surgical treatment.

Although sacral metastases are common tumors in the sacrum, with the development of cancer treatment, many solid

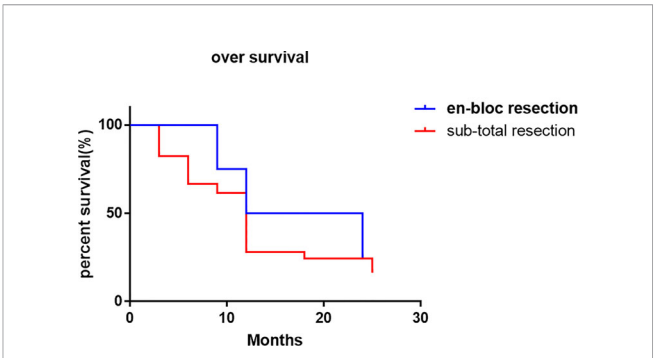

FIGURE 5 | Overall survival rate compared the en-bloc resection and sub-total resection.

tumor patients can get a longer survival time (1). This also increases the incidence rate of bone metastases including sacral metastasis. However, the overall incidence of sacral metastases is still low, resulting in less reports on sacral metastases (15). There are unified norms and standards in the disease. This also increases the significance of our study.

The final prognosis of patients with sacral metastases is closely related to the pathological characteristics of patients with primary diseases. For example, in non-small cell lung cancer, gastrointestinal cancer and other tumors with poor response to systemic treatment (16, 17), although the sacral metastases have been removed, the overall prognosis is still poor. Therefore, the operation of sacral metastases should be as small as possible on the basis of nerve preservation functions. We had a case of lung cancer with sacral metastasis. When systemic chemotherapy drugs and local radiotherapy could not solve the pain caused by sacral lesions, lower limb dysfunction and defecation dysfunction, we gave him limited surgery and internal fixation, and the postoperative symptoms were well relieved. But in some primary diseases for breast cancer or prostate cancer patients with sacral metastases, this kind of patients have a good response of systemic treatment (18, 19). For this kind of patients, in order to solve the local pain and nerve symptoms caused by the metastasis, aggressive treatment modality should be involved, we had a prostate cancer metastasis patients, not only have sacral metastasis, but also There were bilateral proximal femur metastases. In order to solve the pain of the patient, we operated on all the sites, which causes pain in the patient, and continued to use endocrine therapy after the operation. The local symptoms were relieved of the patient and achieved a good prognosis. Another case is if the primary tumor is renal cell carcinoma. The response to systemic treatment of renal cell carcinoma is not very good, however, the prognosis is still good (20). Such patients should also be actively treated. We have a case of renal cancer patients with sacral metastasis, after the first sacral surgery, because the patient's tumor blood supply is extremely rich, in order to reduce the intraoperative and postoperative complications, we conducted CT guided percutaneous radiofrequency ablation for the patient (21). The VAS score of the patients decreased significantly and the quality of life improved.

In this study, the vast majority of sacral metastatic tumors are located above S3. In order to preserve nerve function, en bloc is very difficult for tumors above S3. Therefore, extensive intralesional resection was performed in all these cases. In 4 cases, en bloc resection with preservation of all S1-S3 nerves was performed to maximize nerve function. Moreover, there was no local recurrence of sacrum in our 4 cases, which was the same as that reported by I. Feiz erfan et al. (15). Although en bloc resection can minimize local recurrence, in this group of S4-5 metastatic cases, after en-bloc resection, there are still S1-S3 recurrence or new metastases, which further proves that palliative surgery is still the main treatment for sacral metastases. However, although there is no statistical difference between en bloc resection and sub total resection in local control, there is still a certain trend in local control of en bloc resection, which can better control local recurrence. However, there is no significant difference between the two methods in the control of overall survival rate.

In terms of reconstruction after resection of sacrum tumor, sacroiliac joint instability is the absolute indication for screw rod reconstruction. In patients with pain due to sacroiliac joint instability before operation, after effective screw rod reconstruction, the pain symptoms of patients have been significantly relieved. In addition, in patients without sacroiliac joint instability, there is no significant difference between the two groups, Bone cement reconstruction can also significantly reduce postoperative pain. Therefore, effective sacroiliac joint fixation and bone cement molding can effectively reduce postoperative pain symptoms and improve the quality of life of patients.

Gaps in sacral operative area often lead to poor wound healing (22, 23). In this group of cases, there were 8 cases of poor wound healing, 5 cases of wound healing after the first debridement, 2 cases of wound healing after the second debridement, 1 case of wound sinus formation. This often needs the cooperation of plastic surgeons to solve the problem of poor wound healing. At the same time, minimally invasive surgery, such as percutaneous radiofrequency ablation, has a certain application space. Minimally invasive surgery can alleviate the local pain symptoms of patients (21), and will not cause wound complications. The incidence of wound complications will be increased if preoperative radiotherapy was performed. Whether a part of patients with sacral metastases can be considered for surgical treatment first, and then continue to use radiotherapy control in case of local recurrence or progression should also be considered (24).

However, this study also has some limitations. Firstly, as a retrospective study, there is no control group, so it is impossible to compare the priority and selectivity of non-surgical method and surgical method in the treatment of sacral metastases. Secondly, there is no separate list of primary pathological tumor species for single analysis, and it is impossible to analyze and judge the treatment methods, prognosis and complications of sacral metastases from the perspective of different primary disease. Therefore, it is necessary to conduct a randomized controlled study to analyze the control and complications of different treatment methods for sacral metastases. It is also necessary to expand the number of single primary pathological types of sacrum metastases for different studies

In conclusion, the treatment of sacral metastases is still based on the treatment of primary diseases, and palliative treatment is still the main course to relieve symptoms of sacral metastasis. This study retrospectively analyzed the treatment methods of sacral metastatic tumors, mainly focused on the surgical treatment of sacral metastases, analyzed the general situation and disease characteristics of patients with sacral metastases, analyzed the advantages and complications of surgery, radiofrequency ablation and other methods in sacral metastases, and concluded that en-bloc resection is somehow an effective method for the treatment of sacral metastases but have no significant influence on the over survival. Therefore, the

treatment of sacral metastases still needs to be combined with the systemic treatment of the primary disease in order to obtain a better prognosis.

DATA AVAILABILITY STATEMENT

The original contributions presented in the study are included in the article/supplementary material. Further inquiries can be directed to the corresponding author.

ETHICS STATEMENT

The project was approved by the ethics committee of Shanghai General Hospital, and all patients signed informed consent.

AUTHOR CONTRIBUTIONS

Conceptualization: MS and WS. Data curation: MS and DZ. Formal analysis: HW. Funding acquisition: MS, WS, YH, and ZC. Investigation: MS, WS, XM, and JS. Methodology: CW and PZ. Project administration: MS, WS, and ZC. Resources: MS and WS. Supervision: ZC. Validation: MS. Visualization: MS and WS. Writing—original draft: MS. Writing—review and editing: MS, WS, and ZC. All authors contributed to the article and approved the submitted version.

FUNDING

Supported by National Natural Science Foundation of China (number: 8177101011).

REFERENCES

1. Janjan N. Bone Metastases: Approaches to Management. *Semin Oncol* (2001) 28(4 Suppl 11):28–34. doi: 10.1053/sonc.2001.25444
2. Quraishi NA, Giannoulis KE, Edwards KL, Boszczyk BM. Management of Metastatic Sacral Tumours. *Eur Spine J* (2012) 21(10):1984–93. doi: 10.1007/s00586-012-2394-9
3. Murphy E, Lyons R, Curtin M, Munigangaiah S, McCabe J, Devitt A. Current Concepts and an Update on the Surgical Management of Metastasis to the Sacral Spine. *J Natural Science Biol Med* (2019) 10(2):119–26. doi: 10.4103/jnsbm.JNSBM_104_18
4. Tang X, Guo W, Yang R, Tang S, Ji T. Risk Factors for Blood Loss During Sacral Tumor Resection. *Clin Orthop Relat Res* (2009) 467(6):1599–604. doi: 10.1007/s11999-008-0483-1
5. Gibbs IC, Chang SD. Radiosurgery and Radiotherapy for Sacral Tumors. *Neurosurg Focus* (2003) 15(2):E8. doi: 10.3171/foc.2003.15.2.8
6. Buraimoh MA, Yu CC, Mott MP, Graziano GP. Sacroiliac Stabilization for Sacral Metastasis: A Case Series. *Surg Neurol Int* (2017) 8:287. doi: 10.4103/sni.sni_324_17
7. Gottfried ON, Schmidt MH, Stevens EA. Embolization of Sacral Tumors. *Neurosurg Focus* (2003) 15(2):E4. doi: 10.3171/foc.2003.15.2.4
8. Hirsch FR, Scagliotti GV, Mulshine JL, Kwon R, Curran WJJr., Wu YL, et al. Lung Cancer: Current Therapies and New Targeted Treatments. *Lancet* (2017) 389(10066):299–311. doi: 10.1016/S0140-6736(16)30958-8
9. Gul A, Rini BI. Adjuvant Therapy in Renal Cell Carcinoma. *Cancer* (2019) 125(17):2935–44. doi: 10.1002/cncr.32144
10. Sun XS, Li XY, Chen QY, Tang LQ, Mai HQ. Future of Radiotherapy in Nasopharyngeal Carcinoma. *Br J Radiol* (2019) 92(1102):20190209. doi: 10.1259/bjr.20190209
11. Madaelil TP, Wallace AN, Jennings JW. Radiofrequency Ablation Alone or in Combination With Cementoplasty for Local Control and Pain Palliation of Sacral Metastases: Preliminary Results in 11 Patients. *Skeletal Radiol* (2016) 45(9):1213–9. doi: 10.1007/s00256-016-2404-9
12. Fang Z, Tian R, Jia YT, Xu TT, Liu Y. Treatment of Cerebrospinal Fluid Leak After Spine Surgery. *Chin J Traumatol* (2017) 20(2):81–3. doi: 10.1016/j.cjtee.2016.12.002
13. Yuan H, Sun J, Zhou Z, Qi H, Wang M, Dong D, et al. Diagnosis and Treatment of Acquired Arteriovenous Fistula After Lower Extremity Deep Vein Thrombosis. *Int Angiol* (2019) 38(1):10–6. doi: 10.23736/S0392-9590.19.04063-X
14. Ampil F, Sangster G, Caldito G, Richards T, Ngo Y, Kim D, et al. Palliative Radiotherapy as a Treatment for Carcinoma Invasion of the Sacrum: An Observational Case Series Study. *Anticancer Res* (2018) 38(12):6797–800. doi: 10.21873/anticanres.13051
15. Feiz-Erfan I, Fox BD, Nader R, Suki D, Chakrabarti I, Mendel E, et al. Surgical Treatment of Sacral Metastases: Indications and Results. *J Neurosurg Spine* (2012) 17(4):285–91. doi: 10.3171/2012.7.SPINE09351
16. Herbst RS, Morgensztern D, Boshoff C. The Biology and Management of non-Small Cell Lung Cancer. *Nature* (2018) 553(7689):446–54. doi: 10.1038/nature25183
17. Yang C, Chen F, Wang S, Xiong B. Circulating Tumor Cells in Gastrointestinal Cancers: Current Status and Future Perspectives. *Front Oncol* (2019) 9:1427. doi: 10.3389/fonc.2019.01427
18. Di Zazzo E, Galasso G, Giovannelli P, Di Donato M, Castoria G. Estrogens and Their Receptors in Prostate Cancer: Therapeutic Implications. *Front Oncol* (2018) 8:2. doi: 10.3389/fonc.2018.00002
19. Debiasi M, Polanczyk CA, Ziegelmann P, Barrios C, Cao H, Dignam JJ, et al. Efficacy of Anti-HER2 Agents in Combination With Adjuvant or Neoadjuvant Chemotherapy for Early and Locally Advanced HER2-Positive Breast Cancer Patients: A Network Meta-Analysis. *Front Oncol* (2018) 8:156. doi: 10.3389/fonc.2018.00156
20. Capitanio U, Montorsi F. Renal Cancer. *Lancet* (2016) 387(10021):894–906. doi: 10.1016/S0140-6736(15)00046-X
21. Burgard CA, Dinkel J, Strobl F, Paprottka PM, Schramm N, Reiser M, et al. CT Fluoroscopy-Guided Percutaneous Osteoplasty With or Without Radiofrequency Ablation in the Treatment of Painful Extraspinal and Spinal Bone Metastases: Technical Outcome and Complications in 29 Patients. *Diagn Interv Radiol* (2018) 24(3):158–65. doi: 10.5152/dir.2018.17265
22. Gao S, Zheng Y, Liu X, Tian Z, Zhao Y. Effect of Early Fasting and Total Parenteral Nutrition Support on the Healing of Incision and Nutritional Status in Patients After Sacrectomy. *Orthop Traumatol Surg Res* (2018) 104(4):539–44. doi: 10.1016/j.otsr.2018.02.006
23. Guo Y, Palmer JL, Shen L, Kaur G, Willey J, Zhang T, et al. Bowel and Bladder Continence, Wound Healing, and Functional Outcomes in Patients Who Underwent Sacrectomy. *J Neurosurg Spine* (2005) 3(2):106–10. doi: 10.3171/spi.2005.3.2.0106
24. Du Z, Guo W, Yang R, Tang X, Ji T, Li D. What Is the Value of Surgical Intervention for Sacral Metastases? *PLoS One* (2016) 11(12):e0168313. doi: 10.1371/journal.pone.0168313

Conflict of Interest: The authors declare that the research was conducted in the absence of any commercial or financial relationships that could be construed as a potential conflict of interest.

frontiers in Oncology

ORIGINAL RESEARCH
published: 02 August 2021
doi: 10.3389/fonc.2021.652040

Development of a tRNA-Derived Small RNA Prognostic Panel and Their Potential Functions in Osteosarcoma

Zhenming Tang[†], *Shuhui Zhang*[†] *and Zhougui Ling*[*]

Department of Pulmonary and Critical Care Medicine, The Fourth Affiliated Hospital of Guangxi Medical University, Liuzhou, China

Background: Therapeutic outcomes of osteosarcoma treatment have not significantly improved in several decades. Therefore, strong prognostic biomarkers are urgently needed.

Methods: We first extracted the tRNA-derived small RNA (tsRNA) expression profiles of osteosarcoma from the GEO database. Then, we performed a unique module analysis and use the LASSO-Cox model to select survival-associated tsRNAs. Model effectiveness was further verified using an independent validation dataset. Target genes with selected tsRNAs were predicted using RNAhybrid.

Results: A LASSO-Cox model was established to select six prognostic tsRNA biomarkers: tRF-33-6SXMSL73VL4YDN, tRF-32-6SXMSL73VL4YK, tRF-32-M1M3WD8S746D2, tRF-35-RPM830MMUKLY5Z, tRF-33-K768WP9N1EWJDW, and tRF-32-MIF91SS2P46I3. We developed a prognostic panel for osteosarcoma patients concerning their overall survival by high-low risk. Patients with a low-risk profile had improved survival rates in training and validation dataset.

Conclusions: The suggested prognostic panel can be utilized as a reliable biomarker to predict osteosarcoma patient survival rates.

Keywords: osteosarcoma, tsRNA, miRNA-seq, prognostic panel, survival

OPEN ACCESS

Edited by:
Dianwen Song,
Shanghai First People's Hospital, China

Reviewed by:
Xudong Zhang,
University of California, Riverside, United States
Shaoqiu Chen,
University of Hawaii, United States

***Correspondence:**
Zhougui Ling
lzg228@163.com

[†]*These authors have contributed equally to this work*

Specialty section:
This article was submitted to Molecular and Cellular Oncology, a section of the journal Frontiers in Oncology

Received: *11 January 2021*
Accepted: *31 March 2021*
Published: *02 August 2021*

Citation:
Tang Z, Zhang S and Ling Z (2021) Development of a tRNA-Derived Small RNA Prognostic Panel and Their Potential Functions in Osteosarcoma. Front. Oncol. 11:652040. doi: 10.3389/fonc.2021.652040

INTRODUCTION

Osteosarcoma is one of the most common primary malignant tumors in bone development from the mesenchymal cell line and occurs mostly in adolescents with a worldwide incidence of 3.4/1,000,000 per year (1). Rapid tumor growth is due to the direct or indirect form of tumor osteoid and bone tissue through the cartilage stage (2). The disease puts a heavy burden on children and their parents and brings both irreparable psychological trauma and financial strain to patients' families and society. Although a combination of neoadjuvant chemotherapy and extensive surgical resection somewhat improves patient outcomes, the overall 5-year disease-free survival rate is only about 65% (3). The traditional prognostic factors for osteosarcoma patients are broad, including tumor size, location, grade, metastasis, and sensitivity to chemotherapy. This diversity of prognostic factors prevents a direct comparison between the criteria. Since metastasis and sensitivity to chemotherapy are important prognostic indicators of

osteosarcoma, they have been criticized on multiple grounds. In the last three decades, there has been no improvement in the survival of osteosarcoma patients. Thus, it is of great importance to identify new early-stage diagnostic biomarkers and novel therapeutic targets for early diagnosis and quantitative assessment of osteosarcoma prognosis to improve patient survival. tRNA derived small RNA (tsRNA) is a kind of new small non-coding RNA, usually 18 to 40 nucleotides in length, produced by the precursor tRNA or mature tRNA (4). tsRNA can be divided into three different categories, including precursor tRNA, derived small RNA with poly-U residue characteristic of 3' terminal (3'U tRF), Mature tRNA derived fragment (tRF), and tRNA half molecules (tRH). tRF can be further divided into three subtypes: 5'tRF 3'tRF and Inter tRF. The biogenesis of different tsRNAs is regulated by different mechanisms. For instance, during the maturation of tRNA, 3'U tRF is produced by RNase Z, and angiogenin cleavage of anticodon rings of mature tRNA generates tRHs, indicating that tsRNA expression is regulated by space and time under physiological conditions, playing a significant role in many biological processes (5). Moreover, tsRNAs can regulate mRNA translation, retro-element reverse transcriptional, and post-transcriptional processes (6). Hence, the function of tsRNA is likely to be elucidated by examining its interactions with mRNA. A growing number of studies show the importance of aberrant tsRNA expression during cancer development and staging resulting from activation of oncogenes and inactivation of tumor suppressors (7). The potential importance of tsRNAs as non-invasive diagnostic factors, prognostic biomarkers, and therapeutic targets has been seriously considered.

TABLE 1 | Clinical characteristics of osteosarcoma.

Cohort	MGH	TARGET	Independent Validation
Num. of patients	74	88	30
Age in years, mean (SD)	29.39 (0.23)	15.17 (0.06)	28.16 (0.55)
Sex			
Male, count (%)	49 (66.2)	51 (58.0)	11 (36.7)
Metastases(%)			
No	57 (77)	Not	22 (73.3)
Yes	17 (23)	Reported	8 (26.7)
Chemotherapy regime			
MAP or AP	29	Not	Not Reported
MAP and other	40	Reported	
Other	3		
Not available	2		
Chemo-response			
Optimal	25	Not	Not Reported
Suboptimal	26	Reported	
Not available	23		
Events			
Death	28	29	11
Recurrences	36	Not Reported	15
Follow Up time (moths), mean (SD)	98.2 (0.92)	50.8 (0.43)	96.16 (2.07)

METHODS

Dataset

The miRNA-seq dataset collected from (Massachusetts General Hospital) is available in the SRA repository (SRP237494). The mRNA dataset was obtained from the TARGET-OS project (dbGap phs000468). When data were separated into training and validation sets, the training to validation ratio was 7:3. Independent validation patient samples were collected from the Fourth Affiliated Hospital of Guangxi Medical University.

Clinical Samples

This study was a prognostic cohort test approved by the Fourth Affiliated Hospital of Guangxi Medical University's ethics committee. Blood samples were collected from 30 patients (**Table 1**), which included patients with OS in our hospital from January 2011 to March 2020. Informed written consent was obtained from each patient. Blood samples were centrifuged at 3,000 g for 15 minutes at 4°C and then stored at -80°C.

Reverse Transcription-Quantitative PCR (RT-qPCR)

According to the manufacturer's protocol, total RNA from OS blood was extracted using TRIzol reagent (Invitrogen; Thermo Fisher Scientific, Inc.) Consequently, complementary DNA (cDNA) was synthesized using the QuantiTect Reverse Transcription Kit (QIAGEN, Inc.) Relative expression qPCR was conducted on StepOne™ Real-Time PCR System (Thermo Fisher Scientific, Inc.) using QuantiNova SYBR® Green PCR Kit (QIAGEN, Inc.). The thermocycling conditions were as follows: 95°C for 30 sec, followed by 40 cycles of amplification at 95°C for 5 sec, 59°C for 30 sec and 72°C for 30 sec. Relative expression was measured using the 2-ΔΔCq method the expression of U6 was utilized as the internal control for tsRNA. The sequences of the primers used in this study were as follows:

tRF-33-6SXMSL73VL4YDN, 5'-CGTATTCGACGATCGGCCGTGA-3', and 5'-TACTCTGCGTAGATCGGTTTCCG-3';

tRF-32-6SXMSL73VL4YK, 5'- CAGCGACGATCGGCCGTGATCGT-3', and 5'- AGTGGTTAGTACTCTGCG-3';

tRF-32-M1M3WD8S746D2, 5'-ATCCGTATTCGACGCGGCCC-3', and 5'-CTCCCGGTGTGGGAA-3';

tRF-35-RPM830MMUKLY5Z, 5'-CTGCTTGCATGGGTAGCGTGG-3', and 5'-CGCTGGATTTCGTGCACCG-3';

tRF-33-K768WP9N1EWJDW, 5'-CGTGCACGCCCCTGGCGGT-3', and 5'-TTAGGATTCGGCGC-3';

tRF-32-MIF91SS2P46I3,5'-TATTCGACGCGGCTAGCTC-3', and 5'- GACTCT CGCAGA-3'

U6-F 5'-CGATACAGAGAAGATTAGCATGGC-3', and U6-R 5'-AACGCTTCACGAATTTGCGT-3';

Small RNA Sequence Processing and Expression Analysis

All bone biopsies were sequenced on the NextSeq 500 (Illumina) at a final concentration of 2 pM. After quality control, the

sequencing fastq reads adapters were trimmed and filtered for ≥ 16 nt using Cutadpt 2.1 (8). Trimmed reads were aligned to mature-tRNA on the entire genome using MINTmap (9). The workflow is shown in **Figure 1A**.

Statistical Analysis

To identify prognostic biomarkers that predict overall survival, Kaplan–Meier was applied to analyze the correlation between tsRNA and overall survival, and the log-rank test was used to associate survival curves. Multivariate survival analysis was adopted to adjust the risk score and clinicopathological characteristics. All analyses were performed using R software (version 4.0.2).

LASSO Regression Analysis

To solve the possible over fitting caused by high-dimensional tsRNA expression levels compared to the small number of samples, using a LASSO-regularized linear model is a popular solution (10). Compared to a typical liner model, such as logistic regression, LASSO can use L1 regularization to shrink the coefficient estimates to zero (11). By using 'penalized' regression, LASSO can effectively reduce the number of dimensions. We used LASSO regression to eliminate partial tsRNAs. Ten-fold cross-validation was performed to test the linear model and the 'glmnet' package in R was used to perform the LASSO regression analysis.

RESULTS

Clinical Characteristics of Osteosarcoma Dataset

Table 1 MGH shows the clinicopathological characteristics of the osteosarcoma dataset. All 80 samples were analyzed through miRNA-seq, and 74 samples remained after filtering by the condition of having at least 5% tumor cellularity. The average age of the patients was relatively low (29.39 years), 49 of 74 (66.2%) were male, and the metastasis rate of patients was 23%.

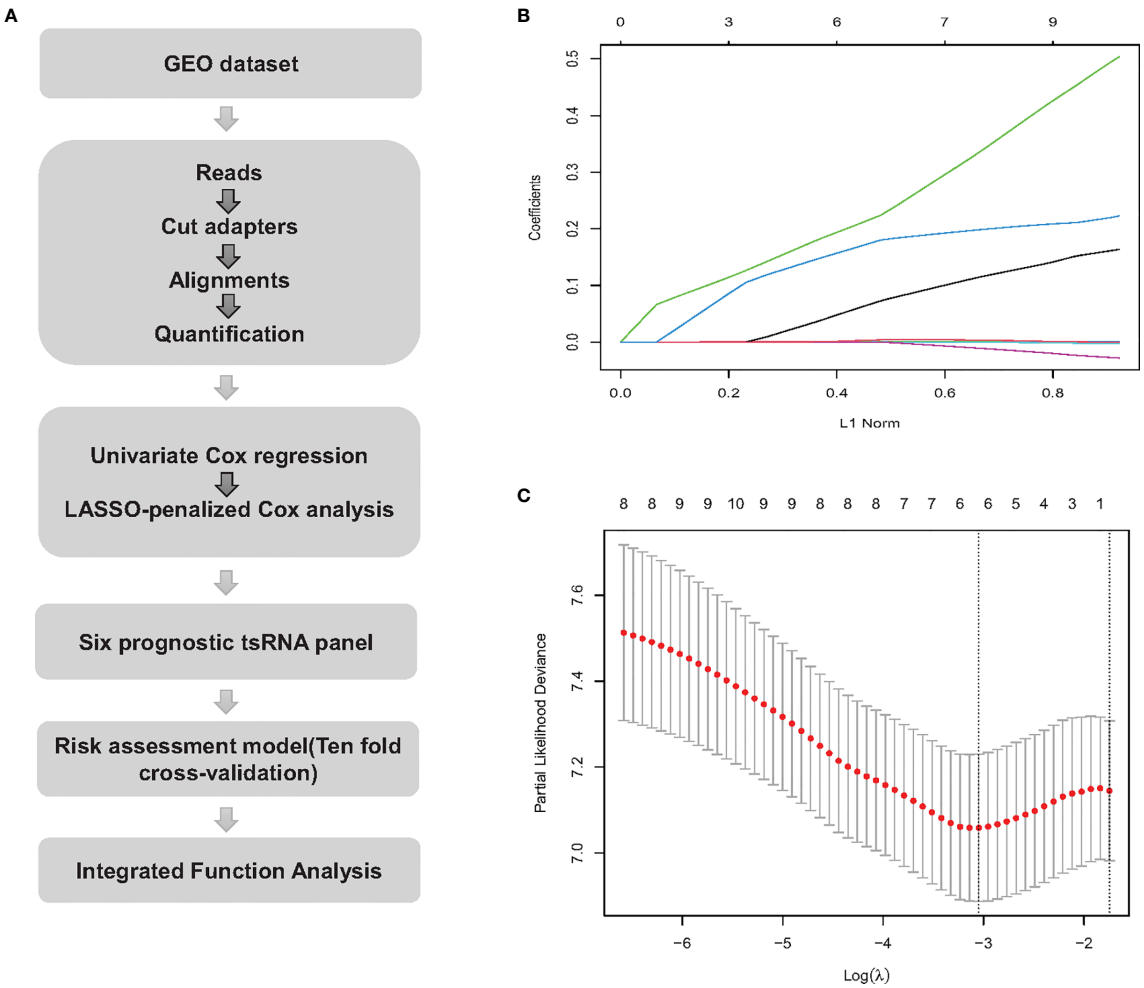

FIGURE 1 | Workflow and LASSO-Cox regression analysis. **(A)** tsRNA expression extraction process and downstream analysis. **(B)** LASSO coefficient profiles of the 10 tsRNAs. The L1 Norm at the optimal value by 1 s.e. criteria return six non-zero coefficients. **(C)** The two dotted vertical lines are drawn at the optimal values by 1 s.e. criteria (left line) and minimum criteria (right line).

The median follow-up was 98.2 months (SD 0.92), and 28 (37.8%) patients died. **Table 1** TARGET displays the clinical information of 88 RNA-seq osteosarcoma samples. Compared with MGH, the average age (15.17 SD 0.06) of the TARGET sample was lower and the follow-up time (50.8 SD 0.43) was shorter.

tsRNA Association With the Survival From the Osteosarcoma

Table 2 describes a list of 10 tsRNAs that p-value < 0.05 level with hazard ratio (HR) and 95% confidence interval (CI) when the univariate Cox models were evaluated. We performed a LASSO-Cox regression model (**Figure 1A**) to build a prognostic classifier, and six tsRNAs selected from the 10 tsRNA candidates: tRF-33-6SXMSL73VL4YDN, tRF-32-6SXMSL73VL4YK, tRF-32-M1M3WD8S746D2, tRF-35-RPM830MMUKLY5Z, tRF-33-K768WP9N1EWJDW, and tRF-32-MIF91SS2P46I3. Next, we built the panel using a formula to calculate each patient's risk score according to their specific six tsRNA expression data (**Figures 1B, C**). We further analyzed these six tsRNAs in patients who relapsed and died from osteosarcoma. Although the expression of some tsRNAs between the two groups shows a trend of separation, no significant differences were observed between them (**Figures 2A, B**). However, LASSO-Cox modeling had an excellent effect on the prognosis analysis of patients with osteosarcoma. Applying the LASSO-Cox regression models, the risk score formula was equal to (0.017*tRF-33-6SXMSL73VL4YDN) + (0.011* tRF-32-6SXMSL73VL4YK) +(2.391*tRF-32-M1M3WD8S746D2) + (0.068*tRF-35-RPM830MMUKLY5Z) + (9.684*tRF-33 K768WP9N1EWJDW) + (7.848*tRF-32-MIF91SS2P46I3). In this equation, the highest risk value was 100 and the lowest risk value was 0. After re-calculating the risk score of every patient, patients with lower risk scores (cutoff = 66.7) typically had better survival rates than those with higher risk scores (**Figure 3A**). The training data set, internal validation (**Figures 3B, C**), and intendent validation set (**Figure 3D**) were applied to verify the model's predictive ability.

Multivariable Analysis and Ten-Fold Cross-Validation

After multivariable adjustment by clinical variables, the combined tsRNA score model showed excellent predictive power superior to either the tsRNA or clinical score models alone (HR 3.15, 95% CI 0.15–0.66, p<0.001), which was verified in the training (HR 3.44, 95% CI 0.09-0.93, p<0.05) and validation datasets (HR 3.33, 95% CI 0.06-1.41, p<0.05) (**Table 3**). To provide accurate and reliable results, we performed ten-fold cross-validation across the entire dataset (**Supplementary Table S2**). In each fold, the p-value of the risk score in the Kaplan–Meier survival curve was validated.

Sequence Matched mRNAs

To predict mRNAs that may interact with the six tsRNAs, we identified a list of mRNAs with p-value less than 0.05 (**Supplementary Table S1**) using univariate Cox analysis. The sequences of distinguished mRNAs were obtained through the UCSC genome browser, and a Percent Identity Matrix was obtained by aligning the sequences of mRNAs with tsRNAs (**Supplementary Figure S1**). We selected the mRNA with the highest matching scores for the corresponding tRNAs: tRF-33-6SXMSL73VL4YDN, tRF-32-6SXMSL73VL4YK with ADCK5; tRF-33-K768WP9N1EWJDW with MYL3; tRF-32-MIF91SS2P46I3 with CTDSP1; tRF-35-RPM830MMUKLY5Z with CTTNBP2NL; and tRF-32-M1M3WD8S746D2 with CMTM1.

Functional Annotation for Target Genes of Six tsRNAs

To investigate the biological functions of the six tsRNAs, the target genes of the six tsRNA were predicted using RNAhybrid when the tsRNAs had maximum energy less than −25. Furthermore, we carried out the biological process (BP) and cellular component (CC) enrichment analyses for the tsRNA target genes. As shown in the results, the most enriched BP was related to detecting chemical stimuli involved in sensory perception (**Figure 4A**). Several signaling pathways, including sensory perception of smell, skin development, epidermal cell differentiation, and keratinocyte differentiation were affected. In CC enrichment analyses, the most enriched component was related to plasma membrane signaling receptor complex. Intermediate filament cytoskeleton, intermediate filament, and immunoglobulin complex were also significant (**Figure 4B**).

DISCUSSION

With the rapid development of miRNA sequencing and increasing computing power, the non-coding RNAs (ncRNAs)

TABLE 2 | A list of top 10 tsRNAs with p-value less than 0.05 with hazard ratio (HR) and 95% confidence interval (CI) when the univariate Cox models were assessed.

Name	GtRNAdb names	tRF Sequence	p Values	Hazard Ratio	95% CI
tRF-33-6SXMSL73VL4YDN	tRNA-His-GTG-1-9	GGCCGTGATCGTATAGTGGTTAGTACTCTGCGT	0.00598179	0.4288	0.23-0.799
tRF-32-6SXMSL73VL4YK	tRNA-His-GTG-1-9	GGCCGTGATCGTATAGTGGTTAGTACTCTGCG	0.00861906	0.446	0.24-0.83
tRF-33-K768WP9N1EWJDW	tRNA-Glu-CTC-2-1	CCCCTGGCGGTCTAGTGGTTAGGATTCGGCGCT	0.01088018	0.4466	0.238-0.838
tRF-32-PW5SVP9N15WVN	tRNA-His-GTG-1-9	GCCGTGATCGTATAGTGGTTAGTACTCTGCGT	0.01456028	0.4683	0.252-0.872
tRF-32-MIF91SS2P46I3	tRNA-Lys-CTT-4-1	CGGCTAGCTCAGTCGGTAGAGCATGGGACTCT	0.01852132	0.4947	0.269-0.911
tRF-32-XSXMSL73VL4YK	tRNA-His-GTG-1-9	TGCCGTGATCGTATAGTGGTTAGTACTCTGCG	0.02326819	0.5022	0.275-0.918
tRF-35-RPM830MMUKLY5Z	tRNA-Leu-TAG-1-1	GGTAGCGTGGCCGAGCGGTCTAAGGCGCTGGATTT	0.02560955	0.5133	0.281-0.938
tRF-40-2VR008R959KUMKF6	tRNA-Asp-GTC-3-1	CACGCGGGAGACCGGGGTTCGATTCCCCGACGGGGAGCCA	0.04114561	1.8876	1.022-3.487
tRF-32-M1M3WD8S746D2	tRNA-Glu-TTC-2-2	CGGCCCGGGTTCGACTCCCGGTGTGGGAACCA	0.04215268	0.5412	0.297-0.985
tRF-34-6SXMSL73VL4YHE	tRNA-His-GTG-1-9	GGCCGTGATCGTATAGTGGTTAGTACTCTGCGTT	0.0436662	0.5498	0.302-1.001

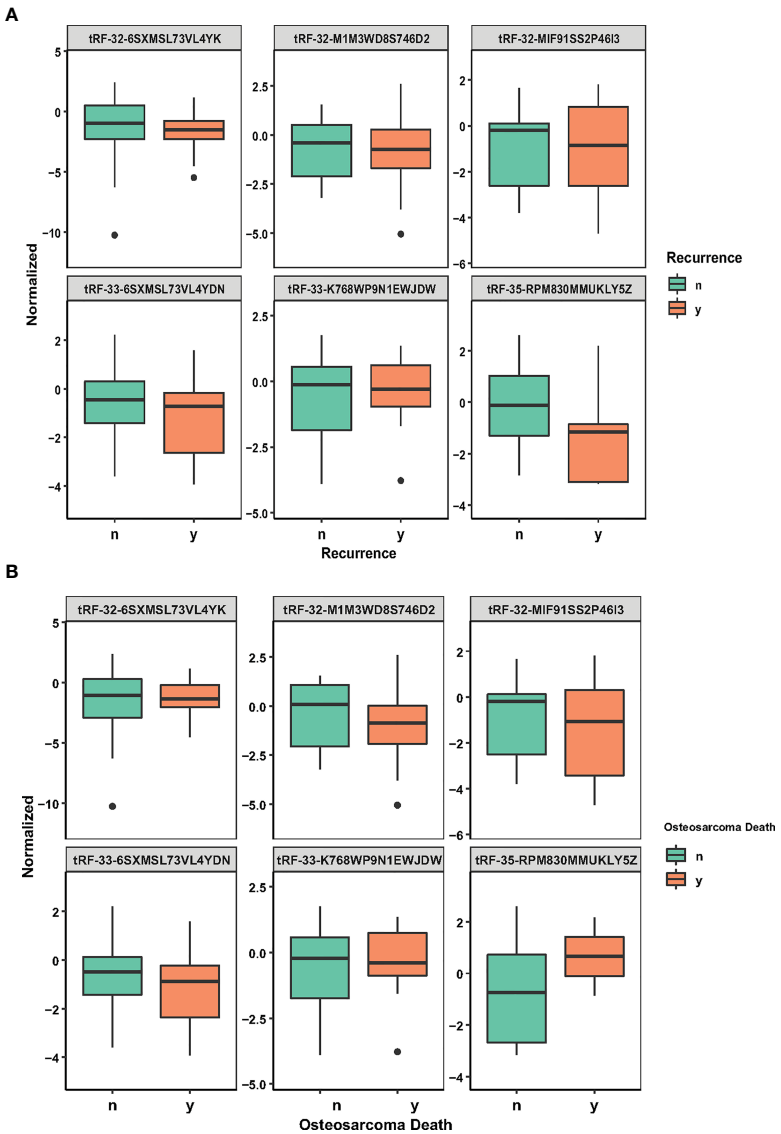

FIGURE 2 | tsRNA expression in recurrence and osteosarcoma death. **(A)** Six LASSO-selected tsRNA expression levels in patients with recurrence and non-recurrence. **(B)** Six LASSO-selected tsRNA expression levels in surviving patients and patients with death from osteosarcoma. The lines from top to bottom are tRF-33-6SXMSL73VL4YDN, tRF-32-6SXMSL73VL4YK, tRF-32-M1M3WD8S746D2, tRF-35-RPM830MMUKLY5Z, tRF-33-K768WP9N1EWJDW, and tRF-32-MIF91SS2P46I3.

can now be comprehensively separated and identified. The recent discoveries of various ncRNAs has opened a new way to explain biological control and irregularities. Growing evidence shows that transfer RNA (tsRNA) contributes to biological control and characteristics connected with cancer progression (12). tsRNA has prominent potential as a new cancer diagnosis and prognosis marker, especially the diagnosis of cancer through peripheral blood (13). However, it has not been extensively investigated (5, 14–16).

Osteosarcoma is the most frequent primary malignant bone tumor in adolescents. Before the 1970s, the routine treatment for high-grade OS was amputation (17). Yet despite adjuvant chemotherapy greatly improving patients' survival rate in the 1970s to 1980s, the diagnosis and treatment techniques have not been renewed for decades. Thus, it is crucial to develop prognostic markers from tsRNA which could help judge therapeutic benefits to osteosarcoma patients. Towards this goal, we have identified a prognostic panel based on tsRNA factors predicting osteosarcoma patients' overall survival.

In this paper, we have identified a potential tsRNA prognostic panel for osteosarcoma and assessed their risk scores on overall survival, and we provided a new informative pattern to display the impact of the patients' ncRNAs on overall survival probability. However, using tsRNA is a novel approach for

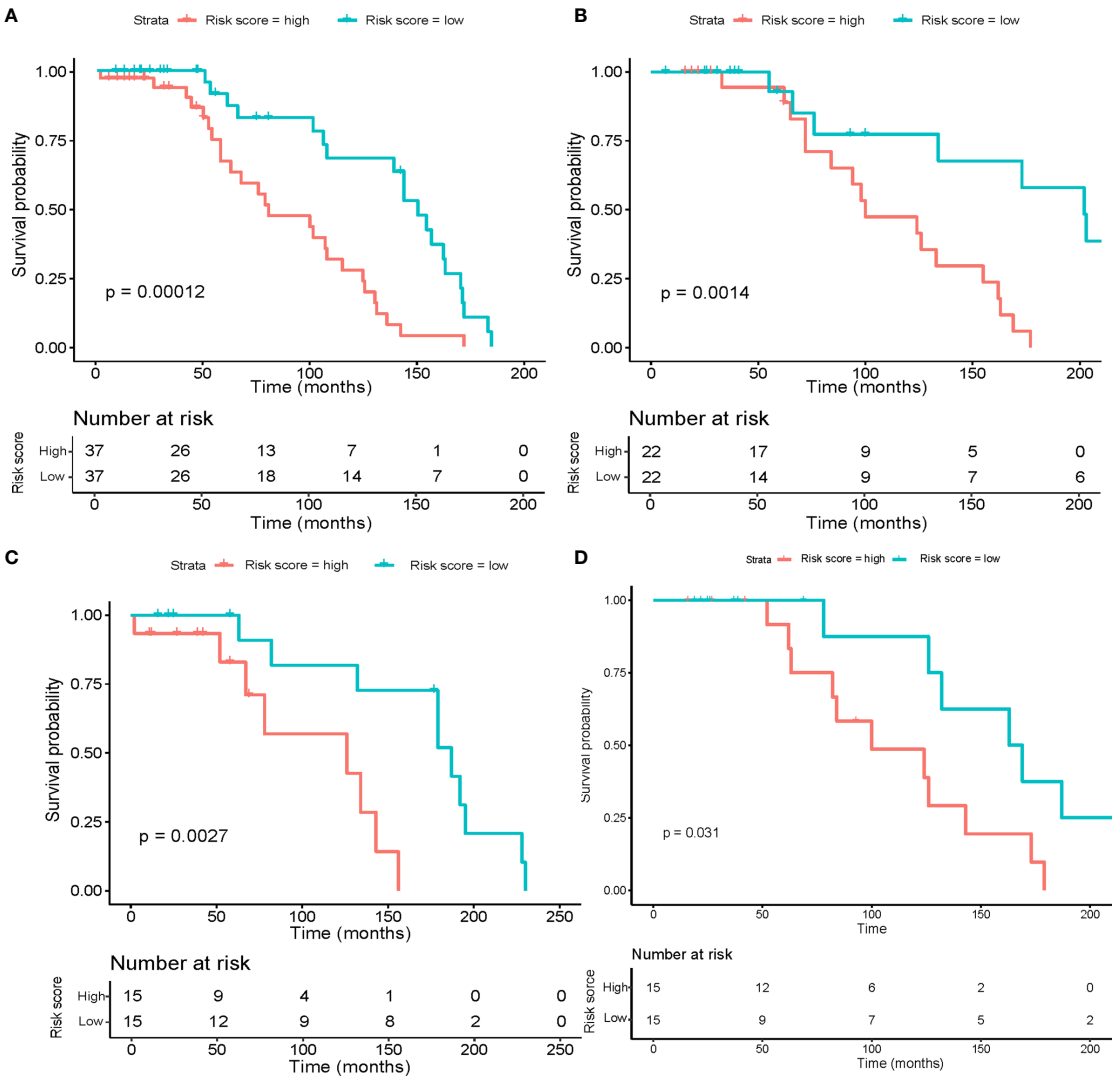

FIGURE 3 | Risk score calculated by the six tsRNA panel and Kaplan–Meier survival analysis results. The OS patients were separated into high-risk and low-risk groups using the median cutoff value. P-values were assessed using the log-rank test. **(A)** Kaplan–Meier survival analysis in the entire dataset. **(B)** Kaplan–Meier survival analysis in the training set. **(C)** Kaplan–Meier survival analysis in the internal validation set. **(D)** Kaplan–Meier survival analysis in the independent validation set.

osteosarcoma prognosis, and a clear understanding of tsRNA mechanisms is still lacking. Here, we use sequence matching and RNAhybrid to predict the target genes.

AarF domain containing kinase 5(ADCK5) is a member of an atypical kinase family, which may be involved in transferase activity transferring phosphorus-containing groups as well as protein serine/threonine kinase activity (18). Evidence shows that it is overexpressed in many carcinomas and regulates the expression of tumor oncogene human pituitary tumor transforming gene-1 (PTTG1) to enhance the migration and invasion capabilities of cancer cells (19). Myosin light chain 3 (MYL3) encodes ventricular/cardiac isoform protein, which significantly decreased during fat accumulation in bovine skeletal muscle (20). Carboxy-Terminal Domain RNA Polymerase II Polypeptide A Small Phosphatase 1 (CTDSP1) is related to the drug resistance of colorectal cancers (21). Chemokine-like factor (CKLF)-like MARVEL transmembrane

TABLE 3 | Multivariate Cox regression analysis of the risk score with overall survival across the whole dataset.

Parameters	p Values	Hazard ratio	95% CI
Risk score (High)	0.00238	3.1486	0.15-0.67
Age (> 30)	0.02614	0.9792	1.00-1.04
Sex (male)	0.53186	1.2503	0.39-1.61
Recurrence Yes	0.29736	1.5309	0.29-1.45
Disease Grade3/3	0.39023	1.347	0.37-1.46
Disease Grade3/4	0.45715	0.611	0.46-5.99
Disease Grade4/4	0.9011	1.0894	0.23-3.54

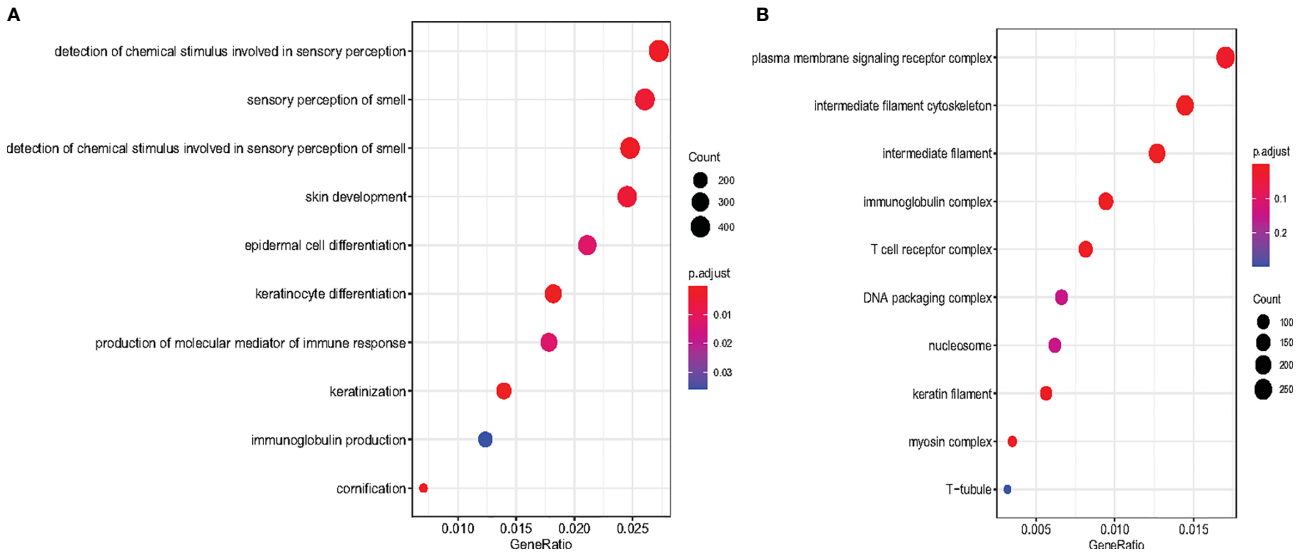

FIGURE 4 | Scatter plot for Biological Process enrichment analysis and Cellular Component enrichment of tsRNA target genes. **(A)** The top 10 Biological Process are presented in the bubble chart. The area of the circle indicates the tsRNA target gene number. **(B)** The top 10 cellular component enrichment are presented in the bubble chart.

domain-containing 1 (CMTM1) was upregulated in testis and many tumor tissues, and also raised cell proliferation rates and resistance to tumor necrosis factor-α (TNF-α)-induced apoptosis (22). From the biological process (BP) and cellular component (CC) enrichment analyses, the six tsRNA may be involved mainly in detecting chemical stimuli participating in sensory perception and the plasma membrane signaling receptor complex. Although it has not yet been proven that these pathways are closely related to osteosarcoma, these results provide new perspectives for later analysis on these tsRNAs.

There are some limitations to our study. Due to the low incidence of osteosarcoma and resulting paucity of samples for miRNA sequencing, it is difficult to locate adequate miRNA-seq samples for further verification. To the extraction of RNA expression, it can be more convenient by using sRNAtools (23). We will continue to collect specimens in future studies to validate our prognostic markers.

DATA AVAILABILITY STATEMENT

The original contributions presented in the study are included in the article/**Supplementary Material**. Further inquiries can be directed to the corresponding author.

ETHICS STATEMENT

The studies involving human participants were reviewed and approved by the Fourth Affiliated Hospital of Guangxi Medical University's ethics committee. The patients/participants provided their written informed consent to participate in this study.

AUTHOR CONTRIBUTIONS

ZL had the idea and launched the investigation. ZT collected and processed data. ZT and SZ composed the manuscript. All authors contributed to the article and approved the submitted version.

FUNDING

This work was supported in part by funding from the Key Research and Development Program of Guangxi Zhuang Autonomous Region (No. AB16380152) and in part from the Key Research and Development Program of Liuzhou (2018BJ10509).

ACKNOWLEDGMENTS

We thank the miRNA-seq raw data uploader Massachusetts General Hospital and the TARGET-OS project.

SUPPLEMENTARY MATERIAL

The Supplementary Material for this article can be found online at: https://www.frontiersin.org/articles/10.3389/fonc.2021.652040/full#supplementary-material

REFERENCES

1. Tang X-F, Cao Y, Peng D-B, Zhao G-S, Zeng Y, Gao Z-R, et al. Overexpression of Notch3 is Associated With Metastasis and Poor Prognosis in Osteosarcoma Patients. *Cancer Manag Res* (2019) 11:547. doi: 10.2147/CMAR.S185495
2. Luetke A, Meyers PA, Lewis I, Juergens HJ. Ctr. Osteosarcoma Treatment–Where do We Stand? A State of the Art Review. *Cancer Treat Rev* (2014) 40 (4):523–32. doi: 10.1016/j.ctrv.2013.11.006
3. Clark JC, Dass CR, Choong PFM. Jocr, Oncology C. A Review of Clinical and Molecular Prognostic Factors in Osteosarcoma. *J Cancer Res Clin Oncol* (2008) 134(3):281–97. doi: 10.1007/s00432-007-0330-x
4. Garcia-Silva MR, Cabrera-Cabrera F, Güida MC, Cayota A. Hints of tRNA-derived Small RNAs Role in RNA Silencing Mechanisms. *Genes* (2012) 3 (4):603–14. doi: 10.3390/genes3040603
5. Zhu L, Li J, Gong Y, Wu Q, Tan S, Sun D, et al. Exosomal tRNA-Derived Small RNA as a Promising Biomarker for Cancer Diagnosis. *Mol Cancer* (2019) 18(1):1–5. doi: 10.1186/s12943-019-1000-8
6. Cao J, Cowan DB, Wang D-Z. tRNA-Derived Small Rnas and Their Potential Roles in Cardiac Hypertrophy. *Front Pharmacol* (2020) 11. doi: 10.3389/fphar.2020.572941
7. Balatti V, Nigita G, Veneziano D, Drusco A, Stein GS, Messier TL, et al. tsRNA Signatures in Cancer. *Proc Natl Acad Sci* (2017) 114(30):8071–6. doi: 10.1073/pnas.1706908114
8. Tanja M, Salzberg SL. FLASH: Fast Length Adjustment of Short Reads to Improve Genome Assemblies. *Bioinformatics* (2011) 27(21):2957–63.
9. Pliatsika V, Loher P, Telonis AG, Rigoutsos I. Mintbase: A Framework for the Interactive Exploration of Mitochondrial and Nuclear tRNA Fragments. *Bioinformatics* (2016) 32(16):2481–9. doi: 10.1093/bioinformatics/btw194
10. Tibshirani R. Regression Shrinkage and Selection Via the Lasso. *J R Stat Soc Series B Stat Methodol* (1996) 58(1):267–88. doi: 10.1111/j.2517-6161.1996.tb02080.x
11. Gui J, Li H. Penalized Cox Regression Analysis in the High-Dimensional and Low-Sample Size Settings, With Applications to Microarray Gene Expression Data. *Bioinformatics* (2005) 21(13):3001–8. doi: 10.1093/bioinformatics/bti422
12. Zhu L, Ge J, Li T, Shen Y, Guo J. tRNA-Derived Fragments and tRNA Halves: The New Players in Cancers. *Cancer Lett* (2019) 452:31–7. doi: 10.1016/j.canlet.2019.03.012
13. Gu W, Shi J, Liu H, Zhang X, Zhou JJ, Li M, et al. Peripheral Blood Non-Canonical Small Non-Coding RNAs as Novel Biomarkers in Lung Cancer. *Mol Cancer* (2020) 19(1):1–6. doi: 10.1186/s12943-020-01280-9
14. Li S, Cong X, Gao H, Lan X, Li Z, Wang W, et al. Tumor-Associated Neutrophils Induce EMT by IL-17a to Promote Migration and Invasion in Gastric Cancer Cells. *J Exp Clin Cancer Res* (2019) 38(1):1–13.
15. Zhou J, Wan F, Wang Y, Long J, Zu X. Cm, Research. Small RNA Sequencing Reveals a Novel tsRNA-26576 Mediating Tumorigenesis of Breast Cancer. *Cancer Manag Res* (2019) 11:3945. doi: 10.2147/CMAR.S199281
16. Zuo Y, Chen S, Yan L, Hu L, Bowler S, Zitello E, et al. Development of a tRNA-Derived Small RNA Diagnostic and Prognostic Signature in Liver Cancer. *Genes Dis* (2021). doi: 10.1016/j.gendis.2021.01.006
17. Misaghi A, Goldin A, Awad M. Osteosarcoma: A Comprehensive Review. *SICOT-J* (2018) 4:12. doi: 10.1051/sicotj/2017028
18. ADCK5 Gene Available at: https://www.genecards.org/cgi-bin/carddisp.pl?gene=ADCK5.
19. Qiu M, Li G, Wang P, Li X, Lai F, Luo R, et al. Aarf Domain Containing Kinase 5 Gene Promotes Invasion and Migration of Lung Cancer Cells Through ADCK5-SOX9-PTTG1 Pathway. *Exp Cell Res* (2020) 392(1):112002. doi: 10.1016/j.yexcr.2020.112002
20. Zhang Q, Lee H-G, Han J-A, Kim EB, Kang SK, Yin J, et al. Differentially Expressed Proteins During Fat Accumulation in Bovine Skeletal Muscle. *Meat Sci* (2010) 86(3):814–20. doi: 10.1016/j.meatsci.2010.07.002
21. Matsuoka H, Ando K, Swayze EJ, Unan EC, Mathew J, Hu Q, et al. CTDSP1 Inhibitor Rabeprazole Regulates DNA-PKcs Dependent Topoisomerase I Degradation and Irinotecan Drug Resistance in Colorectal Cancer. *PloS One* (2020) 15(8):e0228002. doi: 10.1101/2020.01.07.897355
22. Wang J, Zhang G, Zhang Y, Luo Y, Song Q, Qiu X, et al. Cmtm1_v17 Is a Novel Potential Therapeutic Target in Breast Cancer. *Oncol Rep* (2014) 32 (5):1829–36. doi: 10.3892/or.2014.3429
23. Liu Q, Ding C, Lang X, Guo G, Chen J, Su X. Small Noncoding RNA Discovery and Profiling With sRNAtools Based on High-Throughput Sequencing. *Brief Bioinform* (2021) 22(1):463–73. doi: 10.1093/bib/bbz151

Conflict of Interest: The authors declare that the research was conducted in the absence of any commercial or financial relationships that could be construed as a potential conflict of interest.

Publisher's Note: All claims expressed in this article are solely those of the authors and do not necessarily represent those of their affiliated organizations, or those of the publisher, the editors and the reviewers. Any product that may be evaluated in this article, or claim that may be made by its manufacturer, is not guaranteed or endorsed by the publisher.

frontiers in Oncology

SYSTEMATIC REVIEW
published: 11 August 2021
doi: 10.3389/fonc.2021.617295

The Roles of Magnetic Resonance-Guided Focused Ultrasound in Pain Relief in Patients With Bone Metastases: A Systemic Review and Meta-Analysis

Xiaying Han[1†], *Runzhi Huang*[2,3,4†], *Tong Meng*[1*], *Huabin Yin*[1*] *and Dianwen Song*[1*]

[1] Department of Orthopedics, Shanghai General Hospital, Shanghai Jiaotong University School of Medicine, Shanghai, China, [2] Department of Orthopedics, The First Affiliated Hospital of Zhengzhou University, Zhengzhou, China, [3] Division of Spine, Department of Orthopedics, Tongji Hospital affiliated to Tongji University School of Medicine, Shanghai, China, [4] Tongji University School of Medicine, Shanghai, China

Objective: Cancer pain, the most common skeleton-related event of bone metastases, significantly disturbs patients' life. MRI-guided focused ultrasound (MRgFUS) is a therapeutic option to relieve pain; however, its efficacy and safety have not been fully explored. Therefore, we aim to conduct a meta-analysis on studies reporting MRgFUS for patients with bone metastases.

Methods: Randomized controlled trials (RCT) and non-RCTs on MRgFUS treatment for patients with bone metastases were collected using PubMed, MEDLINE In-Process (US National Library of Medicine), National Institutes of Health (US National Library of Medicine), Embase (Elsevier), Web of Science, CINAHL, and the Cochrane Library between August 2007 and September 2019. Data on quantitative pain assessment before/after MRgFUS, response rate, and complication were extracted and analyzed.

Results: Fifteen eligible studies with 362 patients were selected in this meta-analysis. The average pain score was 6.74 (95% CI: 6.30–7.18) at baseline, 4.15 (95% CI: 3.31–4.99) at 0–1 week, 3.09 (95% CI: 2.46–3.72) at 1–5 weeks, and 2.28 (95% CI: 1.37–3.19) at 5–14 weeks. Compared with baseline, the pain improvement at 0–1 week was 2.54 (95% CI: 1.92–3.16, $p < 0.01$), at 1–5 weeks was 3.56 (95% CI: 3.11–4.02, $p < 0.01$), and at 5–14 weeks was 4.22 (95% CI: 3.68–4.76, $p < 0.01$). Change from baseline in OMEDD at 2 weeks after treatment was −15.11 (95% CI: −34.73, 4.50), at 1 month after treatment was −10.87 (95% CI: −26.32, 4.58), and at 3 months after treatment was −5.53 (95% CI: −20.44, 9.38). The overall CR rate was 0.36 (95% CI: 0.24–0.48), PR rate was 0.47 (95% CI: 0.36–0.58), and NR rate was 0.23 (95% CI: 0.13–0.34). Among 14 studies including 352 patients, 93 (26.4%) patients with minor complications and 5 (1.42%) patients with major complications were recorded.

OPEN ACCESS

Edited by:
Maja Cemazar, Institute of Oncology Ljubljana, Slovenia

Reviewed by:
Nicolò Gennaro, Ente Ospedaliero Cantonale (EOC), Switzerland
Motohiro Kawasaki, Shikoku Medical Center for Children and Adults, Japan

****Correspondence:***
Tong Meng
mengtong@medmail.com.cn
Huabin Yin
yinhuabin@aliyun.com
Dianwen Song
dianwen_song@126.com

[†]These authors have contributed equally to this work and share first authorship

Specialty section:
This article was submitted to Molecular and Cellular Oncology, a section of the journal Frontiers in Oncology

Received: *14 October 2020*
Accepted: *19 July 2021*
Published: *11 August 2021*

Citation:
Han X, Huang R, Meng T, Yin H and Song D (2021) The Roles of Magnetic Resonance-Guided Focused Ultrasound in Pain Relief in Patients With Bone Metastases: A Systemic Review and Meta-Analysis. Front. Oncol. 11:617295. doi: 10.3389/fonc.2021.617295

Conclusion: This meta-analysis identifies MRgFUS as a reliable therapeutic option to relieve cancer pain for patients with metastatic bone tumors with controllable related complications.

Keywords: MRgFUS, bone metastases, safety, efficacy, cancer pain

INTRODUCTION

Bone is the third most common distant metastatic organ secondary to lung and liver (1), and about 30% of patients with malignancies have experienced bone metastases during their follow-up (2). Bone metastases often induce skeleton-related events, such as local pain, pathologic fracture, and spinal cord compression (3), which subsequently reduce the life quality and decrease the overall survival (OS) (4). Among all the symptoms, cancer pain is the most common one and significantly disturbs patients' normal life. Thus, there is a pressing need to control it effectively and improve the quality of life.

Generally, conventional radiotherapy (RT) is the main therapeutic option to relieve local pain and restore normal function in patients with symptomatic bone metastases. In terms of pain relief, RT provides a relief rate of 60% to 80% (5, 6). Besides, analgesics are also optional therapeutic methods and achieve good pain control. However, their adverse effects, such as drug resistance and addiction, cannot be neglected (7, 8). With the advance of medical technology, thermal ablation is regarded as an alternative local therapy for painful bone metastasis with excellent response rates and safety (9–13). It can directly induce irreversible damage or coagulative necrosis of tumor cells by heat effects (14). Generally, thermal ablation includes radiofrequency ablation (RFA), microwave ablation (MWA), cryoablation (CA), laser ablation (LA), and magnetic resonance-guided focused ultrasound (MRgFUS) ablation (15).

Focused ultrasound is a non-invasive technology proposed by Lele et al. 40 years ago (16). It delivers acoustic energy to heat the lesion in an ablation temperature (over 65°C) locally and subsequently induces local tumor tissue coagulation and necrosis. In addition, it also destroys the nerve on the affected periosteum, which alleviates cancer pain in both osteoblasts and osteolytic bone metastases (17–19). MRI-guided focused ultrasound (MRgFUS) therapy is a novel focused ultrasound method, which enables oncologists to perform ablation precisely and provides real-time temperature monitoring by MR thermometers (20, 21). Compared with other invasive and interventional therapies with non-uniform dose distribution, the distribution of MRgFUS therapeutic dose is uniform (22).

Although preliminary clinical studies of MRgFUS have shown excellent response rates and safety to relieve painful bone metastases, reliable data regarding long-term efficacy and complications are still scarce. In this regard, we aim to perform a meta-analysis to evaluate the pain relief efficacy and safety of MRgFUS in patients with bone metastases. Our results may provide a more reliable basis for the clinical applications of MRgFUS in painful bone metastases.

MATERIALS AND METHODS

The study was in accordance with the guidelines included in the Preferred Reporting Items for Systematic Reviews and Meta-Analyses (PRISMA) Statement (23) and Cochrane's guidelines for systematic reviews of interventions (15, 24). The PubMed, MEDLINE In-Process (US National Library of Medicine), National Institutes of Health (US National Library of Medicine), Embase (Elsevier), Web of Science, CINAHL, and the Cochrane Library were chosen to search literatures for original clinical studies regarding the roles of MRgFUS in pain relief in patients with bone metastases. Keywords included "focused ultrasound," "MRgFUS," "HIFU," "painful," "bone," "bone metastases," "pain management," and their expansions (15).

The inclusion criteria were as follows: the type of study included randomized controlled trial (RCT), non-RCT between August 2007 and September 2019, and the research objects were patients with bone metastases. The intervention measures were that the trial group was given MRgFUS with cases more than 10; it was not limited whether there was a control group, and if a control group was set, the intervention measures were not limited. The exclusion criteria were as follows: studies reporting molecular, focused, *in vitro*, or animal studies, or patients who also underwent other therapies (e.g., RT, cementoplasty) (15); the evaluation indicators do not include pain grade scores; case report; and review. We used the "Methodological index for non-randomized studies" (MINORS) items to assess the quality of the included single-arm clinical research methodology (25).

The main evaluation indicators include pain grade scores, the change from baseline in oral morphine equivalent dose (OMEDD), and the response rate. All but one paper included in the study used 10-point scales to assess pain and the one paper used 100-point scales. The data of the one paper was transformed from a 100-point scale into a 10-point scale for comparison purposes (15). Change from baseline in OMEDD means changes from baseline in the OMEDD at each evaluation point after treatment of patients with bone metastases. Pain grade scores were evaluated at four time intervals: baseline (pretreatment), 0–1 week, 1–5 weeks, and 5–14 weeks. If an author reports multiple pain assessments in the same time interval (e.g., 6 and 7 weeks), only the latest one is considered (e.g., a 7-week evaluation reported in a time interval of 5 to 14 weeks) (15). The change of OMEDD was recorded at three evaluation points after treatment of patients with bone metastases: at 2 weeks, at 1 month, and at 3 months. The response rate includes complete response (CR), partial response (PR), and no response (NR). CR is defined as a pain score of 0 without medication increase; PR is

defined as a drop of 2 points on a 10-point scale without an increase in pain medications or a drop of 25% in pain medication without increase in the reported pain score; NR is defined as no drop of score and no changes in medication use (26, 27). Other evaluation indicators include QLQ-BM22 subscale scores, QLQ-C15, QLQ-C30, biomarker evaluation including alkaline phosphatase and lactic acid dehydrogenase, and median overall survival time. Secondary evaluation indicators include the types of complications and the complication ratio with respect to major complications and minor complications. Complications were evaluated and classified based on the unified and standardized grading system developed by the Society of Interventional Radiology (SIR) (15, 28, 29).

Two independent investigators (X.H. and R.H.) extracted the following data from each included study: the first author, year of publication, sample size, type of study, follow-up time, and evaluation indicators. Any discrepancy was resolved through discussion. All data obtained was carefully checked to ensure accuracy (30). The literature screening and data extraction were independently completed and cross-checked by two researchers. If there is a disagreement, it will be decided by the third researcher (T.M.).

The STATA statistical software (Version 8, STATA, College Station, TX) was used for meta-analysis of the pain grade scores in each follow-up period. The meta-analysis was performed using the generic inverse variance. *I* statistic was used to access statistical heterogeneity among studies. *I* values of 25%, 50%, and 75% defined mild, moderate, and severe heterogeneity, respectively (30). The fixed-effects model was used to conduct the meta-analysis of non-heterogeneity research; the random-effects model was used to conduct the meta-analysis of heterogeneous research (31). The presence of publication bias was accessed by using the funnel plot. $p < 0.05$ meant statistically significant (30).

RESULTS

A total of 127 studies were initially screened, and 52 duplicate studies were removed. After reviewing available titles and abstracts, 60 studies were excluded for various reasons: no relation (n = 35) or other types of studies (i.e., review, n = 5; case report, n = 5). Finally, a total of 15 studies were included in this study (**Figure 1**).

The basic characteristics of the selected studies are presented in **Table 1** including the patients' characteristics and treatment parameters. In total, this study comprised 362 patients. The research objects in most studies were adults and one study included all children (40). The distribution of the study samples were shown on the world map and the patients were mainly from China (n = 112), the United States (n = 112), Israel (n = 38), Italy (n = 23), France (n = 17), Netherlands (n = 15), Canada (n = 21), Japan (n = 10), South Korea (n = 5), and the United Kingdom (n = 9) (**Figure 2**). As most of the included studies were single-arm clinical researches, we chose the MINORS items to evaluate the quality of studies. Each item has a score of 0–2, and the highest score is 24. The quality assessment is shown in **Table 2** and **Figure 3**. The quality of studies conducted by the MINORS score and the mean MINORS score was 14.6 (range: 9–24). Most of the studies scored low on unbiased assessment of outcomes due to lack of blinding and control groups. The funnel plot was used to detect bias in studies included in the meta-analysis and no publication bias was found (**Supplementary Figure 1**).

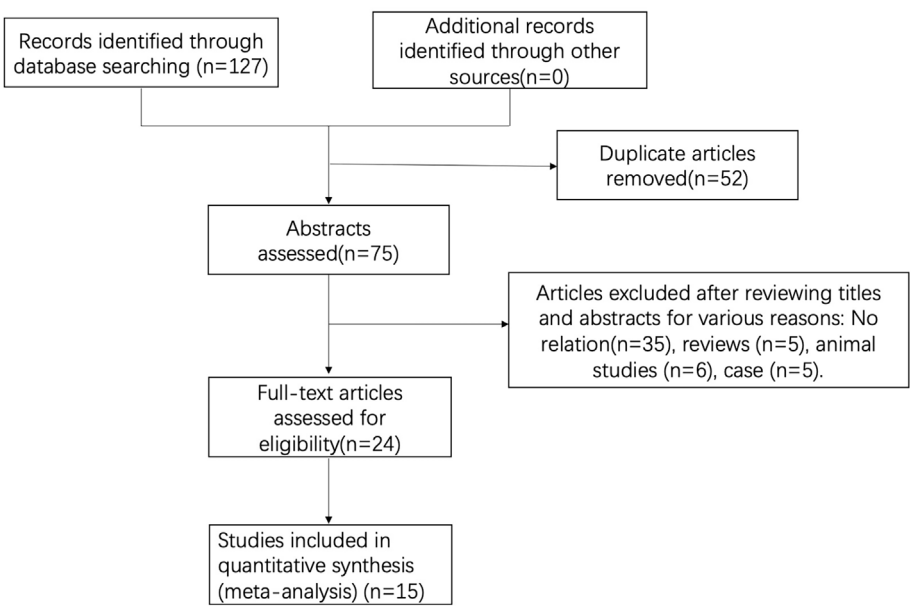

FIGURE 1 | Flow diagram of the literature search and study selection process.

TABLE 1 | Basic characteristics of the included 15 studies.

Author-publication time	*n*	Age of patient, range, (mean)	Metastasis type	Metastasis location, *n* (%)	Primary tumor, *n* (%)	Type of Study	MRgFUS treatment length; range, (mean)	Sonications, range, (mean)	Sonication energy, range, (mean)	Acoustic power (mean)	Follow-up time	Evaluation index
Anzidei-2016 (27)	23	37–82 (63.6)	Osteolytic 10 (43.5); Sclerotic 7 (30.4); Mixed 6 (26.1)	Non-axial skeleton 11 (47.8); Axial skeleton 12 (52.2)	Lung 6 (26.1); Breast 5 (21.7); Prostate 4 (17.4); Colon 3 (13.1); Others 5 (21.7)	Non-RCT	55–180 min (110.4 min)	15–29(23.5)	860–2899 J (1644 J)	114 W	1, 3, and 6 months after treatment	VAS; CR; PR; NR
Bertrand-2018 (32)	17	46–89 (61.4)	\	Non-axial skeleton 11 (64.7); Axial skeleton 6 (35.3)	Lung 7 (41.1); Breast 5 (29.4); Kidney 2 (11.8); Larynx 1 (5.9); Endometria 1 (5.9); Prostate 1 (5.9);	Non-RCT	\	6–40(15.1)	\	100 W	Before treatment, at 1 week, and at 1 month after treatment	VAS; OMEDD; CR; PR; NR
Catane-2007 (33)	13	\	Osteolytic 7 (53.8); Osteoblastic 5 (38.5); Mixed 1 (7.7)	Non-axial skeleton 11 (84.5); Axial skeleton 2 (15.4)	Breast 4 (30.8); Prostate 2 (15.4); Bile duct (7.8); Ovaries 1 (7.8); Esophagus1 (7.8); Kidney 1 (7.8); Rectum 1 (7.8); Undetermined 1 (7.8)	Non-RCT	22–162 min (71.8min)	11–39 (25)	418–1890 J (1067.6 J)	54 W	Mean follow-up was 59 days: 0, 3, 15, 30, 90, 180 days after treatment	VAS
Chan-2017 (34)	10	42–78 (64.5)	\	Non-axial skeleton 9 (90); Axial skeleton 1 (10)	Breast 2 (20); Prostate 2 (20); Neuroendocrine NOS 1 (10); Liver 1 (10); Esophagus 1 (10); Pancreas 1 (10); Lung 1 (10); Orbit 1 (10)	Non-RCT	42–78 min (64.5min)	12–51 (29.8)	300–1400J (850 J)	34.1 W	Before, day 14, and day 30 after treatment	Brief Pain Inventory scores; CR; PR; NR
Chen-2018 (19)	26	54.7	Osteolytic 9 (34.6); Osteoblastic 11 (42.3); Mixed 6 (23.1)	Non-axial skeleton 18 (69.2); Axial skeleton 8 (30.8)	Lung 12 (46.2); Breast 5 (19.2); Colon 3 (11.5); Prostate 3 (11.5); Thyroid 2 (7.7); Kidney 1 (3.8)	Non-RCT	\	\	\	\	0, 2, 4, 6, 8, 10, 12 months after treatment	VAS; QLQ-BM22
Huisman-2014 (35)	11	53–86 (62.1)	Osteolytic 6 (55.5); Osteoblastic 1 (9.1); Mixed 4 (36.4)	Non-axial skeleton 6 (55.5); Axial skeleton 5 (45.5)	Kidney 2 (18.2); Colorectal 2 (18.2); Breast 2 (18.2); Sarcoma 1 (9.1); Prostate 1 (9.1); Lung 1 (9.1); Colorectal 1 (9.1); Mesothelioma 1 (9.1)	Non-RCT	20–73 min (458min)	6–28 (15.5)	300–3000 J (1492.3 J)	20–150 W (85.4 W)	Before treatment, 3 days and 1 month after treatment	NRS; CR; PR; NR
Hurwitz-2014 (36)	112	9.1–83.6 (62.7)	Osteoblastic 25 (22.3); Osteolytic 59 (52.7); Mixed 27 (24.1); Unknown 1 (0.9)	Non-axial skeleton 84 (75); Axial skeleton 28 (25)	Breast 34 (30.4) Prostate 15 (13.4) Kidney 9 (8.0) Lung 17 (15.2) Missing 2 (1.8) Other 35 (31.2)	RCT	83 min	\	\	\	3, 7, 14, 30, 60, 90 days and 1 year after treatment	VAS; OMEDD; CR; PR; NR
Li-2010 (22)	12	32–72 (46.8)	\	Non-axial skeleton 5 (41.7); Axial skeleton 7 (58.3)	Lung (4); Liver (5); Kidney (1); Mediastinum (1); Colon (1)	Non-RCT	27.5–647.6 min (230.9 min)	\	\	\	0, 1, 4–6 weeks, 4–6 months after treatment	Biomarker evaluation; CR; PR; NR
Liberman-2008 (37)	25	40–85 (61)	Osteolytic 20 (64.5); Osteoblastic 10 (32.3); Mixed1 (3.2)	Non-axial skeleton 27 (87.1); Axial skeleton 4 (13)	Kidney 6 (19.4); Colorectal 2 (6.5); Lung 1 (3.2); Breast 11 (35.5); Prostate 5 (16.1); Other 6 (19.4)	Non-RCT	22–162 min (66 min)	8–32 (17.3)	440–1890 J (1135 J)	\	0, 3, 13, 30, 90 days after treatment	VAS; OMEDD; CR; PR; NR
Lee-2017 (13)	21	40–83 (59)	\	Non-axial skeleton 20 (95); Axial skeleton 1 (5)	Breast 4 (19); Nasopharyngeal 4 (19); Colorectal 3 (14); Non-small-cell lung 3 (14); Liver (10); Prostate 2 (10); Kidney 1 (5); Cervical 1 (5); Thymic 1 (5).	RCT	\	\	\	\	0, 8, 13, 30, 90 days after treatment	VAS; OMEDD; CR; PR; NR; median overall survival time
Namba-2019 (38)	10	41–80 (69)	Osteolytic 4 (40); Osteoblastic; and Mixed	Non-axial skeleton 8 (80); Axial skeleton 2 (20)	Prostate 2 (20); Myeloma 2 (20); Liver 1 (10); Uterus 1 (10); Lung 1 (10); Thyroid 1 (10); Breast 1 (10); Adenoid cystic carcinoma 1 (10);	Non-RCT	\	\	976 J	\	0, 7, 30, and 90 days after treatment	NRS; NR
Gianfelice-2008 (39)	11	38–84 (58.6)	Osteolytic 8 (72.7); Osteoblastic 2 (18.2); Mixed 1 (9.1)	Non-axial skeleton 11 (100); Axial skeleton 0 (0)	Breast 5 (45.5); Kidney 4 (36.4); Liver 1 (9.1); Lung 1 (9.1)	Non-RCT	28–103 min	12–18	466–1853 J	\	0, 1, 3, 14, 30, 90 days after treatment	VAS; CR; PR; NR
Wang-2019 (40)	30	3–14 (4.27)	Osteoblastic 4 (46.67); Osteolytic 5 (16.67); Mixed type 11 (36.67).	Non-axial skeleton 15 (50); Axial skeleton 15 (50)	Neuroblastoma 12 (40.00); Acute leukemia 7 (23.33); Nephroblastoma 6 (20.00); Lymphoma 5 (16.67); Other 2 (6.67)	Non-RCT	123 ± 21 min	13 ± 8	\	\	0, 7, 30, 60, 90 days after treatment	VAS+NRS
Harding-2018 (41)	18	36–72 (57)	\	Non-axial skeleton 15 (50); Axial skeleton 1 (5.6)	Breast 7 (38.9); Lung 4 (22.2); Liver 4 (22.2); Renal 3 (16.7)	Non-RCT	\	\	\	\	0, 7, 14, 30, 60, and 90 days after treatment	QLQ-C15-PAL; NR; QLQ-BM22
Gu-2015 (42)	23	45–73 (59)	\	\	\	Non-RCT	\	\	\	\	0, 7, 14, 30, 60, and 90 days after treatment	NRS

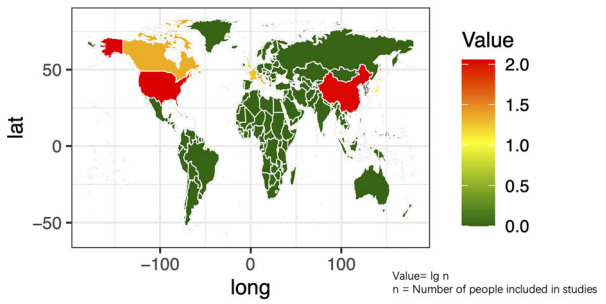

FIGURE 2 | The distribution of the research population in the included studies on the world map.

Figures 4–7 showed the results from meta-analysis of all included studies. The results of pain grade scores are shown in **Figure 4**. Eleven studies (317 patients) assessed pain grade scores at baseline, with a high heterogeneity (I^2 = 98.1%). The average reported pain scores at baseline was 6.74 (95% CI: 6.30–7.18). Nine studies (268 patients) assessed pain grade scores at 0–1 week with a high heterogeneity (I^2 = 98.7%). The mean reported pain scores at 0–1 week was 4.15 (95% CI: 3.31–4.99). In addition, 10 trials (291 patients) assessed pain grade scores at 1–5 weeks with a high heterogeneity (I^2 = 98.2%). The average reported pain scores was 3.09 (95% CI: 2.46–3.72) at 1–5 weeks. Nine trials (289 patients) assessed pain grade scores at 5–14 weeks with a high heterogeneity (I^2 = 99.7%). The mean reported pain scores was 2.28 (95% CI: 1.37–3.19) at 5–14 weeks.

Generally, the pain scores gradually decreased from baseline to the last follow-up (**Figure 5**). Compared with baseline, the symptom of pain was significantly improved at 0–1 week, with the mean reduced pain scores of 2.54 (95% CI: 1.92–3.16, p < 0.01). Besides, compared with baseline, the pain was further improved at 1–5 weeks with a mean reduced pain score of 3.56 (95% CI: 3.11–4.02, p < 0.01). Moreover, we also found significant pain improvement at 5–14 weeks, with a mean reduced pain score of 4.22 (95% CI: 3.68–4.76, p < 0.01).

OMEDD was also an important index and three trials (158 patients) assessed OMEDD at 2 weeks after treatment (**Figure 6**), with a high heterogeneity (I^2 = 86.4%). Change from baseline in OMEDD at 2 weeks after treatment was −15.11 (95% CI: −34.73, 4.5). Additionally, four studies (175 patients) evaluated OMEDD at 1 month after treatment, with a high heterogeneity (I^2 = 78.3%). Change from baseline in OMEDD at 1 month after treatment was −10.87 (95% CI: −26.32, 4.58). Three trials (158 patients) assessed OMEDD at 3 months after treatment, with a high heterogeneity (I^2 = 76.8%). Change from baseline in OMEDD at 3 months after treatment was −5.53 (95% CI: −20.44, 9.38).

Eleven trials (256 patients) assessed response rate. The results revealed that the overall CR rate was 0.36 (95% CI: 0.24–0.48, **Figure 7A**) and the overall PR rate was 0.47 (95% CI: 0.36–0.58, **Figure 7B**); the overall NR rate was 0.23 (95% CI: 0.13–0.34, **Figure 7C**).

Two studies used the QLQ-BM22 subscale scores to evaluate the survival quality of patients with bone metastases (19, 41).

TABLE 2 | MINORS quality assessment.

Author-publication time	A clearly stated aim	Inclusion of consecutive patients	Prospective collection of data	Endpoint appropriate to the study aim	Unbiased evaluation of endpoints	Follow-up period appropriate to the major endpoint	Loss to follow up less than 5%	Prospective calculation of the study size	An adequate control group	Contemporary groups	Baseline equivalence of groups	Adequate statistical analyses	Total
Anzidei-2016 (27)	2	2	2	2	0	2	2	2	0	0	0	0	12
Bertrand-2018 (32)	2	2	2	2	0	2	2	2	0	0	0	0	14
Catane-2007 (33)	2	1	2	2	0	2	0	0	0	0	0	0	9
Chan-2017 (34)	2	2	2	2	0	2	0	0	0	0	0	0	10
Chen-2018 (19)	2	2	2	2	0	2	2	2	0	0	0	0	14
Huisman-2014 (35)	2	2	2	2	0	2	0	2	0	0	0	0	12
Hurwitz-2014 (36)	2	2	2	2	2	2	2	2	2	2	2	2	24
Li-2010 (22)	2	2	2	2	0	2	2	0	0	0	0	0	12
Liberman-2008 (37)	2	2	2	2	0	2	2	2	0	0	0	0	14
Lee-2017 (13)	2	2	2	2	0	2	2	2	2	2	2	2	22
Namba-2019 (38)	2	2	2	2	0	2	0	2	2	2	2	2	20
Gianfelice-2008 (39)	2	2	2	2	0	2	2	2	0	0	0	0	14
Wang-2019 (40)	2	2	2	2	0	2	2	2	0	0	0	0	14
Harding-2018 (41)	2	2	2	2	0	2	2	2	0	0	0	0	14
Gu-2015 (42)	2	2	2	2	0	2	2	2	0	0	0	0	14
Not reported	0	0	0	0	14	0	4	3	12	12	12	12	69
Reported, inadequate	0	1	0	0	0	0	0	0	0	0	0	0	1
Reported, adequate	15	14	15	15	1	15	11	12	3	3	3	3	110

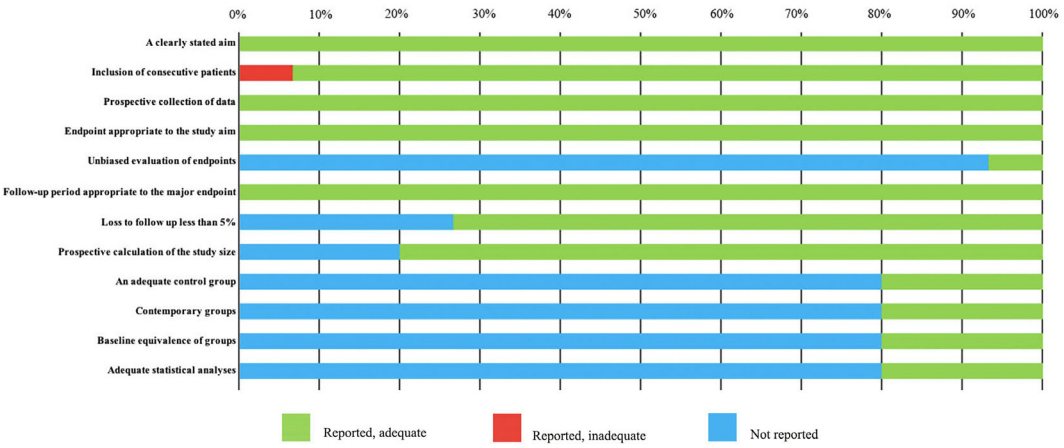

FIGURE 3 | MINORS quality assessment.

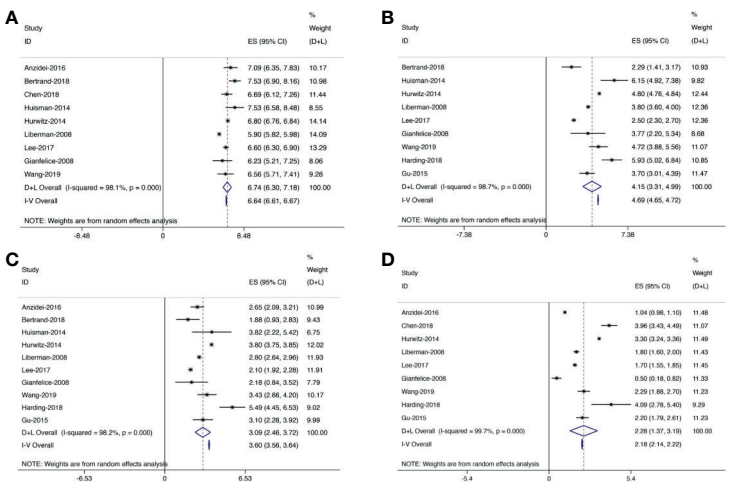

FIGURE 4 | Forest plot for inclusion of all included studies assessing pain at different time points; diamonds represent overall pain scores for random and fixed effect models with 95% CI. **(A)** Pain assessment at baseline. **(B)** Pain assessment at 0–1 week. **(C)** Pain assessment at 1–5 weeks. **(D)** Pain assessment at 5–14 weeks.

QLQ-BM22 included functional interference, psychosocial aspects, painful site, and pain characteristics. During the first 2 months, the scores of both studies decreased significantly. As time went by, the scores gradually increased. In addition, two studies used QLQ-C15 (19, 41), one study used QLQ-C30 (40), one study used biomarker evaluation including alkaline phosphatase and lactic acid dehydrogenase (22), and one study used median overall survival time (13). All abovementioned indicators showed good therapeutic effects with the treatment of MRgFUS.

There are 14 studies including 352 patients documenting the complications after MRgFUS. Among these studies, 93 (26.4%) patients had minor complications. The main reported minor complications of MRgFUS included sonication pain, position pain, early postprocedural pain, grade I skin burn, and limbs numbness (**Table 3**). Five (1.42%) patients had major complications, which are composed of fractures, third-degree skin burn, hip flexor neuropathy, and sciatic nerve injury.

DISCUSSION

Pain is the most common symptom of patients with cancer, and more than 70% of patients with bone metastasis experience severe persistent bone pain (43, 44). Generally, radiotherapy, chemotherapy, medication, and surgical treatment can be used to relieve bone pain. However, they are not ideal for the analgesic effects. MRgFUS, a safe, effective, and non-invasive ablation method, is approved for painful metastatic bone tumors by the US Food and Drug Administration (FDA) in

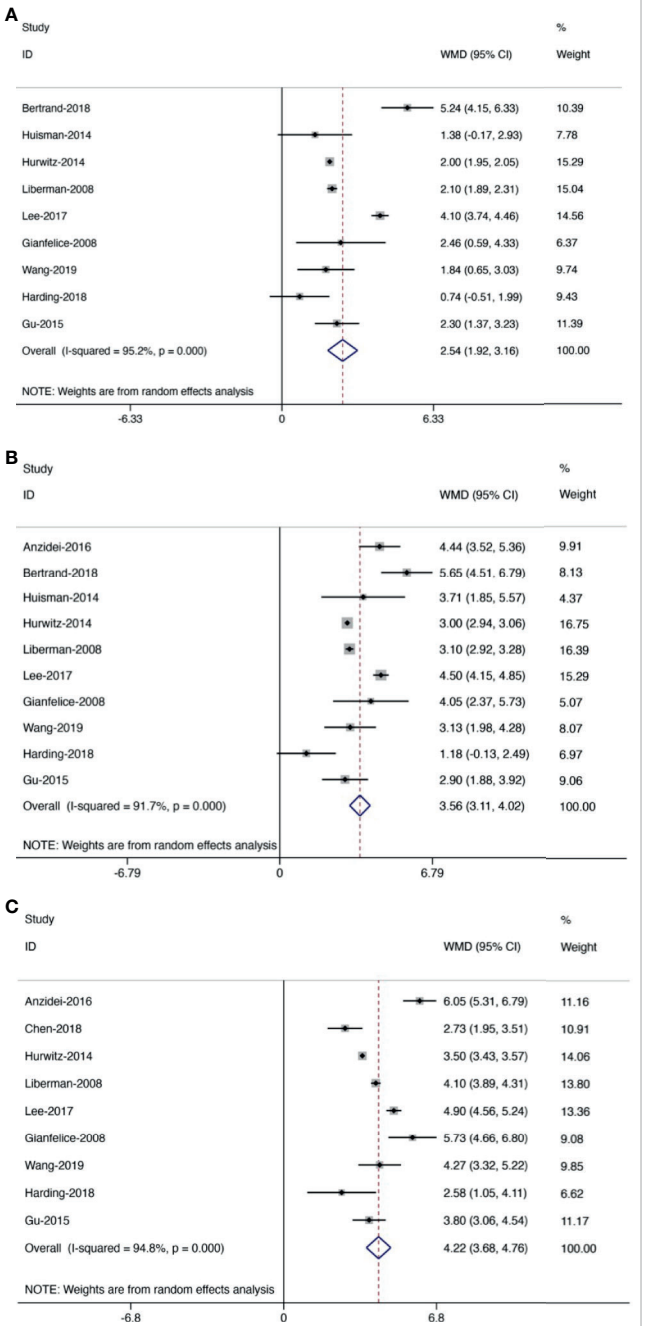

FIGURE 5 | Forest plot for inclusion of all included studies assessing pain improvement at different time points compared with baseline; diamonds represent overall pain scores for random and fixed effect models with 95% CI. Meta-analysis of pain improvement at different time points. **(A)** At 0–1 week. **(B)** At 1–5 weeks. **(C)** At 5–14 weeks.

2012. However, its therapeutic effects are not very clear. As the meta-analysis on the efficacy of MRgFUS in alleviating the pain in patients with bone metastases, our results revealed that pain grade scores and the usage amount of OMEDD gradually decreased. The conclusion is consistent with the study reported by Baal et al. (45). Besides, the overall CR rate of MRgFUS was 0.36 (95% CI: 0.24–0.48), with a PR rate of 0.47 (95% CI: 0.36–0.58) and a NR rate of 0.23 (95% CI: 0.13–0.34). In addition, among 352 patients who have undergone MRgFUS, 93 (26.4%) patients had minor complications and 5 (1.42%) patients had major complications.

Most patients who suffered from metastatic bone pain would experience intermittent dull pain initially. Gradually, pain became severe and persistent over a few weeks or months (43, 46). Metastatic bone pain has a complex etiology, such as inflammatory pain and pathological neuralgia. Cancer cells and their related stromal cells may release factors. The released factors can not only promote the pathological growth of nerve fibers and the formation of neuroma (47–49), but also sensitize and activate bone nociceptors, thus attaining peripheral and central nerve hypersensitivity (47, 50), consequently leading to the development and persistence of bone pain.

Therapeutically, conventional RT is the initial option for painful bone metastasis and offers a 60% to 80% response rate (13, 51). However, among these responders, relapses frequently occur with an incidence of 30% (52). MRgFUS is more efficient than RT in terms of long-term pain palliation and high response rate (range from 66% to 87%). Thus, it provides an alternative treatment method to overcome radioresistance and is recommended for patients with bone metastasis for whom RT is considered to have failed (12, 13, 36, 47).

OMEDD is another index to evaluate the effects of pain relief. Morphine is commonly used in bone metastases due to its powerful analgesic effects. Generally, it produces pharmacological effects by simulating the endogenous anti-pain substance enkephalin and activating central nervous opioid receptors. Thus, it works better on persistent dull pain than intermittent sharp pain and visceral colic (53). However, it is prone to generate drug resistance and addiction. As the dose increases, severe conditions such as respiratory depression and even coma death may occur (54). Therefore, the application of morphine should be tightly controlled. With the treatment of MRgFUS, we found that the change from baseline in OMEDD at 2 weeks was −15.11 (95% CI: −34.73, 4.5), indicating that MRgFUS may reduce the use of morphine. Baal et al. used different analysis methods, showing that the average of 55.8% and 33.0% of patients could discontinue or reduce pain medication use after treatment of MRgFUS (45), similar to the conclusion we got.

As MRgFUS realizes real-time magnetic resonance dynamic imaging and dynamic temperature monitoring throughout the operation, its complications are relatively low (12, 55). The summary was consistent with the studies of Gennaro et al. (15) and Baal et al. (45). Nevertheless, it is important to take measures to avoid them. Among all the complications, the most common one was a minor complication—sonication pain, which can be expected and usually goes away 1 day after treatment (28). Additionally, sonication pain can also be reduced by local, regional, or general anesthesia (12). As a major complication, skin burn frequently occurs during the procedure. To reduce its

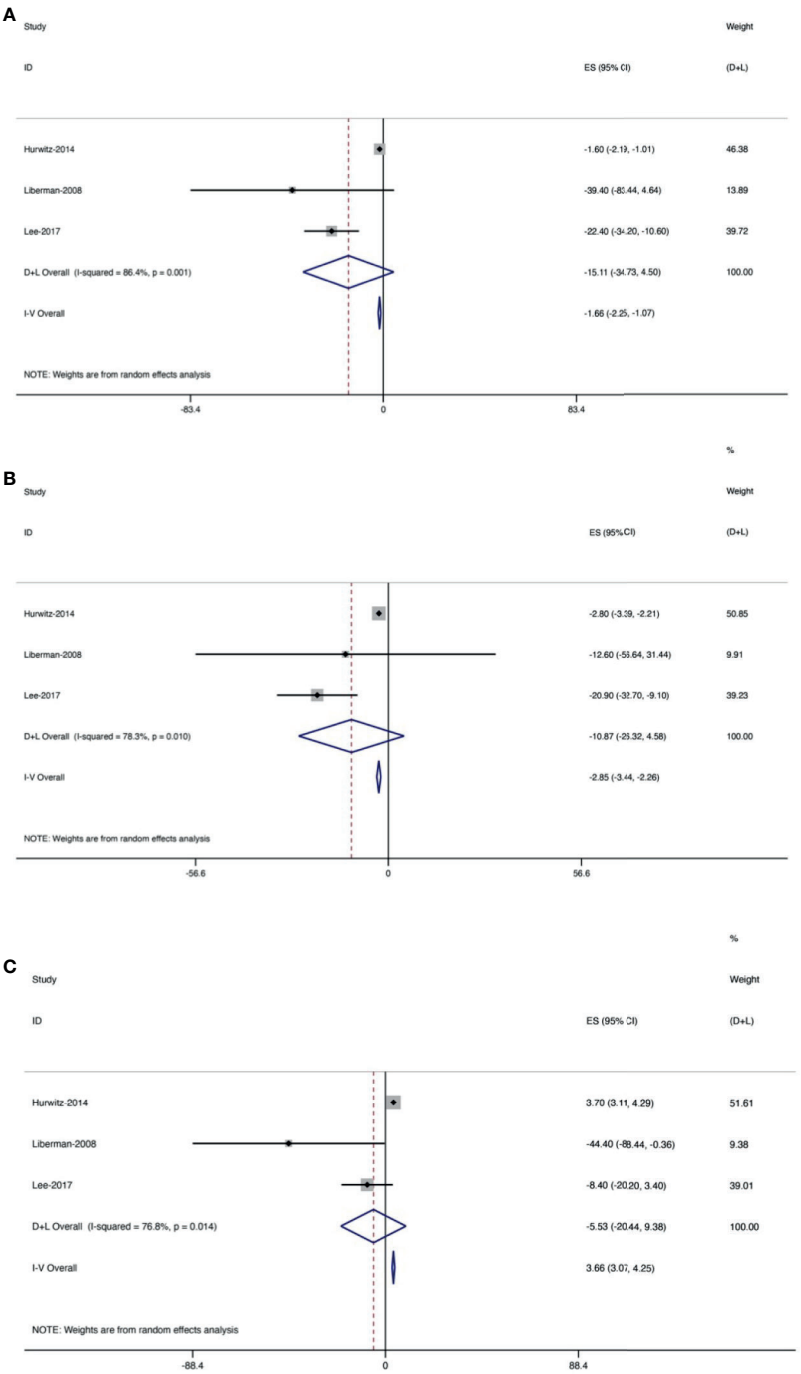

FIGURE 6 | Forest plot for changes from baseline in the oral morphine equivalent dose (OMEDD) at each evaluation point after treatment of patients with bone metastases. **(A)** At 2 weeks. **(B)** At 1 month. **(C)** At 3 months.

risk, the long-term low-output power MRgFUS or short-term high-output power MRgFUS with skin hypothermy treatment through irradiation intervals is recommended (56).

This study has limitations: First, the clinical heterogeneity was found among different studies, which may be associated with differences in gender, age, location, etc. Second, the included studies in this meta-analysis are single-arm ones and lack randomized controlled trials. Third, the pain score functions as one of the evaluation indicators, but it is subjective and uncertain. Other evaluation indicators, such as biomarker evaluation, are only reported in a few literatures, which make the results insufficient.

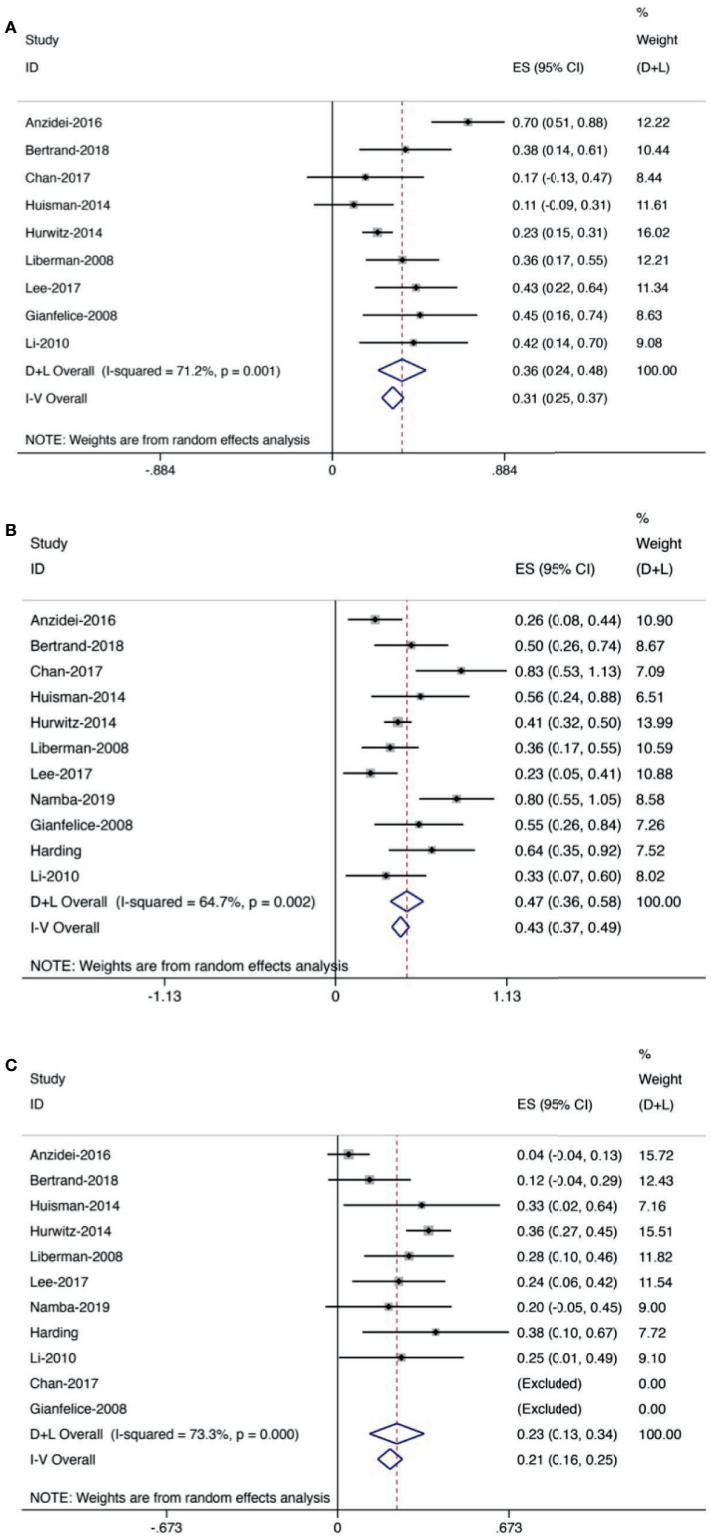

FIGURE 7 | Forest plot for inclusion of all included studies of response rate. **(A)** Complete response rate. **(B)** Partial response rate. **(C)** No response rate.

TABLE 3 | Complications of MRgFUS.

Author-publication time	Number of minor complications	Type of minor complications	Number of major complications	Type of major complications
Anzidei-2016 (27)	0		0	
Bertrand-2018 (32)	0		0	
Catane-2007 (33)	0		0	
Chan-2017 (34)	0		0	
Chen-2018 (19)	0		0	
Huisman-2014 (35)	2	Pain after treatment (*n* = 1), grade I skin burn (*n* = 1)	0	
Hurwitz-2014 (36)	59	Sonication pain (*n* = 36), position pain (*n* = 9) postprocedural pain (*n* = 5), fatigue (*n* = 2) neuropathy (*n* = 1), skin burn (*n* = 1), blood in urine (*n* = 1), fever (*n* = 1), myositis (*n* = 1), skin rash (*n* = 1), skin numbness (*n* = 1)	4	Fracture (*n* = 2), grade III skin burn (*n* = 1), hip flexor neuropathy (*n* = 1)
Li-2010 (22)	15	Grade I skin burns (*n* = 12), grade II skin burn (*n* = 2), affected limbs numbness (*n* = 3)	0	
Liberman-2008 (37)	1	Grade II skin burn (*n* = 1)	1	Sciatic nerve injury (*n* = 1)
Lee-2017 (13)	12	Grade II myositis (*n* = 1), Positioning pain (*n* = 3), Sonication pain (*n* = 7), Dermatitis (*n* = 1)	0	
Gianfelice-2008 (39)	0		0	
Wang-2019 (40)	0		0	
Harding-2018 (41)	0		0	
Gu-2015 (42)	4	Lower limbs numbness (*n* = 1), Sonication pain (*n* = 3)	0	

In summary, this meta-analysis identifies MRgFUS as a reliable therapeutic option to relieve cancer pain for patients with metastatic bone tumors with controllable related complications. In order to further confirm the effectiveness and safety of MRgFUS in relieving pain in patients with metastatic bone tumors, more detailed, multi-regional, multi-ethnic randomized controlled trials are needed in the future.

DATA AVAILABILITY STATEMENT

The original contributions presented in the study are included in the article/**Supplementary Material**. Further inquiries can be directed to the corresponding authors.

AUTHOR CONTRIBUTIONS

XH screened literature and extracted the data from each included study, analyzed data and wrote the article. RH screened literature and extracted the data from each included study, checked the data processing results. TM carried out data inspection and article revision. HY proposed amendments. DS put forward ideas for articles and made a decision. All authors contributed to the article and approved the submitted version.

FUNDING

This study was partially supported by Shanghai Rising-Star Program (No. 21QA1407500), the Shanghai Jiaotong University Medical-Industrial Intersection Project (Key) (ZH2018ZDA18), the National Natural Science Foundation of China (No. 81772856), and the Youth Fund of Shanghai Municipal Health Planning Commission (20174Y0117).

SUPPLEMENTARY MATERIAL

The Supplementary Material for this article can be found online at: https://www.frontiersin.org/articles/10.3389/fonc.2021.617295/full#supplementary-material

Supplementary Figure 1 | Funnel plot of pain improvement at different follow-up period compared with baseline.

REFERENCES

1. Clement-Demange L, Clezardin P. Emerging Therapies in Bone Metastasis. *Curr Opin Pharmacol* (2015) 22:79–86. doi: 10.1016/j.coph.2015.04.004
2. Patrick DL, Cleeland CS, von Moos R, Fallowfield L, Wei R, Ohrling K, et al. Pain Outcomes in Patients With Bone Metastases From Advanced Cancer: Assessment and Management With Bone-Targeting Agents. *Support Care Cancer* (2015) 23(4):1157–68. doi: 10.1007/s00520-014-2525-4
3. Pellerin O, Medioni J, Vulser C, Déan C, Oudard S, Sapoval M. Management of Painful Pelvic Bone Metastasis of Renal Cell Carcinoma Using Embolization, Radio-Frequency Ablation, and Cementoplasty: A Prospective Evaluation of Efficacy and Safety. *Cardiovasc Interventional Radiol* (2014) 37(3):730–6. doi: 10.1007/s00270-013-0740-x
4. Scully SP, Ghert MA, Zurakowski D, Thompson RC, Gebhardt MC. Pathologic Fracture in Osteosarcoma: Prognostic Importance and Treatment Implications. *J Bone Joint Surg Am* (2002) 84(1):49–57. doi: 10.2106/00004623-200201000-00008
5. Hartsell WF, Scott CB, Bruner DW, Scarantino CW, Ivker RA, Roach M3rd, et al. Randomized Trial of Short- Versus Long-Course Radiotherapy for Palliation of Painful Bone Metastases. *J Natl Cancer Inst* (2005) 97(11):798–804. doi: 10.1093/jnci/dji139
6. Wu SY, Wong R, Johnston M, Bezjak A, Whelan T, Wu JS, et al. Cancer Care Ontario Practice Guidelines Initiative Supportive Care Group. Meta-Analysis

of Dose Fractionation Radiotherapy Trials for the Palliation of Painful Bone Metastases. *Int J Radiat Oncol Biol Physics* (2003) 55(3):594–605. doi: 10.1016/S0360-3016(02)04147-0
7. Okunieff P, Milano MT, Porter AT, David M. Chapter 23 - Metastatic Disease: Bone, Spinal Cord, Brain, Liver, and Lung. In: Gunderson LL, Tepper JE, editors. *Clinical Radiation Oncology (Third Edition)*. Philadelphia: W.B. Saunders (2012). p 421–38.
8. Brashears JH. Palliation of Bone Metastases. In: Brady LW, Yaeger TE, editors. *Encyclopedia of Radiation Oncology*. Berlin, Heidelberg: Springer Berlin Heidelberg (2013). p 591–6.
9. Arjun S, , Larson DA, Chang EL. Stereotactic Body Radiosurgery for Spinal Metastases: A Critical Review. *Int J Radiat Oncol Biol Physics* (2008) 71 (3):652–65. doi: 10.1016/j.ijrobp.2008.02.060
10. Callstrom MR, Charboneau JW, Goetz MP, Rubin J, Atwell TD, Farrell MA, et al. Image-Guided Ablation of Painful Metastatic Bone Tumors: A New and Effective Approach to a Difficult Problem. *Skeletal Radiol* (2006) 35(1):1–15. doi: 10.1007/s00256-005-0003-2
11. Callstrom MR, Dupuy DE, Solomon SB, Beres RA, Sloan JA. Percutaneous Image-Guided Cryoablation of Painful Metastases Involving Bone: Multicenter Trial. *Cancer* (2013) 119(5):1033–41. doi: 10.1002/cncr.27793
12. Napoli A, Anzidei M, Marincola BC, Brachetti G, Noce V, Boni F, et al. MR Imaging-Guided Focused Ultrasound for Treatment of Bone Metastasis. *Radiographics* (2013) 33(6):1555–68. doi: 10.1148/rg.336125162
13. Lee HL, Kuo CC, Tsai JT, Chen CY, Wu MH, Chiou JF. Magnetic Resonance-Guided Focused Ultrasound Versus Conventional Radiation Therapy for Painful Bone Metastasis: A Matched-Pair Study. *J Bone Joint Surg Am* (2017) 99(18):1572–8. doi: 10.2106/jbjs.16.01248
14. Webb H, Lubner MG, Hinshaw JL. Thermal Ablation. *Semin Roentgenol* (2011) 46(2):133–41. doi: 10.1053/j.ro.2010.08.002
15. Gennaro N, Sconfienza LM, Ambrogi F, Boveri S, Lanza E. Thermal Ablation to Relieve Pain From Metastatic Bone Disease: A Systematic Review. *Skeletal Radiol* (2019) 48(8):1161–9. doi: 10.1007/s00256-018-3140-0
16. Al-Bataineh O, Jenne J, Huber P. Clinical and Future Applications of High Intensity Focused Ultrasound in Cancer. *Cancer Treat Rev* (2012) 38(5):346–53. doi: 10.1016/j.ctrv.2011.08.004
17. Masciocchi C, Conchiglia A, Gregori LM, Arrigoni F, Zugaro L, Barile A. Critical Role of HIFU in Musculoskeletal Interventions. *Radiol Med* (2014) 119(7):470–5. doi: 10.1007/s11547-014-0414-z
18. Errico and Alessia: Surgery: MRgFUS-Non Invasive Treatment for Patients With Painful Bone Metastasis. *Nat Rev Clin Oncol* (2014) 11(6):42–51. doi: 10.1038/nrclinonc.2014.86
19. Chen ZQ, Wang CR, Ma XJ, Sun W, Shen JK, Sun MX, et al. Evaluation of Quality of Life Using EORTC QLQ-BM22 in Patients With Bone Metastases After Treatment With Magnetic Resonance Guided Focused Ultrasound. *Orthop Surg* (2018) 10(3):264–71. doi: 10.1111/os.12383
20. Jenne JW, Preusser T, Gunther M. High-Intensity Focused Ultrasound: Principles, Therapy Guidance, Simulations and Applications. *Z Med Phys* (2012) 22(4):311–22. doi: 10.1016/j.zemedi.2012.07.001
21. Napoli A, Anzidei M, Ciolina F, Marotta E, Cavallo Marincola B, Brachetti G, et al. MR-Guided High-Intensity Focused Ultrasound: Current Status of an Emerging Technology. *Cardiovasc Intervent Radiol* (2013) 36(5):1190–203. doi: 10.1007/s00270-013-0592-4
22. Li C, Zhang W, Fan W, Huang J, Zhang F, Wu P. Noninvasive Treatment of Malignant Bone Tumors Using High-Intensity Focused Ultrasound. *Cancer* (2010) 116(16):3934–42. doi: 10.1002/cncr.25192
23. Moher D, Liberati A, Tetzlaff J, Altman DG, Group P. Preferred Reporting Items for Systematic Reviews and Meta-Analyses: The PRISMA Statement. *PloS Med* (2009) 6(7):e1000097. doi: 10.1371/journal.pmed.1000097
24. Cumpston M, Li T, Page MJ, Chandler J, Welch VA, Higgins JP, et al. Updated Guidance for Trusted Systematic Reviews: A New Edition of the Cochrane Handbook for Systematic Reviews of Interventions. *Cochrane Database Syst Rev* (2019) 10:ED000142. doi: 10.1002/14651858.ED000142
25. Slim K, Nini E, Forestier D, Kwiatkowski F, Panis Y, Chipponi J. Methodological Index for non-Randomized Studies (Minors): Development and Validation of a New Instrument. *ANZ J Surg* (2003) 73(9):712–6. doi: 10.1046/j.1445-2197.2003.02748.x
26. Wassermann J, de la Lande B, Pecking A, Brasseur L. [Pain and Bone Metastases]. *Prog Urol* (2008) 18 Suppl 7:S399–409. doi: 10.1016/S1166-7087(08)74574-3
27. Anzidei M, Napoli A, Sacconi B, Boni F, Noce V, Di Martino M, et al. Magnetic Resonance-Guided Focused Ultrasound for the Treatment of Painful Bone Metastases: Role of Apparent Diffusion Coefficient (ADC) and Dynamic Contrast Enhanced (DCE) MRI in the Assessment of Clinical Outcome. *Radiol Med* (2016) 121(12):905–15. doi: 10.1007/s11547-016-0675-9
28. Ahmed M, Solbiati L, Brace CL, Breen DJ, Callstrom MR, Charboneau JW, et al. Interventional Radiological Society of: Image-Guided Tumor Ablation: Standardization of Terminology and Reporting Criteria–a 10-Year Update. *J Vasc Interv Radiol* (2014) 25(11):1691–705.e4. doi: 10.1016/j.jvir.2014.08.027
29. Sacks D, McClenny TE, Cardella JF, Lewis CA. Society of Interventional Radiology Clinical Practice Guidelines. *J Vasc Interv Radiol 14(9 Pt* (2003) 2): S199–202. doi: 10.1097/01.rvi.0000094584.83406.3e
30. Sun Y, Yu X, Liu J, Zhou N, Chen L, Zhao Y, et al. Effect of Bedtime Administration of Blood-Pressure Lowering Agents on Ambulatory Blood Pressure Monitoring Results: A Meta-Analysis. *Cardiol J* (2016) 23(4):473–81. doi: 10.5603/CJ.a2016.0027
31. Wang L, Gu Z, Zhai R, Zhao S, Luo L, Li D, et al. Efficacy of Oral Cryotherapy on Oral Mucositis Prevention in Patients With Hematological Malignancies Undergoing Hematopoietic Stem Cell Transplantation: A Meta-Analysis of Randomized Controlled Trials. *PloS One* (2015) 10(5):e0128763. doi: 10.1371/journal.pone.0128763
32. Bertrand AS, Iannessi A, Natale R, Beaumont H, Patriti S, Xiong-Ying J, et al. Focused Ultrasound for the Treatment of Bone Metastases: Effectiveness and Feasibility. *J Ther Ultrasound* (2018) 6:8. doi: 10.1186/s40349-018-0117-3
33. Catane R, Beck A, Inbar Y, Rabin T, Shabshin N, Hengst S, et al. MR-Guided Focused Ultrasound Surgery (MRgFUS) for the Palliation of Pain in Patients With Bone Metastases–Preliminary Clinical Experience. *Ann Oncol* (2007) 18 (1):163–7. doi: 10.1093/annonc/mdl335
34. Chan M, Dennis K, Huang Y, Mougenot C, Chow E, DeAngelis C, et al. Magnetic Resonance-Guided High-Intensity-Focused Ultrasound for Palliation of Painful Skeletal Metastases: A Pilot Study. *Technol Cancer Res Treat* (2017) 16(5):570–6. doi: 10.1177/1533034616658576
35. Huisman M, Lam MK, Bartels LW, Nijenhuis RJ, Moonen CT, Knuttel FM, et al. Feasibility of Volumetric MRI-Guided High Intensity Focused Ultrasound (MR-HIFU) for Painful Bone Metastases. *J Ther Ultrasound* (2014) 2:16. doi: 10.1186/2050-5736-2-16
36. Hurwitz MD, Ghanouni P, Kanaev SV, Iozeffi D, Gianfelice D, Fennessy FM, et al. Magnetic Resonance-Guided Focused Ultrasound for Patients With Painful Bone Metastases: Phase III Trial Results. *J Natl Cancer Inst* (2014) 106 (5):dju082. doi: 10.1093/jnci/dju082
37. Liberman B, Gianfelice D, Inbar Y, Beck A, Rabin T, Shabshin N, et al. Pain Palliation in Patients With Bone Metastases Using MR-Guided Focused Ultrasound Surgery: A Multicenter Study. *Ann Surg Oncol* (2009) 16 (1):140–6. doi: 10.1245/s10434-008-0011-2
38. Namba H, Kawasaki M, Izumi M, Ushida T, Takemasa R, Ikeuchi M. Effects of MRgFUS Treatment on Musculoskeletal Pain: Comparison Between Bone Metastasis and Chronic Knee/Lumbar Osteoarthritis. *Pain Res Manag* (2019) 2019:4867904. doi: 10.1155/2019/4867904
39. Gianfelice D, Gupta C, Kucharczyk W, Bret P, Havill D, Clemons M. Palliative Treatment of Painful Bone Metastases With MR Imaging–Guided Focused Ultrasound. *Radiology* (2008) 249(1):355–63. doi: 10.1148/radiol.2491071523
40. Wang B, Li J, Wei X. Short-Term Efficacy and Safety of MR-Guided Focused Ultrasound Surgery for Analgesia in Children With Metastatic Bone Tumors. *Oncol Lett* (2019) 18(3):3283–9. doi: 10.3892/ol.2019.10628
41. Harding D, Giles SL, Brown MRD, Ter Haar GR, van den Bosch M, Bartels LW, et al. Evaluation of Quality of Life Outcomes Following Palliative Treatment of Bone Metastases With Magnetic Resonance-Guided High Intensity Focused Ultrasound: An International Multicentre Study. *Clin Oncol (R Coll Radiol)* (2018) 30(4):233–42. doi: 10.1016/j.clon.2017.12.023
42. Gu J, Wang H, Tang N, Hua Y, Yang H, Qiu Y, et al. Magnetic resonance guided focused ultrasound surgery for pain palliation of bone metastases: early experience of clinical application in China. *Zhonghua Yi Xue Za Zhi* (2015) 95 (41):3328–32. doi: 10.3760/cma.j.issn.0376-2491.2015.41.003

43. Mercadante S. Malignant Bone Pain: Pathophysiology and Treatment. *Pain* (1997) 69(1-2):1–18. doi: 10.1016/s0304-3959(96)03267-8
44. Bonica JJ. Management of Cancer Pain. *Acta Anaesthesiol Scand Suppl* (1982) 74:75–82. doi: 10.1111/j.1399-6576.1982.tb01852.x
45. Baal JD, Chen WC, Baal U, Wagle S, Baal JH, Link TM, et al. Efficacy and Safety of Magnetic Resonance-Guided Focused Ultrasound for the Treatment of Painful Bone Metastases: A Systematic Review and Meta-Analysis[J]. *Skeletal Radiol* (2021) 1–11. doi: 10.1007/s00256-021-03822-8
46. Urch C. The Pathophysiology of Cancer-Induced Bone Pain: Current Understanding. *Palliat Med* (2004) 18(4):267–74. doi: 10.1191/0269216304pm887ra
47. Mantyh P. Bone Cancer Pain: Causes, Consequences, and Therapeutic Opportunities. *PAIN*® (2013) 154:S54–62. doi: 10.1016/j.pain.2013.07.044
48. Black JA, Nikolajsen L, Kroner K, Jensen TS. Multiple Sodium Channel Isoforms and Mitogen-Activated Protein Kinases Are Present in Painful Human Neuromas. *Ann Neurol* (2008) 64(6):644–53. doi: 10.1002/ana.21527
49. Ceyhan GO, Bergmann F, Kadihasanoglu M, Altintas B, Friess H. Pancreatic Neuropathy and Neuropathic Pain–A Comprehensive Pathomorphological Study of 546 Cases. *Gastroenterology* (2009) 136(1):177–86.e1. doi: 10.1053/j.gastro.2008.09.029
50. Tabata M, Murata E, Ueda K, Kato-Kogoe N, Kuroda Y, Hirose M. Effects of TrkA Inhibitory Peptide on Cancer-Induced Pain in a Mouse Melanoma Model. *J Anesthesia* (2012) 26(4):545–51. doi: 10.1007/s00540-012-1377-7
51. Wu JS, Wong R, Johnston M, Bezjak A, Whelan T, Cancer Care Ontario Practice Guidelines Initiative Supportive Care G. Meta-Analysis of Dose-Fractionation Radiotherapy Trials for the Palliation of Painful Bone Metastases. *Int J Radiat Oncol Biol Phys* (2003) 55(3):594–605. doi: 10.1016/s0360-3016(02)04147-0
52. Tong D, Gillick L, Hendrickson FR. The Palliation of Symptomatic Osseous Metastases: Final Results of the Study by the Radiation Therapy Oncology Group. *Cancer* (1982) 50(5):893–9. doi: 10.1002/1097-0142(19820901)50:5<893::aid-cncr2820500515>3.0.co;2-y
53. Luellmann H, Hein L, Mohr K, Bieger D. Color Atlas of Pharmacology. *Color Atlas Pharmacol* (2010) 4(6):435. doi: 10.1186/1479-7364-4-6-435
54. Warnock ML, Ghahremani GG, Rattenborg C, Ginsberg M, Valenzuela J. Pulmonary Complication of Heroin Intoxication. Aspiration Pneumonia and Diffuse Bronchiectasis. *JAMA* (1972) 219(8):1051–3. doi: 10.1001/jama.219.8.1051
55. Lam MK, Huisman M, Nijenhuis RJ, van den Bosch MA, Viergever MA, Moonen CT, et al. Quality of MR Thermometry During Palliative MR-Guided High-Intensity Focused Ultrasound (MR-HIFU) Treatment of Bone Metastases. *J Ther Ultrasound* (2015) 3:5. doi: 10.1186/s40349-015-0026-7
56. Gong Z, Wang B, Yao M, Wong H, Ran H. Research and Application of Temperature Distribution in Focal Area of Biological Body Under HIFU Treatment. *Shanghai Biomed Eng* (2004) 4(25):29–32. doi: 10.3969/j.issn.1674-1242.2004.04.007

Conflict of Interest: The authors declare that the research was conducted in the absence of any commercial or financial relationships that could be construed as a potential conflict of interest.

frontiers in Oncology

ORIGINAL RESEARCH
published: 23 September 2021
doi: 10.3389/fonc.2021.641187

A Zebrafish Model of Metastatic Colonization Pinpoints Cellular Mechanisms of Circulating Tumor Cell Extravasation

Tyler A. Allen[1], Mark M. Cullen[1], Nathan Hawkey[1], Hiroyuki Mochizuki[2], Lan Nguyen[1], Elyse Schechter[1], Luke Borst[3], Jeffrey A. Yoder[2], Jennifer A. Freedman[1,4], Steven R. Patierno[1,4], Ke Cheng[2,5], William C. Eward[6] and Jason A. Somarelli[1,4]**

[1] Duke Cancer Institute, Duke University Medical Center, Durham, NC, United States, [2] Department of Molecular Biomedical Sciences and Comparative Medicine Institute, North Carolina State University, Raleigh, NC, United States, [3] Department of Population Health and Pathobiology, College of Veterinary Medicine, North Carolina State University, Raleigh, NC, United States, [4] Department of Medicine, Division of Medical Oncology, Duke University Medical Center, Durham, NC, United States, [5] Joint Department of Biomedical Engineering, University of North Carolina at Chapel Hill and North Carolina State University, Chapel Hill, NC, United States, [6] Department of Orthopedics, Duke University Medical Center, Durham, NC, United States

OPEN ACCESS

Edited by:
Dianwen Song,
Shanghai First People's Hospital, China

Reviewed by:
Anantha Koteswararao Kanugula, University of Massachusetts Medical School, United States
Michael M. Lizardo, British Columbia Cancer Agency, Canada

***Correspondence:**
Tyler A. Allen
tyler.allen@duke.edu
Jason A. Somarelli
jason.somarelli@duke.edu

Specialty section:
This article was submitted to Molecular and Cellular Oncology, a section of the journal Frontiers in Oncology

Received: 13 December 2020
Accepted: 31 August 2021
Published: 23 September 2021

Citation:
Allen TA, Cullen MM, Hawkey N, Mochizuki H, Nguyen L, Schechter E, Borst L, Yoder JA, Freedman JA, Patierno SR, Cheng K, Eward WC and Somarelli JA (2021) A Zebrafish Model of Metastatic Colonization Pinpoints Cellular Mechanisms of Circulating Tumor Cell Extravasation. Front. Oncol. 11:641187. doi: 10.3389/fonc.2021.641187

Metastasis is a multistep process in which cells must detach, migrate/invade local structures, intravasate, circulate, extravasate, and colonize. A full understanding of the complexity of this process has been limited by the lack of ability to study these steps in isolation with detailed molecular analyses. Leveraging a comparative oncology approach, we injected canine osteosarcoma cells into the circulation of transgenic zebrafish with fluorescent blood vessels in a biologically dynamic metastasis extravasation model. Circulating tumor cell clusters that successfully extravasated the vasculature as multicellular units were isolated under *intravital* imaging (n = 6). These extravasation-positive tumor cell clusters sublines were then molecularly profiled by RNA-Seq. Using a systems-level analysis, we pinpointed the downregulation of KRAS signaling, immune pathways, and extracellular matrix (ECM) organization as enriched in extravasated cells ($p < 0.05$). Within the extracellular matrix remodeling pathway, we identified versican (*VCAN*) as consistently upregulated and central to the ECM gene regulatory network ($p < 0.05$). Versican expression is prognostic for a poorer metastasis-free and overall survival in patients with osteosarcoma. Together, our results provide a novel experimental framework to study discrete steps in the metastatic process. Using this system, we identify the versican/ECM network dysregulation as a potential contributor to osteosarcoma circulating tumor cell metastasis.

Keywords: angiopellosis, circulating tumor cell cluster, tumor cell extravasation, cancer exodus hypothesis, metastasis, osteosarcoma

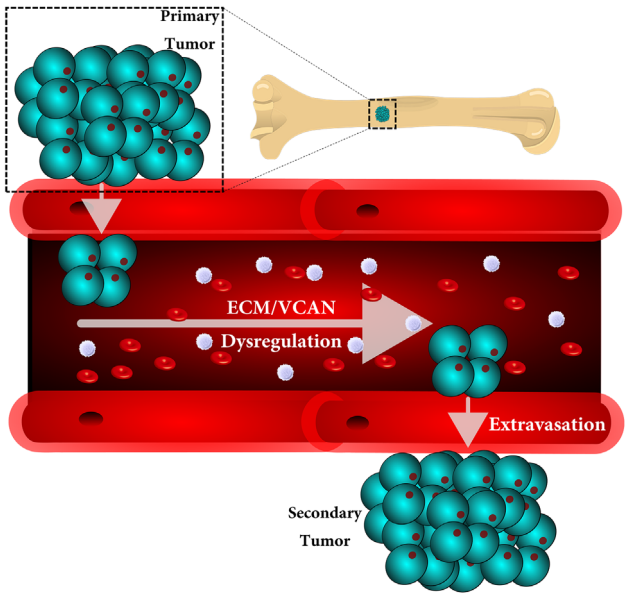

GRAPHICAL ABSTRACT | A graphical abstract of the proposed findings this study identified.

INTRODUCTION

Metastasis is a complex process, involving multiple genetic, epigenetic, biochemical, and physical changes in cancer cells and their associated microenvironments. Although metastasis accounts for the majority of all cancer-related deaths, accumulating data suggests that the majority of metastasis is a result of circulating tumor cells (CTC) clusters, rather than individual tumor cells (1–7). These CTC clusters show an increased ability: 1) to spread throughout the body, 2) withstand the hemodynamic forces of the blood stream, 3) and proliferate once they extravasate at distant sites (8, 9). Additionally, studies have revealed that cell clusters exit circulation through the recently identified extravasation mechanism, known as angiopellosis, in which the blood vessels actively remodel, allowing the clusters to exit while maintaining their multicellularity (5, 10–14). The maintenance of this multicellularity has been shown to provide distinct survival and proliferative advantages, and it has been previously proposed that CTC clusters may be responsible for the majority of cancer metastasis (3, 4, 6, 15, 16).

Utilizing this system, we set out to establish a model to better identify and understand the molecular drivers of extravasation in metastatic osteosarcoma. Osteosarcoma (OS) is a rare, but aggressive primary bone cancer that predominantly affects children and young adults. It is the most common primary bone cancer, and the 5-year survival for patients who present with metastatic disease is, at best, 30% (17–20). Sadly, there have been no new treatments for metastatic OS in the past three to four decades, and an improved understanding of OS metastasis is urgently needed to identify the molecular mechanisms and pinpoint new potential therapeutic targets to prevent metastatic spread (21, 22). Here, we used a zebrafish model of metastasis to infuse fluorescent canine OS cells into Tg(fli1a: egpf) zebrafish with fluorescent blood vessels (5, 10, 23) to test the hypothesis that CTC clusters would exhibit unique molecular profiles associated with their ability to migrate to distant sites and extravasate. Zebrafish vasculature has previously been shown to be a suitable model system to understand the vascular environments in mammals, including humans (12–14, 24–26). The establishment of this model can be used to further identify and study targets or markers involved in the extravasation process.

We used *intravital* imaging to observe CTCs extravasating as clusters. These clusters were then isolated, expanded, and characterized by RNA-Seq. These efforts identified several key pathways commonly enriched in human and canine OS extravasated clusters, including the downregulation of KRAS signaling, interferon gamma response, and other immune pathways, and extracellular matrix remodeling. Among the genes commonly altered in both extravasation models, we identified versican, an extracellular matrix proteoglycan, as a potential mediator of CTC cluster extravasation. Versican, a large aggregating chondroitin sulfate proteoglycan, is an important ECM component associated with tumorigenesis (27, 28). Previous *in vitro* and *in vivo* studies have shown that versican enhances cancer cell survival, growth, migration, invasion, angiogenesis, drug resistance, and metastasis and has been shown to induce malignancy in OS cells through the interaction with TGF-beta (29–33). Additionally, an increased expression of versican has been reported in several types of malignancies including brain tumors, leukemia, breast, prostate,

colon, lung, and ovarian cancers, and is generally associated with a poor prognosis (30, 32, 34–37). Our collective data suggest that a combination of *intravital* imaging and molecular characterization in a zebrafish model of metastasis can be used to identify the molecular mechanisms and gene regulatory pathways involved in discrete steps in the metastatic process.

MATERIALS AND METHODS

Animals

All experiments involving live zebrafish were performed in accordance with relevant institutional and national guidelines and regulations and were approved by the North Carolina State University Institutional Animal Care and Use Committee. For zebrafish, the transgenic lines *Tg(fli1a:EGFP)* were used in this study. The resulting embryos were screened at 48 hpf for the expression of transgene expression. In order to prevent pigmentation, 0.2 mM N-phenylthiourea (PTU; Sigma) was applied to all embryos starting at 24 hpf.

Embryo Preparation and Tumor Cell Implantation

Dechorionized 48 hpf zebrafish embryos were anesthetized with 0.004% tricaine (Sigma) and positioned on a 200 mm x 15 mm Petri dish coated with 3% agarose. Canine osteosarcoma cells were trypsinized into single cell suspensions, resuspended in phosphate-buffered saline (PBS; Invitrogen), kept at room temperature before implantation, and implanted within 2 hours. Any non-fluorescent cells were labelled with the fluorescent cell tracker DiI (Invitrogen) according to the instructions of the manufacturer. The cell suspension was loaded into borosilicate glass capillary needles (1 mm o.d. × 0.78 mm i.d.; World Precision Instruments) and the injections were performed using a PV830 Pneumatic Pico pump and a manipulator (WPI). A total of 30–100 cells, were injected at approximately 50 μm above the ventral end of the duct of Cuvier where it opens into the heart. The approximate injection parameters were: injection pressure =300 p.s.i., holding pressure = 10 p.s.i., injection time = 0.2 seconds. Injected tumor cells could normally be seen entering the vasculature 15–30 minutes after injection and starting to arrest in the vessels of the tail as clusters within 2 hours after injection. After implantation with mammalian cells, zebrafish embryos (including non-implanted controls) were maintained at 32°C. Normally, cell injected embryos were euthanized at the end of experiments (~72 hpf) by tricaine overdose. For each cell line or condition, data are representative of ≥three independent experiments, with ≥5 embryos/group. Experiments were discarded when the survival rate of the control group was <80%.

Zebrafish Embryo Preparation and Microscopy

For live imaging in the light-sheet microscope, 48 hpf zebrafish embryos were anesthetized using 0.016% tricaine (Sigma) and then were embedded in 1.3% low-melting-temperature agarose (Sigma; prepared in filtered fish facility water) inside a glass capillary [1.5/2.0-mm inner/outer diameter, 20-mm length (Zeiss)]. The embryos were centered in the capillary and oriented. After gel formation, the section of the agarose cylinder containing the tail of the embryo was extruded from the capillary by inserting wax into the capillary on the side opposite to the fish. The sample chamber of the light-sheet microscope was filled with filtered fish facility water, and the capillary was inserted for imaging. Specimens were maintained at 32°C throughout the imaging period. Fluorescent image acquisition was performed using a Zeiss Lightsheet Z.1. Z-stacks were processed for maximum intensity projections with the Zeiss ZEN software. For timelapse (4D) images, zstacks were taken every 5–15 minutes for a total time of up to 24 hours with a step number between 50 and 200 and step size of 0.3–2.0 μm. Images were adjusted for brightness and contrast using the Zeiss ZEN Software. Confirmation of injected cell migration from inside of the lumen to surrounding tissue was done using the Zeiss ZEN software 3D retendering capability.

Cell Culture

Canine osteosarcoma cell lines: D17 and HMPOS were cultured in IMDM/10% (v/v) fetal bovine serum/2 mM L-glutamine/100 U/ml penicillin/100 μg/ml streptomycin (all Life Technologies, Germany). All cell lines were cultured at 37°C and 5% (v/v) CO_2. All lines were authenticated and tested negative for mycoplasma contamination.

Isolation and Culturing of Injected Tumor Cells From Zebrafish Embryos

Following confirmation of extravasation of injected tumor cells, the embryos section containing the extravasated cells were dissected within 24 hours post injection. Dissected embryos sections were transferred to phosphate-buffered saline (PBS) containing 50 U/mL penicillin (Gibco) and 0.05 mg/mL streptomycin (Gibco) (PBS/PS) for at least 15 min. The PBS/PS solution was refreshed once and individual embryos were transferred into a sterile tube (embryo + 500 uL PBS/PS) for 5 minutes. Embryos were then transferred to 200 uL of a 1% bleaching solution for 5 min. After replacing the bleaching solution with PBS/PS immediately and incubating for 5 min, embryos were centrifuged at 1,200 g (rcf) for 2 min at room temperature and the supernatant was discarded. Next, we added 300 uL of TripLE (Gibco) and incubated for 45 minutes at 37°C in a thermomixer, while mixing at 800 rpm. Next, we pipetted the embryo-TripLE, with a 200-uL tip, several times up and down under sterile conditions (cell culture hood), and immediately centrifuged (4 min, 1,200 g at room temperature). We discard the supernatant and resuspended with 400 uL of PBS and centrifuge (4 min, 1,200 g at room temperature). We resuspended the cell pellets in 200 uL of growth media and transferred the cell suspension to a 96-well plate (200 ul of media per well).

RNA-Seq Analysis

Following isolation from the zebrafish and the *in vitro* establishment of extravasation-positive cell lines, total RNA

was purified with the miRNeasy extraction kit (Qiagen) according to the manufacturer guidelines from cell pellets. RNA quality was assessed on a Bioanalyzer 2100 instrument using the RNA 6000 Nano Kit (Agilent). mRNA-seq sequencing libraries were prepared from 1 μg of purified RNA using the Illumina's TruSeq Stranded mRNA Library Prep Kit. Deep sequencing was performed on a Nextseq500 sequencer (Illumina) using 75 bp paired-end reads. Raw BCL (base call) files generated from the NextSeq sequencer were converted to FASTQ files using the bcl2fastq Conversion Software v2.18. During BCL to FASTQ processing, bcl2fastq also separates multiplexed samples, removes adapters, trims low quality bases, and removes low quality reads. Raw RNA-seq data in the FASTQ file format was quality controlled during and after sequencing to identify the potential technical issues. Cleaned sequencing reads were then mapped to the canine reference genome using STAR to generate read counts for each of the annotated genes (38). Gencode transcript annotations were supplied to facilitate the mapping of reads spanning known splicing junctions. The raw gene read count data was normalized using the voom approach (39). The differential expression analysis was performed using the linear model approach provided by the limma package (40). For the differential expression analysis, we only kept those genes with more than 30 raw read counts in at least two biological samples. The extravasation-positive D17 and HMPOS cells were analyzed against wild-type D17 and HMPOS cells grown *in vitro* without introduction to the zebrafish environment. The p-values for the coefficient/contrast of interest were adjusted for multiple testing using the Benjamini and Hochberg's method (41), which controls the expected false discovery rate (FDR). The significance threshold for gene differential expression was defined as a fold change greater than 2 and FDR less than 0.05. Venn diagrams were generated in Biovenn (42). Pathway analysis was performed using gene set enrichment analysis (43). Gene regulatory networks were inferred and annotated using GeneMANIA (44) within Cytoscape v3.8. For the pathways of interest identified by gene set enrichment analysis (Reactome extracellular matrix organization, Hallmark KRAS signaling UP, Hallmark IFNγ response), the list of genes in each pathway was obtained from MSigDB and used as an input for GeneMANIA. Networks were annotated using the log2 fold change from the RNA-Seq data for each cell line. The Cytoscape network analyzer tool was used to infer network interaction parameters, and a sum rank statistic was created from the following parameters: degree, clustering coefficient, closeness, betweenness, neighborhood connectivity, and stress.

Data Availability

All RNA-Seq data is available at NCBI GEO, Accession: GSE164246.

Statistical Analysis

Parametric and nonparametric analyses were used throughout the study. For continuous distribution data sets, we used either the Student's t-test or the Mann–Whitney Wilcoxon test for two groups. For multiple groups, either ANOVA followed by Fisher least square difference *post hoc* test or the Kruskal–Wallis followed by the Mann–Whitney–Wilcoxon was used. For two groups characterized as a frequency (percentage), we used comparison of proportions. P-values are presented either in the figure legend or figure panels.

The R2 genomics web tool (https://hgserver1.amc.nl/cgi-bin/r2/main.cgi) was used to plot Kaplan Meier curves to analyze the prognostic value of *VCAN* expression in osteosarcoma patients. The settings for this analysis were "Kaplan scan a single gene" and using the default time cut-offs. These data are from a previously published study and included 88 osteosarcoma patients, the clinical characteristics of whom are described in the originally-published study (PMID: 22454324; GEO accession number: GSE33383). Briefly, 64.3% of the patients in this cohort were male, 34.5% were female, and 1.2% with unknown gender. A total of 76.2% of the patients were under 20 years of age, 22.6% were over 20 years of age, and 1.2% (1) of the patients have unknown age. Primary tumor locations included the femur (47.6%), tibia/fibula (33.3%), humerus (13.1%), axial skeleton (1.2%), and unknown/other (4.8%). Histological subtype included osteoblastic (61.9%), chondroblastic (10.7%), fibroblastic (8.3%), telangiectatic (4.8%), minor subtype (13.1%), and unknown (1.2%). A total of 45.2% of the patients were grade 1 or 2, 39.3% were grades 3 or 4, and 16.7% were unknown or with tumor grades not available. Among the cohort, 82.1% of the patients had no metastasis at diagnosis, 16.7% had metastasis at diagnosis, and 1.2% had an unknown status of metastasis at diagnosis (45).

RESULTS

Circulating Canine Osteosarcoma Cells Extravasate as Clusters Through Angiopellosis

Two fluorescently labeled canine osteosarcoma cell lines (HMPOS and D17) were infused into the circulation of *Tg (fli1a:EGFP)* zebrafish with fluorescent blood vessels. We observed and isolated three biological replicates of the extravasated cell clusters (n = 3) (**Figure 1A**). Following cell infusion, zebrafish were microscopically observed for up to 48 hours. The clusters extravasated using angiopellosis, maintaining multicellularity, as noted by the characteristic remodeling of the vasculature around the clusters until the successful exit into the extravascular tissue (**Figure 1B** and **Supplementary Video 1**) (5, 10, 24).

A Systems-Level Approach Identifies Differential Expression of Core Pathways Involved in Proliferation, Immune Surveillance, and Extracellular Matrix Remodeling

To understand the molecular mechanisms by which tumor cell clusters successfully extravasated, we isolated the extravasation-positive clusters of HMPOS (a highly metastasizing sub-line of the POS osteosarcoma line) (46, 47) and a second metastatic osteosarcoma line, D17 (48), and performed RNA Sequencing

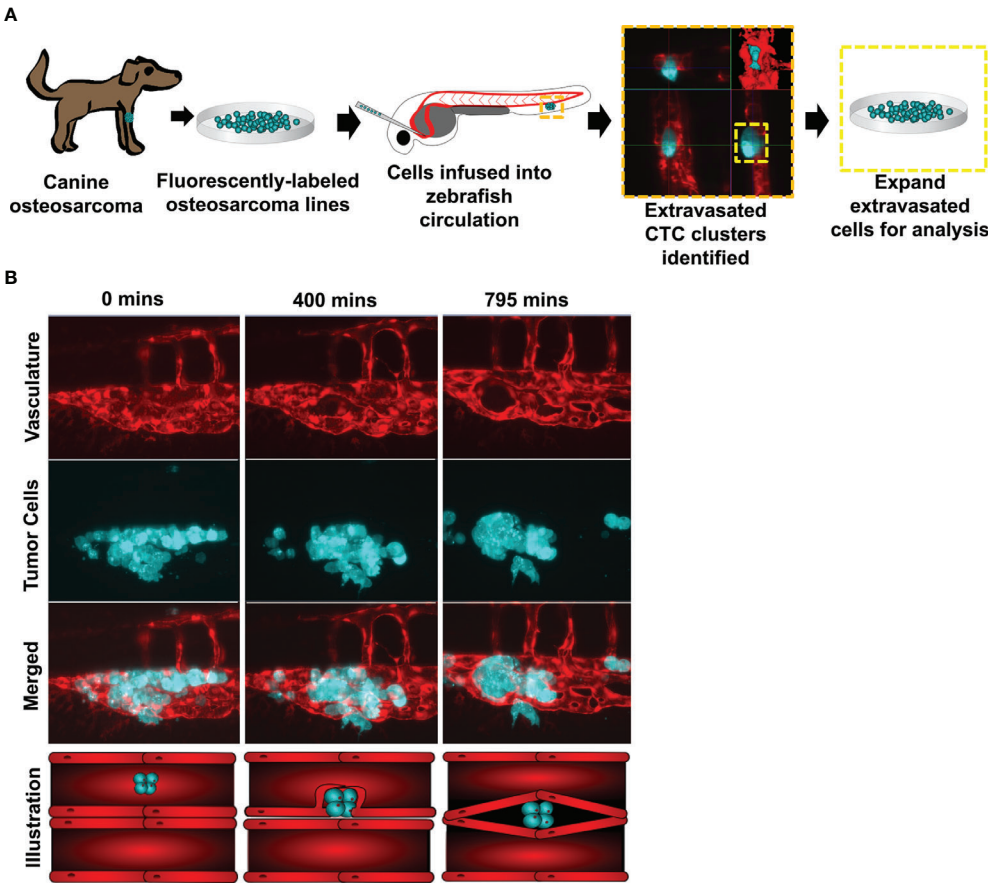

FIGURE 1 | Circulating canine osteosarcoma clusters extravasate by angiopellosis. **(A)** Illustration of the project workflow. Canine osteosarcoma cell lines were fluorescently labeled and infused into the circulation of *Tg(fli1a:egpf)* with fluorescent blood vessels. Tumor cells which extravasated as clusters were isolated and expanded, and these sub-lines were then molecularly profiled. **(B)** Representative image of infused D17 tumor cells aggregating as clusters in zebrafish circulation. Tumor cell clusters begin to extravasate through the endothelial cells of the blood vessels during metastasis. The tumor cluster is eventually completely removed from the inside of the vessels and is lodged in an extravascular cavity while maintaining multicellularity and not disassociating into single cells. SB = 20μM.

(RNA-Seq) on the resulting sub-lines (**Figure 2A**). Analysis of the RNA-Seq data from extravasated osteosarcoma cells revealed 391 (HMPOS) and 2,023 (D17) upregulated genes and 798 (HMPOS) and 2,338 (D17) downregulated genes ($p < 0.05$) (**Figure 2A** and **Supplementary Figure 1**). To identify the pathways that are commonly altered in the extravasated cell clusters, we applied a systems-level analysis of the RNA-Seq data. We first used gene set enrichment analysis to identify the pathways that were positively and negatively enriched in extravasated cells. While no positively-enriched pathways were common to both cell lines, the pathways enriched in downregulated genes in extravasated cells from both HMPOS and D17 lines included the KRAS signaling, interferon gamma response and other immune response pathways, and extracellular matrix organization (**Figures 2B, C**).

Next, we constructed gene regulatory networks for the enriched pathways from extravasated HMPOS and D17 cells. Gene regulatory networks provide a visual representation of gene interaction pathways, with the genes represented as circular nodes and the interactions between genes represented by lines (edges). Networks were visualized by overlaying the RNA-Seq log2 fold change values for each gene in the pathway, with larger red nodes representing a higher mRNA upregulation and larger blue nodes representing a larger mRNA downregulation in extravasated cells (**Supplementary Figures 2**, **3**). Qualitatively, these networks reveal largely unique patterns between the two cell lines, with distinct subsets of genes from unique locations within the network altered in each cell line (**Supplementary Figures 2**, **3**). To provide a more quantitative understanding of these differences between the cell lines, we next applied network analysis to these pathways, which outputs a suite of quantitative metrics to define the overall connectedness of the gene regulatory network. Networks were analyzed for the following parameters: degree, clustering coefficient, closeness, betweenness, neighborhood connectivity, and stress. We then plotted the sum rank score of these network parameters by the log2 fold change for each gene with a significant up- or downregulation in the network (**Supplementary Figures 2**, **3**). These analyses show an overall downregulation of

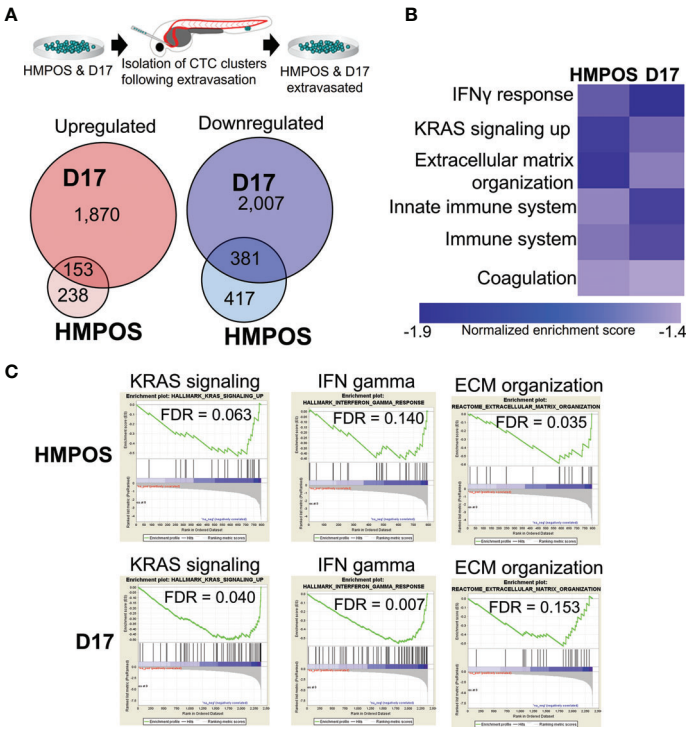

FIGURE 2 | Extravasated circulating tumor cells display differential expression of genes and pathways. **(A)** Overlaps in the upregulated and downregulated genes in extravasated circulating tumor cells. **(B)** Heat map of pathways commonly downregulated in extravasated circulating tumor cells. **(C)** Enrichment plots for KRAS signaling, IFN gamma response, and extracellular matrix (ECM) organization in HMPOS and D17 extravasated cells.

nodes across a range of connectivity within the network for both cell lines, with D17 cells having more downregulated genes in the network (**Supplementary Figures 2**, **3**). Despite the differences between the cell lines, several mRNA alterations with a high network connectedness were commonly altered in both cell lines (**Supplementary Figures 2**, **3**).

Extravasated Cells Upregulate Versican, Which Contributes to Extracellular Matrix Remodeling and Cellular Migration

We focused next on the extracellular matrix remodeling pathway as a known phenotypic driver of migration/invasion and metastasis. Like the other gene regulatory networks, extracellular matrix remodeling is commonly downregulated in both HMPOS and D17 extravasated cells (**Figures 3A, B**), but displays largely-unique gene-level changes in each cell line (**Figures 3A, B**). Most of the genes in the network are downregulated, with a very few upregulated highly-connected genes in the network (**Figures 3C, D**). One of the few commonly-altered genes in both cell lines, however, is versican. Versican is an extracellular matrix proteoglycan that regulates matrix remodeling, migration, and invasion (49). Interestingly, versican is significantly upregulated in both HMPOS and D17 extravasated cells and among the most connected genes in the ECM organization pathway (**Figures 3E, F**).

Analysis of the extracellular matrix remodeling network indicates that versican interacts with 58% of the core extracellular matrix remodeling network (42/72 nodes) within the pathway (**Figure 4A**, yellow nodes). Indeed, versican is in the top 10 most interconnected members of the network for neighborhood connectivity, betweenness centrality, and number of edges (**Figures 3B–D**). Together, these analyses indicate that versican is commonly upregulated in extravasated cells and interacts with a majority of nodes in the extracellular matrix remodeling pathway.

Versican was ranked in the top nodes based on neighborhood connectivity, betweenness centrality, and number of edges in the extracellular matrix remodeling pathway (**Figures 4B–D**). Also consistent with a role in extravasation and metastasis, an elevated versican expression is prognostic for a poorer metastasis-free survival (**Figure 4E**) and overall survival in osteosarcomas (**Figure 4F**).

DISCUSSION

The ability of CTCs to survive in circulation, extravasate at distant sites, and form new tumors is extremely rare (3, 50); however, when successful, these events often represent the precursors to a deadly disease (1, 51–53). During dissemination, CTCs must endure harsh conditions, including novel microenvironments, exposure to different cell types and signals, immune targeting, anchorage-independent growth, and shear force from circulation

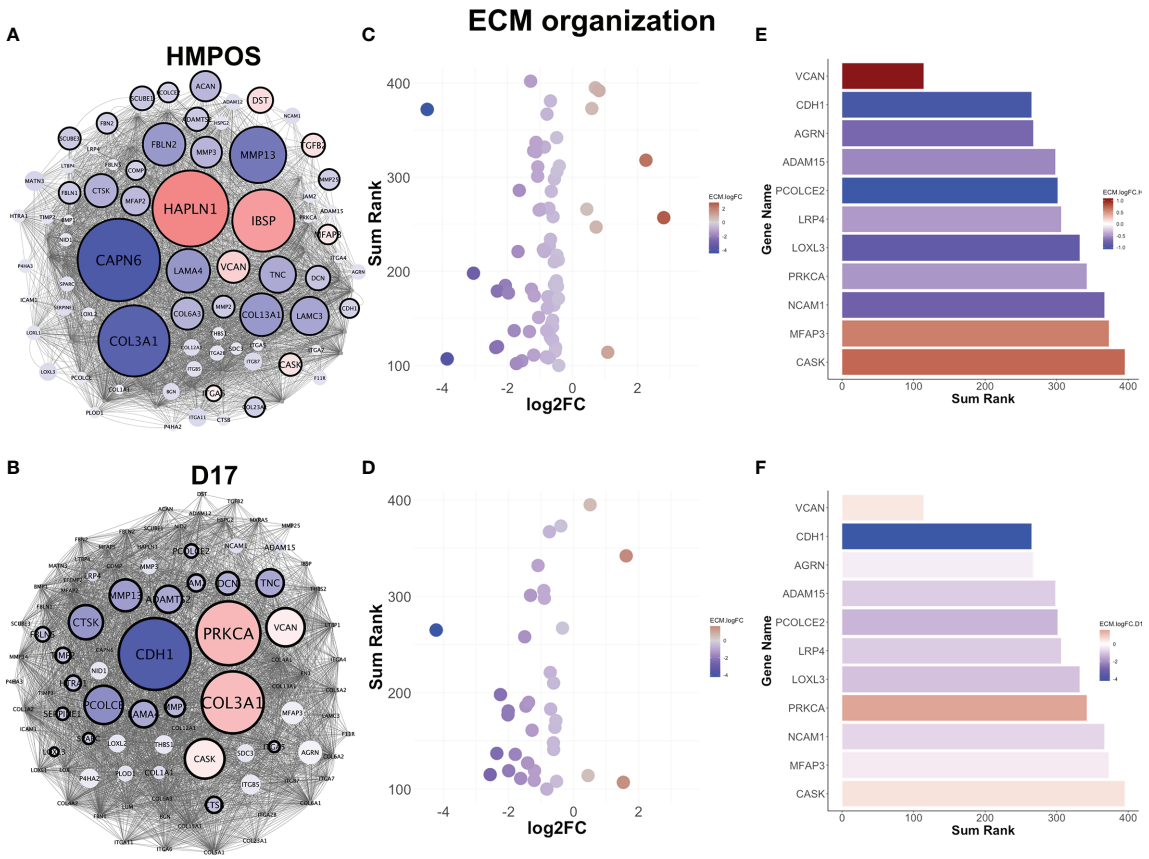

FIGURE 3 | Extravasated circulating tumor cells downregulate extracellular matrix remodeling. **(A)** Gene regulatory networks for the extracellular matrix remodeling pathway in HMPOS and **(B)**. D17. Blue denotes downregulation and red denotes upregulation (FDR < 0.05). Nodes are scaled proportionally to log2FC, with larger nodes depicting greater log2FC between extravasated and parental cell lines. **(C)** Scatter plot of sum rank of network connectivity parameters by log2FC for HMPOS and **(D)** D17. **(E)** Bar graphs of top connected genes in the pathway, colored by log2FC for HMPOS and **(F)** D17.

(1, 3, 6, 8, 12). Studies have shown that when CTCs form clusters, their ability to survive the metastatic process and seed distant sites is markedly increased. Some have postulated that the majority of cancer metastases occur as a result of these clusters rather than by individual CTCs (1–3, 50). The mechanisms through which these CTC clusters extravasate are only beginning to be understood. For example, melanoma and cervical CTC clusters have been observed extravasate out of blood vessels through *angiopellosis*, in which endothelial cells remodel the vessel architecture around the CTC clusters (5, 10, 12, 50, 54). This allows CTC clusters to maintain their multicellular phenotype (5). The establishment of relevant models to pinpoint and further investigate the specific markers of extravasation are limited, but this zebrafish model serves as a unique method to leverage the ability to perform *intravital* imaging and subsequent cell isolation to interrogate this process more fully (2, 3, 8, 13, 25, 27, 51).

Canine OS cells were specifically used in this project to 1) identify targets for further validation in human cells and 2) to leverage companion animal cancer data to investigate metastasis in both canines and humans. Many biologic behaviors of OS are conserved between people and dogs, and evidence suggests that leveraging the power of cross-species analyses facilitates the understanding of fundamental drivers of cancer mechanisms, as well as factors contributing to cancer initiation and progression (55–58). The ability of tumor cells from varying species and cancer types to undergo angiopellosis suggest that this mechanism of extravasation may be a common feature of CTC clusters. Prior studies have shown that non-tumor cells and cell membrane-coated microparticles possess the ability to undergo *angiopellosis*, suggesting that this phenomenon is not exclusive to CTCs, but may be utilized by CTCs during the metastasis process. Our data have pinpointed potential molecular drivers of extravasation, including the downregulation of proliferative signals (e.g., KRAS signaling), immune evasion, and versican-mediated ECM dysregulation during the metastasis process. Angiopellosis may serve as a physiological mechanism hijacked by specific types of cancer cells allowing for extravasation, similar to other extravasation mechanisms like cancer-mediated necrosis of endothelial cells, and transmigratory cup formation in neutrophil extravasation (59, 60). Further studies are needed to explore whether other non-cancerous cells utilize a similar gene dysregulation during *angiopellosis*.

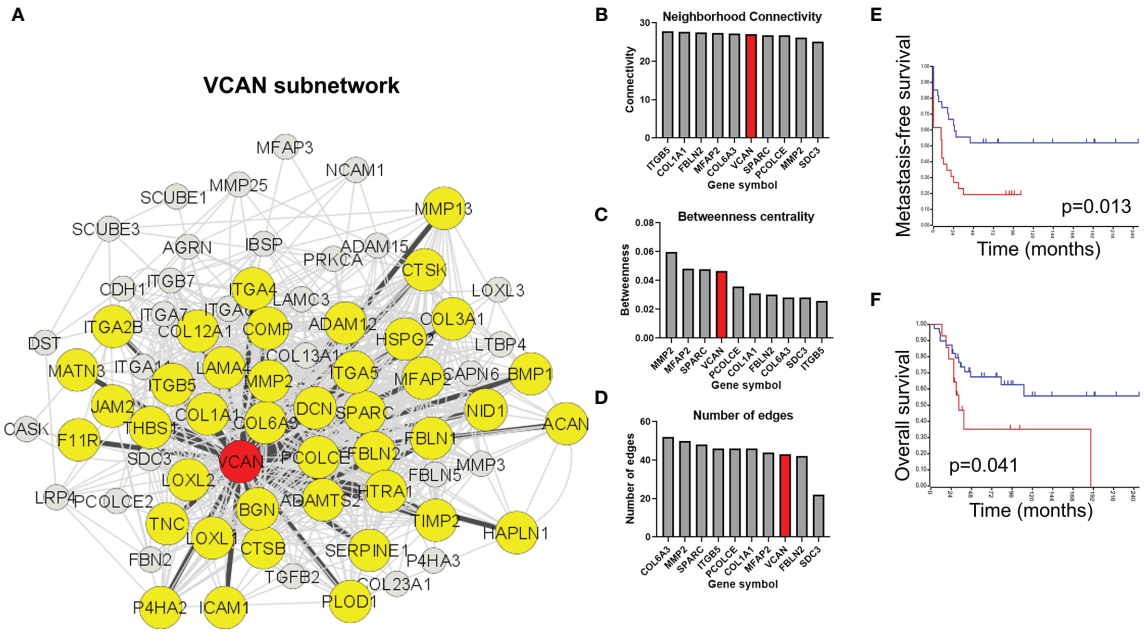

FIGURE 4 | Versican-mediated extracellular matrix organization is enriched in extravasated circulating tumor cells. **(A)** Versican is commonly upregulated in both cell lines and interacts with a core subset of the extracellular matrix organization pathway. Yellow nodes indicate proteins that share at least one interaction with versican. **(B)** Ranking of top nodes based on neighborhood connectivity, **(C)** betweenness centrality, and **(D)** number of edges in the extracellular matrix remodeling pathway. Prognostic value of VCAN for **(E)** metastasis-free survival and **(F)** overall survival in osteosarcoma patients.

Consistent with our analyses of osteosarcoma patient data, prior studies have shown that elevated levels of versican are associated with poor prognosis for patients with a wide range of malignant tumors (28, 30, 36). Indeed, versican and other ECM proteoglycans have been shown to impact the tumor cell behavior in myriad cancer types, in both human and canine models (61). While the exact mechanism by which versican promotes OS progression remains to be fully elucidated, previous studies suggest that versican contributes to the formation of a macromolecular complex in the ECM, which may account for the increased invasion and metastasis through promoting cancer cell motility and increased cell-cell adhesion (28, 62, 63).

In addition to its role in cellular migration, it is also possible that versican acts by altering cell adhesion, which contributes to the maintenance of tumor-propagating-like features of CTC clusters and augments their ability to proliferate at distant sites. Consistent with this, the cluster phenotype in CTCs is known to induce cells to express a more stem cell-like biology through the DNA methylation of binding sites typically occupied by stemness and proliferation regulators, including *OCT4*, *NANOG*, *SOX2*, and *SIN3A* (6, 64–67). Interestingly, the clustering of stem cells has been shown to protect their active pluripotent pathways with the disruption of cell-cell junctions resulting in the downregulation of proliferation regulators coupled with loss of stemness features (68–71). Previous studies have shown that the rates of CTC extravasation as either clusters or individual cells is similar, and while both could exit the vasculature similarly, the CTC clusters showed an increased ability to continue proliferation once out of the circulation, which contributed to their increased metastatic potential (2, 5). In this context, the dysregulation of versican and ECM may play an integral role in the cluster ability of CTCs by granting them an increased ability to form and maintain clusters, which gives them an increased chance to form tumors following extravasation. Additionally, versican-mediated alterations in cell adhesion may contribute to the interaction and adhesion of CTCs to the endothelial layer, which is known to play an important role in extravasation. Further studies are needed to fully elucidate 1) the impact of versican on CTC cluster formation and maintenance, 2) its localization during this process, and 3) its impact on CTC endothelial layer interactions/adhesion.

One unique advantage of this extravasation model system is that we can directly observe, capture, and molecularly interrogate CTC clusters exiting the vasculature. Current limitations in oncological imaging and detection normally prevent tumors from being isolated/identified unless they are still in the circulation or not until the CTCs have already extravasated and formed detectable tumor masses (4, 15, 51, 72). The need to address the specifics of CTC cluster metastasis/extravasation is paramount, as the cluster phenotype exhibits a markedly higher metastatic potential over their individual cell counterparts (1, 2, 5). The present study attempts to address some of these limitations and improve our understanding of the molecular underpinnings of CTC cluster extravasation.

This study had several limitations. The RNA-Seq analysis was performed on clusters that were isolated from zebrafish, but

the control cells for this analysis were the parental cells, instead of un-extravasated cells exposed to the zebrafish circulation. Despite multiple attempts to isolate these cells, the non-extravasated cells were not able to be successfully isolated, due to the reliance of the isolation system on the cells of interest being outside of the vasculature; a common limitation in this type of study (2, 11, 73–76). In addition, we were not able to obtain microscopic images to clearly reveal the level of detail necessary to confirm the extravasation of CTC clusters by angiopellosis. This study was instead focused on isolating the extravasated cells for downstream processing. Furthermore, to achieve sufficient levels of RNA for analysis, cells were expanded following isolation, rather than sequenced immediately following isolation, which serves as an additional variable in the RNA-seq results. Another limitation is the possibility that versican upregulation is a part of global dysregulation and regulated in conjunction with other ECM genes by an upstream regulator. Future studies will be needed to further investigate this potential, but also serves as a promising direction to better understand the global role of ECM in cancer progression.

This study focused on the molecular profiling of the CTC clusters that extravasated, rather than individual CTCs transiting the circulation. Due to this, it is important to note that the profiles identified may be exclusive to the CTC clusters that extravasate, rather than all CTCs. Overall, the observation of VCAN dysregulation in the canine OS cell lines used provide a starting point for more complex *in vivo* studies using this model to understanding the dynamics of extravasation and metastasis. Future studies are needed to investigate differences in the extravasation potential across different OS models and characterize their cluster morphology and underlying genomics. Additionally, future studies will examine a panel of high, low, and non-metastatic OS cell lines to determine the difference in the behavior and gene expression between cancers of varying metastatic/extravasation potential.

In summary, this study establishes the zebrafish *intravital* imaging model as a means to further investigate the specific steps of the extravasation process and identifies key pathway alterations that may drive extravasation during metastasis. These pathways may represent novel therapeutic targets to prevent CTC cluster formation, migration ability, and metastatic potential. Together, these data 1) establish a useful model to provide key insights into the biology of CTCs, extravasation, and metastasis, and 2) highlight an important connection between the phenotypic features of CTCs, including their ability to extravasate as multicellular clusters and their unique molecular features that may lead to the successful formation of secondary tumors.

DATA AVAILABILITY STATEMENT

The datasets presented in this study can be found in online repositories. The names of the repository/repositories and accession number(s) can be found below: NCBI GEO [accession: GSE164246].

ETHICS STATEMENT

The animal study was reviewed and approved by the North Carolina State University Institutional Animal Care and Use Committee. Code: 13-083-B.

AUTHOR CONTRIBUTIONS

Conceptualization: TA. Methodology: TA, MC, and HM. Formal analysis: TA, HM, LN, ES, and JS. Investigation: TA, HM, LN, ES, and JS. Resources: TA, JS, WE, LB, JY, and KC. Writing—original draft preparation: TA. Writing—review and editing: TA, JS, WE, JF, SP, KC, and MC. Visualization: TA, JS, MC, LN, and HM. Supervision: TA, JS, and KC. Funding acquisition: TA, KC, JS, and WE. All authors contributed to the article and approved the submitted version.

FUNDING

This research was funded by Andy's Army Canine Cancer Awareness Project (to TA, HM), the Carter Chinnis Charitable Trust (to WE), and National Cancer Institute (F31 CA217153 to TA). The funders had no role in the design of the study; in the collection, analyses, or interpretation of data; in the writing of the manuscript, or in the decision to publish the results.

ACKNOWLEDGMENTS

We thank Paige Nemec for her help with this study. We thank Eva Johannes (NCSU-CMIF) for her assistance with the light sheet microscopy, Antonio Planchart for providing the Tg(fli1a:egpf) zebrafish line, and Andrew Baltzegar (NCSU-GSL) for his assistance with performing the RNA-Sequencing. JS acknowledges support from the Triangle Center for Evolutionary Medicine and Duke Cancer Institute.

SUPPLEMENTARY MATERIAL

The Supplementary Material for this article can be found online at: https://www.frontiersin.org/articles/10.3389/fonc.2021.641187/full#supplementary-material

Supplementary Figure 1 | Top differentially expressed genes compared to parental lines. **(A)** A bi-clustering heatmap visualizing the expression profile of the top 30 differentially expressed genes in the D17 cell line sorted by their p-value by plotting their FKPM expression values in each biological replicate/samples. **(B)** A bi-clustering heatmap visualizing the expression profile of the top 30 differentially expressed genes in the HMPOScell line sorted by their p-value by plotting their FKPM expression values in each biological replicate/samples.

Supplementary Figure 2 | Extravasated circulating tumor cells downregulate KRAS signaling. **(A)** Gene regulatory networks for the KRAS signaling pathway in HMPOS and **(B)** D17. Blue denotes downregulation and red denotes upregulation (FDR<0.05). Nodes are scaled proportionally to log2FC, with larger nodes depicting greater log2FC between extravasated and parental cell lines. **(C)** Scatter plot of sum rank of network connectivity parameters by log2FC for HMPOS and **(D)** D17. **(E)** Bar graphs of top connected genes in the pathway, colored by log2FC for HMPOS and **(F)** D17.

Supplementary Figure 3 | Extravasated circulating tumor cells downregulate the interferon gamma response pathway. **(A)** Gene regulatory networks for the interferon gamma response pathway in HMPOS and **(B)** D17. Blue denotes downregulation and red denotes upregulation (FDR<0.05). Nodes are scaled proportionally to log2FC, with larger nodes depicting greater log2FC between extravasated and parental cell lines. **(C)** Scatter plot of sum rank of network connectivity parameters by log2FC for HMPOS and **(D)** D17. **(E)** Bar graphs of top connected genes in the pathway, colored by log2FC for HMPOS and **(F)** D17.

Supplementary Video 1 | A representative time-lapse video of circulating tumor cell clusters (cyan) extravasating from the inside/lumen of zebrafish blood vessels (red) into the surrounding extravascular cavity. SB = 20 μm.

REFERENCES

1. Weiss L. Metastatic Inefficiency. *Adv Cancer Res* (1990) 54:159–211. doi: 10.1016/s0065-230x(08)60811-8
2. Aceto N, Bardia A, Miyamoto DT, Donaldson MC, Wittner BS, Spencer JA, et al. Circulating Tumor Cell Clusters are Oligoclonal Precursors of Breast Cancer Metastasis. *Cell* (2014) 158:1110–22. doi: 10.1016/j.cell.2014.07.013
3. Aceto N, Toner M, Maheswaran S, Haber DA. En Route to Metastasis: Circulating Tumor Cell Clusters and Epithelial-To-Mesenchymal Transition. *Trends Cancer* (2015) 1:44–52. doi: 10.1016/j.trecan.2015.07.006
4. Cheung KJ, Padmanaban V, Silvestri V, Schipper K, Cohen JD, Fairchild AN, et al. Polyclonal Breast Cancer Metastases Arise From Collective Dissemination of Keratin 14-Expressing Tumor Cell Clusters. *Proc Natl Acad Sci USA* (2016) 113:E854–863. doi: 10.1073/pnas.1508541113
5. Allen TA, Asad D, Amu E, Hensley MT, Cores J, Vandergriff A, et al. Circulating Tumor Cells Exit Circulation While Maintaining Multicellularity, Augmenting Metastatic Potential. *J Cell Sci* (2019) 132:jcs231563. doi: 10.1242/jcs.231563
6. Gkountela S, Castro-Giner F, Szczerba BM, Vetter M, Landin J, Scherrer R, et al. Circulating Tumor Cell Clustering Shapes DNA Methylation to Enable Metastasis Seeding. *Cell* (2019) 176:98–112.e114. doi: 10.1016/j.cell.2018.11.046
7. Szczerba BM, Castro-Giner F, Vetter M, Krol I, Gkountela S, Landin J, et al. Neutrophils Escort Circulating Tumour Cells to Enable Cell Cycle Progression. *Nature* (2019) 566:553–7. doi: 10.1038/s41586-019-0915-y
8. Au SH, Storey BD, Moore JC, Tang Q, Chen Y-L, Javaid S, et al. Clusters of Circulating Tumor Cells Traverse Capillary-Sized Vessels. *Proc Natl Acad Sci* (2016) 113:4947. doi: 10.1073/pnas.1524448113
9. Rejniak KA. Circulating Tumor Cells: When a Solid Tumor Meets a Fluid Microenvironment. *Adv Exp Med Biol* (2016) 936:93–106. doi: 10.1007/978-3-319-42023-3_5
10. Allen TA, Gracieux D, Talib M, Tokarz DA, Hensley MT, Cores J, et al. Angiopellosis as an Alternative Mechanism of Cell Extravasation. *Stem Cells* (2017) 35:170–80. doi: 10.1002/stem.2451
11. Gupta GP, Nguyen DX, Chiang AC, Bos PD, Kim JY, Nadal C, et al. Mediators of Vascular Remodelling Co-Opted for Sequential Steps in Lung Metastasis. *Nature* (2007) 446:765–70. doi: 10.1038/nature05760
12. Follain G, Osmani N, Azevedo AS, Allio G, Mercier L, Karreman MA, et al. Hemodynamic Forces Tune the Arrest, Adhesion, and Extravasation of Circulating Tumor Cells. *Dev Cell* (2018) 45:33–52.e12. doi: 10.1016/j.devcel.2018.02.015
13. Follain G, Osmani N, Fuchs C, Allio G, Harlepp S, Goetz JG. Using the Zebrafish Embryo to Dissect the Early Steps of the Metastasis Cascade. *Methods Mol Biol (Clifton NJ)* (2018) 1749:195–211. doi: 10.1007/978-1-4939-7701-7_15
14. Tobia C, Gariano G, De Sena G, Presta M. Zebrafish Embryo as a Tool to Study Tumor/Endothelial Cell Cross-Talk. *Biochim Biophys Acta* (2013) 1832:1371–7. doi: 10.1016/j.bbadis.2013.01.016
15. Hayashi M, Zhu P, McCarty G, Meyer CF, Pratilas CA, Levin A, et al. Size-Based Detection of Sarcoma Circulating Tumor Cells and Cell Clusters. *Oncotarget* (2017) 8:78965–77. doi: 10.18632/oncotarget.20697
16. Donato C, Kunz L, Castro-Giner F, Paasinen-Sohns A, Strittmatter K, Szczerba BM, et al. Hypoxia Triggers the Intravasation of Clustered Circulating Tumor Cells. *Cell Rep* (2020) 32:108105. doi: 10.1016/j.celrep.2020.108105
17. Mirabello L, Troisi RJ, Savage SA. Osteosarcoma Incidence and Survival Rates From 1973 to 2004: Data From the Surveillance, Epidemiology, and End Results Program. *Cancer* (2009) 115:1531–43. doi: 10.1002/cncr.24121
18. Egenvall A, Nødtvedt A, von Euler H. Bone Tumors in a Population of 400 000 Insured Swedish Dogs Up to 10 Y of Age: Incidence and Survival. *Can J Veterinary Res = Rev Can Recherche Veterinaire* (2007) 71:292–9.
19. Tsuchiya H, Kanazawa Y, Abdel-Wanis ME, Asada N, Abe S, Isu K, et al. Effect of Timing of Pulmonary Metastases Identification on Prognosis of Patients With Osteosarcoma: The Japanese Musculoskeletal Oncology Group Study. *J Clin Oncol* (2002) 20:3470–7. doi: 10.1200/JCO.2002.11.028
20. Kempf-Bielack B, Bielack SS, Jürgens H, Branscheid D, Berdel WE, Exner GU, et al. Osteosarcoma Relapse After Combined Modality Therapy: An Analysis of Unselected Patients in the Cooperative Osteosarcoma Study Group (COSS). *J Clin Oncol* (2005) 23:559–68. doi: 10.1200/JCO.2005.04.063
21. Simpson S, Dunning MD, de Brot S, Grau-Roma L, Mongan NP, Rutland CS. Comparative Review of Human and Canine Osteosarcoma: Morphology, Epidemiology, Prognosis, Treatment and Genetics. *Acta Vet Scand* (2017) 59:71–1. doi: 10.1186/s13028-017-0341-9
22. Visonneau S, Cesano A, Jeglum KA, Santoli D. Adjuvant Treatment of Canine Osteosarcoma With the Human Cytotoxic T-Cell Line TALL-104. *Clin Cancer Res* (1999) 5:1868.
23. Delov V, Muth-Köhne E, Schäfers C, Fenske M. Transgenic Fluorescent Zebrafish Tg(fli1:EGFP)y1 for the Identification of Vasotoxicity Within the zFET. *Aquat Toxicol* (2014) 150:189–200. doi: 10.1016/j.aquatox.2014.03.010
24. Kanada M, Zhang J, Yan L, Sakurai T, Terakawa S. Endothelial Cell-Initiated Extravasation of Cancer Cells Visualized in Zebrafish. *PeerJ* (2014) 2:e688–8. doi: 10.7717/peerj.688
25. Stoletov K, Kato H, Zardouzian E, Kelber J, Yang J, Shattil S, et al. Visualizing Extravasation Dynamics of Metastatic Tumor Cells. *J Cell Sci* (2010) 123:2332. doi: 10.1242/jcs.069443
26. Stoletov K, Klemke R. Catch of the Day: Zebrafish as a Human Cancer Model. *Oncogene* (2008) 27:4509–20. doi: 10.1038/onc.2008.95
27. Liotta LA, Kohn EC. The Microenvironment of the Tumour-Host Interface. *Nature* (2001) 411:375–9. doi: 10.1038/35077241
28. Mitsui Y, Shiina H, Kato T, Maekawa S, Hashimoto Y, Shiina M, et al. Versican Promotes Tumor Progression, Metastasis and Predicts Poor Prognosis in Renal Carcinoma. *Mol Cancer Res MCR* (2017) 15:884–95. doi: 10.1158/1541-7786.Mcr-16-0444
29. Du WW, Yang W, Yee AJ. Roles of Versican in Cancer Biology–Tumorigenesis, Progression and Metastasis. *Histol Histopathol* (2013) 28:701–13. doi: 10.14670/hh-28.701
30. Yang W, Yee AJ. Versican V2 Isoform Enhances Angiogenesis by Regulating Endothelial Cell Activities and Fibronectin Expression. *FEBS Lett* (2013) 587:185–92. doi: 10.1016/j.febslet.2012.11.023
31. Gao R, Cao C, Zhang M, Lopez MC, Yan Y, Chen Z, et al. A Unifying Gene Signature for Adenoid Cystic Cancer Identifies Parallel MYB-Dependent and MYB-Independent Therapeutic Targets. *Oncotarget* (2014) 5:12528–42. doi: 10.18632/oncotarget.2985
32. Fujii K, Karpova MB, Asagoe K, Georgiev O, Dummer R, Urosevic-Maiwald M. Versican Upregulation in Sézary Cells Alters Growth, Motility and Resistance to Chemotherapy. *Leukemia* (2015) 29:2024–32. doi: 10.1038/leu.2015.103
33. Nikitovic D, Zafiropoulos A, Katonis P, Tsatsakis A, Theocharis AD, Karamanos NK, et al. Transforming Growth Factor-β as a Key Molecule Triggering the Expression of Versican Isoforms V0 and V1, Hyaluronan Synthase-2 and Synthesis of Hyaluronan in Malignant Osteosarcoma Cells. *IUBMB Life* (2006) 58:47–53. doi: 10.1080/15216540500531713

34. Ricciardelli C, Mayne K, Sykes PJ, Raymond WA, McCaul K, Marshall VR, et al. Elevated Levels of Versican But Not Decorin Predict Disease Progression in Early-Stage Prostate Cancer. *Clin Cancer Res an Off J Am Assoc Cancer Res* (1998) 4:963–71.
35. Suwiwat S, Ricciardelli C, Tammi R, Tammi M, Auvinen P, Kosma VM, et al. Expression of Extracellular Matrix Components Versican, Chondroitin Sulfate, Tenascin, and Hyaluronan, and Their Association With Disease Outcome in Node-Negative Breast Cancer. *Clin Cancer Res an Off J Am Assoc Cancer Res* (2004) 10:2491–8. doi: 10.1158/1078-0432.ccr-03-0146
36. Ghosh S, Albitar L, LeBaron R, Welch WR, Samimi G, Birrer MJ, et al. Up-Regulation of Stromal Versican Expression in Advanced Stage Serous Ovarian Cancer. *Gynecologic Oncol* (2010) 119:114–20. doi: 10.1016/j.ygyno.2010.05.029
37. Suhovskih AV, Aidagulova SV, Kashuba VI, Grigorieva EV. Proteoglycans as Potential Microenvironmental Biomarkers for Colon Cancer. *Cell Tissue Res* (2015) 361:833–44. doi: 10.1007/s00441-015-2141-8
38. Dobin A, Davis CA, Schlesinger F, Drenkow J, Zaleski C, Jha S, et al. STAR: Ultrafast Universal RNA-Seq Aligner. *Bioinformatics* (2013) 29:15–21. doi: 10.1093/bioinformatics/bts635
39. Law CW, Chen Y, Shi W, Smyth GK. Voom: Precision Weights Unlock Linear Model Analysis Tools for RNA-Seq Read Counts. *Genome Biol* (2014) 15:R29. doi: 10.1186/gb-2014-15-2-r29
40. Ritchie ME, Phipson B, Wu D, Hu Y, Law CW, Shi W. Smyth, G.K. Limma Powers Differential Expression Analyses for RNA-Sequencing and Microarray Studies. *Nucleic Acids Res* (2015) 43:e47. doi: 10.1093/nar/gkv007
41. Benjamini Y, Hochberg Y. Controlling the False Discovery Rate: A Practical and Powerful Approach to Multiple Testing. *J R Stat Society Ser B (Methodological)* (1995) 57:289–300. doi: 10.1111/j.2517-6161.1995.tb02031.x
42. Hulsen T, de Vlieg J, Alkema W. BioVenn - a Web Application for the Comparison and Visualization of Biological Lists Using Area-Proportional Venn Diagrams. *BMC Genomics* (2008) 9:488. doi: 10.1186/1471-2164-9-488
43. Subramanian A, Tamayo P, Mootha VK, Mukherjee S, Ebert BL, Gillette MA, et al. Gene Set Enrichment Analysis: A Knowledge-Based Approach for Interpreting Genome-Wide Expression Profiles. *Proc Natl Acad Sci USA* (2005) 102:15545–50. doi: 10.1073/pnas.0506580102
44. Franz M, Rodriguez H, Lopes C, Zuberi K, Montojo J, Bader GD, et al. GeneMANIA Update 2018. *Nucleic Acids Res* (2018) 46:W60–4. doi: 10.1093/nar/gky311
45. Kuijjer ML, Rydbeck H, Kresse SH, Buddingh EP, Lid AB, Roelofs H, et al. Identification of Osteosarcoma Driver Genes by Integrative Analysis of Copy Number and Gene Expression Data. *Genes Chromosomes Cancer* (2012) 51:696–706. doi: 10.1002/gcc.21956
46. Kadosawa T, Nozaki K, Sasaki N, Takeuchi A. Establishment and Characterization of a New Cell Line From a Canine Osteosarcoma. *J Veterinary Med Sci* (1994) 56:1167–9. doi: 10.1292/jvms.56.1167
47. Barroga EF, Kadosawa T, Okumura M, Fujinaga T. Establishment and Characterization of the Growth and Pulmonary Metastasis of a Highly Lung Metastasizing Cell Line From Canine Osteosarcoma in Nude Mice. *J Veterinary Med Sci* (1999) 61:361–7. doi: 10.1292/jvms.61.361
48. Legare ME, Bush J, Ashley AK, Kato T, Hanneman WH. Cellular and Phenotypic Characterization of Canine Osteosarcoma Cell Lines. *J Cancer* (2011) 2:262–70. doi: 10.7150/jca.2.262
49. Wight TN, Kinsella MG, Evanko SP, Potter-Perigo S, Merrilees MJ. Versican and the Regulation of Cell Phenotype in Disease. *Biochim Biophys Acta* (2014) 1840:2441–51. doi: 10.1016/j.bbagen.2013.12.028
50. Cheung KJ, Ewald AJ. A Collective Route to Metastasis: Seeding by Tumor Cell Clusters. *Sci (New York N.Y.)* (2016) 352:167–9. doi: 10.1126/science.aaf6546
51. Yu M, Stott S, Toner M, Maheswaran S, Haber DA. Circulating Tumor Cells: Approaches to Isolation and Characterization. *J Cell Biol* (2011) 192:373–82. doi: 10.1083/jcb.201010021
52. Alix-Panabières C, Pantel K. Circulating Tumor Cells: Liquid Biopsy of Cancer. *Clin Chem* (2013) 59:110–8. doi: 10.1373/clinchem.2012.194258
53. Luzzi KJ, MacDonald IC, Schmidt EE, Kerkvliet N, Morris VL, Chambers AF, et al. Multistep Nature of Metastatic Inefficiency: Dormancy of Solitary Cells After Successful Extravasation and Limited Survival of Early Micrometastases. *Am J Pathol* (1998) 153:865–73. doi: 10.1016/s0002-9440(10)65628-3
54. Xu S, Ware KE, Ding Y, Kim SY, Sheth MU, Rao S, et al. An Integrative Systems Biology and Experimental Approach Identifies Convergence of Epithelial Plasticity, Metabolism, and Autophagy to Promote Chemoresistance. *J Clin Med* (2019) 8(2):205. doi: 10.3390/jcm8020205
55. Fan TM, Khanna C Comparative Aspects of Osteosarcoma Pathogenesis in Humans and Dogs. *Vet Sci* (2015 2:210–30. doi: 10.3390/vetsci2030210
56. Somarelli JA, Boddy AM, Gardner HL, DeWitt SB, Tuohy J, Megquier K, et al. Improving Cancer Drug Discovery by Studying Cancer Across the Tree of Life. *Mol Biol Evol* (2020) 37:11–7. doi: 10.1093/molbev/msz254
57. Somarelli JA, Rupprecht G, Altunel E, Flamant EM, Rao S, Sivaraj D, et al. A Comparative Oncology Drug Discovery Pipeline to Identify and Validate New Treatments for Osteosarcoma. *Cancers* (2020) 12. doi: 10.3390/cancers12113335
58. Gordon I, Paoloni M, Mazcko C, Khanna C. The Comparative Oncology Trials Consortium: Using Spontaneously Occurring Cancers in Dogs to Inform the Cancer Drug Development Pathway. *PLoS Med* (2009) 6: e1000161. doi: 10.1371/journal.pmed.1000161
59. Carman CV, Springer TA. A Transmigratory Cup in Leukocyte Diapedesis Both Through Individual Vascular Endothelial Cells and Between Them. *J Cell Biol* (2004) 167:377–88. doi: 10.1083/jcb.200404129
60. Strilic B, Yang L, Albarrán-Juárez J, Wachsmuth L, Han K, Müller UC, et al. Tumour-Cell-Induced Endothelial Cell Necroptosis via Death Receptor 6 Promotes Metastasis. *Nature* (2016) 536:215–8. doi: 10.1038/nature19076
61. Dos Reis DC, Damasceno KA, de Campos CB, Veloso ES, Pêgas GRA, Kraemer LR, et al. Versican and Tumor-Associated Macrophages Promotes Tumor Progression and Metastasis in Canine and Murine Models of Breast Carcinoma. *Front Oncol* (2019) 9:577. doi: 10.3389/fonc.2019.00577
62. Ricciardelli C, Russell DL, Ween MP, Mayne K, Suwiwat S, Byers S, et al. Formation of Hyaluronan- and Versican-Rich Pericellular Matrix by Prostate Cancer Cells Promotes Cell Motility. *J Biol Chem* (2007) 282:10814–25. doi: 10.1074/jbc.M606991200
63. Ween MP, Oehler MK, Ricciardelli C. Role of Versican, Hyaluronan and CD44 in Ovarian Cancer Metastasis. *Int J Mol Sci* (2011) 12:1009–29. doi: 10.3390/ijms12021009
64. Niwa H. How Is Pluripotency Determined and Maintained? *Dev (Cambridge England)* (2007) 134:635–46. doi: 10.1242/dev.02787
65. Kim J, Chu J, Shen X, Wang J, Orkin SH. An Extended Transcriptional Network for Pluripotency of Embryonic Stem Cells. *Cell* (2008) 132:1049–61. doi: 10.1016/j.cell.2008.02.039
66. van den Berg DL, Snoek T, Mullin NP, Yates A, Bezstarosti K, Demmers J, et al. An Oct4-Centered Protein Interaction Network in Embryonic Stem Cells. *Cell Stem Cell* (2010) 6:369–81. doi: 10.1016/j.stem.2010.02.014
67. McDonel P, Demmers J, Tan DW, Watt F, Hendrich BD. Sin3a is Essential for the Genome Integrity and Viability of Pluripotent Cells. *Dev Biol* (2012) 363:62–73. doi: 10.1016/j.ydbio.2011.12.019
68. Li D, Zhou J, Wang L, Shin ME, Su P, Lei X, et al. Integrated Biochemical and Mechanical Signals Regulate Multifaceted Human Embryonic Stem Cell Functions. *J Cell Biol* (2010) 191:631–44. doi: 10.1083/jcb.201006094
69. Li L, Wang S, Jezierski A, Moalim-Nour L, Mohib K, Parks RJ, et al. A Unique Interplay Between Rap1 and E-Cadherin in the Endocytic Pathway Regulates Self-Renewal of Human Embryonic Stem Cells. *Stem Cells* (2010) 28:247–57. doi: 10.1002/stem.289
70. Li L, Bennett SA, Wang L. Role of E-Cadherin and Other Cell Adhesion Molecules in Survival and Differentiation of Human Pluripotent Stem Cells. *Cell Adhesion Migration* (2012) 6:59–70. doi: 10.4161/cam.19583
71. Pieters T, van Roy F. Role of Cell-Cell Adhesion Complexes in Embryonic Stem Cell Biology. *J Cell Sci* (2014) 127:2603–13. doi: 10.1242/jcs.146720
72. Adams DL, Martin SS, Alpaugh RK, Charpentier M, Tsai S, Bergan RC, et al. Circulating Giant Macrophages as a Potential Biomarker of Solid Tumors. *Proc Natl Acad Sci USA* (2014) 111:3514–9. doi: 10.1073/pnas.1320198111
73. Bos PD, Zhang XHF, Nadal C, Shu W, Gomis RR, Nguyen DX, et al. Genes That Mediate Breast Cancer Metastasis to the Brain. *Nature* (2009) 459:1005–9. doi: 10.1038/nature08021
74. Kim S, Takahashi H, Lin W-W, Descargues P, Grivennikov S, Kim Y, et al. Carcinoma-Produced Factors Activate Myeloid Cells Through TLR2 to Stimulate Metastasis. *Nature* (2009) 457:102–6. doi: 10.1038/nature07623
75. Picker LJ, Kishimoto TK, Smith CW, Warnock RA, Butcher EC. ELAM-1 is an Adhesion Molecule for Skin-Homing T Cells. *Nature* (1991) 349:796–9. doi: 10.1038/349796a0

76. Qian B-Z, Li J, Zhang H, Kitamura T, Zhang J, Campion LR, et al. CCL2 Recruits Inflammatory Monocytes to Facilitate Breast-Tumour Metastasis. *Nature* (2011) 475:222–5. doi: 10.1038/nature10138

Conflict of Interest: The authors declare that the research was conducted in the absence of any commercial or financial relationships that could be construed as a potential conflict of interest.

Publisher's Note: All claims expressed in this article are solely those of the authors and do not necessarily represent those of their affiliated organizations, or those of the publisher, the editors and the reviewers. Any product that may be evaluated in this article, or claim that may be made by its manufacturer, is not guaranteed or endorsed by the publisher.

Advantages of publishing in Frontiers

OPEN ACCESS
Articles are free to read for greatest visibility and readership

FAST PUBLICATION
Around 90 days from submission to decision

HIGH QUALITY PEER-REVIEW
Rigorous, collaborative, and constructive peer-review

TRANSPARENT PEER-REVIEW
Editors and reviewers acknowledged by name on published articles

Frontiers
Avenue du Tribunal-Fédéral 34
1005 Lausanne | Switzerland

Visit us: www.frontiersin.org
Contact us: frontiersin.org/about/contact

REPRODUCIBILITY OF RESEARCH
Support open data and methods to enhance research reproducibility

DIGITAL PUBLISHING
Articles designed for optimal readership across devices

FOLLOW US
@frontiersin

IMPACT METRICS
Advanced article metrics track visibility across digital media

EXTENSIVE PROMOTION
Marketing and promotion of impactful research

LOOP RESEARCH NETWORK
Our network increases your article's readership